STEADY LAMINAR AND TURBULENT FLOW THROUGH VASCULAR STENOSIS MODELS

A THESIS

Presented to

The Faculty of the Division

of Graduate Studies

By

Mohan D. Deshpande

In Partial Fulfillment

of the Requirements for the Degree

Doctor of Philosophy in the

School of Aerospace Engineering

Georgia Institute of Technology

June, 1977

STEADY LAMINAR AND TURBULENT FLOW THROUGH

VASCULAR STENOSIS MODELS

Approved:

D. P. Giddens, Chairman

L. H. Bangert

J. C. Wu

Date approved by Chairman: 4/11/77

ACKNOWLEDGMENTS

I wish to express my sincere appreciation to my advisor, Prof. D. P. Giddens, for his suggestion of the dissertation topic, and for his constant advice and encouragement. His guidance in interpreting the results was both stimulating and enlightening.

I am very obliged to Dr. R. A. Cassanova for his generous help and cooperation while conducting the experiments.

I also wish to thank Prof. L. H. Bangert and Prof. J. C. Wu for their careful reading of the manuscript and for their useful suggestions.

Assistance given by Mr. W. A. Carpenter in the analysis of the experimental data is gratefully appreciated.

The financial assistance given by the K. C. Mahindra Education Trust, Bombay and the School of Aerospace Engineering is gratefully acknowledged.

Finally, I am grateful to my parents for their constant encouragement and for being a source of inspiration.

TABLE OF CONTENTS

LIST OF TABLES

LIST OF ILLUSTRATIONS

Figure Page

NOMENCLATURE

a_o	radius of the unoccluded tube
C_1, C_2, C_D	constants in the k-ε model equations
f_D	Doppler frequency ($f_s - f_i$)
f_i	frequency of incident light
f_s	frequency of scattered light
h	interval between grid points in R-direction
H	total head
i	counter for grid points in Z-direction
i	semiangle between laser beams
i_o	semiangle between laser beams in air
j	counter for grid points in R-direction
k	interval between grid points in Z-direction
k	turbulence kinetic energy (both dimensional and nondimensional)
K	constant in the transformation of Z-coordinate
ℓ	length scale of turbulence
n	direction normal to the wall
p	pressure
P	nondimensional pressure $pa_o/\rho\nu U$
r	radial coordinate
r_o	wall radius as a function of z
R	nondimensional radial coordinate r/a_o
R_o	nondimensional wall radius as a function of Z

Re	Reynolds number $Ua_o/\nu = 2\bar{u}a_o/\nu$
s	direction tangential to wall
t	thickness of the test-section wall
$\bar{u}$	average velocity in the unoccluded tube
u_*	friction velocity $\sqrt{\lvert\tau_w\rvert}$
u'	longitudinal velocity fluctuation
U	maximum velocity on the axis far away from stenosis in laminar flow
v_r	radial velocity
v_z	axial velocity
v_ϕ	azimuthal velocity
v'	radial velocity fluctuation
V_R	nondimensional radial velocity $v_r/2\bar{u}$
V_Z	nondimensional axial velocity $v_z/2\bar{u}$
V_ϕ	nondimensional aximuthal velocity $v_\phi/2\bar{u}$
w'	azimuthal velocity fluctuation
y_w	distance between measuring volume and wall towards the laser
y(air)	distance traversed by laser to move measuring volume by y_w
Y	nondimensional distance from the wall
z	axial coordinate measured from the throat of the stenosis (for entrance flow problem z is measured from entrance plane)
Z	nondimensional axial coordinate z/a_o
Z_o	half length of stenosis
α	the height of stenosis
δ	change in direction of beam due to tube wall

ε	rate of dissipation of turbulence kinetic energy k (both dimensional and nondimensional)
η	transformed axial coordinate Tanh (KZ)
θ	inclination of the wall to the axis
κ	von Karman constant
λ	wavelength of incident laser light
μ	refractive index of plexiglas w.r.t. water (1.12)
μ_p	refractive index of plexiglas (1.49)
μ_w	refractive index of water (1.33)
ν	kinematic viscosity
ν_e	effective viscosity in turbulent flow k^2/ε
ρ	density of fluid
σ_k, σ_e	turbulent Prandtl/Schmidt numbers for diffusion of k and ε respectively
τ	shear stress
τ_w	shear stress on wall
ϕ	dummy variable representing ψ, ω/R, k or ε
ϕ	azimuthal angle
ψ	nondimensional stream function
ω	nondimensional vorticity $\partial V_R/\partial Z - \partial V_Z/\partial R$
ω_w	nondimensional vorticity on wall

SUMMARY

A theoretical and experimental study of steady flow through vascular stenosis models has been conducted. One motivation for this study is the possibility that hemodynamic factors may participate in the genesis and proliferation of atherosclerosis. In addition, it is believed that flow disturbances caused by the stenosis may be of value in the early diagnosis of the vascular disease.

Axisymmetric, incompressible, steady flow was examined. The laminar flow field was computed for four stenosis models of moderate to severe constriction using the Navier-Stokes equations. Then, a two-equation (equations for turbulence kinetic energy and its dissipation rate) turbulence model was employed to predict the turbulent flow through the stenosis models. Finally, turbulent flow was studied experimentally for a single geometry with 75 percent area reduction. The turbulent entrance flow in a pipe was analyzed computationally as a test case. Results from laminar theory were compared with experimental data available in the literature, and the turbulent flow calculations were compared with the measurements obtained in the present research.

The results show that the critical Reynolds number at which the laminar flow separates is smaller for more severe stenoses. The length of the laminar recirculation region

increases with the Reynolds number. The pressure drop across stenosis and the maximum shear stress on the wall increase with an increase in the reduction of area and an increase in Reynolds number. Comparison with the available experimental data is good. Those experiments indicate that flow becomes unstable for relatively low Reynolds numbers. The Reynolds number for which the computations were carried out covered the entire range for which the flow remains laminar.

The turbulent computations were obtained for Reynolds numbers 10×10^3, 15×10^3, 30×10^3 and 3.88×10^5. The Reynolds number of major interest was 15,000 since the experiments were executed at this value. A procedure to solve linear equations forming coupled tridiagonal-type matrices was devised to solve the difference equations originating from the equations for turbulence kinetic energy and its dissipation rate. This algorithm was useful in obtaining converged solutions.

In vitro measurements in a water flow system were performed primarily for a Reynolds number of 15,000. They included mean velocity, axial and azimuthal velocity fluctuations, and their energy spectra. A laser Doppler anemometer was used for this purpose. The location of the reattachment point and the pressure distribution on the wall were measured for several Reynolds numbers up to a maximum of approximately 16,000.

The general features of the predicted turbulent flow

were in agreement with the measurements. Theory and experiment were in good agreement in the region upstream of the minimum area of constriction. The predicted recirculation region was thinner and shorter than that observed experimentally. This is believed to be partially due to the weakness in the wall boundary conditions in the recirculating region. The underprediction of the size of the recirculating region had a strong influence on the mean velocity, turbulence kinetic energy, and the pressure distribution in the flow field immediately distal (downstream) to the stenosis.

The length of the recirculating region and the distance travelled by a disturbance are less sensitive to the Reynolds number in the turbulent flow than in high Reynolds number laminar flows. The wall shear stress and the pressure distribution are similar to that in the laminar flow. The convergent section attenuates the longitudinal velocity fluctuations u' and amplifies the azimuthal velocity fluctuations w'. A high turbulence intensity is generated in the shear layer distal to the throat. A large fraction of the energy in the fluctuations in the recirculating region is at lower frequencies. The turbulence fluctuations reach their final asymptotic downstream values more slowly than the mean velocity does.

Thus, the results of this research have led to an extensive description of stenotic flows which (i) points to a strong possibility that wall shear stress may initiate

emboli formation (this is a cause of the phenomena of transient ischemic episodes and sudden cerebro- and cardiovascular accidents), (ii) corroborates previous in vivo evidence that the poststenotic flow field may be extremely turbulent, and (iii) reinforces the hypothesis that a detection of turbulence may be a feasible method for the diagnosis of localized atherosclerotic plaques, provided noninvasive measurements can be employed.

CHAPTER I

INTRODUCTION

A leading cause of death in modern societies is atherosclerosis, a disease of the arteries. Although numerous theories have been proposed on the inception and progression of this disease, the actual causative mechanisms have yet to be established. Recent research has indicated that the initiation and proliferation of atherosclerosis are complex phenomena and that it is quite probable that several factors, operating simultaneously, are responsible for its development. A theory that explains all aspects should identify and account for every contributing factor, and this requires a thorough understanding of the activity and environment of the artery, both prior to onset of the disease and subsequent to its formation. The present study of laminar and turbulent flows through modelled, subtotal vascular stenoses or constrictions was initiated with the goal of contributing to the knowledge of the fluid dynamic environment of localized lesions. This knowledge may aid in developing insight into the problems of the genesis, progression, and early detection of atherosclerosis.

Atherosclerosis is characterized by arterial lesions involving lipid accumulation in the tunica intina, the inner

layer of the arterial wall. Fatty dots and streaks, considered by some to represent early lesions, are found even in infancy [1]. Not all the fatty streaks develop into plaques so that there is an apparent reversibility at some level of the process. In the next stage gelatinous, gray elevations are present and the more advanced stage consists of fibrous plaques with or without atheroma, which is a necrotic fatty substance (athere means porridge or gruel in Greek). Progressive development of the disease reduces the distensibility of the artery (hence the word sclerosis, meaning hardening) and decreases the lumen area as the plaque enlarges to encroach upon the vessel opening.

There are metabolic, hemodynamic, and arterial tissue changes associated with atherosclerosis. The former two alterations are very difficult to observe and hence almost everything known about the disease is from the characteristic atherosclerotic plaques. This amounts to considering only one aspect of the disease, and this is usually at a later stage of development. Predilection of the atherosclerotic lesions to form at particular sites of the vascular tree, most notably regions of vascular branching and bifurcation and the aortic arch, brings some credibility to the suspicions that hemodynamic factors participate in the genesis and proliferation of atherosclerosis. Fry [2,3] has interpreted the disease development as an ensemble of processes that occur in the intimal tissue system in response to a variety

of physical (local flow conditions) and chemical stimuli. He considers the importance of elevated local shear stress on the vessel wall, the damage caused on these linings in case of extremely high stresses, and the unstable flow patterns as factors contributing to increased lipid flux from plasma to the wall. He further explains that intimal regions chronically exposed to moderately elevated unidirectional shear stresses develop intimal fibrosis characterized by a dense, highly oriented subendothelial collagenous sheet which seems to decrease permeability to proteins. Caro et al. [4], Caro [5], and Nerem et al. [6] have studied the role of wall shear stress in facilitating lipoprotein uptake and the preferential occurrence of atheromatous lesions in man in the regions of low shear stress and conclude that the development of early lesions is related to a locally reduced efflux of accumulating material from wall to blood. The arterial wall has its own metabolism and should not be considered as an inert tubing. Lipids can also enter the vessel wall from outside [7]. Sako [8] concluded from his in vivo experiments that turbulent and increased blood flow and hypertension are abetting factors in the production of experimental atherosclerosis in dogs. Gossner's paper [9] provides a review of hemodynamic theories of atherosclerosis.

Regardless of the exact initiating factors, the development of localized arterial stenosis may lead to disordered blood flow within and downstram of the constricted

regions. Thus, the ability to describe flow through a partial occlusion adds to the insight needed to solve the puzzle of the pathology of atherosclerosis. Beyond that, there is widespread interest in determining whether the disordered flow patterns can be used to detect localized arterial disease in its early stages, particularly before it becomes clinically significant. Poststenotic dilatation, (PSD), an excess of arterial dilatation, is commonly observed behind stenosed aortic or pulmonary valves or behind other arterial stenoses. Roach [10] reports several cases of artificially induced PSD using a band to create arterial stenoses in animals and notes the disappearance of these dilatations once the band is removed. Hemodynamics is likely to be a primary factor in the etiology of PSD. High shear stresses and turbulence in the stenosed flow are also of interest due to their association with thrombus formation and hemolysis. Smith et al. [11] and Stein and Sabbah [12] demonstrated that thrombus formation was enhanced by the presence of turbulence in the flow. Mustard et al. [13] arrive at similar conclusions for abruptly changing flows in bifurcations and branchings. Leverett et al. [14] explored various mechanical factors causing hemolysis. Using a rotational viscometer they proved that shear stress beyond a threshold value of 1,500 dynes/cm^2 damages red blood cells significantly and that this damage is due to the action of shear acting directly on the cells.

An interesting application of flow through stenoses in a different biomedical situation is reported by Ritter et al. [15] and Aiello et al. [16]. They were able to diagnose an obstruction in the urinary tract using a urinary drop spectrometer to measure time-interval histograms of drops from urine jet breakup. The breakup of a liquid jet depends upon the initial flow conditions which are influenced in this case by a constriction and its position.

Arterial flow is pulsatile. In the present study, however, it will be treated as steady to simplify the mathematics. The information obtained is valuable as it gives an insight into the fluid dynamics of stenotic flow, and measures the influence of factors such as geometry and Reynolds number. Also, for severe constrictions, the pulsatility of the flow decreases until, for very severe stenoses, the flow becomes quasi-steady. The next important question to be settled concerns the nature of the flow, i.e. if flow should be treated as laminar, turbulent, or transitional. Lighthill [17] quotes the flow in the circulatory system to remain laminar when R_{max} (Reynolds number based on peak velocity and vessel diameter) is less than 4000 and turbulent when R_{max} is greater than 8000. Reynolds numbers in the human aorta span this range. The figures quoted above should be taken with great caution. In the case of complex geometries in the normal case, i.e. heart valves and vessel branching, or in the abnormal case of a stenosis, flow can

become transitional at surprisingly low Reynolds numbers. Young and Tsai [18] report the presence of transition and turbulence in their steady flow model studies at Reynolds numbers Re as low as 140 and 200, respectively. Existence of turbulence in the blood stream of experimental animals has been directly confirmed in the work of Seed and Wood [20], Nerem and Seed [21] and Giddens et al. [22]. Stein and Sabbah [23] studied the presence of turbulence in the human ascending aorta using hot film anemometer probe. In all the eight subjects having aortic valvular disease or a prosthetic aortic valve, turbulent flow occurred during the period of ejection. These investigators state that out of the seven normal subjects, one with high cardiac output showed turbulent flow while in the other six flow was highly disturbed during ejection. Stein et al. [24] have also shown that the turbulence intensity measured behind an orifice in a tube is sensitive to the hematocrit. For a given Reynolds number it was 2 to 3 times higher for 20 percent hematocrit compared to turbulence intensity in the plasma. At 40 percent hematocrit, however, this increase in turbulence intensity was negligible. A physiologic case is likely to include laminar, turbulent, transitional, and possibly a reverse transitional situation. The transitional region is an important case. Unfortunately, it is very difficult to treat since required fluid mechanical models and appropriate in vivo information are not available.

Hence, this study is restricted to the cases where flow remains completely laminar or completely turbulent.

There are many examples of studies of poststenotic flows. Young and Tsai [18,19] have examined certain flow characteristics in models of arterial stenosis under steady and pulsatile flow conditions. These experiments yielded, in the case of steady flow, a description of the extent of separated flow regions and a measure of pressure losses across the constriction. The nature of flow distal (downstream) to the partial occlusions, i.e. laminar, transitional or turbulent, was also discussed. Golia and Evans [25] obtained experimental data for the onset of separation and the length of the recirculation zone for annular constricted tubes.

Lee and Fung [26] obtained numerical solutions of the Navier-Stokes equations using finite difference techniques and a conformal transformation of the flow domain. Steady flow was considered through a rigid tube with 50 percent area reduction at the stenosis. Separation occurred at Reynolds number 9.9. For values larger than this a region of recirculation existed downstream of the minimum area of constriction. Numerical instabilities limited the calculations to Reynolds numbers below 25.

Morgan and Young [27] have employed momentum and energy integral equations to find approximate solutions to the axial velocity component of flow in the region of

stenoses. Agreement with experimental data on the results for separation and reattachment points and for pressure drop across stenoses was reasonably good. However, the method did not give the radial velocity component and treated the axial momentum equation as a parabolic partial differential equation by neglecting the second derivative of velocity in the axial direction.

Cheng et al. [28,29] have reported on numerical computations of an oscillating flow past square wall obstacles in plane conduits. Daly [30] obtained a numerical solution for pulsatile flow through stenosed canine femoral arteries. He used the volume flow rate reported by McDonald [31] as an input. Flow separation was observed in the wake of the stenoses during systole and during the diastolic flow reversal. The phase difference between velocity and pressure gradient was found to decrease with an increase in the severity of stenosis. Computations were not extended for the entire flow cycle in case of stenosis with 61 percent area reduction due to numerical instabilities. Schneck [32] used a successive approximation iteration scheme to obtain solutions for pulsatile flow in a diverging circular tube. Davis [33] applied an extended Pohlhausen method for an oscillating flow in a mildly constricted tube. A finite element method was employed by Cheng [34] for solving low Reynolds number flow through a constricted two-dimensional channel. Chow and Soda studied a slightly different problem of laminar flow and

blood oxygenation in two-dimensional [35] and axisymmetric [36] channels with boundary irregularities which were mild and varied sinusoidally. They utilized an asymptotic series solution procedure.

Numerical solutions for a number of closely related problems have been reported. Macagno and Hung studied laminar flow through a sudden expansion in a two-dimensional channel [37] and axisymmetric tube [38]. Vrentas and Duda [39], on the other hand, studied the flow through an axisymmetric contraction. Mills [40] and Zampaglione and Greppi [41] examined the flow through a pipe orifice.

Goldstein [42] conducted experiments for flow over a downstream facing step. Seeley and Young [43] carried out in vitro steady flow studies to understand the influence of the geometry of stenoses on pressure drop. They concluded that the pressure drop over multiple stenoses cannot be obtained by adding the pressure drops over isolated stenoses. Clark [44,45] studied steady and unsteady flow through stenosed valves to obtain pressure flow relations.

The research efforts referenced above were for laminar case. At the beginning of this study there was no report of a detailed description of the flow through a smoothly contoured stenoses and there was no direct comparison of theoretical results with experimental data. Such a comparison should heighten the confidence in a given numerical approach and the experimental data, and should

point out the limitations of the theoretical model.

The corresponding efforts for turbulent flow case are fewer in number. This is due to two reasons: (i) It was taken for granted that flow in the circulatory system remains laminar. (ii) Detailed turbulent flow computations have become popular only in the past decade and are still in their infancy. They are also more difficult to execute.

Tsai and Young [46] measured the centerline turbulence intensities for several Reynolds numbers from 350 to 1000 for a stenosis with 89 percent area reduction. Spectral measurements were made by Kim and Corcoran [47] behind square shaped plugs of varying orifice diameter. The Reynolds number range was from 800 to 2,000. A hot film probe was used to measure turbulence velocities and energy spectra were obtained by digital techniques. There was an increase in turbulence intensity as the Reynolds number increased and as the orifice diameter decreased. High frequency content was also seen to be increased for a more severe constriction.

Cassanova [48] made a detailed experimental investigation of steady and pulsatile flow through partial occlusions. A conical hot film probe was used to measure velocity and a Fourier analyzer to obtain energy spectra. Both contoured and sharp-edged occlusions were tested. Steady flow experiments covered a Reynolds number range of 635 to 2540 and velocity profiles and energy spectra were recorded.

They showed the presence of vortex rings immediately downstream of the constriction, with velocity fluctuations in a narrow band. These vortex rings break up into more randomly distributed fluctuations farther downstream. In the case of pulsatile flow, velocity wave forms and energy spectra were obtained for different frequency parameters and Reynolds numbers.

Krall and Sparrow [49] made experimental studies of heat transfer in the separated region behind orifice plates of various diameters. They found out that heat transfer in the separated and redeveloping region was several times higher than the fully developed value, more so for narrower orifice diameter and lower Reynolds number. Heat transfer was not very sensitive to Prandtl number changes. They assumed the position where Nusselt number peaked to coincide with the reattachment point, which occurred between 1.25 and 2.5 pipe diameters. Back and Roschke [50,51] obtained the reattachment lengths experimentally in an abrupt expansion in a pipe for a Reynolds number (based on the narrower tube diameter and bulk velocity) range between 20 and 4,200. This length peaked for Reynolds number of 250; after a sudden drop it again increased gradually for Reynolds numbers larger than 1,000. Runchal and Spalding [52] used a mixing length model to simulate the experiments of Krall and Sparrow [49]. The mixing length was adjusted to secure the proper length of recirculation region. The same problem was solved using

a two-equation turbulence model by Gosman et al. and reported as part of the lecture series [53].

Chin et al. [54] and Chin [55] studied flow in a rectangular cavity experimentally and computationally using a mixing length model. Mixing length was chosen in different regions to correspond to different well known flow cases. Prediction of velocity in the cavity was good. Prediction of heat transfer and pressure coefficient was less satisfactory. Their numerical procedure also required some approximation of the vorticity transport equation and still numerical instabilities arose for shallow cutouts.

Thus, a literature survey revealed no attempts to predict turbulent flow in a stenosed tube. There are also no detailed measurements of turbulence intensity. In our attempt to predict this flow we face another difficulty. The turbulence models available are good for very large Reynolds numbers and attempts to improve them for intermediate Reynolds numbers, which are of interest to us, are not always successful. However, this should not preclude one from using them in such a situation. The results can be compared with the experimental data to check their validity. Further, the application of turbulence models to different flow situations helps in testing these models and may lead to methods of improving them.

Considering all these factors, the aims of the present investigation are as follows.

(1) To compute the steady, laminar flow through axisymmetric subtotal stenosis models with smooth contours and compare the results with available experimental data. Severe degrees of stenoses and physiologically realistic large Reynolds numbers are to be included.

(2) To extend the computations to a turbulent flow case using a two-equation (k-ε model where k is turbulence kinetic energy and ε its dissipation rate) turbulence model which is superior to mixing length models and permits computation of turbulence kinetic energy. Again, elliptic partial differential equations are to be solved to account for the strongly elliptic nature of the problem evidenced by the existence of a recirculation region.

(3) To conduct detailed experiments for a single case of geometry and Reynolds number where time-averaged velocity and certain components of turbulence intensity are to be measured using a laser Doppler anemometer (LDA) and pressure distribution is to be determined using water manometers. These data will be used to compare with the theoretical results and thus point out any shortcomings of the model in predicting the flow.

(4) To combine the results obtained as above and obtain a comprehensive flow picture, subject to the assumptions made. This picture can be of assistance in examining relations between atherosclerosis and fluid mechanics.

While developing the computer program to predict the

turbulent flow through stenosis models, turbulent entrance flow in a pipe was solved to gain experience and to test the model and numerical approach employed.

CHAPTER II

LAMINAR FLOW COMPUTATIONS

The theoretical investigation presented in this chapter was the first part undertaken in the study. The analysis is restricted to steady, laminar flow of an incompressible, Newtonian fluid through a rigid tube which has a localized axisymmetric constriction. No swirling flows have been considered. Clearly, such restrictions prevent a direct application of the results to the in vivo situation. The primary effort here is to provide a comprehensive steady flow treatment of a realistically shaped occlusion contour by obtaining flow field solutions at Reynolds numbers sufficiently large to insure that the full range of laminar flow is covered. The experiments of Young and Tsai [18] are kept in mind in selecting the stenosis geometry so that the predicted results can be directly compared with the measured data.

2.1. Governing Equations and Boundary Conditions

The continuity and Navier-Stokes equations in cylindrical polar coordinates subject to the assumptions mentioned above are taken as the governing relations for the problem [56]. They are

$$\frac{\partial v_r}{\partial r} + \frac{v_r}{r} + \frac{\partial v_z}{\partial z} = 0 \tag{1a}$$

$$v_r \frac{\partial v_r}{\partial r} + v_z \frac{\partial v_r}{\partial z} = -\frac{1}{\rho}\frac{\partial p}{\partial r} + \nu\left[\frac{\partial^2 v_r}{\partial r^2} + \frac{1}{r}\frac{\partial v_r}{\partial r} - \frac{v_r}{r^2} + \frac{\partial^2 v_r}{\partial z^2}\right] \tag{1b}$$

$$v_r \frac{\partial v_z}{\partial r} + v_z \frac{\partial v_z}{\partial z} = -\frac{1}{\rho}\frac{\partial p}{\partial z} + \nu\left[\frac{\partial^2 v_z}{\partial r^2} + \frac{1}{r}\frac{\partial v_z}{\partial r} + \frac{\partial^2 v_z}{\partial z^2}\right], \tag{1c}$$

where r and z are the radial and axial coordinates with the z-axis located along the axis of symmetry and the origin being at the minimum area of constriction. A sketch of the geometry and coordinate system is shown in Figure 1. The radial and axial components of velocity, v_r and v_z, define the total velocity. The pressure, density, and kinematic viscosity are denoted by p, ρ, and ν.

The boundary conditions on velocity at the wall are the usual no slip requirements

$$v_r = v_z = 0 \quad \text{at} \quad r = r_o(z), \tag{2}$$

where $r_o(z)$ describes the local wall radius as a function of z. Hagen-Poiseuille flow (parabolic velocity profile) is assumed at $z = \pm\infty$;

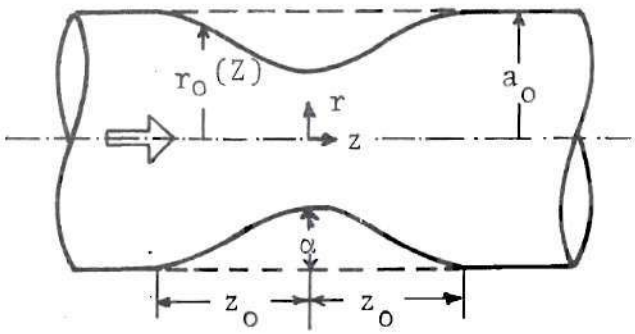

Figure 1. Geometry of Model Stenoses

$$v_z = U(1-r^2/a_o^2)$$

$$z \to \pm\infty \qquad (3)$$

$$v_r = 0$$

Here, U is the maximum velocity and a_o is the radius of the tube in the unoccluded portion.

Nondimensional variables are defined as

$$R = \frac{r}{a_o}; \quad Z = \frac{z}{a_o}; \quad R_o(Z) = \frac{r_o(z/a_o)}{a_o}$$

$$V_R = \frac{v_r}{U}; \quad V_Z = \frac{v_z}{U}; \quad P = \frac{pa_o}{\rho\nu U}$$

$$Re = Ua_o/\nu \quad \text{(Reynolds number)}$$

The stream function ψ and vorticity ω are introduced by

$$V_Z = \frac{1}{R}\frac{\partial\psi}{\partial R}; \quad V_R = -\frac{1}{R}\frac{\partial\psi}{\partial Z} \qquad (4)$$

and

$$\omega = \frac{\partial V_R}{\partial Z} - \frac{\partial V_Z}{\partial R}.$$

Vorticity and stream function can now be related by

$$\omega = - \frac{1}{R} \left(\frac{\partial^2 \psi}{\partial R^2} + \frac{\partial^2 \psi}{\partial Z^2}\right) + \frac{1}{R^2} \frac{\partial \psi}{\partial R}. \tag{5}$$

The total head H is defined as

$$H = P + \frac{Re}{2} \left[V_R{}^2 + V_Z{}^2\right] = \frac{a_o}{\rho v U} \left[p + \frac{\rho}{2} \left(v_r{}^2 + v_z{}^2\right)\right]$$

Equations (1b and 1c) can next be written as

$$\frac{\partial H}{\partial R} = \frac{\partial \omega}{\partial Z} - \frac{Re\ \omega}{R} \frac{\partial \psi}{\partial R}$$

$$\frac{\partial H}{\partial Z} = - \frac{\partial \omega}{\partial R} - \frac{\omega}{R} - \frac{Re\ \omega}{R} \frac{\partial \psi}{\partial Z} \tag{6}$$

Cross differentiation eliminates H and leads to

$$R^2 \left[\frac{\partial}{\partial Z} \left(\frac{\omega}{R} \frac{\partial \psi}{\partial R}\right) - \frac{\partial}{\partial R} \left(\frac{\omega}{R} \frac{\partial \psi}{\partial Z}\right)\right] - \frac{1}{Re} \frac{\partial}{\partial Z} \left[R^3 \frac{\partial}{\partial Z} \left(\frac{\omega}{R}\right)\right]$$

$$- \frac{1}{Re} \frac{\partial}{\partial R} \left[R^3 \frac{\partial}{\partial R} \left(\frac{\omega}{R}\right)\right] = 0 \tag{7}$$

Equations (5 and 7) now provide the governing equations for the problem.

Application of the boundary conditions at $Z = \pm\infty$ causes some difficulty. It is somewhat unsatisfactory to simply impose these at large finite values of $|Z|$ since, with increasing Reynolds number, the disturbances created by the stenoses are sizable even far downstream. A suitable transformation may be introduced to map the infinite region of interest into a finite one. This allows a precise application of the boundary conditions. Further, it enables one to space numerical grid points uniformly (in the transformed variable) and yet economically.

The transformation used in this study is

$$\eta = \text{Tanh}\ (KZ), \tag{8}$$

where K is a constant which can be chosen to group the grid points in an efficient manner. It was taken between 0.04 and 0.3 depending upon stenosis geometry and Reynolds number. Equations (5) and (7) are written in the new coordinate system as

$$R^2\{K(1-\eta^2)\ \frac{\partial}{\partial\eta}\ (\frac{\omega}{R}\ \frac{\partial\psi}{\partial R}) - \frac{\partial}{\partial R}\ [\frac{\omega}{R}\ K(1-\eta^2)\ \frac{\partial\psi}{\partial\eta}]\}$$

$$- \frac{K(1-\eta^2)}{Re}\ \frac{\partial}{\partial\eta}\ [R^3K(1-\eta^2)\ \frac{\partial}{\partial\eta}\ (\frac{\omega}{R})]$$

$$- \frac{1}{Re}\ \frac{\partial}{\partial R}\ [R^3\ \frac{\partial}{\partial R}\ (\frac{\omega}{R})] = 0 \tag{9}$$

$$\frac{\partial}{\partial \eta}\left[\frac{K(1-\eta^2)}{R}\frac{\partial \psi}{\partial \eta}\right] + \frac{\partial}{\partial R}\left[\frac{1}{K(1-\eta^2)R}\frac{\partial \psi}{\partial R}\right] + \frac{\omega}{K(1-\eta^2)} = 0. \quad (10)$$

The boundary conditions in terms of ψ and ω become

$$\psi = R^2/2 - R^4/4 \quad \text{and} \quad \omega/R = 2 \quad \text{at} \quad \eta = \pm 1 \quad (11)$$

$$\psi = 0.25 \quad \text{and} \quad \frac{\partial \psi}{\partial R} = \frac{\partial \psi}{\partial \eta} = 0 \quad \text{at} \quad R = R_o(Z). \quad (12)$$

Using symmetry, boundary conditions employed at the axis are

$$\psi = \omega = 0 \quad \text{at} \quad R = 0. \quad (13)$$

The value of ω/R on the axis is not zero and is obtained by the method described by Gosman et al. [57]. In this method ψ near the axis is expressed as an even powered series in R ($\psi = a_1R^2 + a_2R^4$) at each value of Z, and a_1 and a_2 are evaluated by known values of ψ from the previous iteration. Now equation (5) can be utilized to obtain the relation $(\omega/R) = -8a_2$, on the axis. The boundary condition on ω/R along the wall is to be found from the no slip conditions (equations 12). Methods are available for straight walls using a Taylor series expansion of ψ and ω about their boundary values and in the normal direction to the boundary [58]. The method is extended here to curved walls using Taylor series expansion in both R and Z directions. The

details of the method are given in Appendix A1.

2.2. Numerical Solution

Equations (9 and 10) may be recast into the general form

$$a\left[\frac{\partial}{\partial \eta}\left(\phi \frac{\partial \psi}{\partial R}\right) - \frac{\partial}{\partial R}\left(\phi \frac{\partial \psi}{\partial \eta}\right)\right] - \frac{\partial}{\partial \eta}\left[b_1 R \frac{\partial}{\partial \eta}(c\phi)\right] -$$

$$\frac{\partial}{\partial R}\left[b_2 R \frac{\partial}{\partial R}(c\phi)\right] + Rd = 0. \qquad (14)$$

The first term is due to the convection of the quantity ϕ which may be ψ or ω/R, while the second and third terms arise as a consequence of diffusion. The last term may be regarded as a source contribution.

The numerical scheme employed follows that of Gosman et al. [57] with modifications being required to treat the curved boundaries in the region of stenoses. Difference equations are generated by integrating over a control volume surrounding a point P (shown by dotted lines in Figure 2). The difference form which results expresses values at P in terms of the neighboring nodes (N, E, S, etc.). Upwind differencing is used in approximating the convection terms. Details of deriving the difference equations are given in Appendix A2. The newly calculated values at P are employed in computations at the next point as the solution proceeds, and iterations over the entire field are required to obtain

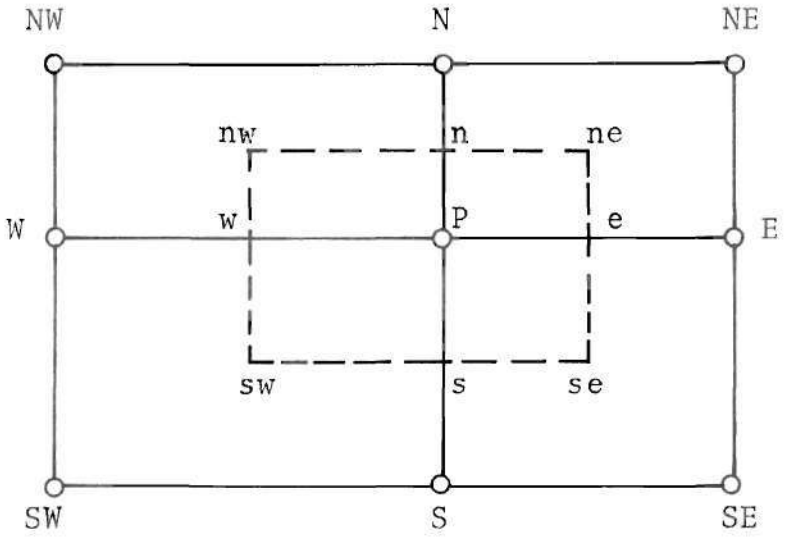

Figure 2. Control Volume for Numerical Scheme

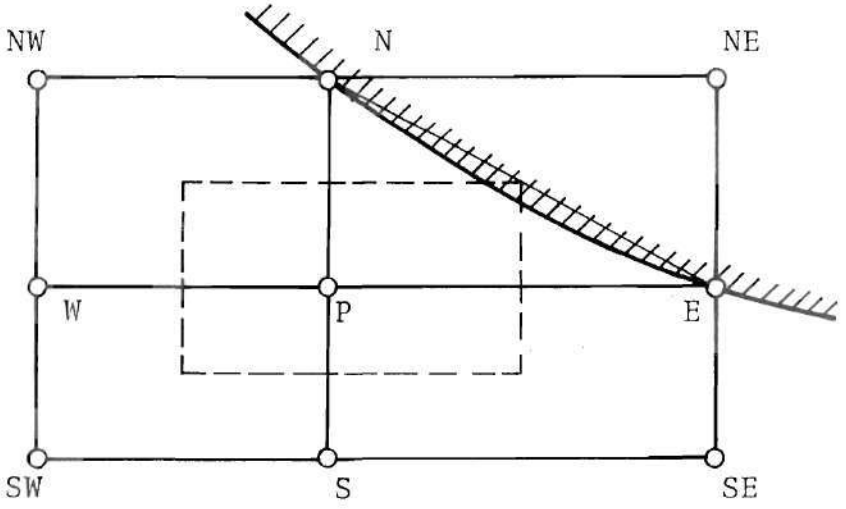

Figure 3. Control Volume Modification Near Curved Boundary

convergence.

The grid nodes are spaced uniformly in the radial direction, and nodes are made to coincide with the wall boundary to avoid interpolation schemes in locating surfaces. This, however, puts some additional restriction in the choice of grid spacing where the boundary is curved since the selection of points in the radial direction then dictates those in the axial coordinate.

The iterations proceed in the following manner. An initial guess is made for the flow field, and boundary conditions on ψ are imposed. The procedure discussed in Appendix A1 is employed to obtain boundary conditions on ω/R at the wall. Then the difference equations are solved for the entire flow to give new values for ψ and ω/R. This process continues until the difference between successive iterations are less than some small number. Initially this was placed at 2×10^{-5} for ψ and 5×10^{-4} for ω. These constraints were later relaxed as experience was gained in the program. Equations (4) are used at this stage to calculate velocity from the stream function and then equations (6) to calculate the pressure distribution.

The numerical procedure was checked for the case of Poiseuille flow with a rather coarse grid spacing consisting of nine points along the radius and 30 points between $Z = -\infty$ and $Z = +\infty$. Initially, guessed values for velocity were taken as zero. After 40 iterations the numerical results

differed from the theoretical parabolic profile in the fourth significant digit. There was no difficulty in starting with zero field values and obtaining solutions for Reynolds numbers as large as 10^6.

In the case of tube geometries containing constrictions, calculations were first done for Re = 0, beginning with parabolic velocity profiles at each station. The converged results were then used as the initial profiles for the next higher Reynolds number. This proved to be a convenient and economical procedure rather than a necessity. If results are required for a single large Reynolds number, they can be obtained directly.

For the computations reported here, 31 grid points were taken in the radial direction ($0 \leq R \leq 1$); and the number of axial stations varied from 91 to 111, with a greater number of points being placed downstream of the occlusion. The number of iterations required was usually from 300 to 400. This required four to six minutes of computer time on the UNIVAC 1108. Various numerical experiments were performed using different numbers and spacings of grid nodes to assure that accuracy was consistently maintained. Flow field regions which do not change considerably with Reynolds number need not have to be computed in every iteration. This saves a considerable amount of computer time.

2.3. Geometry of Stenoses

The numerical scheme can be applied to axisymmetric contours of arbitrary profile. The form of the stenoses chosen for the present studies was

$$R_o(Z) = 1 - \frac{\alpha}{2}\left[1 + \cos\left(\frac{\pi Z}{Z_o}\right)\right]; \quad -Z_o \leq Z \leq Z_o \tag{15}$$

with

$$R_o(Z) = 1; \quad |Z| \geq Z_o$$

where α, Z_o are constants which may be adjusted to allow different lengths and degrees of occlusion (see Figure 1).

Table 1 lists the four models studied. The first, Model MO, closely approximates the contour used by Lee and Fung [26] while the others duplicate the axisymmetric shapes investigated experimentally by Young and Tsai [18]. The table also includes the Reynolds number ranges over which solutions were obtained during the study. It should be emphasized that for all models convergent solutions can be obtained throughout the laminar flow regime so that it is the naturally occurring flow instabilities in the experiments rather than instabilities in the numerical analysis that prevent realistic comparison at large Reynolds numbers.

Table 1. Geometries of Model Stenoses and Reynolds Number Range for Laminar Flow Study

Model	α	Z_o	Area Reduction	Reynolds Number Range for Calculations	Computed Separation Reynolds Number
MO	0.500	1	75%	0 - 300	10.1
M1	0.333	4	56%	0 - 2000	195
M2	0.667	4	89%	0 - 200	17.0
M3	0.667	2	89%	0 - 100	8.75
M4	0.500	2	75%	--*	--

*Not included in Laminar Flow study

2.4. Results

As noted previously, calculations were performed for the various models over a wide range of Reynolds numbers. The following section presents representative results of these computations.

2.4.1. Streamlines and Vorticity Distribution

A good visual description of the flow is rendered by the display of stream function and vorticity contours. Representative cases are shown in Figures 4-6 with streamlines in the top half and vorticity contours in the bottom half of each plot. Contours shown in Figure 4a for a relatively mild constriction M1 and at Reynolds number (0) are symmetrical about the Z = 0 plane. Asymmetry is not clearly noticeable in the streamline patterns at Reynolds number (100) in Figure 4b, but it is readily apparent in the vorticity contours. No recirculation region is present and the flow is but mildly perturbed as it passes through the narrowing.

Figures 5a and 5b illustrate flow behavior in the region of a more severe stenosis (Model M0) at Reynolds numbers (50 and 200) sufficiently large to yield separated flow, being initiated distal to the minimum area. At the lower Reynolds number the circulation region is confined to the downstream neighborhood of the constriction, while it is predicted to extend for a considerable distance downstream for the higher Reynolds number. Figures 6a and 6b are similar displays for a very severe stenosis (Model M2).

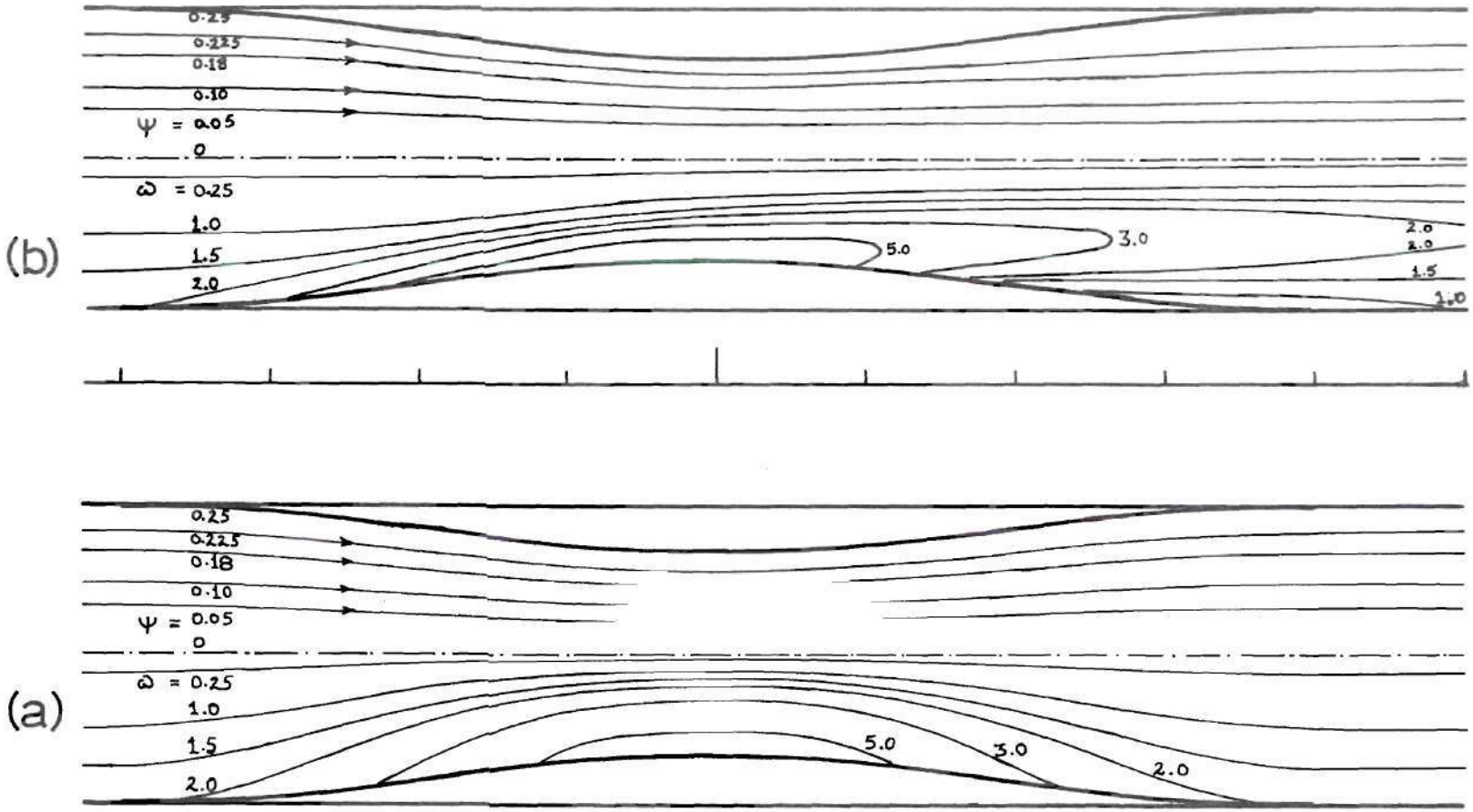

Figure 4. Stream Function and Vorticity Contours for Model M1
(a) Re = 0, (b) Re = 100

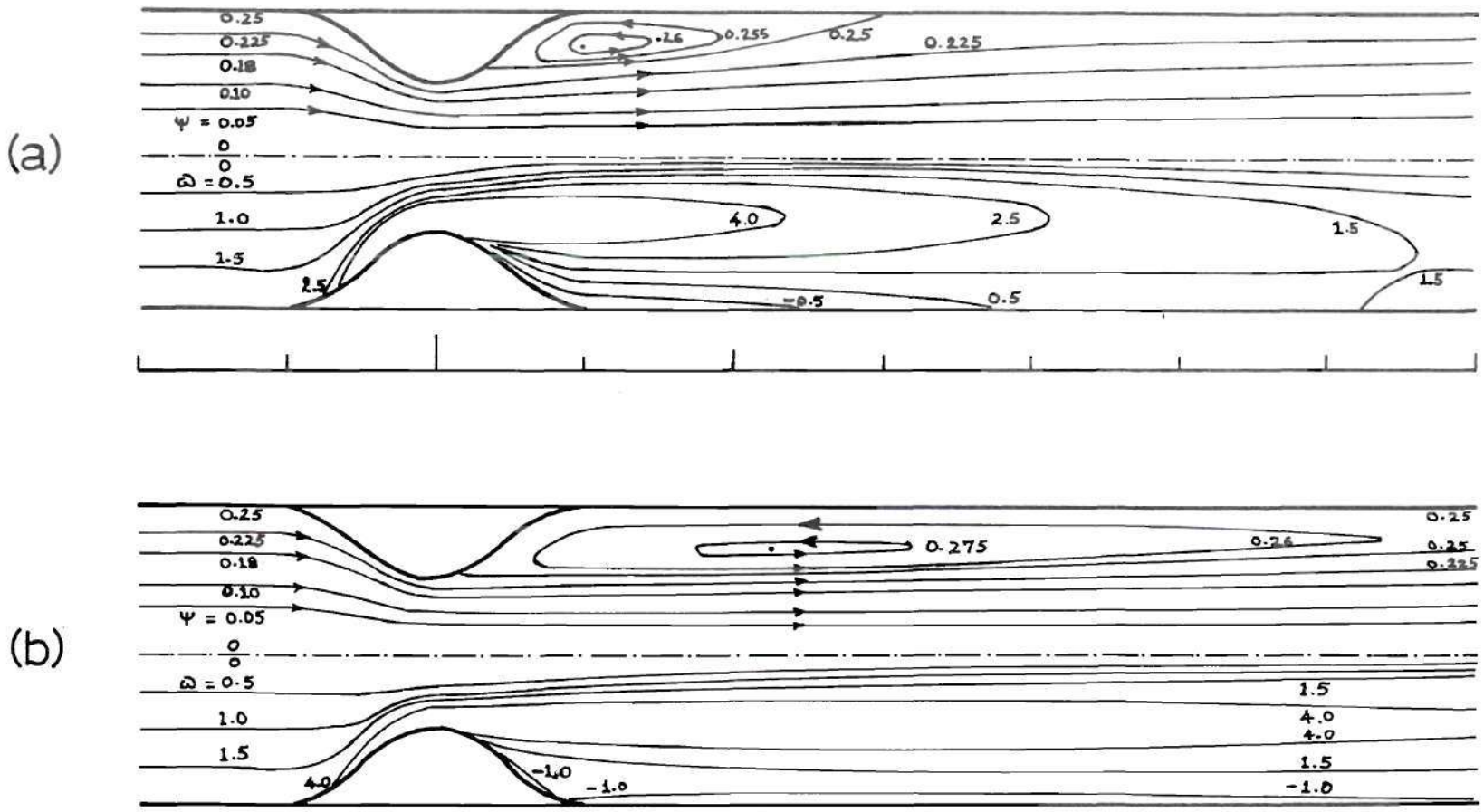

Figure 5. Stream Function and Vorticity Contours for Model MO
(a) Re = 50, (b) Re = 200

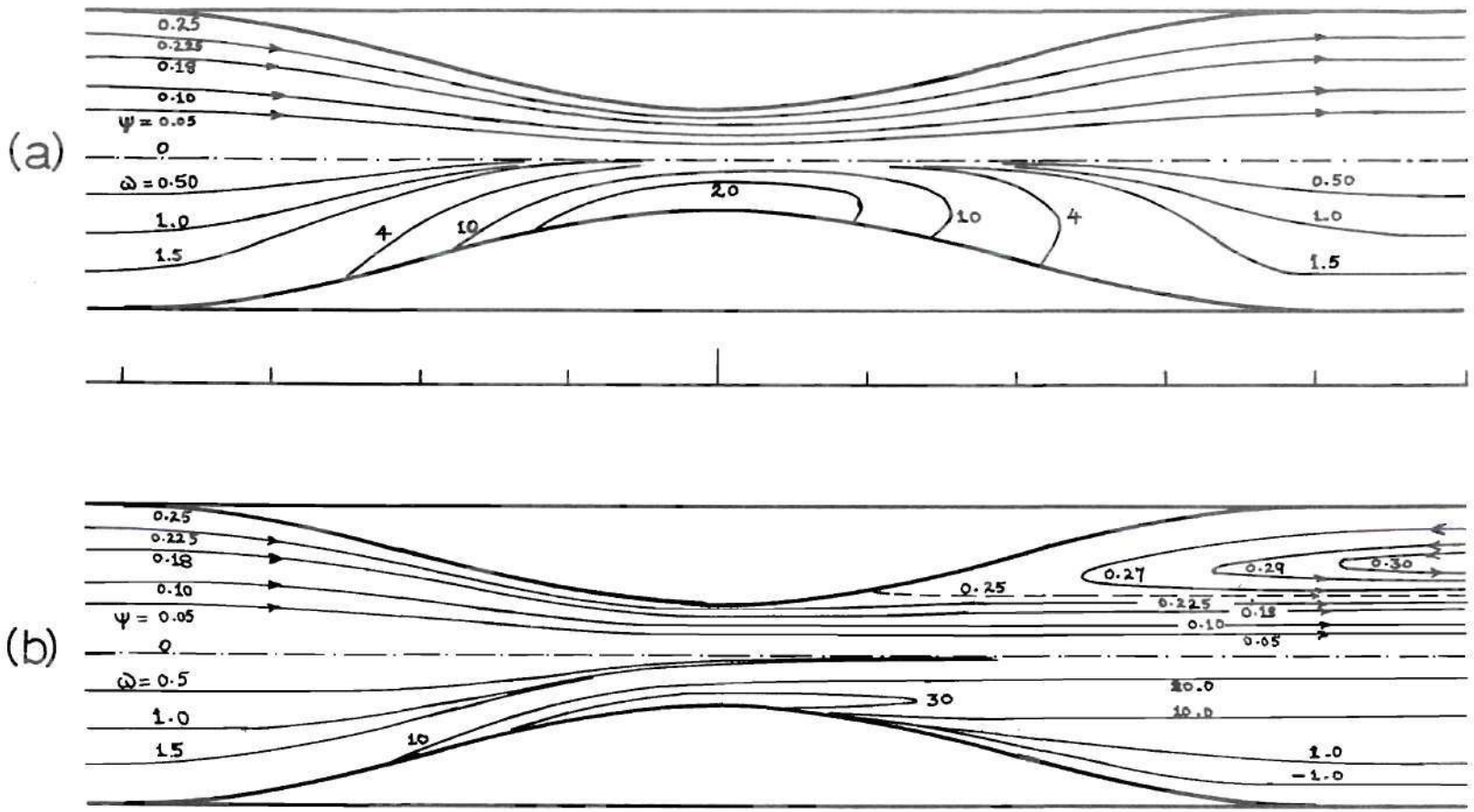

Figure 6. Stream Function and Vorticity Contours for Model M2
(a) Re = 6, (b) Re = 150

Reynolds numbers chosen (6 and 150) correspond to pre-separation and separated cases. The vorticity contours clearly show the regions of high vorticity production and the preferential transport of vorticity in the flow direction. The recirculation region includes low and even negative values of vorticity. It is emphasized that these figures represent theoretical flow fields under the assumptions given. In particular, no provision has been made for the occurrence of flow instabilities. This point will be discussed later.

2.4.2. Separation and Reattachment Points

Calculations were performed corresponding to the axisymmetric cases reported by Young and Tsai [18] so that a direct comparison could be made with experimental data. The locations of separation and reattachment in that work were determined visually using dye injection methods. Calculations also included a case (Model MO) where a limited comparison could be made with the theoretical computations of Lee and Fung [26] for a geometry close to Model MO.

Separation and reattachment points are shown in Figure 7 for Model MO, which does not exhibit separation for Reynolds numbers less than 10.1. Lee and Fung reported a value of 9.9 for their Gaussian geometry. The comparison, which is possible only up to a Reynolds number of 25, is good.

Figures 8 and 9 compare the present theoretical predictions with the experimental observations of Young and

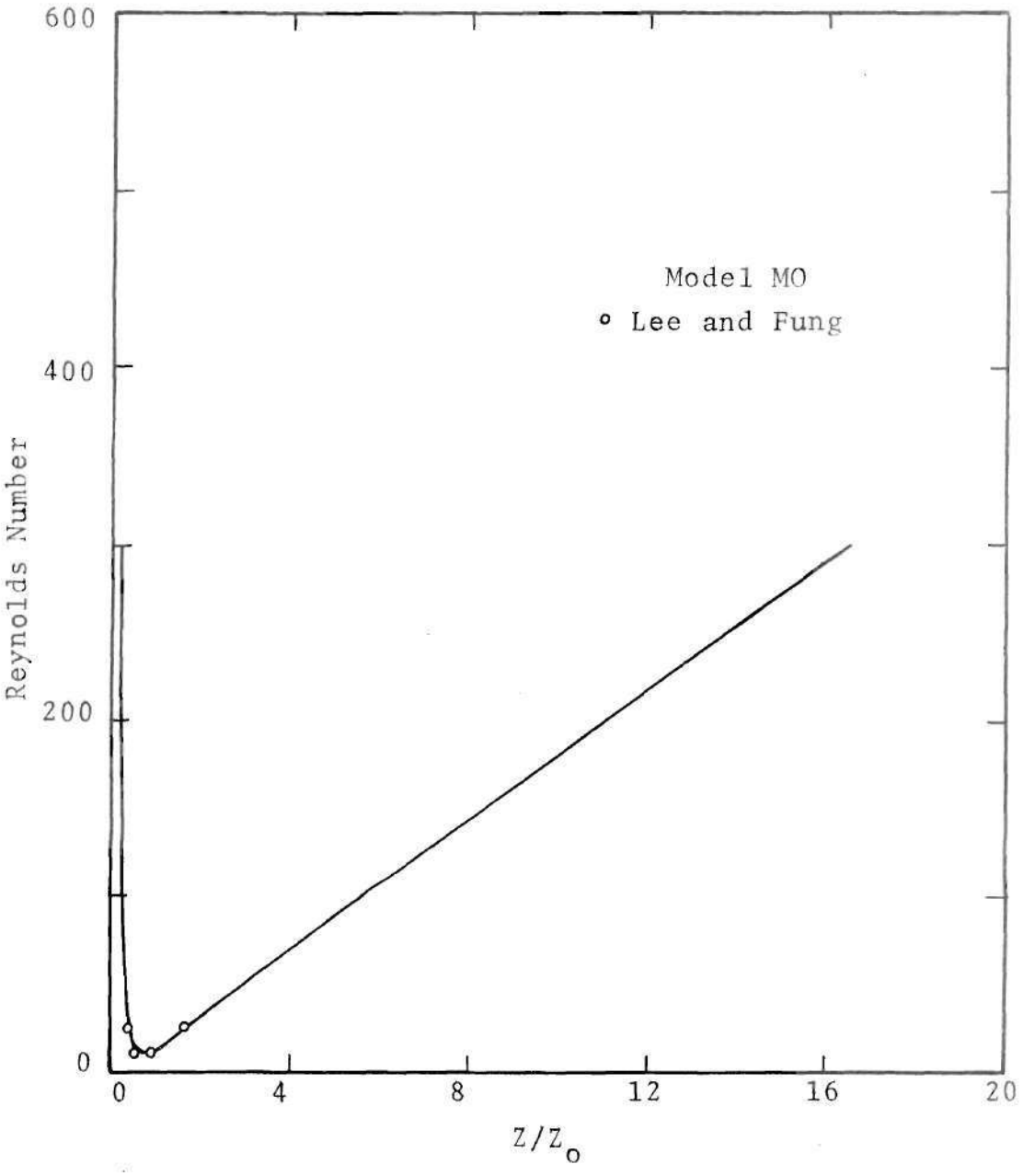

Figure 7. Separation and Reattachment Points for Model MO

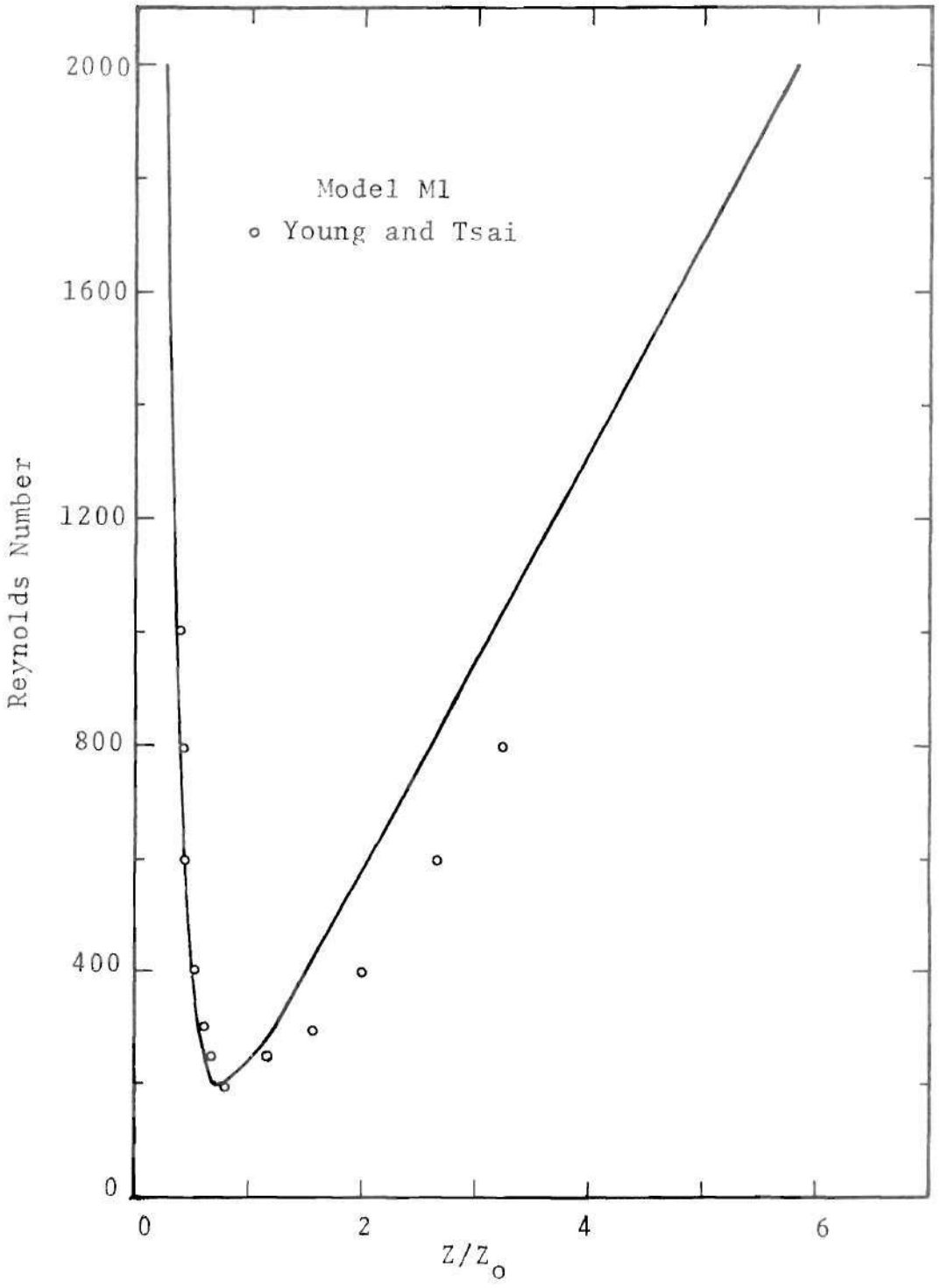

Figure 8. Separation and Reattachment Points for Model M1

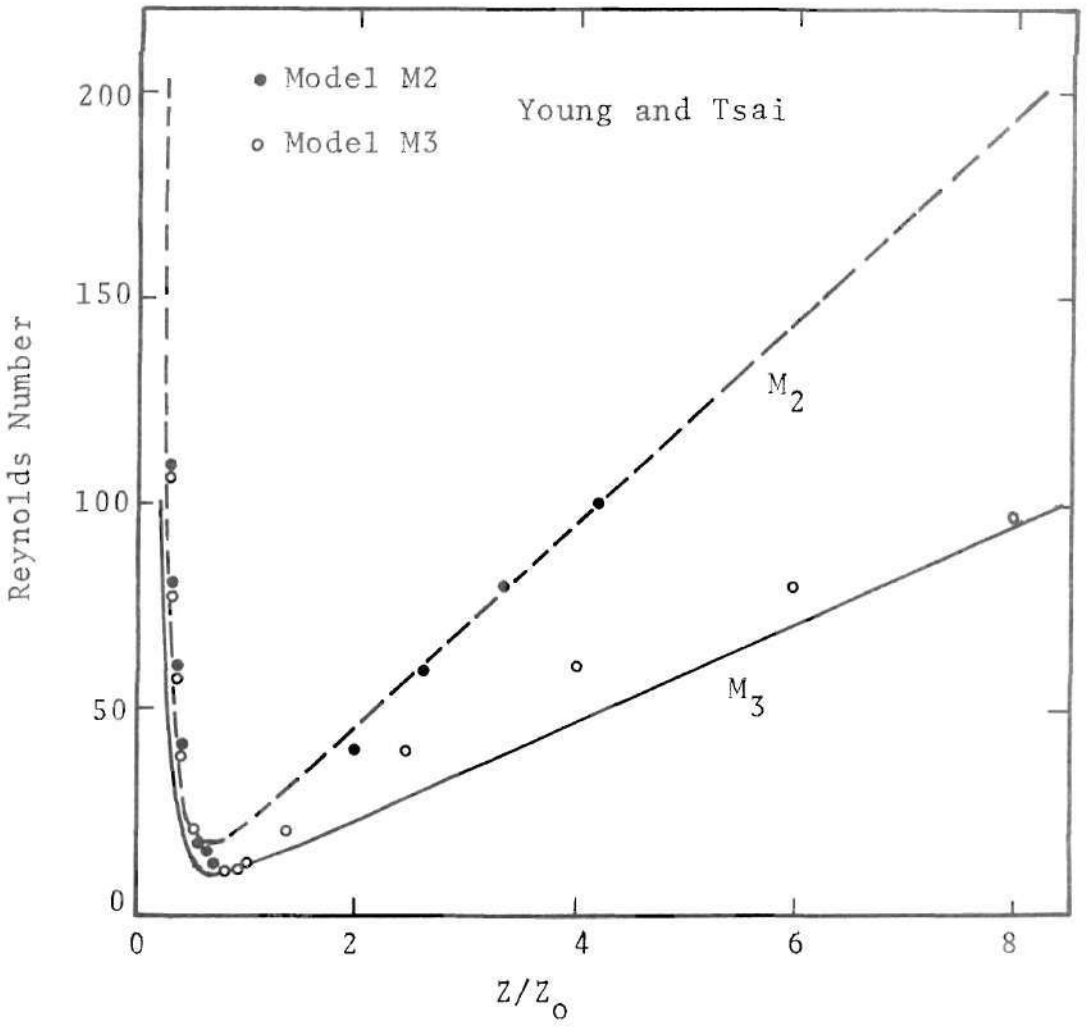

Figure 9. Separation and Reattachment Points for Models M2 and M3

Tsai. For model M1, a relatively mild stenosis, the separation Reynolds number is 195. The theory and experiment agree well for this onset value; and for higher values the locations of the separation points compare favorably (see Figure 8). A greater disagreement is found for the reattachment points. This is not surprising, however, since Young and Tsai report that flow instabilities were recorded for this case for Reynolds numbers as low as 300. Furthermore, the reattachment points are difficult to ascertain experimentally. One usually observes a reattachment zone, rather than a point, due to dye diffusion and, for sufficiently high Reynolds numbers, due to intermittency of the dividing streamline. This problem is particularly difficult for Model M1 with a very thin recirculation region.

Figure 9 illustrates the comparisons for models M2 and M3. The agreement here is rather good--and it is noted that flow instabilities were not observed by Young and Tsai over the Reynolds number range depicted in this figure. One point of interest is that the onset of separation was observed experimentally to occur at a Reynolds number of 10 for both these models, whereas the calculations give values of 8.75 for Model M3 and 17.0 for M2. One is inclined to think that the shorter model M3 should have a lower separation Reynolds number compared to that for M2. It is believed that this is adequate agreement considering the experimental difficulties of delineating this onset at such low flow rates.

2.4.3. Pressure Drop Across Stenosis

At a given Reynolds number the presence of a stenosis increases the resistance which the flow experiences. Although it would be presumptuous to extrapolate this directly to the in vivo vascular system (due to presence of compensatory mechanisms such as vasodilation and collateral circulation), there is a tendency for severe stenoses to reduce the supply of blood to distal regions. Thus, the pressure losses through such constrictions are of interest.

The measurements reported by Young and Tsai [18] were obtained with transducers connected to wall taps located at ±8 diameters from the plane of minimum area. Values of wall pressure of corresponding locations were obtained from the numerical computations and are compared with the experimental data in Figure 10. The range of Reynolds numbers which the theory and this phase of the experiments have in common is rather limited due to two reasons: (i) the experiment is difficult to perform at very low Reynolds numbers, and (ii) flow instabilities, including transition to turbulence, which are not accounted for in the theoretical model occur experimentally at moderate values of Re. Where the two results share a common validity, however, the agreement is quite good.

The pressure distribution along the tube is also of interest. Figures 11, 12 and 13 illustrate the variation of pressure along the axis for Models M1, M2 and M3 for different

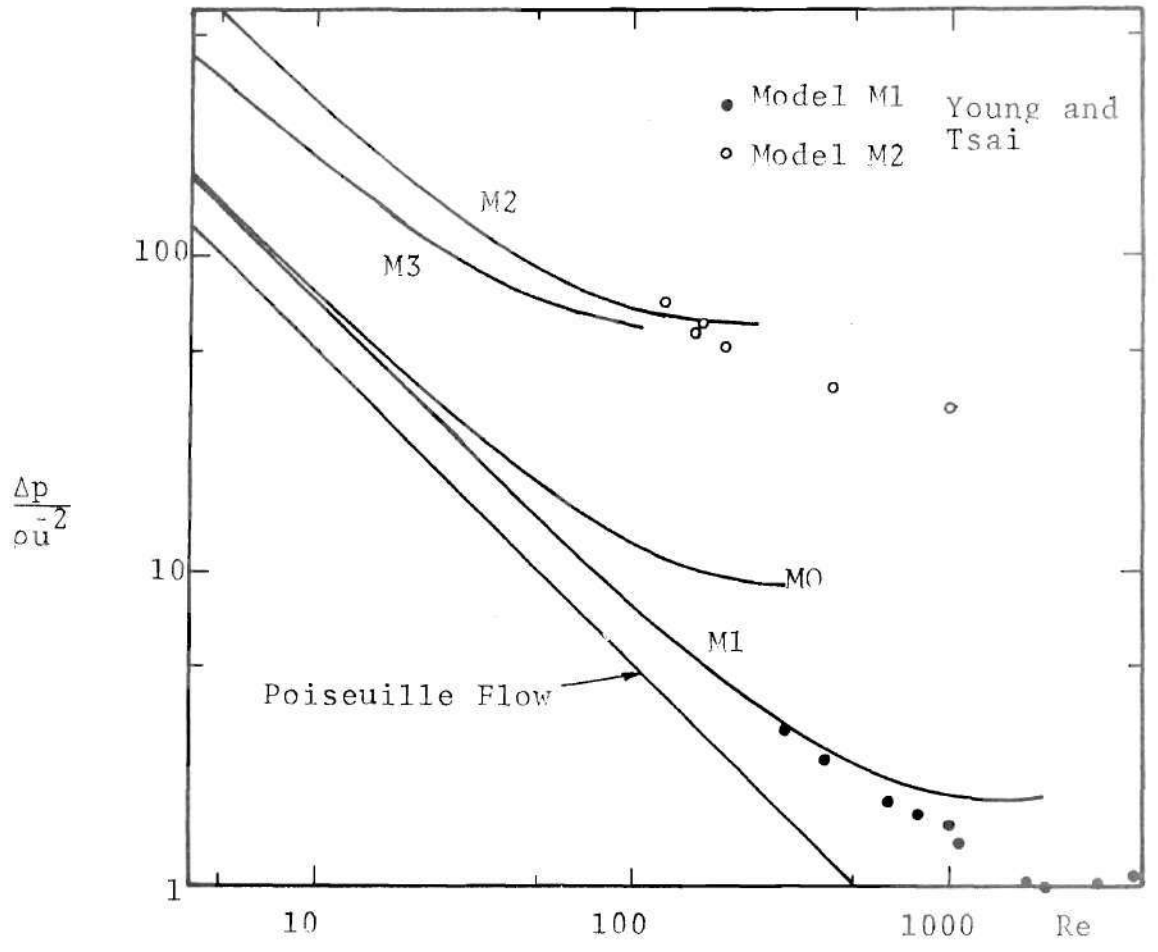

Figure 10. Pressure Drop Across Stenoses in Laminar Flow

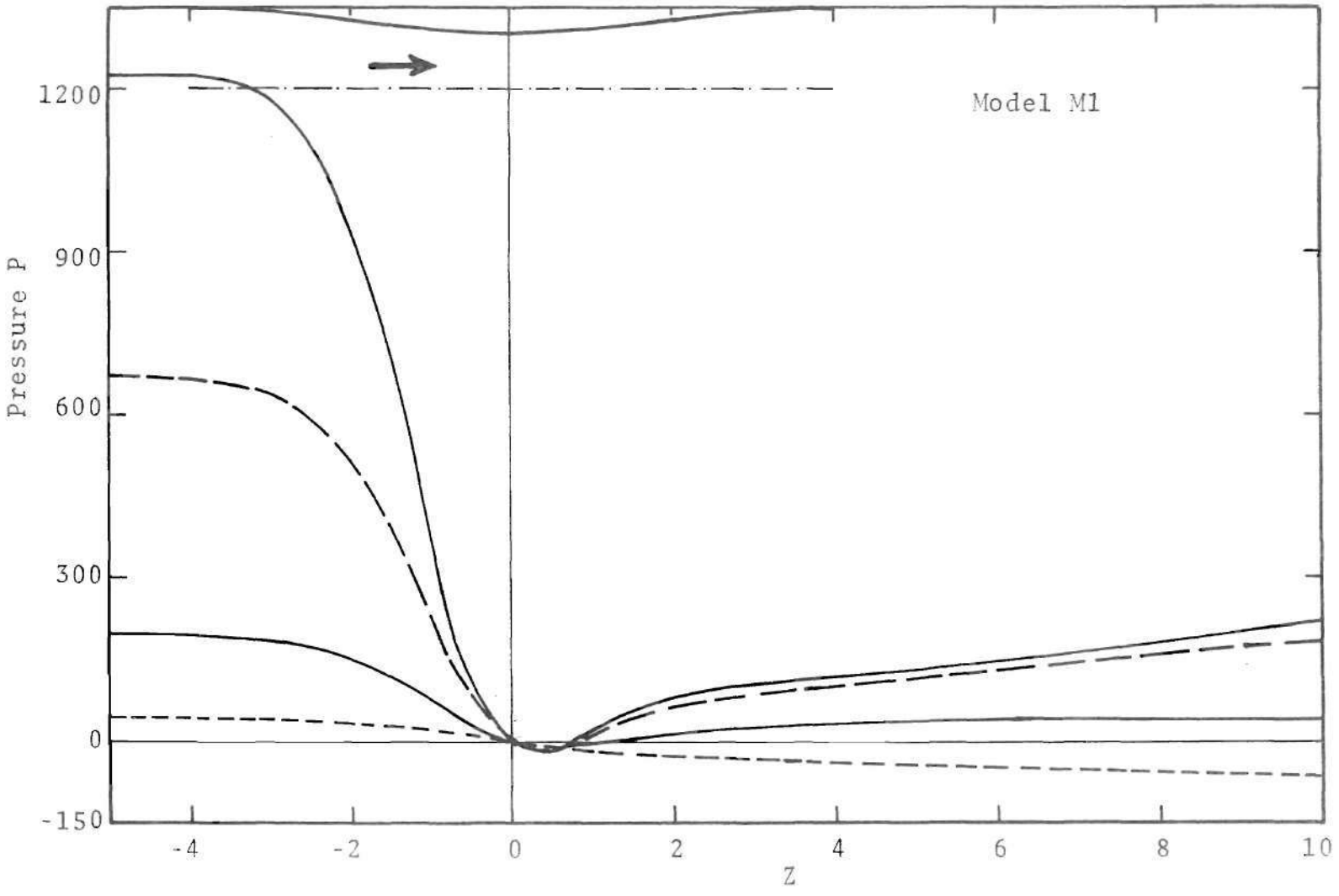

Figure 11. Pressure Distribution in Laminar Flow, Model M1

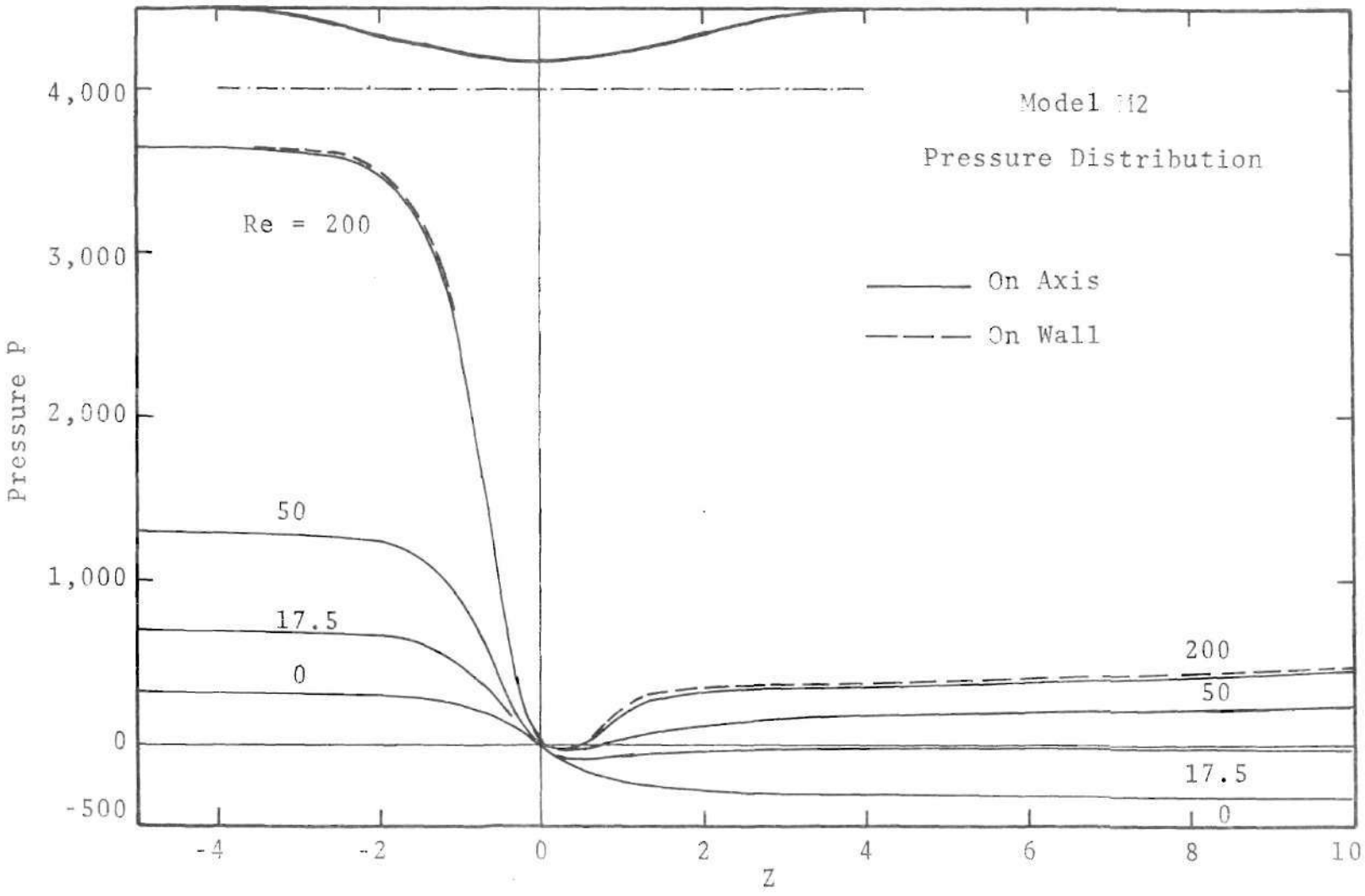

Figure 12. Pressure Distribution in Laminar Flow, Model M2

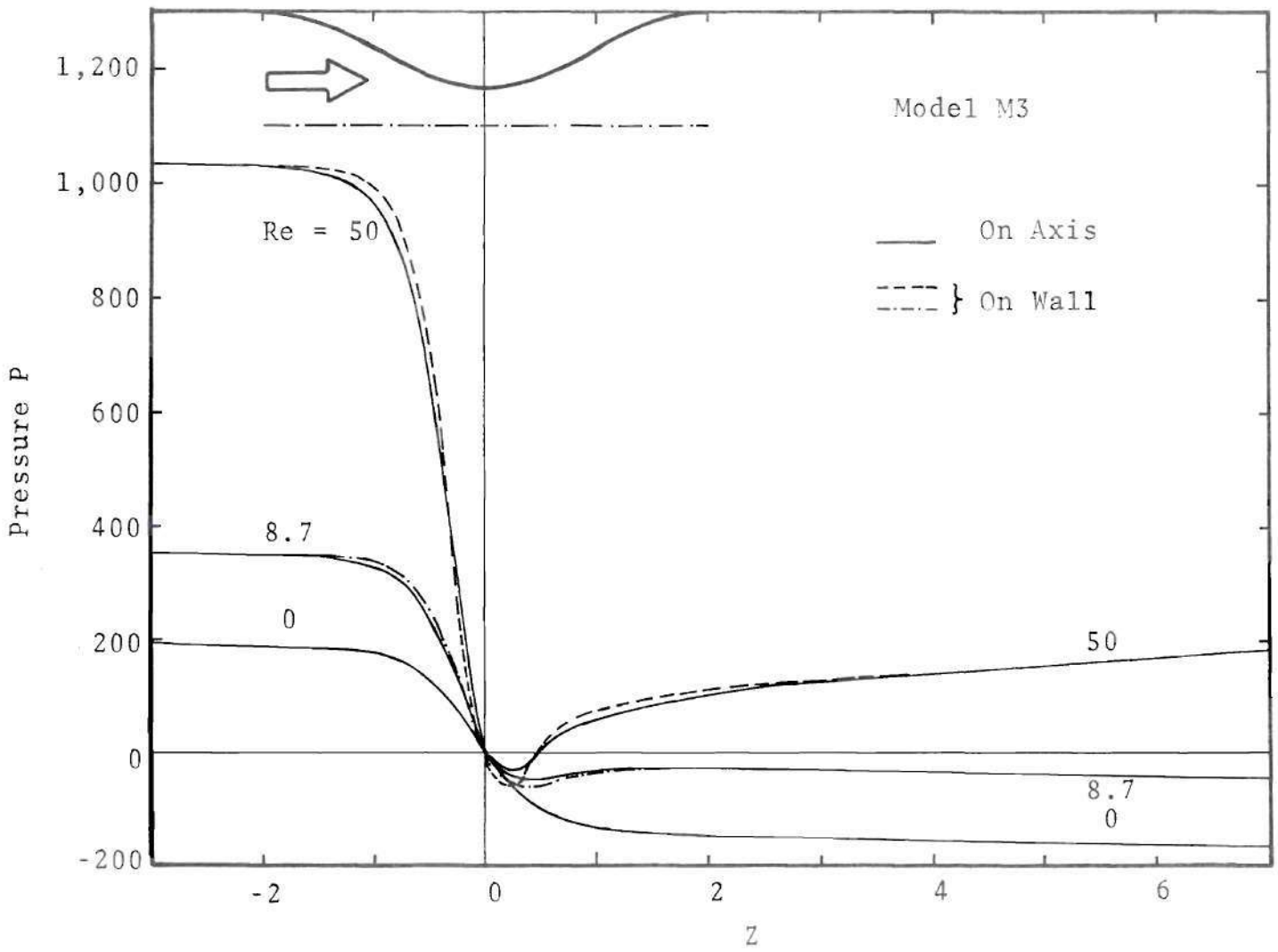

Figure 13. Pressure Distribution in Laminar Flow, Model M3

Reynolds numbers. There is a rapid fall in pressure in the converging portion of the stenoses and local minimum in the pressure is obtained just prior to the separation point. Initial straight segments of these curves correspond to Hagen-Poiseuille flow. The sharp increase in pressure drop due to increase in Reynolds number and the severity of the stenosis is evident. It may be concluded from Figures 12 and 13 that radial pressure gradients are small compared to those in the axial direction. These tend to be still smaller for milder (M1) and longer (M2) stenoses.

In all cases the calculations showed a recovery of the pressure gradient far downstream to the fully developed pipe flow result.

2.4.4. Wall Vorticity (Shear Stress)

The nondimensional wall vorticity ω_w is of considerable interest because of its relation to the value of shear stress acting on the solid surface. The shear stress at the wall is given by

$$\tau_w = \frac{\rho \nu U}{a_o} \omega_w . \qquad (16)$$

Since there is no reliable method of determining wall shear stress experimentally in regions near the recirculation zone, the theoretical calculations offer some insight into the behavior of this quantity. Figure 14 presents the results for Model MO. For Re = 0 the variation in wall vorticity is

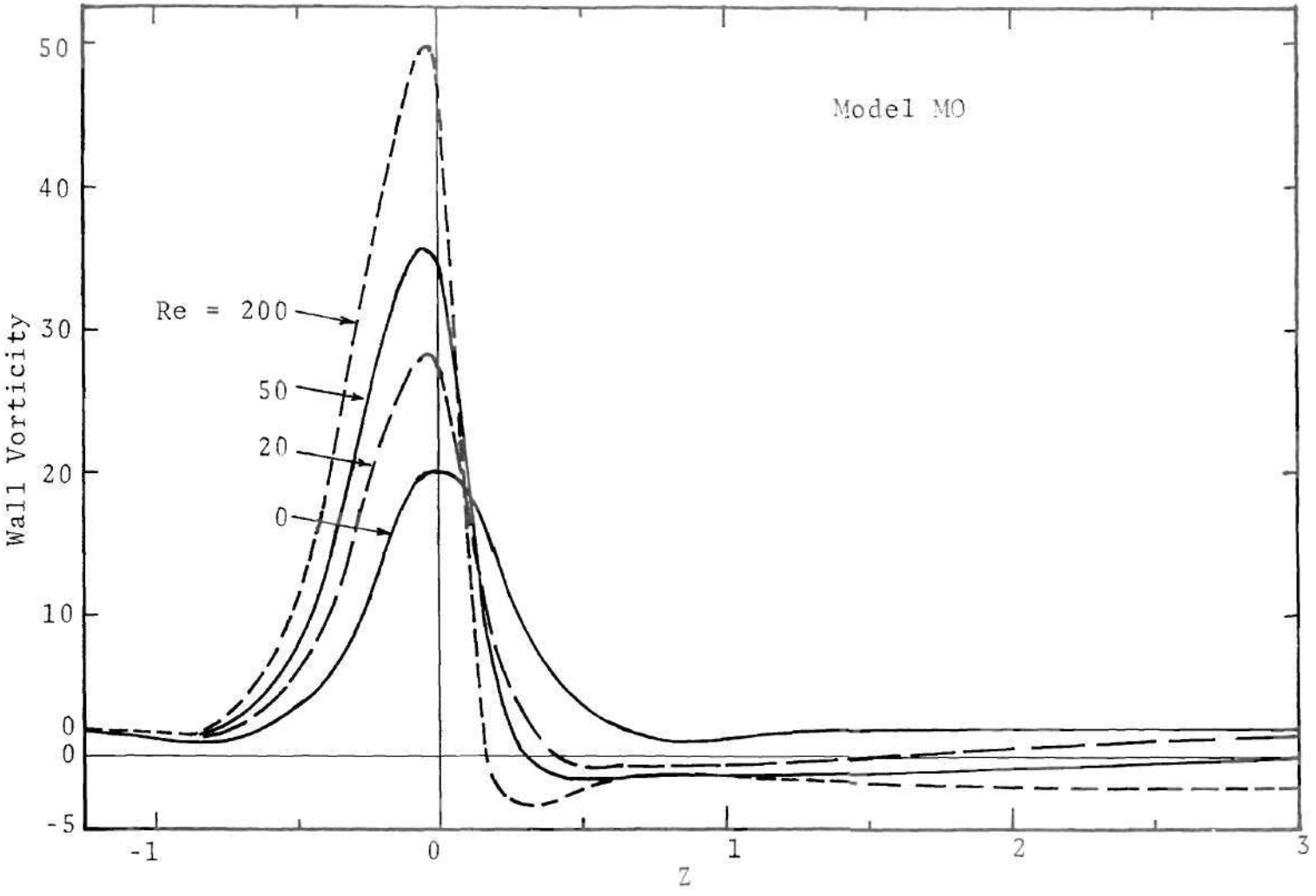

Figure 14. Wall Vorticity in Laminar Flow, Model MO

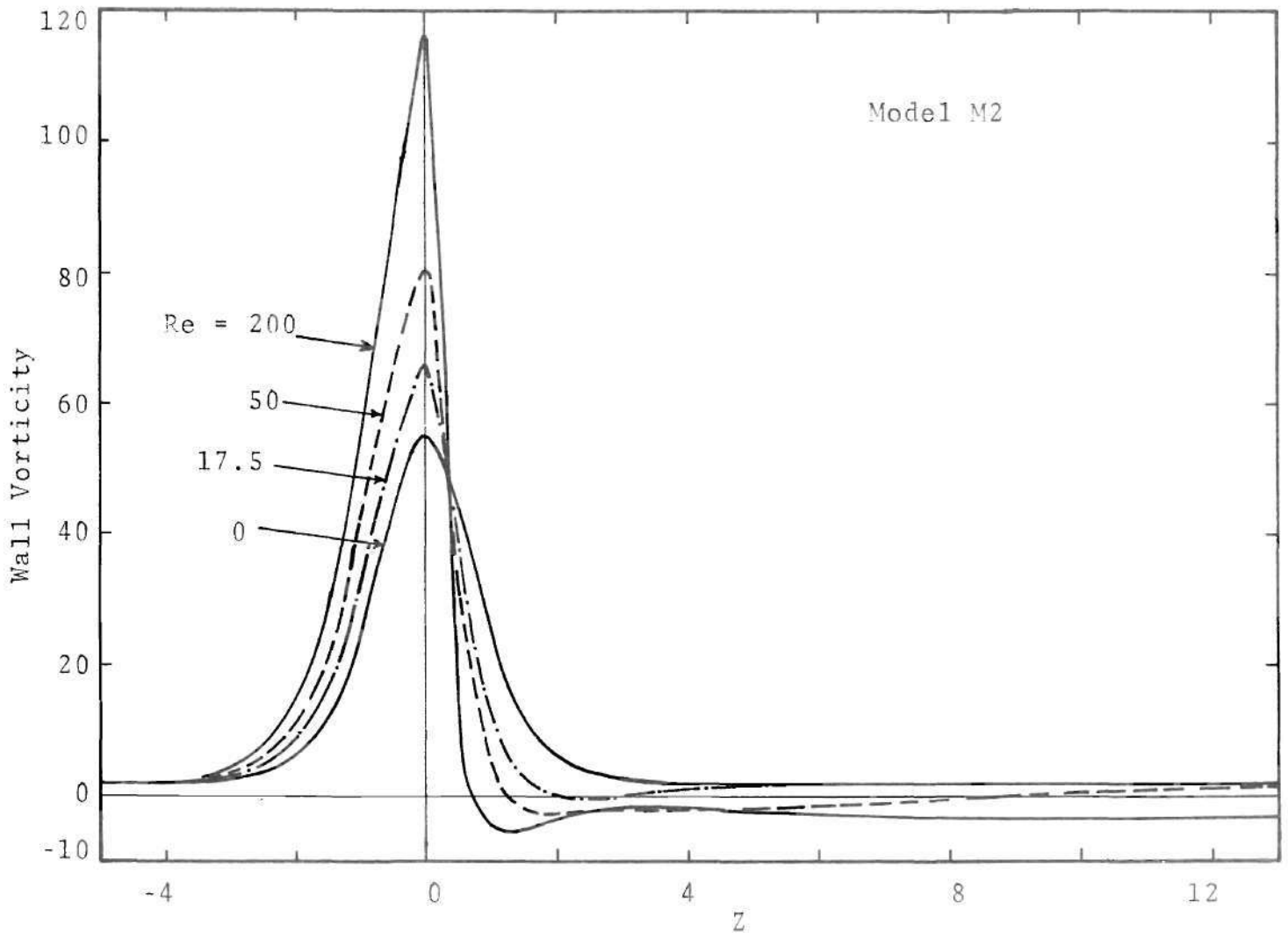

Figure 15. Wall Vorticity in Laminar Flow, Model M2

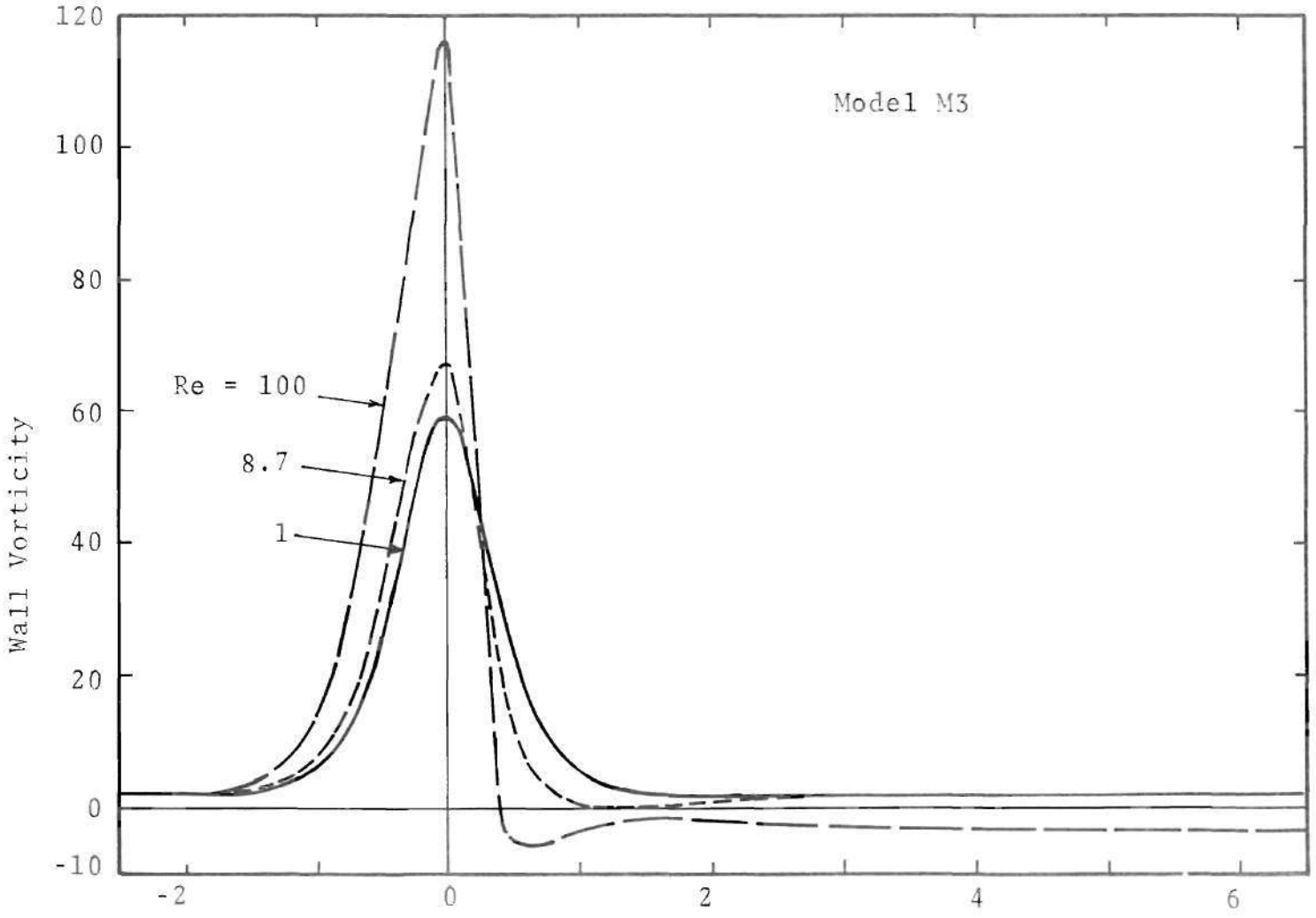

Figure 16, Wall Vorticity in Laminar Flow, Model M3

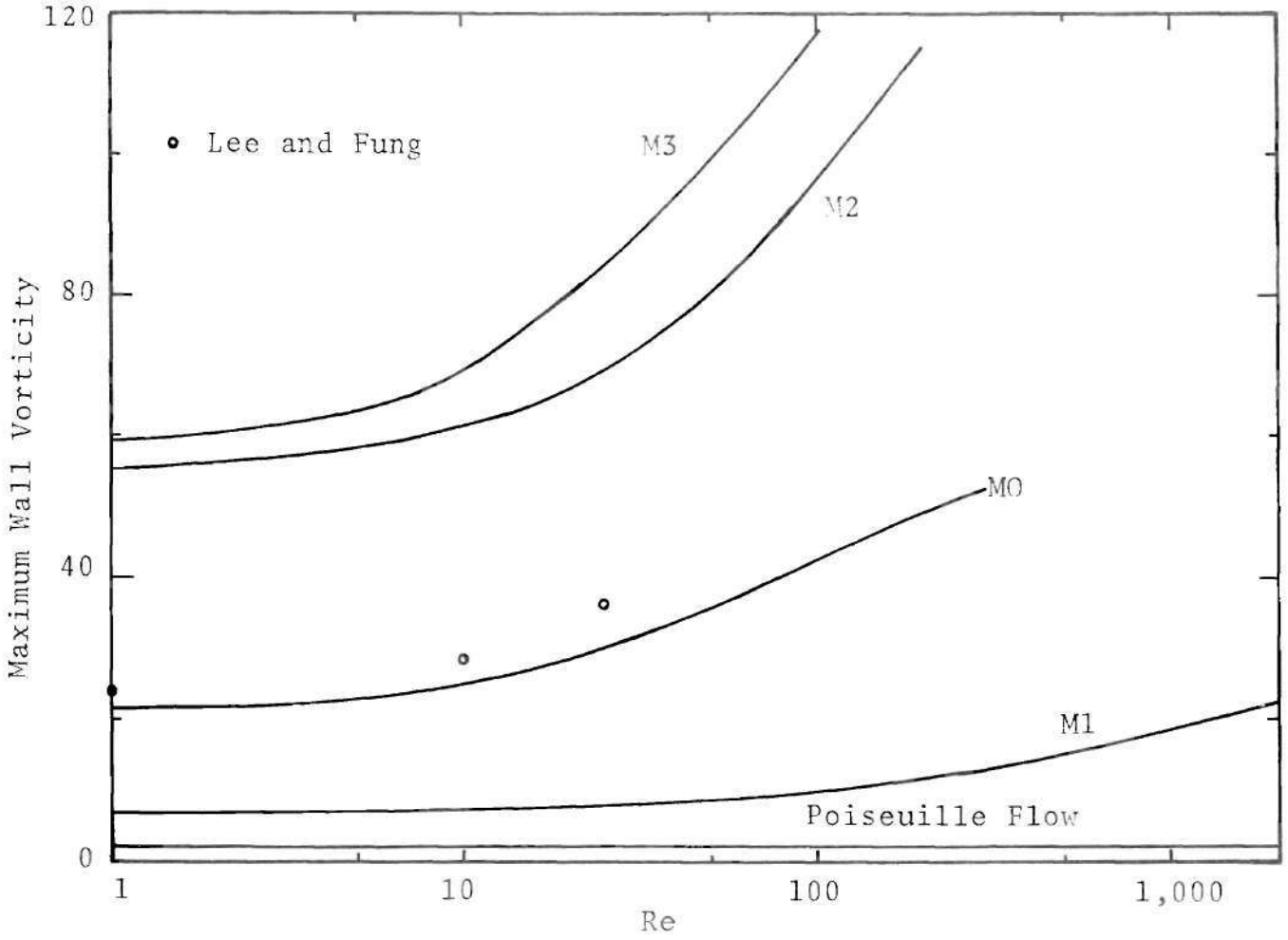

Figure 17. Maximum Wall Vorticity in Laminar Flow, All Models

distributed symmetrically about the plane of maximum area. As Reynolds number increases, this peak stress shifts upstream slightly. At Re = 20 the flow has already formed a separated region as evidenced by negative values of shear stress at the tube surface. This zone increases in extent as the Reynolds number is further increased to 50 and 200.

Figures 15 and 16 show similar curves for models M2 and M3, respectively. Both these figures have cases corresponding to no separation, incipient separation, and extended recirculation regions. Note that here, although the peak shear stress has again migrated upstream somewhat with increasing Reynolds number, this movement is scarcely detectable.

Figure 17 illustrates the maximum values of wall vorticity for all four models as a function of Reynolds number. The Hagen-Poiseuille value of 2.0 is shown for comparison. Computational values by Lee and Fung indicated in the figure correspond to their geometry which resembled Model MO. The rapid increase in wall vorticity with Reynolds number for the severe stenoses is quite apparent. The dimensional value of shear stress τ_w is obtained after multiplying by the velocity U (Equation 16) and hence the increase in τ_w with Reynolds number is more pronounced.

2.4.5. Flow Velocities

The velocity profiles provide a detailed description of the flow field and hence several of them are included in

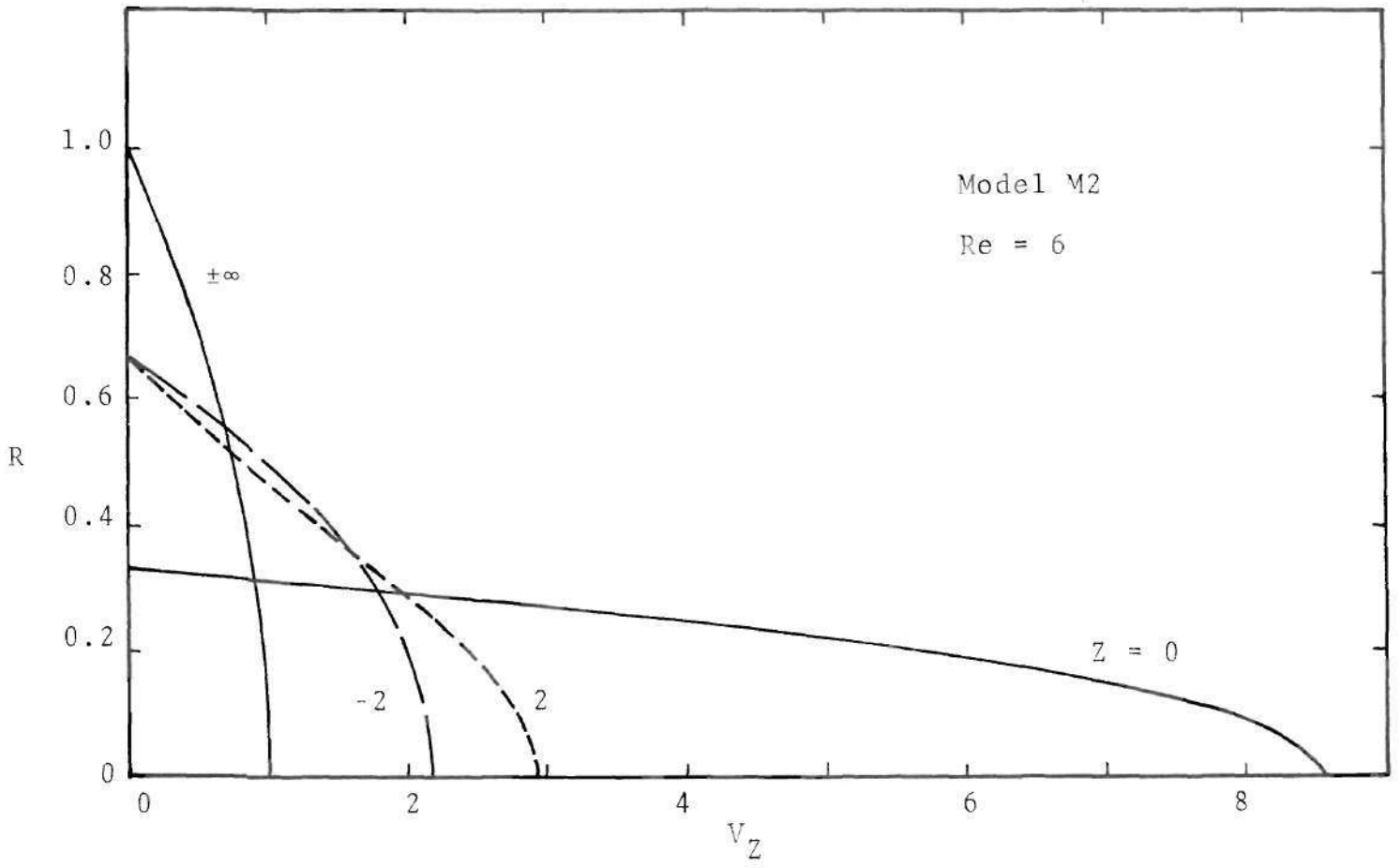

Figure 18a. Axial Velocity Profiles, Model M2, Re = 6

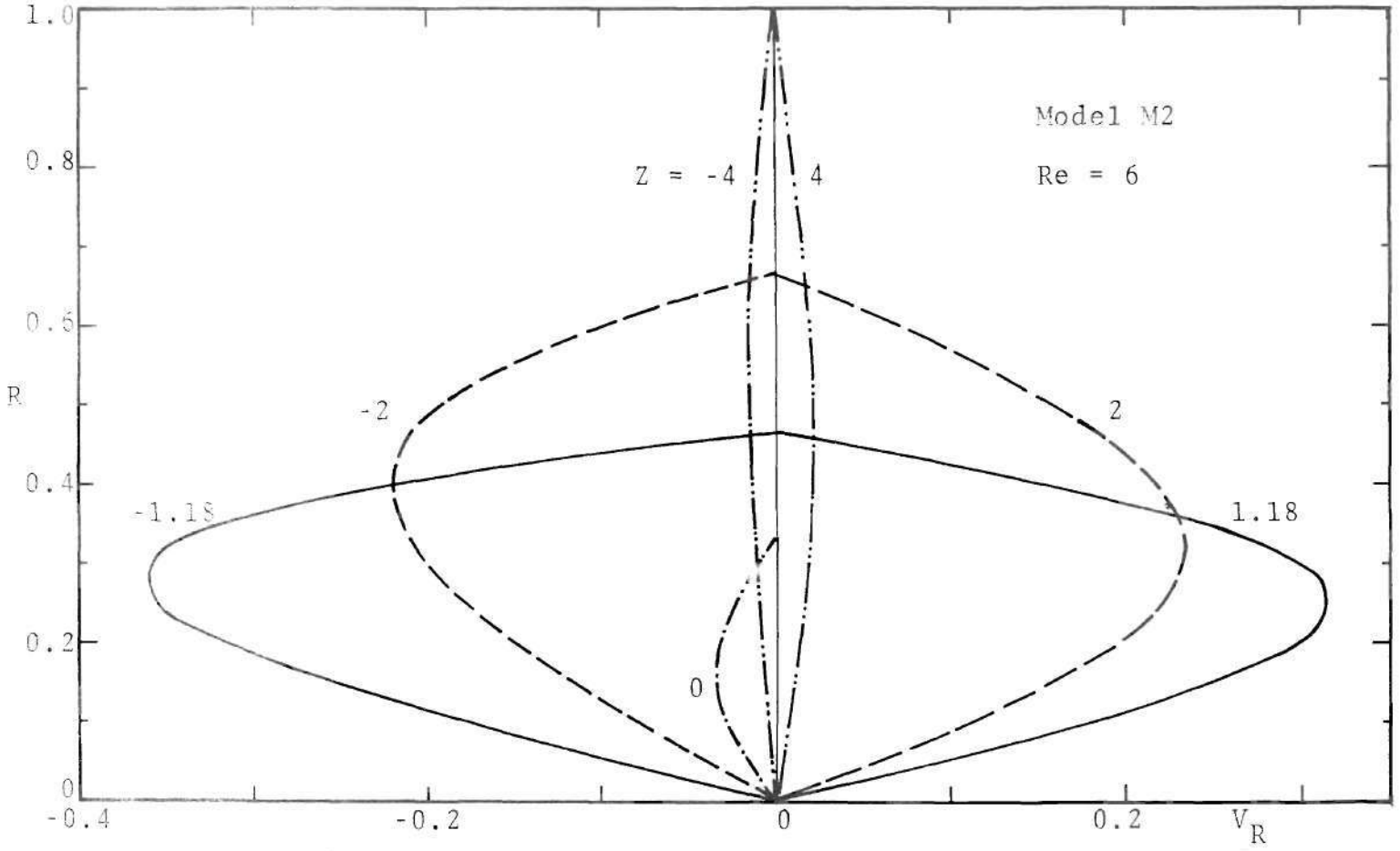

Figure 18b. Radial Velocity Profiles, Model M2, Re = 6

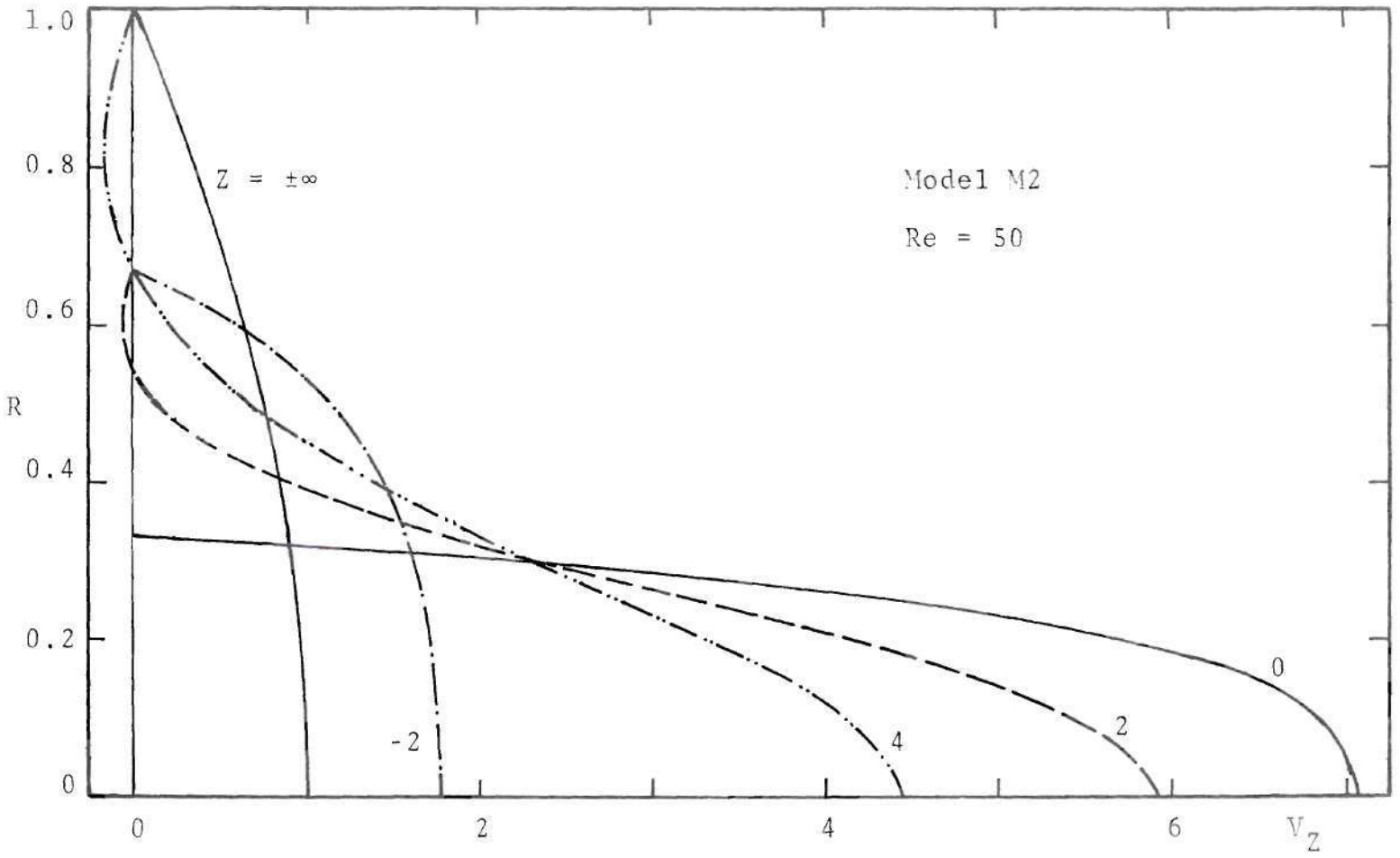

Figure 19a. Axial Velocity Profiles, Model M2, Re = 50

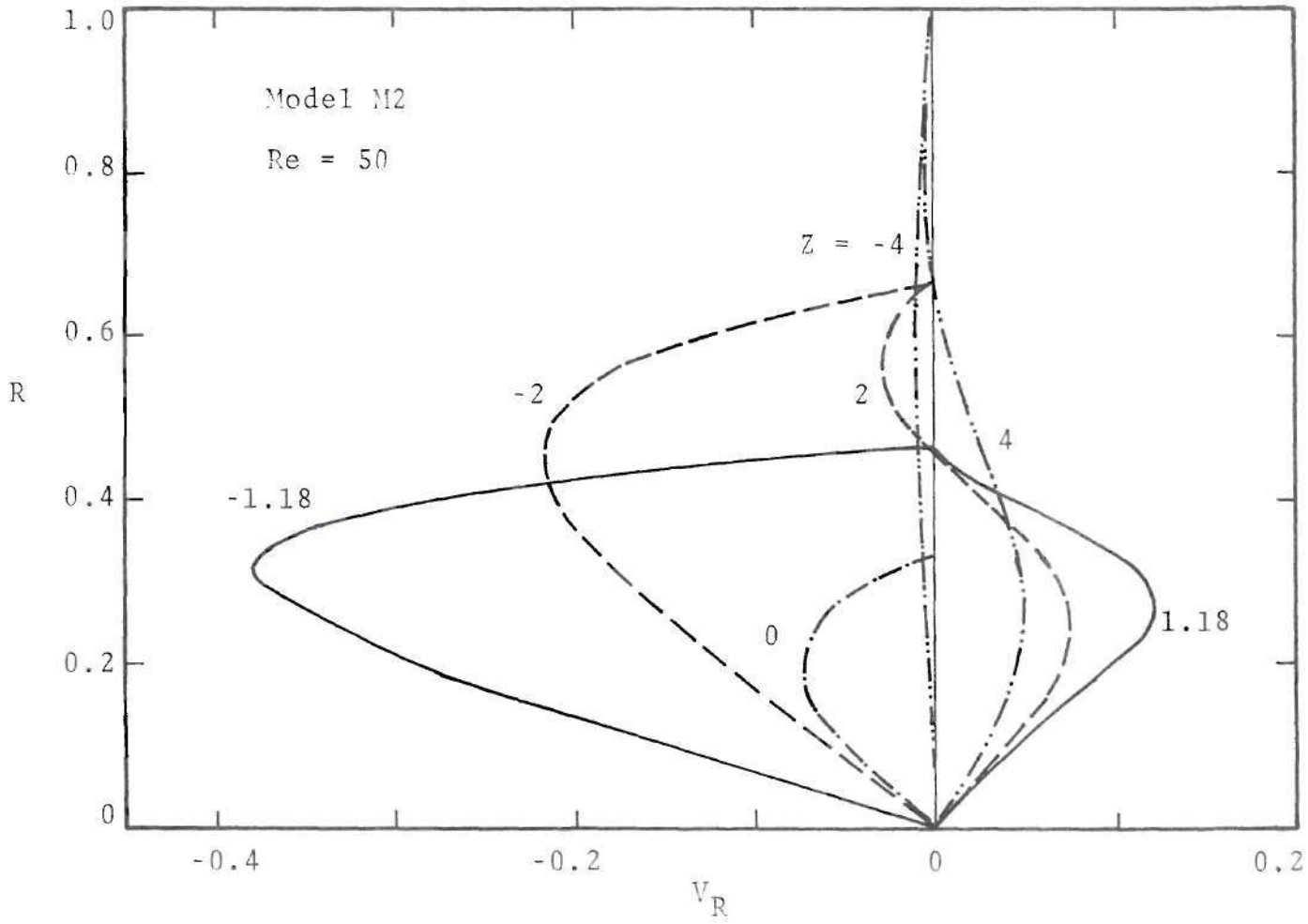

Figure 19b. Radial Velocity Profiles, Model M2, Re = 50

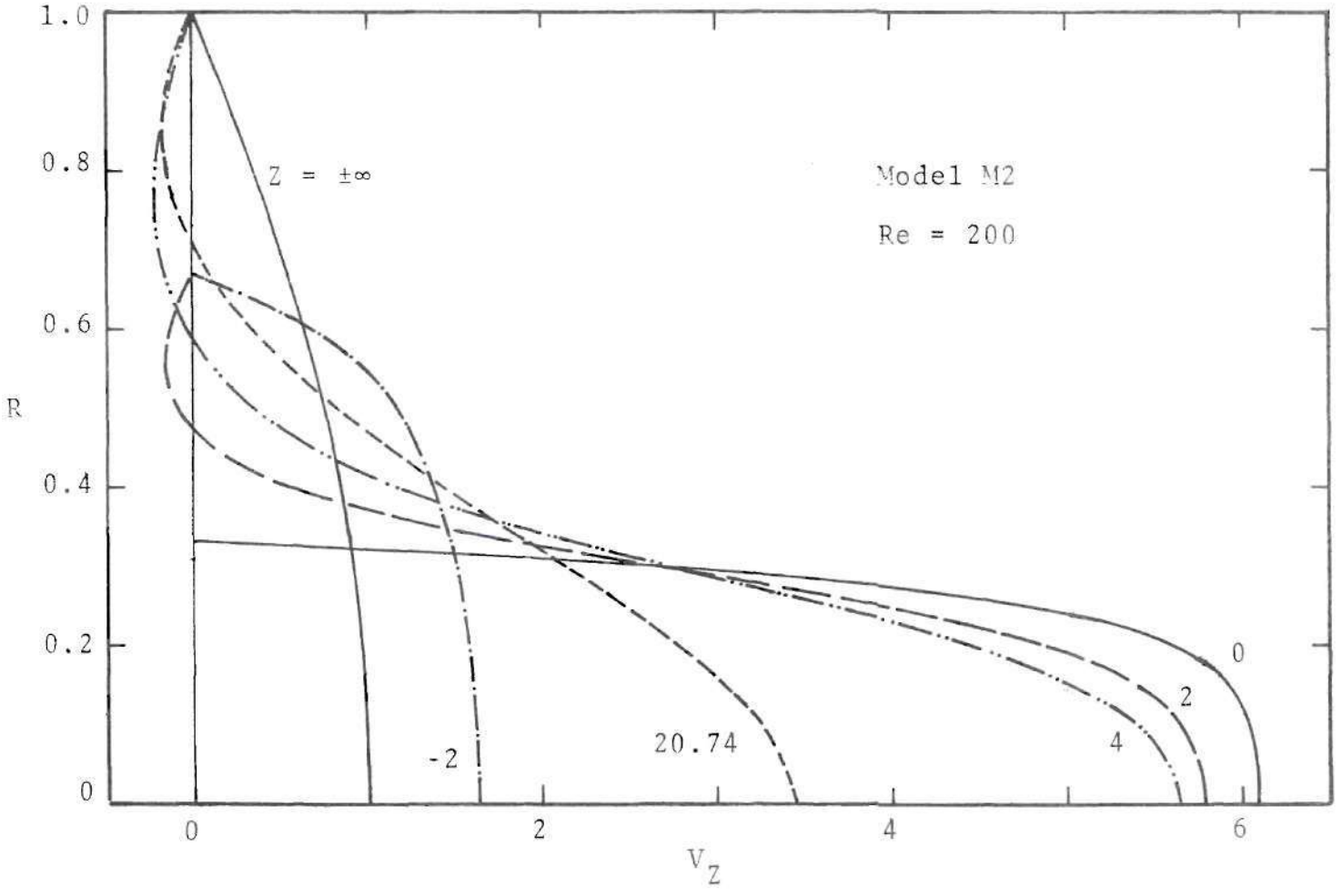

Figure 20a. Axial Velocity Profiles, Model M2, Re = 200

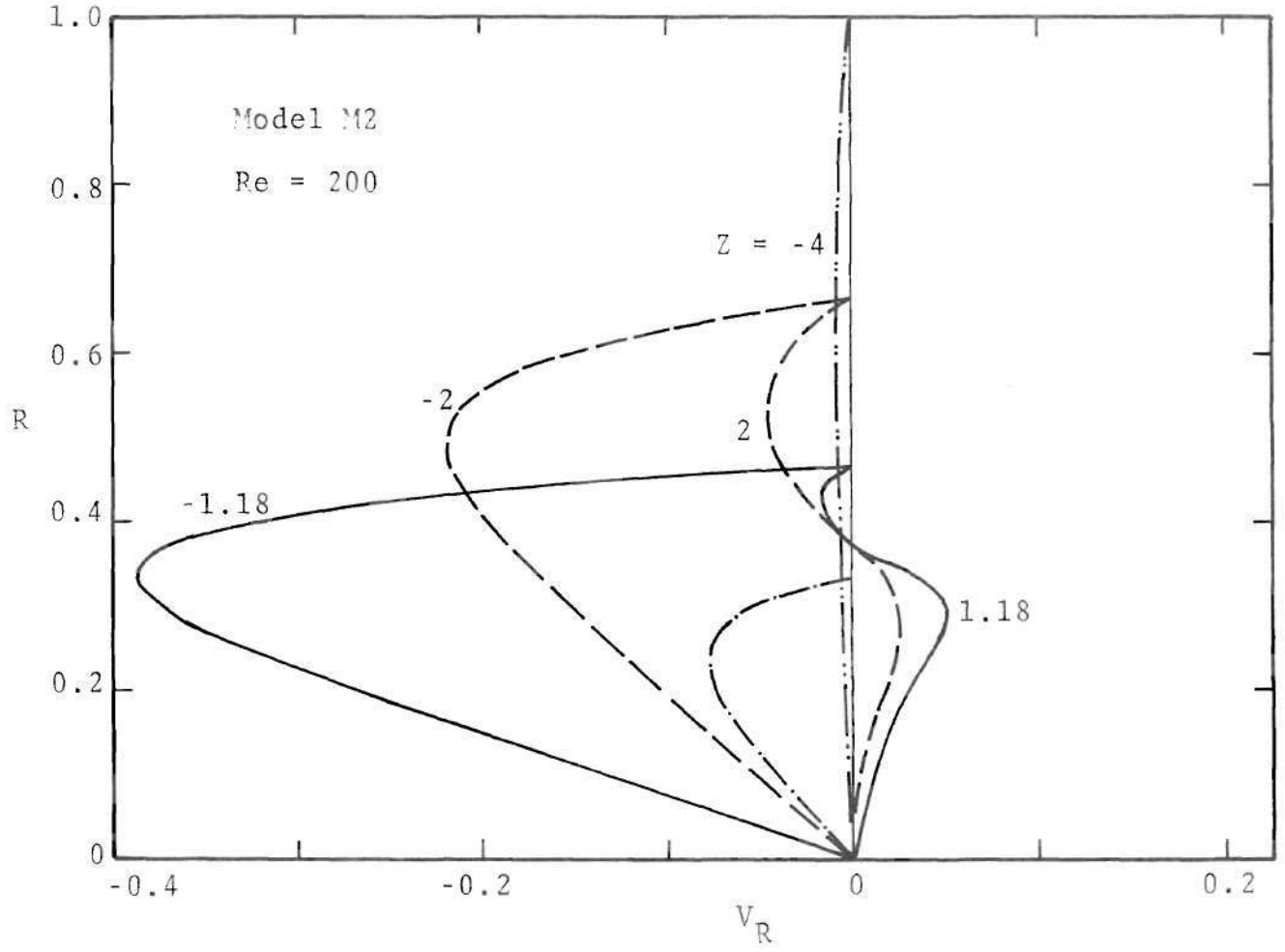

Figure 20b. Radial Velocity Profiles, Model M2, Re = 200

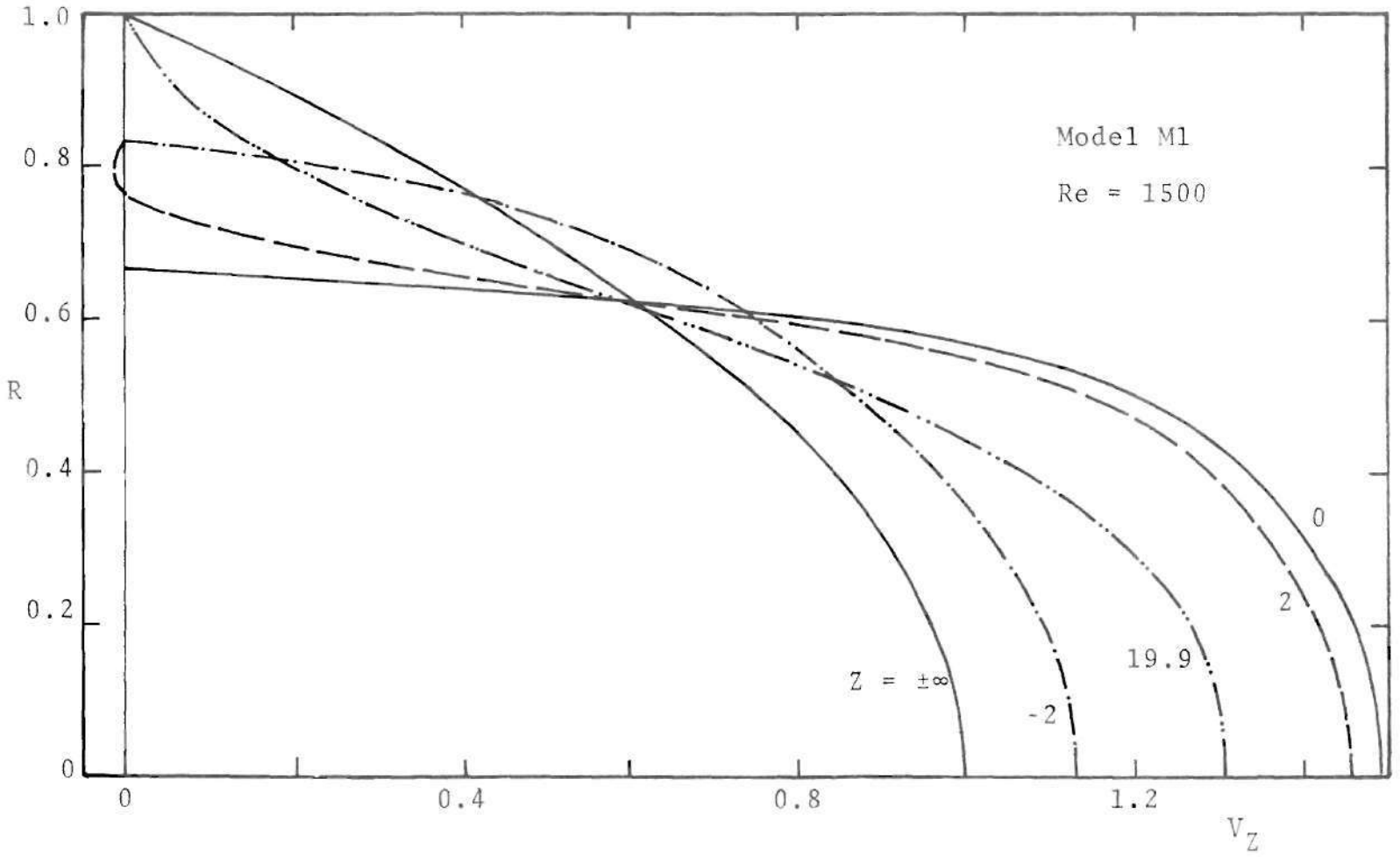

Figure 21a. Axial Velocity Profiles, Model M1, Re = 1500

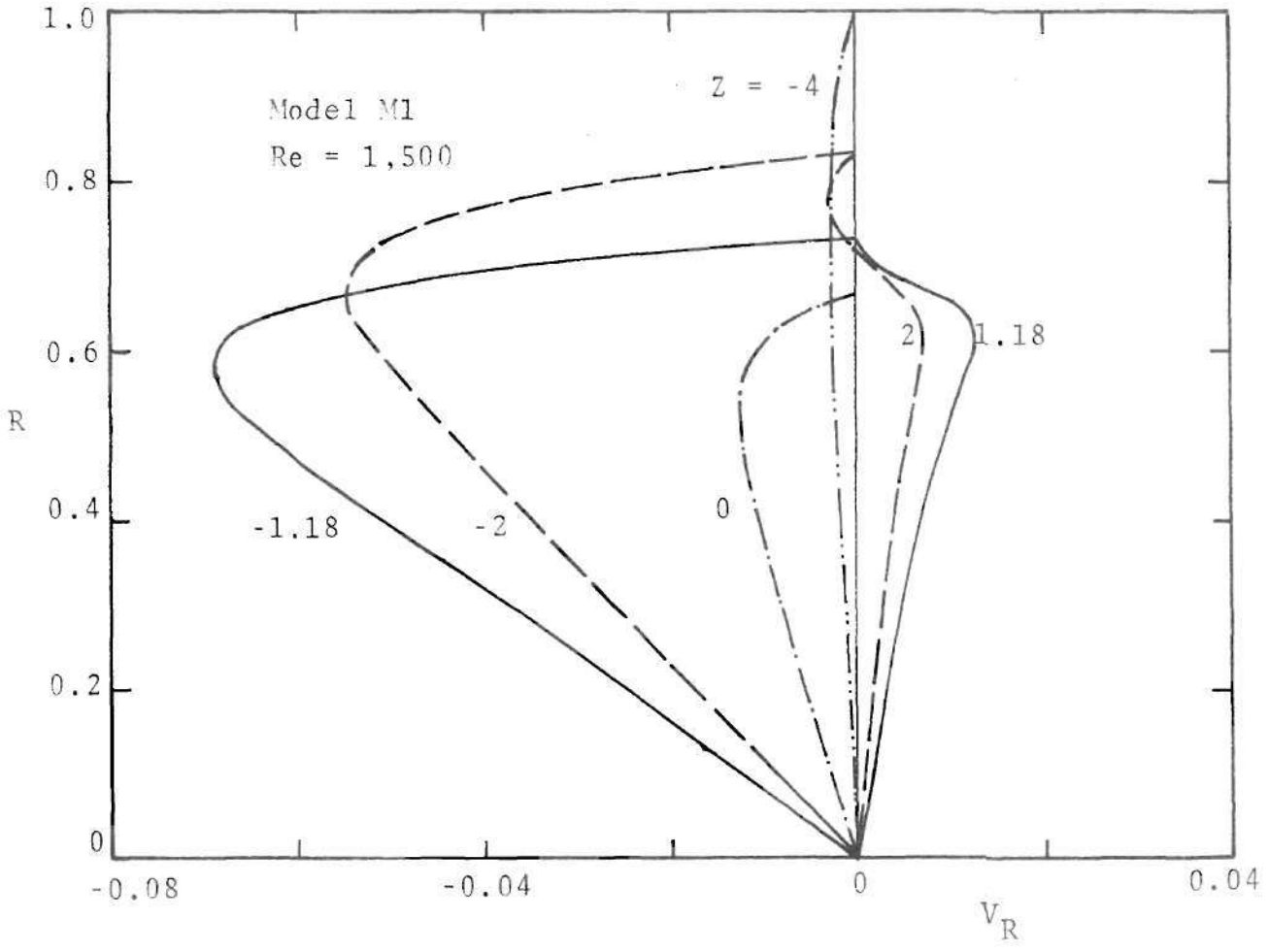

Figure 21b. Radial Velocity Profiles, Model M1, Re = 1500

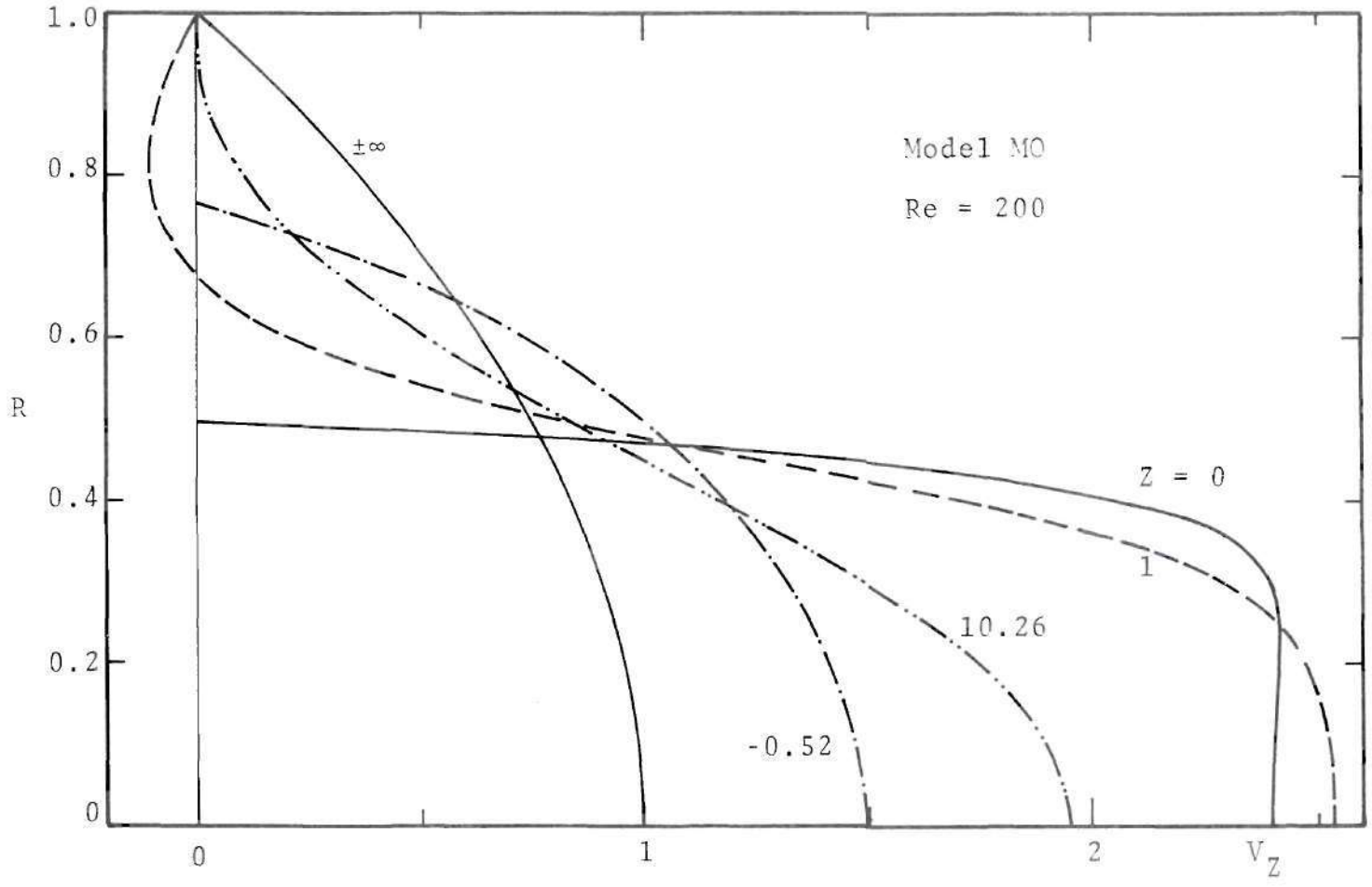

Figure 22a. Axial Velocity Profiles, Model MO, Re = 200

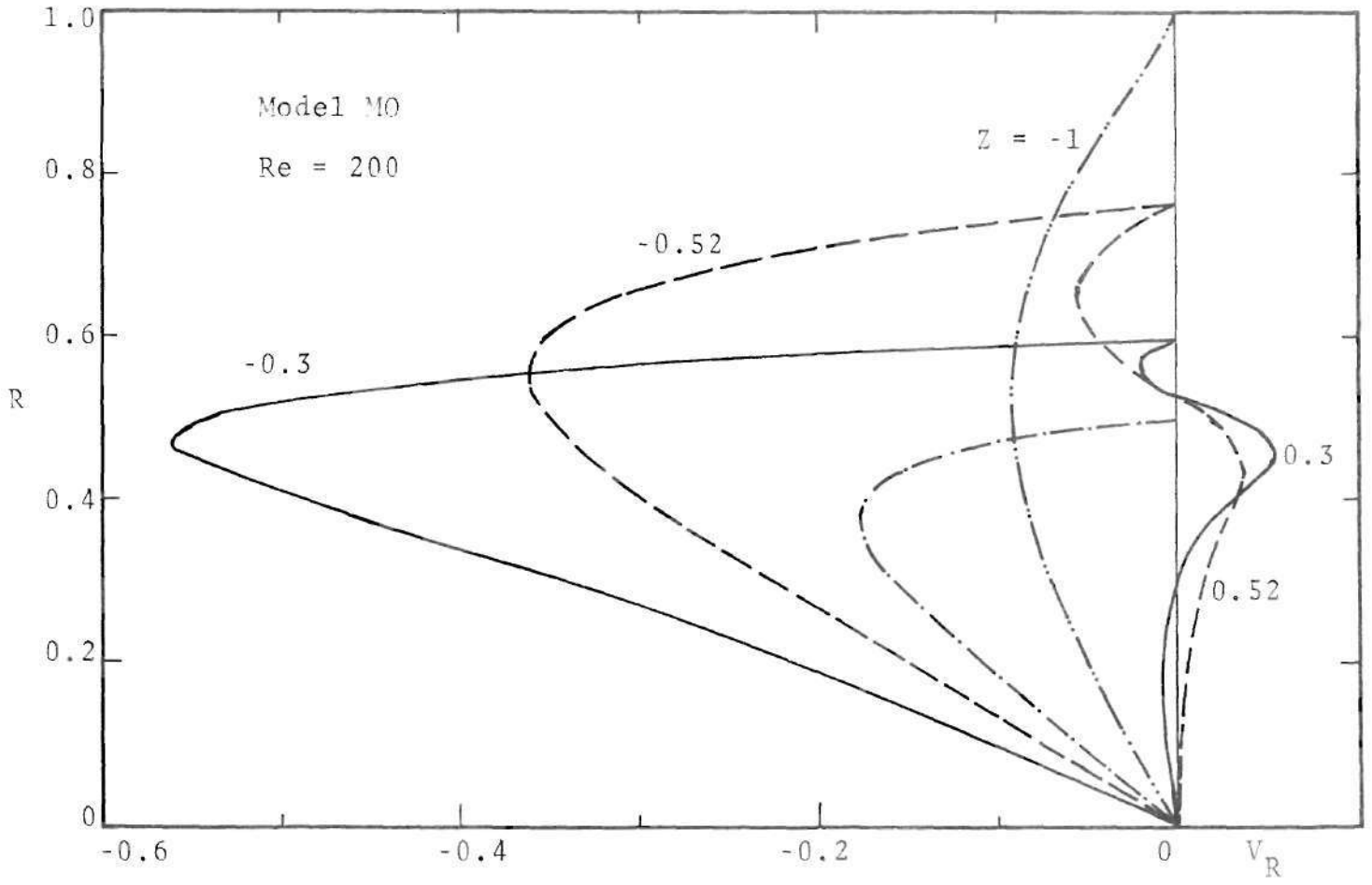

Figure 22b. Radial Velocity Profiles, Model MO, Re = 200

Figures 18-22. Figures 18, 19 and 20 give examples of velocity components for Model M2 and Re = 6, 50 and 200. For the lowest value of Reynolds number the axial velocity component (Figure 18a) is always in the positive direction. The formation of a jet like profile in the vicinity of the throat is apparent. However, the fluid is still accelerating at Z = 0 as evidenced by the slightly negative values of radial velocity (Figure 18b). Thus, the peak velocity occurs distal to the throat.

For Re = 50 and 200 regions of reverse flow are clearly seen (Figures 19 and 20). Both velocity components undergo a change in sign within the recirculation region at these stations, indicating the strongly elliptic nature of the problem. Again, the fluid is still experiencing an acceleration at Z = 0 in both the cases. The magnitude of radial component of velocity in the core of the flow distal to the stenoses is seen to decrease as the Reynolds number is increased; on the other hand the negative portion of this component in the recirculation region increases with Reynolds number. Figures 21a and 21b are similar plots of axial and radial velocity components for Model M1 for a relatively high Reynolds number of 1,500. A thin recirculating region is present with a weak reverse flow.

Figure 22a is an interesting example where the maximum velocity does not occur on the centerline. For this relatively short stenosis M0, the peaks occur symmetrically

at R = 0.23 for Re = 200. A high value of radial velocity for the same case is indicated in Figure 22b. At Z = -0.3, it is 12 percent greater than the average velocity in the unoccluded tube.

Centerline velocity in an axisymmetric flow is a sensitive quantity, and its variation with axial location gives a good overall picture of the flow. It is recorded for Models MO, M1, M2, and M3 in Figures 23-26, respectively, for various Reynolds numbers corresponding to no separation, incipient separation, and extended recirculation cases. Such a plot is symmetrical for Re = 0; and as the Reynolds number is increased, the region of influence extends distal to the stenosis. A slowly decaying centerline velocity is indicative of the presence of a recirculation region. For high values of Reynolds number the decrease in velocity is approximately linear in Z. The centerline velocity (in the nondimensional form) at the throat and the peak it reaches, just distal to the minimum area, decrease as the Reynolds number is increased. This behavior can be clearly seen in Figure 27 which is replotted for all models from the previous plots. This can be thought of as due to a more abrupt contraction of the stream tube by the stenosis at a higher Reynolds number. This results in blunter velocity profiles near the throat as may be seen, for example, from Figures 18a, 19a and 20a. For the same reason, the shorter stenosis Model M3 attains a blunter velocity profile and lower velocity compared

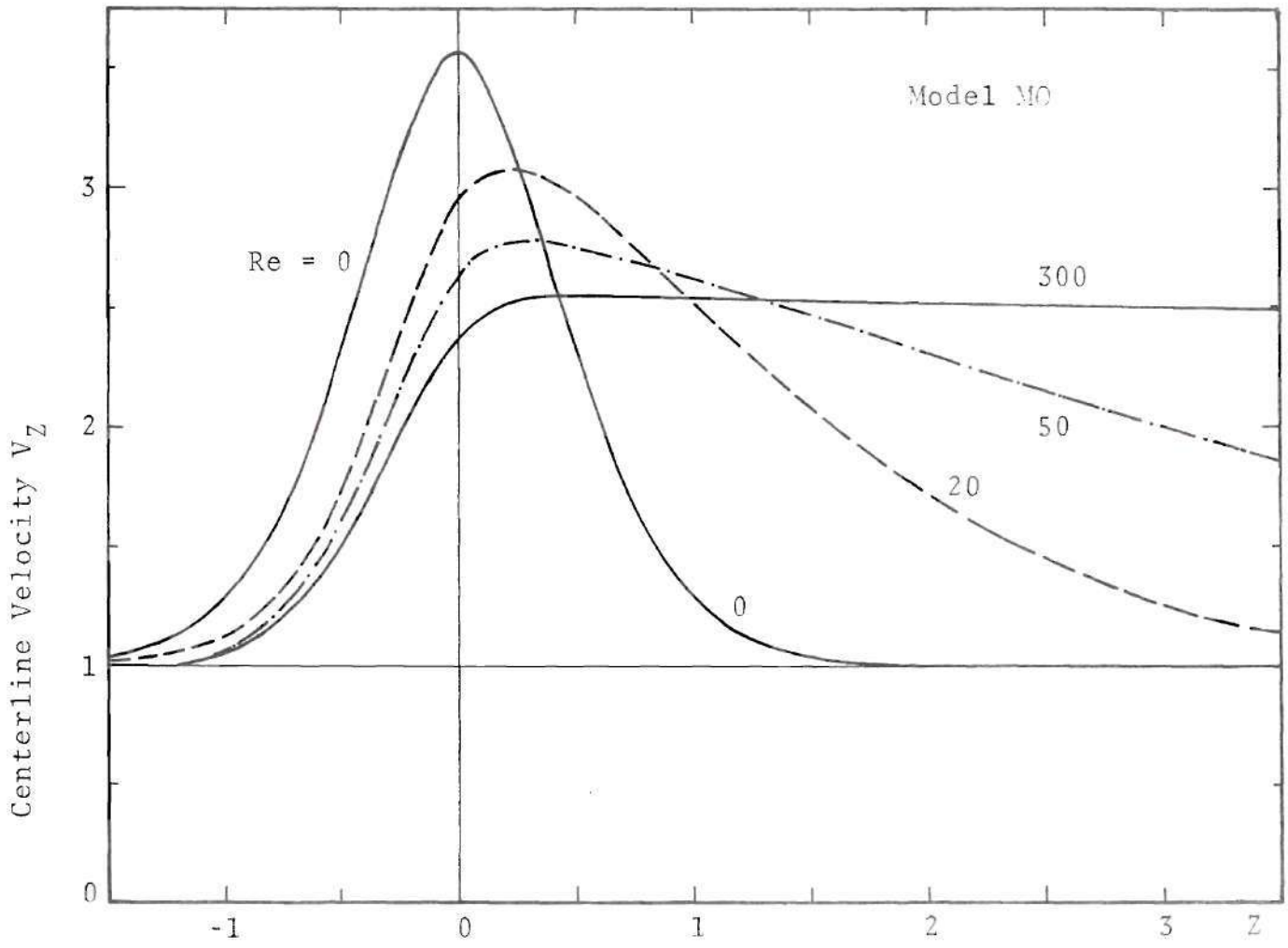

Figure 23. Axial Variation of Centerline Velocity, Model MO

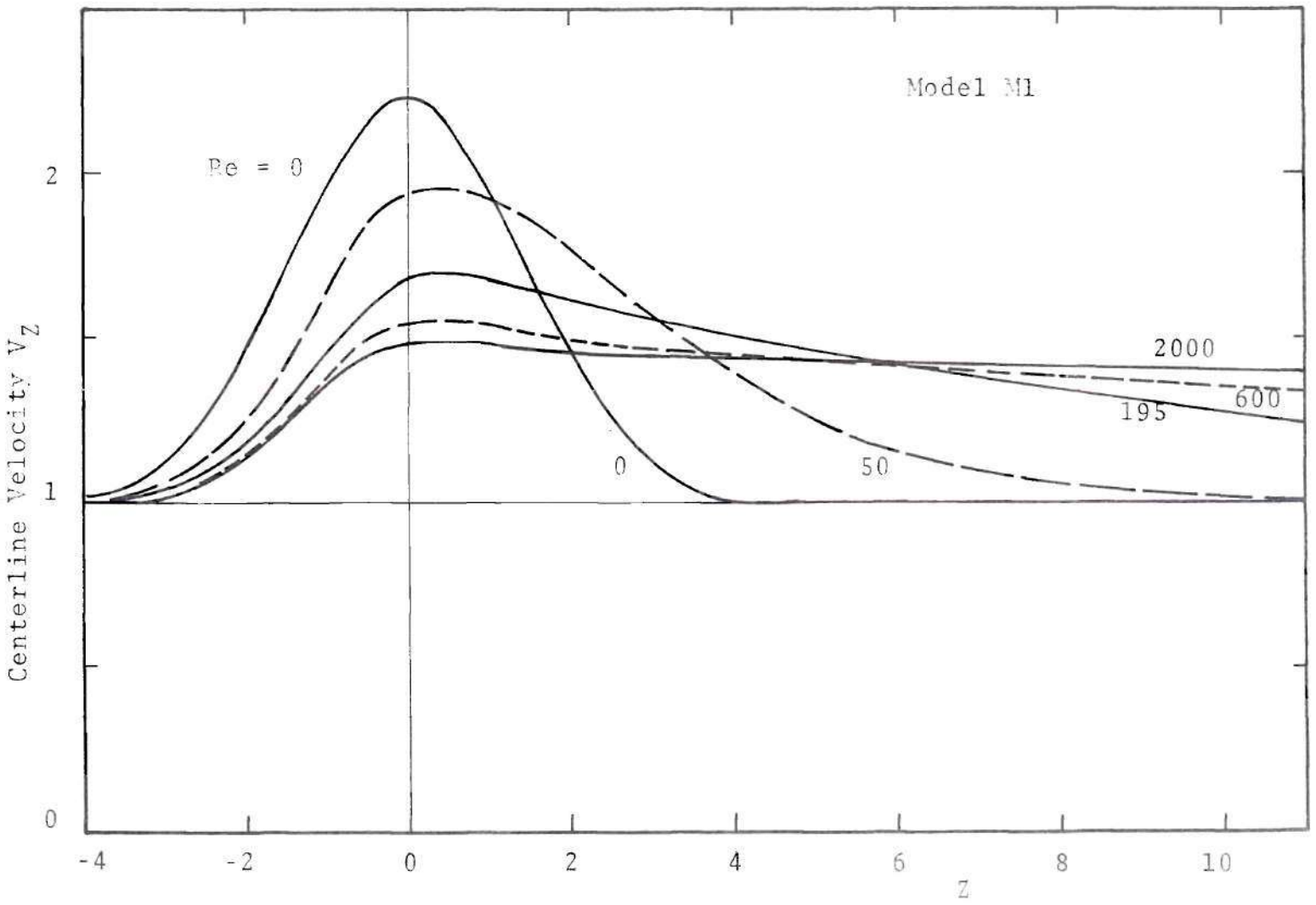

Figure 24. Axial Variation of Centerline Velocity, Model M1

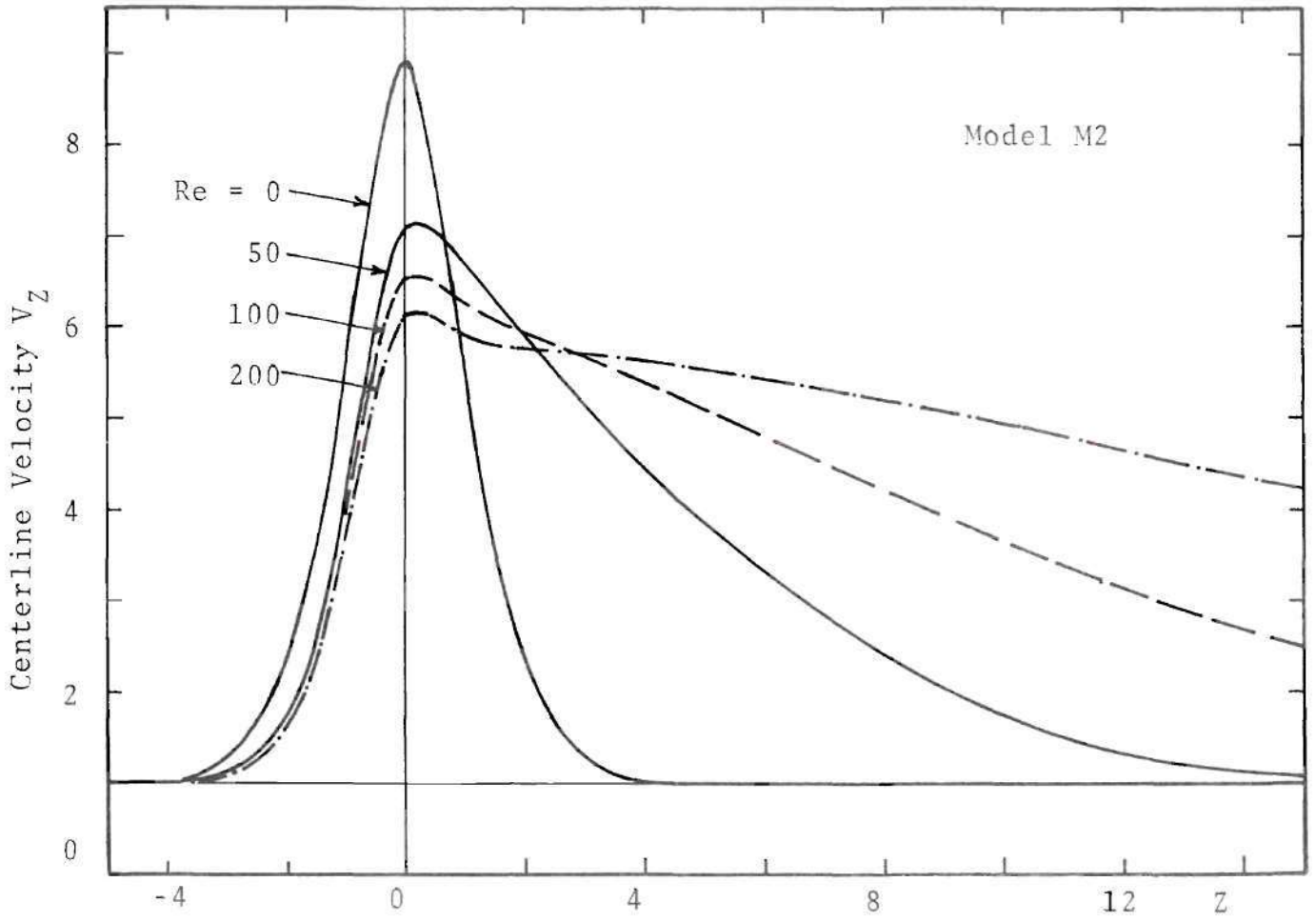

Figure 25. Axial Variation of Centerline Velocity, Model M2

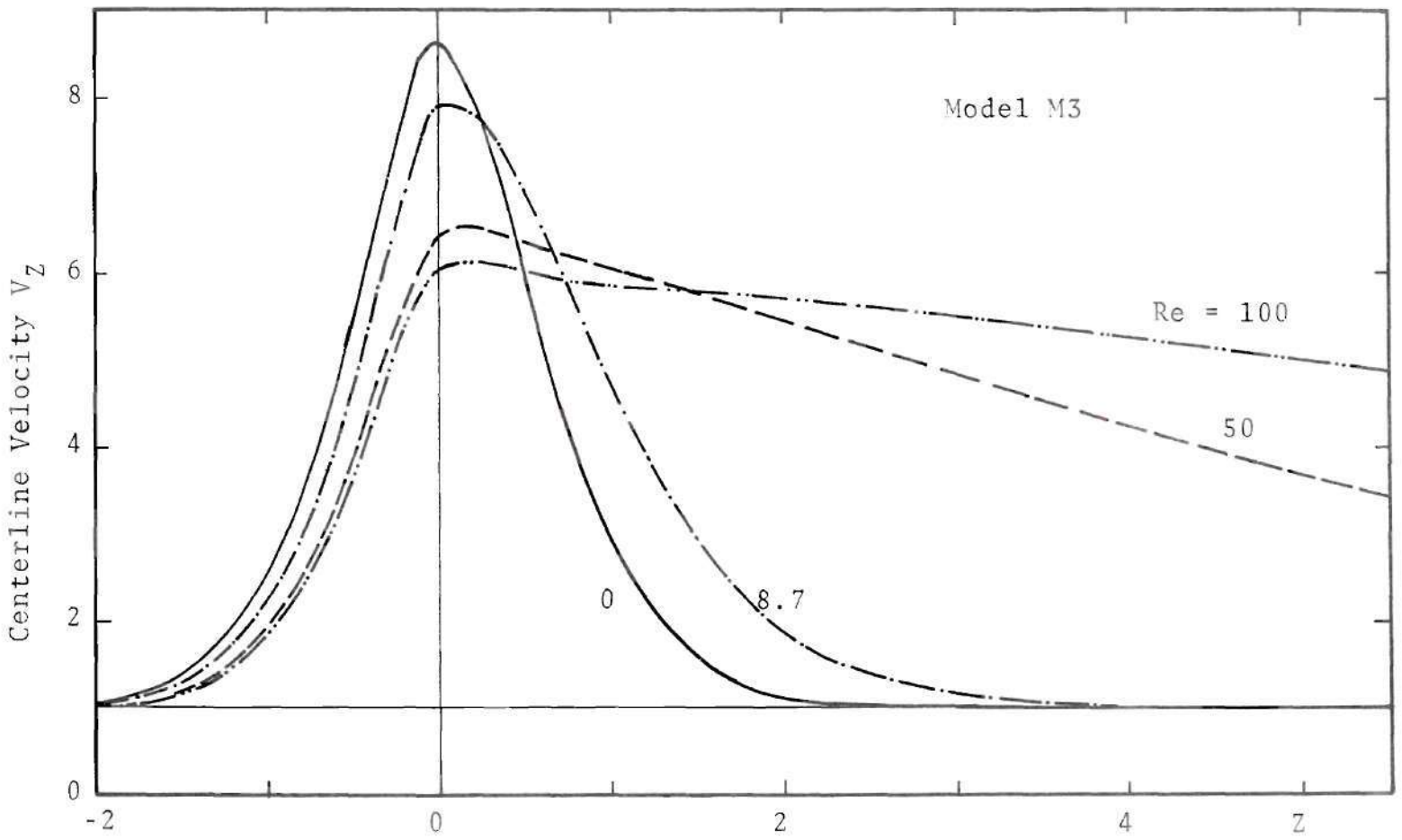

Figure 26. Axial Variation of Centerline Velocity, Model M3

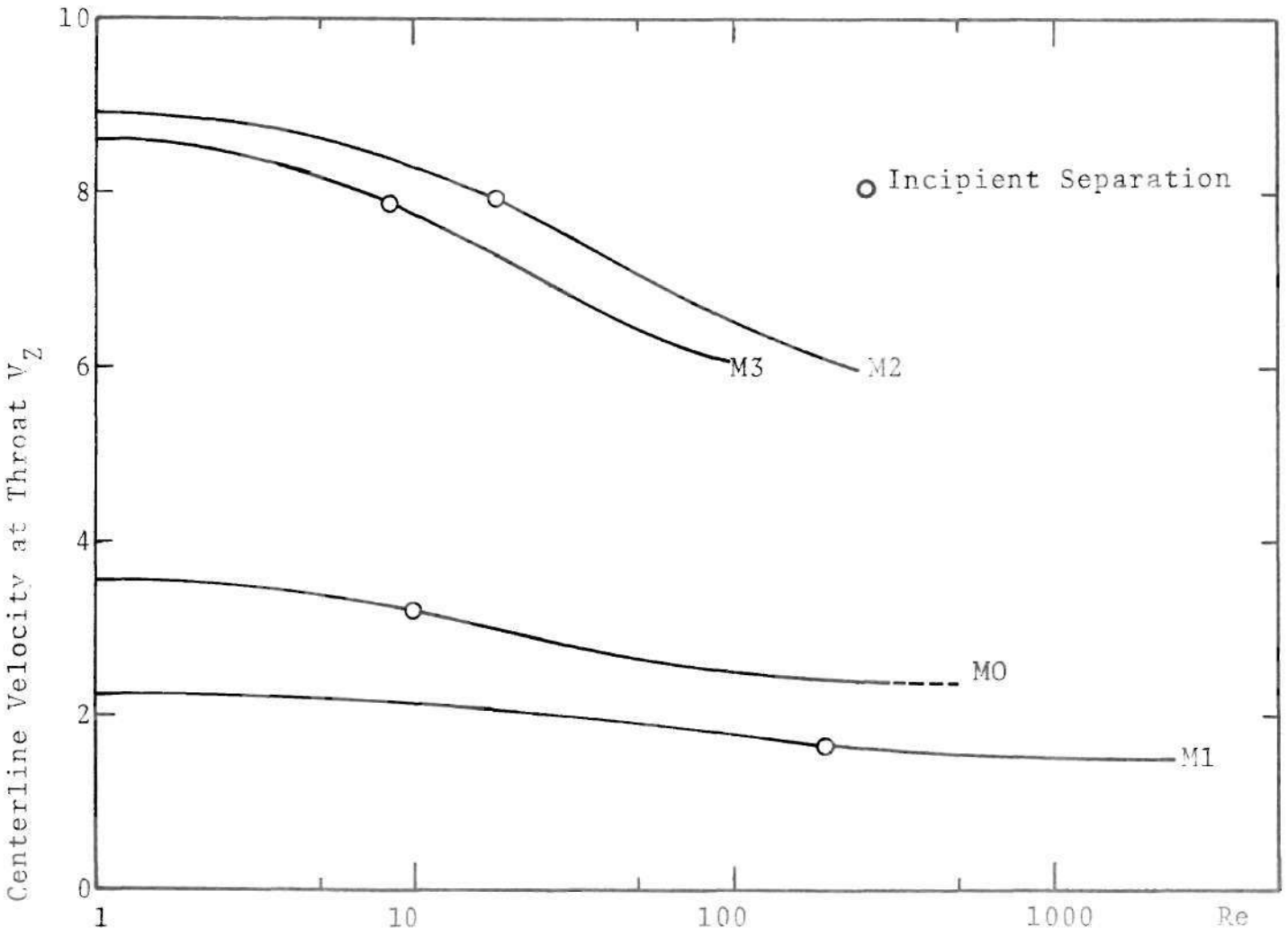

Figure 27. Centerline Velocity at Throat as a Function of Reynolds Number, All Models

to Model M2. The separation Reynolds number indicated in Figure 27 for each of the models seems to coincide with the point of inflection in the curve. This is due to the significant changes brought about in the flow by the separation.

2.5. Discussion

The laminar flow computations presented in this chapter clearly fall short of providing flow field predictions for an actual arterial flow. The greatest disparity is that unsteady terms have been omitted. This actually causes two weaknesses. The first is that pulsatile flow is not incorporated. But a second, and very important, consequence is that flow instabilities are not included. Therefore, propagating vortices and transition to turbulence are eliminated from consideration. As mentioned in the first chapter, these phenomena are much more prevalent in arterial hemodynamics than had been thought previously. The case of assuming the flow to remain fully turbulent is considered in the subsequent chapters.

Another shortcoming is the assumption of axisymmetric stenoses. Lesions which occur in the vascular system are usually irregular in shape and are frequently located near vessel branching or bifurcation, and they may be localized or multiple. Thus, the biological velocity field is three dimensional. Some qualitative observations may be made in

the light of the experimental results of Young and Tsai [18], who studied several nonaxisymmetric stenosis geometries in addition to the axisymmetric contours previously discussed. They concluded that flow was sensitive to both shape and percent reduction in area. Their results showed an increase in pressure drop for nonaxisymmetric cases. This increase was small for severe stenoses at low Reynolds numbers. Further the separation Reynolds number tends to be lower for unsymmetric contours whenever the comparison is made for mild stenoses. This value is already very small for severe stenoses and seems to be less sensitive to change in shape.

In spite of these deficiencies, the present results have extended steady flow laminar calculations to include contoured, as opposed to unrealistic rectangular, stenoses and have presented a comparison with available experimental data. The range of Reynolds numbers which can be achieved without convergence difficulties or without excessive computer time spans the cases where experimental observations indicate a completely laminar flow. Agreement with measured quantities is good, although hopefully future experimental investigations can provide velocity profiles which would allow a much more detailed comparison. The calculations indicate extended regions of flow recirculation and large values of wall shear stresses along the proximal wall of the stenoses. Implications of these to arterial disease will be discussed in Chapter VI. The study reported under this chapter has been published in a technical journal [59].

CHAPTER III

TURBULENT FLOW COMPUTATIONS

The analytical study of turbulent flow through a model stenosis is described in this chapter. In developing the computational procedure it was found that turbulent entrance flow in a pipe was valuable as a test case and this is also included.

It was mentioned in the first chapter that flow can become transitional and turbulent in the circulatory system in the presence of complicated geometries such as heart valves, vessel branching, or stenoses. That point is reemphasized here with the assistance of the in vivo data obtained by Giddens et al. [22]. Figure 28 presents a graphic picture of the flow disturbances caused by increasing the degree of constriction. These hot film records were made two centimeters distal to the minimum area in a canine aorta of 1.2 centimeter diameter. The peak and mean Reynolds numbers were approximately 2,000 and 1,100, respectively. It is interesting to note that laminar assumptions break down even for mild stenosis cases at this Reynolds number range. One may also note the decrease in pulsatility and the increase in the high frequency components of disturbance velocity as the occlusion becomes more severe. These pictures, along

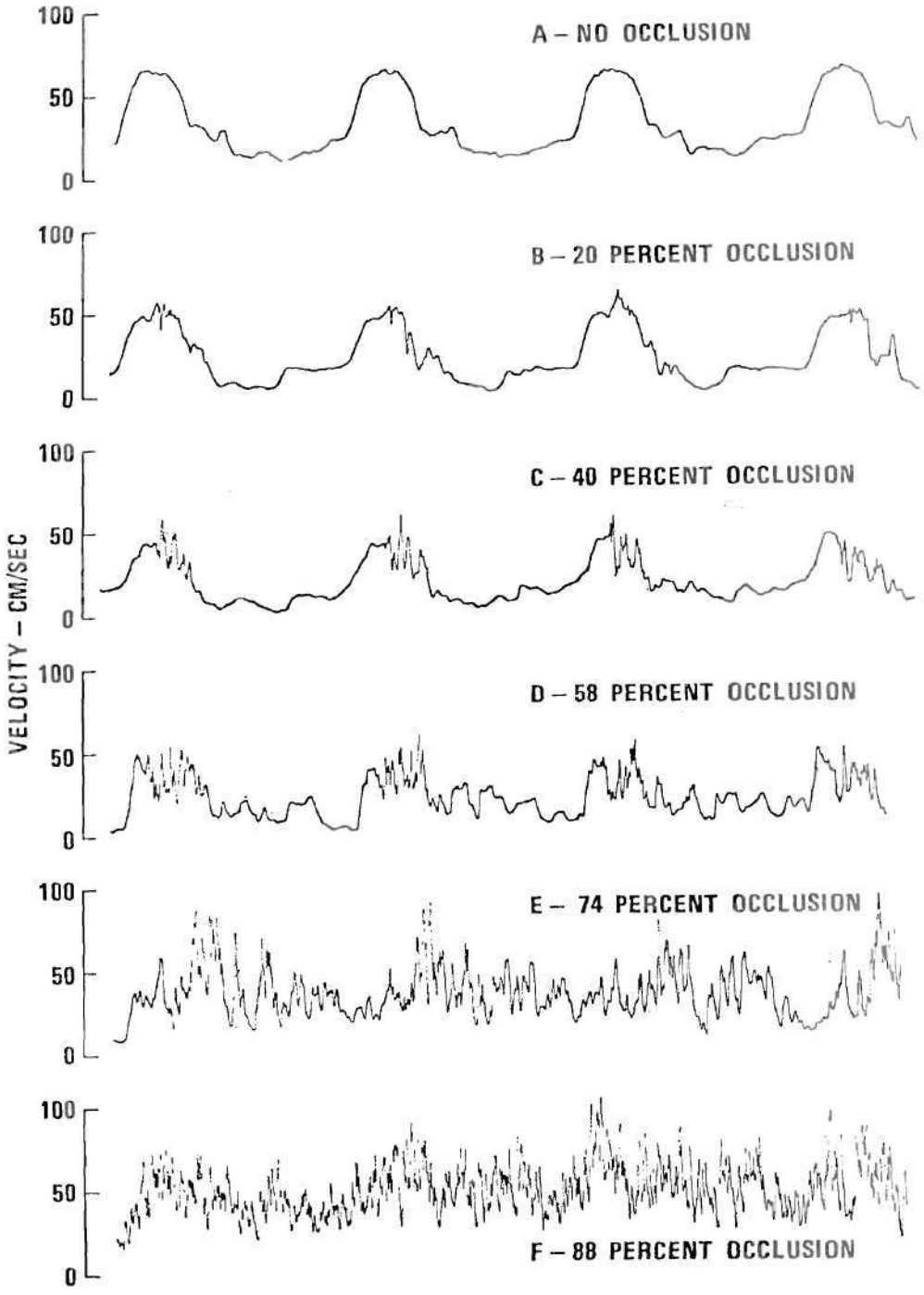

Figure 28. Velocity Waveforms in a Canine Aorta for Different Degrees of Occlusion

with the other data quoted in the first chapter, highlight the fact that the laminar flow investigation of the second chapter does not complete the intended study.

Simplifying assumptions used in the study of turbulent flow are again those of postulating a steady flow of an incompressible fluid through a rigid tube with an axisymmetric geometry. The flow is assumed to remain fully turbulent everywhere. This brings in a restriction that the Reynolds number is sufficiently high. No allowances are made for intermittancy or relaminarization of the flow. Recirculation is expected to occur and is accounted for in the mathematical model.

3.1. Turbulence Modeling

The continuity and momentum equations are to be solved again. Turbulence stresses, however, are incorporated into the momentum equations; and this is the central problem of any analytical study of the turbulent flows. Due to the difficult nature of this closure problem, several modeling techniques have been proposed [60-62].

Of these several methods available, the "Two-equation turbulence model" was chosen. It derives its name from the fact that two equations are solved to simulate the turbulence phenomena; one equation governing the transport of turbulence kinetic energy k, and a second one governing the transport of another turbulence quantity which, along with k can be

used to determine the eddy viscosity ν_e at each point in the field. The second dependent variable chosen here is ε--the rate of dissipation of turbulence kinetic energy k.

The well-known mixing length model can be thought of as a zero-equation model because the mixing length is specified empirically without solving any equation. One-equation models are only marginally superior to the mixing length model [61]. The two-equation model avoids ad hoc adjustments of the functions and aims at making the empirical constants in the equations more general. There have been attempts to improve this model further by employing more equations. Hanjalic and Launder [63], and Hanjalic [64] used a three-equation model (one more equation for the turbulent shear stress) to treat flows in which the shear stress and the mean rate of strain vanish at different locations. The agreement between the predictions and the experimental data is very good for the fully developed channel flow cases. Some investigators [65,66,67] have attempted a detailed closure by resorting to the complete Reynolds stress equations. The increase in the number of dependent variables increases the effort required to construct the model and adjust the constants present in them and in acquiring the input information required. Even when a more sophisticated closure is attempted, an equation for ε is still employed and remains as a weak point. There is also a great deal of uncertainty in dealing with the boundary conditions. Pope and Whitelaw [66]

applied the complete Reynolds stress and the k-ε models to study wakes. In the particular cases they studied the complete Reynolds stress model was not a significant improvement over the k-ε model except in predicting the individual normal stresses. In the present study, the individual normal stresses are not predicted. The k-ε model chosen has been used widely by several researchers for engineering computations [68-71]. Despite its potential shortcomings, this model was chosen as the medium of computation. The two equation model is general without the necessity to specify any ad hoc functions, the constants in the equations are tested by several investigators, and it is relatively simple to apply as compared to models using more equations. It is probably the optimum choice for the present recirculating flow predictions until more definitive models evolve in the future.

At high Reynolds numbers ε varies as $k^{3/2}/\ell$, where ℓ is the length scale of turbulence. This leads to an expression for the familiar quantity--turbulent kinematic viscosity

$$\nu_e = \sqrt{k}\,\ell = k^2/\varepsilon. \tag{17}$$

This scalar function of space relates the shear stress τ and the rate of strain. However, ν_e is not employed here to predict the individual normal stresses.

Governing equations for k and ε are taken from the literature along with the constants involved. The coordinate system and the nondimensional variables of the second chapter are retained throughout, i.e. a_o and $2\bar{u}$ are used to nondimensionalize length and velocity where a_o is the radius of the tube in the unoccluded portion and $\bar{u}$ is the average velocity in this region. For the entrance flow problem, Z = 0 corresponds to the entrance lip of the tube. Also, k, ε and ν_e denote the nondimensional variables hereafter, in this chapter. While presenting the results, however, dimensional values are employed. The four governing relations can be cast into the standard form of equation (14), repeated here

$$a\left[\frac{\partial}{\partial \eta}\left(\phi \frac{\partial \psi}{\partial R}\right) - \frac{\partial}{\partial R}\left(\phi \frac{\partial \psi}{\partial R}\right)\right] - \frac{\partial}{\partial \eta}\left[b_1 R \frac{\partial}{\partial R}(c\phi)\right] -$$

$$\frac{\partial}{\partial R}\left[b_2 R \frac{\partial}{\partial R}(c\phi)\right] + Rd = 0. \qquad (18)$$

In this equation ϕ can be ω/R, ψ, k or ε. The terms in each equation and the numerical values of the five constants C_D, C_1, C_2, σ_k and σ_ε are listed in Table 2. The numerical values of these constants quoted in the literature are arrived at by the efforts of numerous investigators who have applied this model to experimentally known flows.

Table 2. Governing Equations Given by the k-ε Turbulence Model

$$a\left[\frac{\partial}{\partial \eta}\left(\phi \frac{\partial \psi}{\partial R}\right) - \frac{\partial}{\partial R}\left(\phi \frac{\partial \psi}{\partial \eta}\right)\right] - \frac{\partial}{\partial \eta}\left[b_1 R \frac{\partial}{\partial \eta}(c\phi)\right] - \frac{\partial}{\partial R}\left[b_2 \frac{\partial}{\partial R}(c\phi)\right] + Rd = 0$$

	ϕ	a	b_1	b_2	c	d
1	ω/R	R^2	R^2N	$\frac{R^2}{N}$	ν_e	$-R^2 \frac{S_\omega}{N}$
2	ψ	0	$\frac{N}{R^2}$	$\frac{1}{NR^2}$	1	$-\frac{\omega}{NR}$
3	k	1	$N \frac{\nu_e}{\sigma_k}$	$\frac{\nu_e}{N\sigma_k}$	1	$-G + \frac{C_D \varepsilon}{N}$
4	ε	1	$N \frac{\nu_e}{\sigma_\varepsilon}$	$\frac{\nu_e}{N\sigma_\varepsilon}$	1	$-C_1 \frac{\varepsilon}{k} G + \frac{C_2 \varepsilon^2}{kN}$

Where,

Constants

$C_1 = 1.45$ $\quad \sigma_k = 1.0$

$C_2 = 0.18$ $\quad \sigma_\varepsilon = 1.3$

$C_D = 0.09$

Table 2 (Cont.)

$$N = \frac{\partial \eta}{\partial Z} = K\,(1-\eta^2)$$

$$G = \frac{\nu_e}{N}\left[2\left(\frac{\partial V_R}{\partial R}\right)^2 + 2N^2\left(\frac{\partial V_Z}{\partial \eta}\right)^2 + 2\left(\frac{V_R}{R}\right)^2 + \left(\frac{\partial V_Z}{\partial R} + N\frac{\partial V_R}{\partial \eta}\right)^2\right]$$

$$S_\omega = \frac{2}{R}\left[\frac{\partial^2 \nu_e}{\partial Z^2}\frac{\partial V_Z}{\partial R} - \frac{\partial^2 \nu_e}{\partial Z \partial R}\left(\frac{\partial V_Z}{\partial Z} - \frac{\partial V_R}{\partial R}\right) - \frac{\partial^2 \nu_e}{\partial R^2}\frac{\partial V_R}{\partial Z}\right]$$

$$\nu_e = k^2/\varepsilon$$

κ = von Karman constant = 0.4

3.2. Boundary Conditions

Appropriate conditions are to be specified all around the boundary for each of the variables ω/R, ψ, k and ε.

On the axis, because of symmetry

$$\omega = \psi = \frac{\partial k}{\partial R} = \frac{\partial \varepsilon}{\partial R} = 0 \quad \text{at} \quad R = 0. \tag{19}$$

Application of the boundary condition for ω/R on the axis is described in the second chapter.

Downstream boundary conditions are applied at $\eta = 1$ ($Z = \infty$) for both stenotic and entrance flow problems. The flow is assumed to be fully developed at this boundary. Fully developed values for all the four variables are computed earlier and stored. Application of these boundary conditions in the gradient form, i.e. specifying that gradients in the Z direction go to zero, did not alter the results significantly.

Imposing the upstream boundary conditions involves an uncertainty which might affect the comparison of theory with the experimental data. Seldom are these boundary conditions measured experimentally in the great detail required for the application of the theoretical models. This always is the case with ε. However, it should not be a serious problem away from the upstream boundary. Computations proved that the results in the region away from the upstream boundary are not sensitive to small changes in the inlet conditions.

In the stenotic flow case the upstream boundary conditions are applied two radii upstream of the stenosis, i.e. at $Z = -(Z_o+2)$. Flow is assumed to have passed through a long tube and thus is taken to be fully developed at this section. These values are available from a fully developed computations as mentioned above.

For the entrance flow problem, the experimental data of references [72-74] are kept in mind in selecting the upstream boundary conditions which are applied at $Z = 0$. The value of k at this boundary is guessed to be a constant and the turbulent viscosity is estimated to be 75 percent of the fully developed value. Equation (17) determines the value of ε once k and ν_e are known.

The wall boundary conditions are the most difficult to specify. This is due to two reasons. Though both k and ε go to zero on the wall, this information cannot be utilized effectively as the turbulence models are not applicable in the viscous layer next to the wall. Further, the large gradients of the flow properties in this region require very close spacing of the numerical grid points even if one attempts to extend the turbulence models into the viscous layer. The usual practice to circumvent this difficulty is to apply the boundary conditions in some approximate form at a point outside the viscous layer where viscous stresses can be neglected in comparison to turbulent stresses. This practice is satisfactory in the boundary layer flows where

the law of the wall can be employed to establish certain boundary conditions. The lack of such information in a general flow has led the earlier workers [52,67] to resort to the same procedure employed in a boundary layer flow even when the flow departs from the boundary layer class.

The value of the stream function on the wall is 0.25. The boundary conditions for the other three variables are applied at the first grid point away from the wall. The logarithmic form of the law of the wall [56] is assumed to be valid and is used to evaluate the wall shear stress τ_w from the known velocity. Then

$$\omega = \partial V_Z/\partial Y = \sqrt{\tau_w}/(\kappa Y) \tag{20}$$

where κ is the Karman constant and Y is the nondimensional distance measured from the wall ($Y = R_o - R$). The boundary condition for k is obtained from the transport equation for k by neglecting the convection and diffusion terms and equating generation and dissipation of kinetic energy. This leads to

$$k = \sqrt{\tau_w}/C_D \tag{21}$$

on the wall. The law of the wall is used again to obtain the boundary condition

$$\varepsilon = \tau_w^{3/2}/(C_D \kappa Y). \tag{22}$$

In the recirculation region τ_w is negative and equations (20, 21 and 22) cannot be applied. Launder [67] manipulated these equations in the hope of applying them even when τ_w is negative. In the nondimensional form, equations applied near the wall are finally

$$\begin{aligned}
Y_+ &= Y \; Re \; C_D^{1/4} \sqrt{k} \\
U_+ &= \ln (EY_+)/\kappa \\
\tau_w &= C_D^{1/4} \sqrt{k} \; V_Z/U_+ \\
u_* &= \sqrt{|\tau_w|} \\
\omega &= u_* \; \text{sign} \; (\tau_w)/(\kappa Y) \\
\varepsilon &= \tau_w \; \omega/C_D \\
k &= (\varepsilon \kappa Y \; C_D^{1/4})^{2/3} \\
E &= 9.793
\end{aligned} \tag{23}$$

These equations have not been compared with any experimental data in recirculating flows and should be considered as only tentative. They give, however, the same results as equations (20, 21 and 22) when τ_w is positive. This makes it very convenient in applying them all along the wall when a recirculation region is suspected to be present adjacent only to a part of this length.

A different kind of problem arises when equations (20, 21 and 22) are used for the entrance flow problem. It is tacitly assumed in the use of these equations that the shear stress on the wall τ_w is the same as the shear stress τ at the first grid point where k and ε are evaluated. This assumption fails if there is a large shear stress gradient normal to the wall, or if the point under consideration is far away from the wall; in other words, if the $y_* = y\, u_*/\nu$ value is large for the point. Due to a thin boundary layer near the lip of the tube, this situation arises. But equations (20, 21 and 22) are too attractive to be discarded, and an integration technique for the momentum equation is devised to evaluate the local shear stress to be used in these equations in place of τ_w. All the terms except the shear stress term are evaluated in the momentum equation at the first and second grid points away from the wall. Variation of these terms between the wall and the first grid point is then obtained by a curve fitting. With this information the momentum equation is integrated from the wall to the first

grid point to evaluate the local shear stress at this point from the known wall stress. The method was found to be satisfactory for the entrance flow problem, by comparing calculated results with experimental data.

The law of the wall is incorporated in the wall boundary conditions. It is desirable that the equation for ε recover this trend near the wall. This requires a compatibility relation among the five empirical constants in the governing relations. The equation for ε is simplified near the wall by neglecting the convection term and then by substituting the wall function expressions (20, 21 and 22) in the remaining terms to arrive at the algebraic relation

$$\frac{\kappa^2}{\sigma_\varepsilon}\sqrt{C_D} + C_1 C_D - C_2 = 0 \qquad (24)$$

This compatibility condition requires the value of σ_ε to be 0.97 near the wall if the other four constants are to be unaltered. On the other hand, σ_ε should be taken as 1.3 (Table 2) to secure good agreement between theory and experimental results for the free turbulence mixing. Hence, σ_ε is allowed to vary from 1.3 at the tube axis to 0.97 near the wall. This is not a very large change and a sinusoidal variation with zero slopes at both the ends is employed.

3.3. Numerical Solution

The four governing relations for ω/R, ψ, k and ε written in the form of equation (18) were solved numerically subject to appropriate boundary conditions. The numerical approach employed was the same as that explained in the second chapter as the form of the governing equations has not been changed. However, it turned out to be more difficult to obtain a converged solution when the number of equations was increased to four. Both a point by point and a line by line elimination method of solution of the difference equations failed to converge. In the line by line elimination method a tridiagonal matrix for each dependent variable ϕ was formed on every line of constant η. The form of these linear algebraic equations for the j node is

$$A_j \ \phi_{j-1} + B_j \ \phi_j + C_j \ \phi_{j+1} = \bar{D}_j, \qquad (25)$$

with j being counted in the radial direction. The coefficients A, B, C and D were evaluated from the most recent values of the dependent variables in the iteration procedure. Boundary conditions provide the first and the last value of ϕ for each line. Standard recursion relations are available to solve this system [75]. This procedure either failed to converge or the rate of convergence was very slow and the changes between successive iterations did not reduce beyond a certain limit; the results obtained were not reliable. A

modified approach was attempted by rewriting equations for k and ε in the form

$$A_j k_{j-1} + B_j k_j + C_j k_{j+1} = D_j \varepsilon_j + E_j = \bar{D}_j \tag{26}$$

$$a_j \varepsilon_{j-1} + b_j \varepsilon_j + c_j \varepsilon_{j+1} = d_j k_j + e_j = \bar{d}_j . \tag{27}$$

The presence of the cross terms ε and k on the right hand side of the equations for k and ε can be seen to be due to the form of the source terms of these equations. In equation (25) these cross terms were eliminated by evaluating them from the values of the previous iteration and lumping them in the coefficient $\bar{D}$.

A method was devised to solve this coupled tridiagonal type of system of equations simultaneously. This consists of writing recursion relations similar to those for a tridiagonal form of equations (25) and then evaluating them by proper manipulation. The recursion relations and the details of the derivation are presented in Appendix A3. This technique of solving the equations for k and ε simultaneously resulted in a fast convergence and the differences in successive iterations could be made arbitrarily small until round-off errors became a limitation. The importance of the method was that the results were reliable and were obtained with less computing time. The faster convergence rate results in a saving of computing time even though the

time required to solve the coupled system of equations simultaneously at each iteration was a little longer than that required to solve them one after the other. This method of solution also can be used to solve coupled difference forms of equations obtained from the governing relations for ω/R and ψ.

For the case of flow through stenoses, 31 grid points were uniformly spaced in the radial direction and 75 of them in the axial direction. It required 200 to 300 iterations for the solutions to converge corresponding to about two to three minutes of computer time on the CDC 6600 computer. The entrance flow problem was solved with 31 x 99 grid nodes and 131 iterations were sufficient to gain a converged solution, which needed about two minutes of computer time.

CHAPTER IV

EXPERIMENTAL STUDY

Experiments were conducted in the water flow system on Model M4 with a 75% area reduction. The detailed experiments for this model at a single Reynolds number should serve as a basis for comparison with the theoretical computations. The flow system, instrumentation, and the experimental procedure are described in this chapter.

4.1. Water Flow System

A schematic of the experimental arrangement is shown in Figure 29. It consists of the pumps, flowmeters, a settling chamber, the test section tubing including the stenosis, and a constant head return tank.

The two centrifugal pumps (Teel Model 1P677) were operating in parallel. The flow control valve and the rotameter-type flowmeters were used to set the desired flow rate or Reynolds number. These two Fischer and Porter flowmeters were calibrated and found to have nearly linear characteristics as specified by the manufacturer. Discharge from the pumps into the settling chamber was through several holes pointing in all directions. A screen in the settling chamber and a sharp edged tripping ring at the entrance lip of the test section were added to generate turbulence,

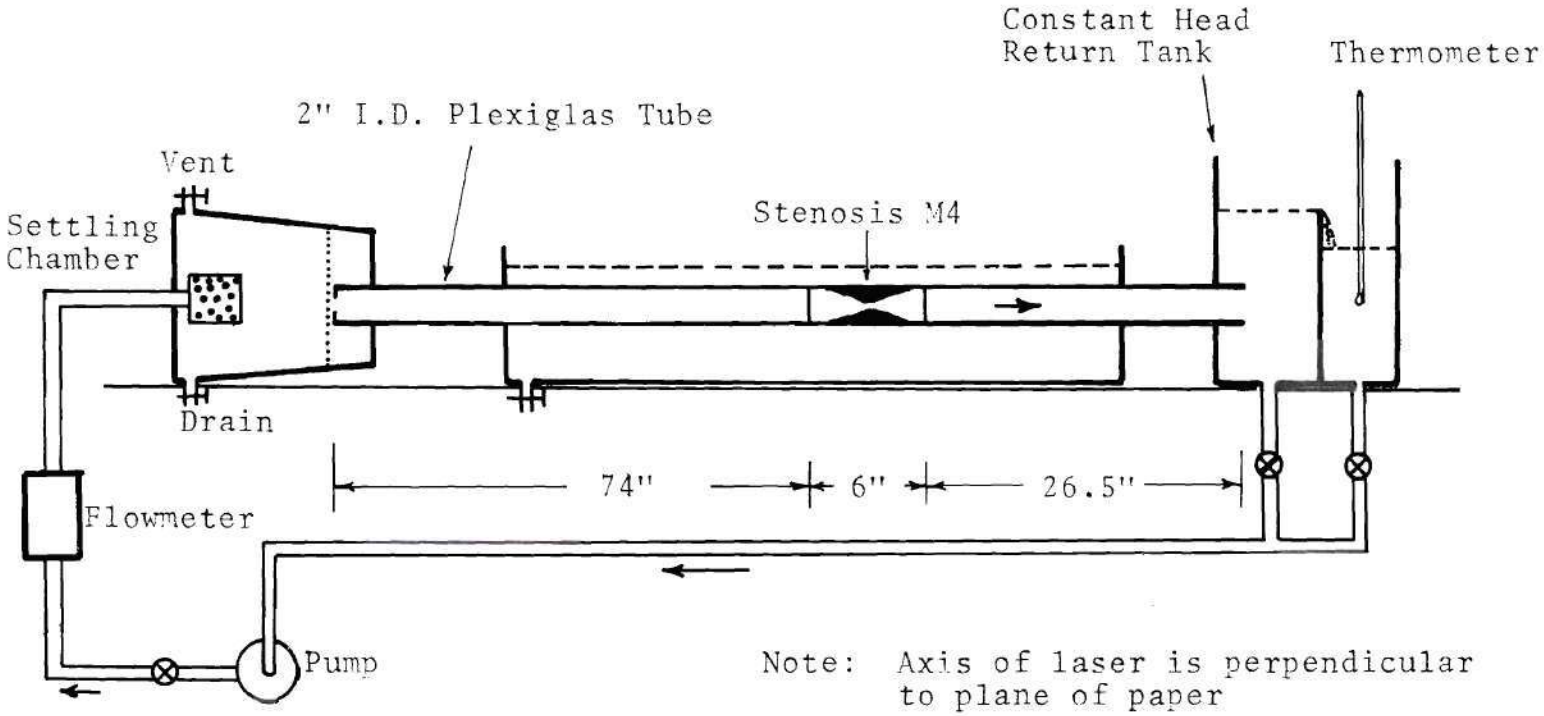

Figure 29. Schematic of the Flow System

thereby helping the flow to develop rapidly.

The test section consisted of three pieces of plexiglas tubing glued together permanently. The entrance and exit lengths consisted of 2-inch internal diameter and 2.5-inch outer diameter plexiglas tubes and were 74 inches and 26.5 inches long, respectively. The cosine geometry of the Model M4 stenosis (refer to equation 15 and Table 1) was machined from a solid plexiglas rod of 2.5-inch diameter and then polished to have good optical properties. The maximum reduction in area was 75%, with the length of the stenosis being 4 inches. This piece was 6 inches long and a length of 1-inch on either side of the stenosis geometry corresponded to the straight portion of the test section. This amounted to an entrance length of 75 inches or 37.5 diameters, sufficient to make the flow at the entrance to the stenosis fully developed, especially when the boundary layer was tripped at the inlet. A tube length of 27.5 inches distal to the stenosis was sufficiently long to measure the desired details of the flow and still ensure the measuring stations being far enough upstream of the downstream exit plane to be unaffected by any disturbances there. A water filled tank with plexiglas walls surrounded most of the length of the test section to minimize the effects of refraction at the curved wall of the tube. The improvement comes from the fact that the refractive index of plexiglas (1.49) is close to that of water (1.33). It will be seen

later that the refractive corrections applied at the stenosis geometry were also minimized by this configuration. The width of this container was kept at three inches, just enough to house the test section. The discharge in the constant head tank returned to pumps through a PVC tube. A thermometer in the return tank sensed the fluid temperature so that fluid viscosity could be determined.

4.2. Instrumentation

A description of the instrumentation and a brief account of the principle of operation are given below. A DISA type 55L, Mark II laser Doppler anemometer [76] was used for velocity measurements. The instantaneous analog velocity signal from this anemometer was filtered using a Krohn-Hite Model 3342R filter to remove frequencies above 512 Hz, thereby avoiding aliasing errors when it was processed using an HP Model 5451A Fourier Analyzer [77] to obtain turbulence levels and energy spectra. An inclined tube water manometer was satisfactory to measure the pressure distribution.

4.2.1. Laser Doppler Anemometer (LDA)

The LDA is a major breakthough in anemometry, which makes use of the Doppler principle to measure the local velocity. The advantages of the LDA are its ability to measure instantaneous velocity without any contact with the flow and independently of the fluid properties. It also has

excellent linear characteristics and the calibration can be verified quickly. It further enables measurement of individual velocity components. On the other hand, the LDA system employed in the present study is best suited for use with clear liquids and the test section walls must be transparent. Extensive correction for refraction at the test section walls is required if there is a complicated geometry. The fluid must be seeded with light-scattering particles and this can be a serious problem for velocity measurements in gases. Despite the considerable improvements made in the electronics of the commercially available LDA, its frequency response is generally inferior to that of a hot film anemometer due to the intrinsic shortcomings of the signal quality. Care is to be taken to choose proper parameters in the LDA system to secure consistent accuracy. It is added, however, without any reservation that the LDA is the best anemometer available for the present study.

When the laser beam passes through the flow, the light is scattered by particles suspended in the fluid. The scattered light carries information about the velocity in the form of Doppler shift which is interpreted by opto-electronic means. If $\hat{e}_i$ and $\hat{e}_s$ are unit vectors in the directions of incident and scattered light waves with frequencies f_i and f_s respectively and $\bar{v}$ the velocity vector of the scattering particle, then the Doppler shift f_D is given by the vector equation

$$f_D = f_s - f_i = \bar{v} \cdot (\hat{e}_s - \hat{e}_i)/\lambda, \tag{28}$$

where λ is the wavelength of the incident light. When the particle is very small it follows the local fluid velocity faithfully. Light is scattered in all directions and the intensity is sensitive to the direction, with the maximum being in the forward direction. The receiving optics, in principle, can be located in any place, though the practical considerations give rise to preferences.

In the differential Doppler mode of operation used (Figure 30), equation (28) reduces to

$$f_D = 2v \sin i/\lambda, \tag{29}$$

where v is the component of velocity in the plane of the beams and perpendicular to the bisector of the included angle 2i.

The source of illumination is a Helium-Neon gas laser (Spectra-Physics 120) with 5 milliwatts output power and wavelength λ = 632.8 nm. The laser and the transducer are attached to a mounting table and can be moved in two perpendicular directions in a horizontal plane and rotated about a vertical axis. The least counts of these motions are 0.001 inch and 0.056 degree.

The LDA transducer consists of a beam splitter, a

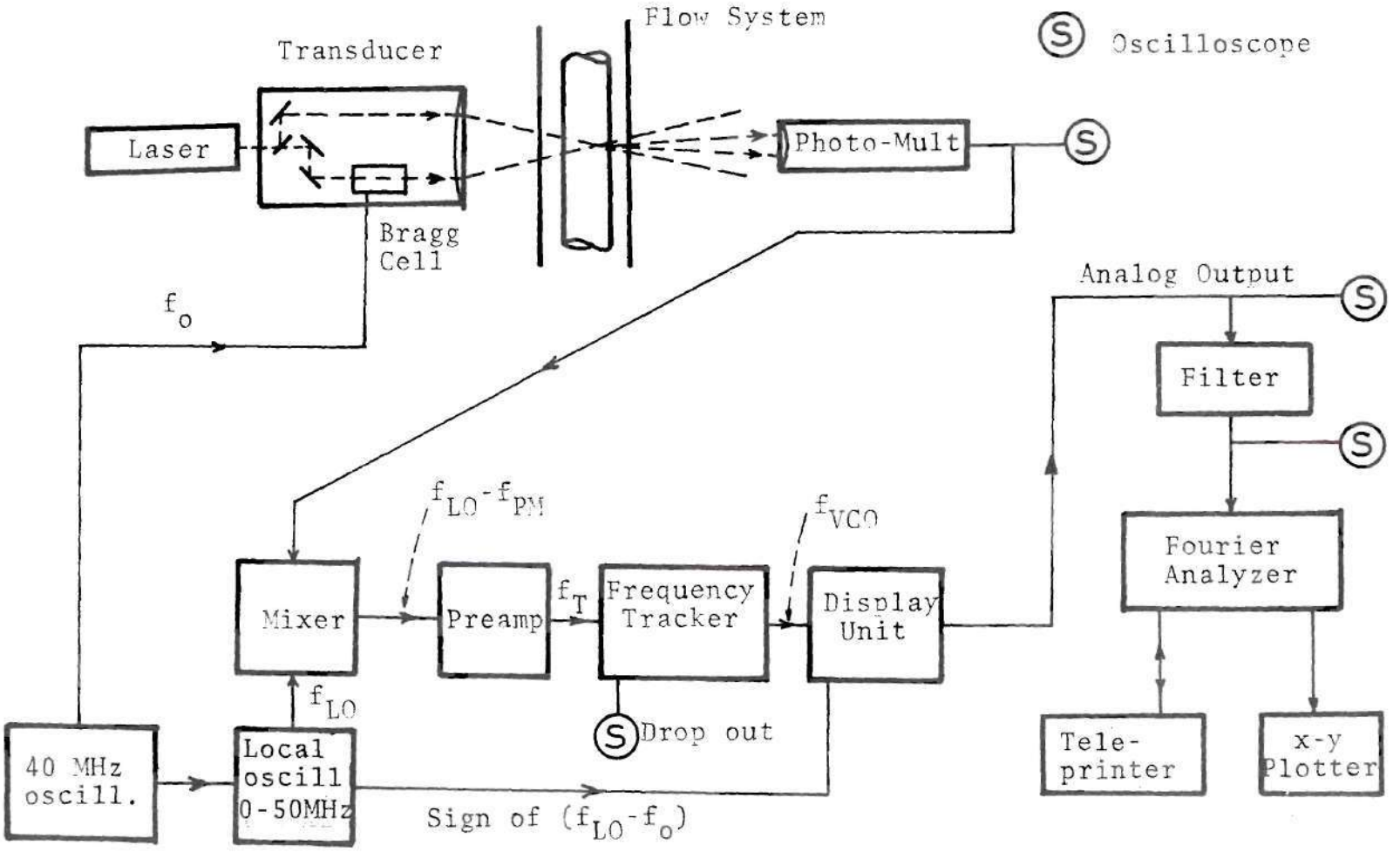

Figure 30. Block Diagram of the LDA and the Fourier Analyzer System

Bragg cell and a focusing lens. There is a provision for selecting three beam separations (8, 4 and 2 cm), and three lenses are available with focal lengths of 12, 30 and 60 cm. These two choices together fix i and the size of the measuring volume. In the present study the 12 cm lens and 4 cm beam separation were employed (8 cm beam separation is not available with the 12 cm lens) to obtain the best possible resolution. This selection yields a semiangle i_o of 9.46 degrees in air and measuring volume dimensions of 0.72 mm length and 0.12 mm width. One of the beams passes though the Bragg cell and encounters a 40 MHz frequency shift.

The photomultiplier (PM) detects the Doppler-shifted light. Its very high frequency response enables detection of the 40 MHz translated Doppler signal. An optical unit and a 0.1 mm diameter pinhole ensure that only the light from the measuring volume reaches the PM tube. In the backscatter mode, the PM along with the pinhole is mounted directly on the LDA transducer unit. The PM exciter supplies an adjustable voltage to the PM tube.

The LDA control unit consists of the Light Modulator (LM) Exciter, the PM Exciter and the range translator. The LM Exciter delivers a 40 MHz signal f_o to the power amplifier of the Bragg cell. The range translator sets the electronic frequency shift, f_{LO} (see Figure 30), between 0 and 50 MHz in steps of 10 kHz. This frequency is derived from the 40 MHz oscillator in the LM Exciter by using a phase-locked

loop and two voltage controlled oscillators (VCO) to cover two ranges. The mixer part of the range translator combines PM signal ($f_o - f_D$) with f_{LO} and delivers the difference $f_T = (f_{LO} - f_o + f_D)$ to the preamplifier of the signal processor. This is the frequency tracked. The frequency translation facility allows an efficient selection of the velocity range. This, along with the 40 MHz frequency shift enables an accurate measurement of the velocity fluctuations around zero mean value.

The signal processor consists of the preamplifier, the tracker and the display unit. The input frequency range of the tracker is 2.25 kHz to 15 MHz and is covered in 7 ranges. The preamplified signal f_T is mixed with the signal f_{VCO} from a voltage controlled oscillator to obtain $f_{IF} = (f_{VCO} - f_T)$. A narrow band filter and a limiter are used to remove noise and amplitude modulations inherent in the Doppler signal. A fast servo loop controls the value of f_{VCO} in such a way that f_{IF} is automatically centered at the middle frequency of a relatively narrow band pass filter in the tracker. Doppler frequency f_D is obtained from f_{VCO} after subtracting $(f_{LO} - f_o + f_{IF})$. The display unit delivers an analog voltage proportional to the instantaneous value of f_D or the velocity. It also displays digitally the mean velocity obtained after integrating for an adjustable time of 0.5 to 150 seconds and then multiplying by the calibration factor.

4.2.2. Fourier Analyzer System

The HP Model 5451 Fourier analyzer system performs analysis of time and frequency data containing frequencies from dc to 25 kHz [77]. The lowpass filtered velocity signal, containing frequencies up to 512 Hz, and of one second duration requires, according to Shannon's sampling theorem, 1024 data points. The sampling time of one second allows a frequency resolution of one Hertz. The discrete finite Fourier transform (where only positive frequencies are used) and self complex conjugate multiplication were used to obtain the energy spectrum. The rms value of turbulence was calculated by integrating the energy spectrum. The number of data samples taken for ensemble averaging to obtain a statistically reliable sample was either 50 or 100 depending upon the nature of the signal. It took nearly three minutes to process 50 data samples, each of one second duration. A teleprinter and an X-Y plotter were the output modes employed.

A digital voltmeter (Fluke Model 8000 A) was used to calibrate the analog output. The attenuator knob was adjusted to avoid overloading of the Krohn-Hite filter and the Fourier analyzer. The normal procedure of signal processing was inadequate to handle the data near the throat of the stenosis, which is characterized by low turbulence intensity and high mean velocity. In such cases a second Krohn-Hite filter was used in series to remove the dc part of the

signal by filtering the frequencies below 0.1 Hz. The validity of this method was checked by processing the signals elsewhere by the two methods. The mean velocity obtained by the digital data processing compared well with that given by the LDA signal processor.

4.3. Preliminary Studies

The reliability of the procedure was checked by several experiments. Experience was gained with LDA by changing frequency range, bandwidth, seeding level, PM location and focussing. A slight seeding using silicon carbide particles of 1.5 μm average diameter (specified by the manufacturer) was adequate. Most of the data taken was with a 1.5 mHz frequency range and 2% bandwidth and only in a few difficult cases with large fluctuations were they increased to 5 mHz frequency range and 4% bandwidth.

The fully developed pipe flow case was studied, and the mass flow rate obtained by integrating the velocity profile agreed to within two percent of that given by the flowmeter. Also, the spectra obtained by the LDA were compared with those obtained by a hot film probe. Figure 31 gives an example. This comparison is to be carefully interpreted as the quantities measured by the LDA and the hot film probe are not exactly the same. This is because the hot film probe, although calibrated to measure the axial component u', will still sense the effects of the v' and w'

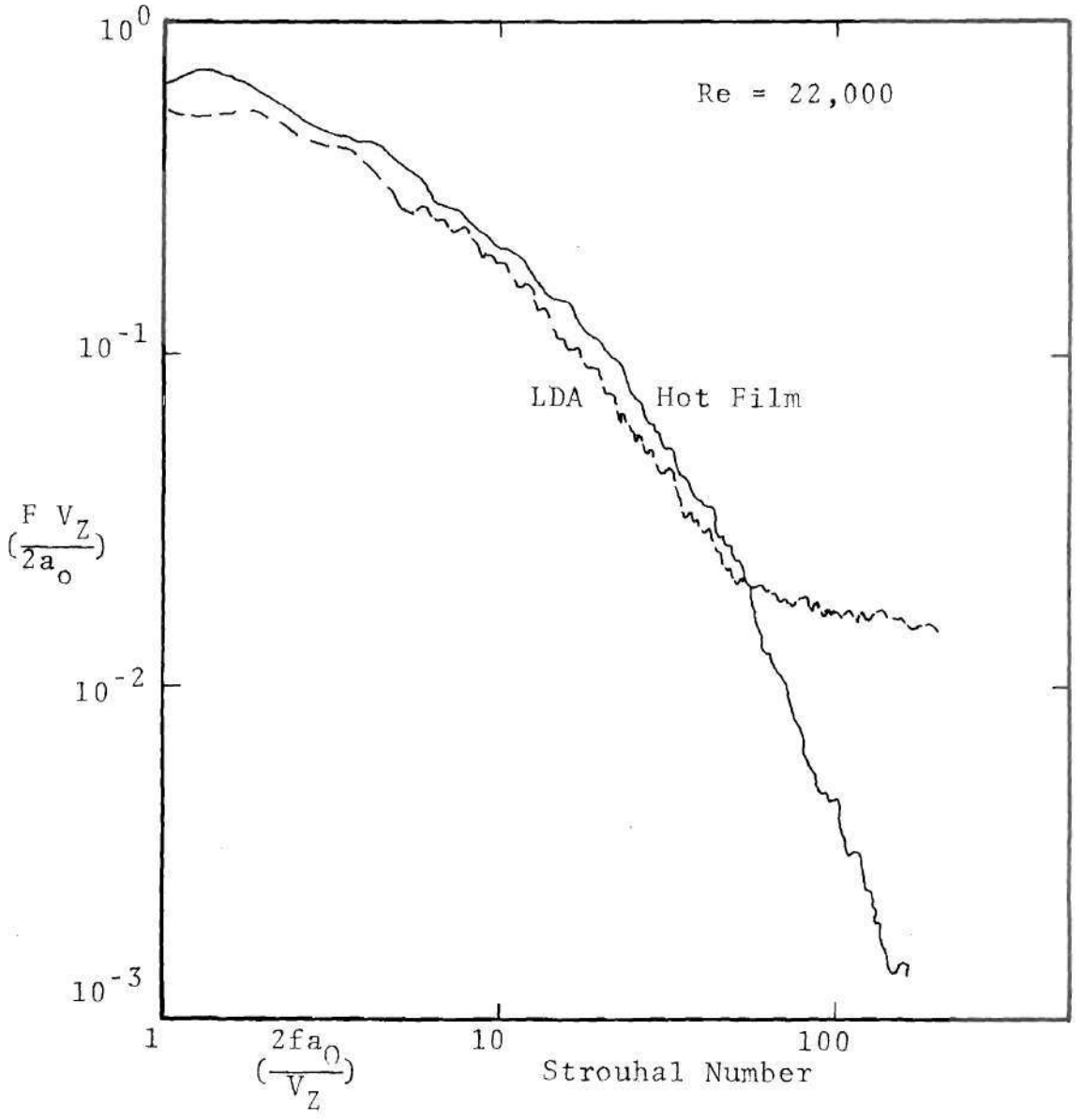

Figure 31. Comparison of the Spectra Obtained by the LDA and the Hot Film Probe

components. These spectra were obtained on the centerline for a fully developed pipe flow for a Reynolds number of 22,000. The agreement is seen to be satisfactory. The noise and the Doppler ambiguity [78] contribute to the spectrum for the Strouhal number fD/V_Z beyond 50 where f is the frequency in radians/second and D is the diameter of the tube. From several such spectra this frequency is seen to be about 200 Hz. Calculations showed that contribution of the spectrum beyond, say, 100 Hertz to the turbulence intensity is very small. The noise should be less important a factor with increasing turbulence intensity because of increased signal to noise ratio [80] and this was encountered in the present measurements.

The value of turbulence intensity on the centerline for the fully developed pipe flow with Reynolds number 15,000 was compared with that obtained by numerous investigators quoted in reference [79]. The value of u' obtained ($u'/\bar{u} = 0.0464$) was found to be slightly higher than the mean value of the turbulence intensity ($u'/\bar{u}$ about 0.040) but was within the experimental scatter. An indirect but detailed comparison of the entire u' and w' profiles with those obtained by Laufer [85] is presented in the next chapter and is seen to be good.

4.4. Experimental Procedure

Detailed flow measurements were made for a Reynolds

number of 15,000. They included profiles of mean velocity, turbulence velocity components u' and w', and their energy spectra at several stations between Z = -4 and 11. Mean velocity profiles were recorded at some of these locations for Reynolds numbers 5,000 and 10,000. Reattachment point location and pressure distribution were measured for several Reynolds numbers up to a maximum of about 16,000.

Figure 32 displays several optical configurations. Refraction at the wall of the plexiglas tank, when the rays pass from air to water (Figure 32a), changes the semiangle i_o and the wavelength λ. These changes exactly compensate each other and the relation between Doppler frequency f_D and velocity v in equation (29) remains unchanged. The position of the measuring volume changes, but this can be accounted for easily. Figures (32b, c and d) are the possible arrangements for the measurement of the velocity components V_Z, V_ϕ and V_R. Due to the difficulties involved in applying optical corrections, as is clear from Figure 32d, and the difficulties in moving the laser in the vertical direction, measurements of V_R (and v') were not attempted. The LDA transducer was rotated by 90° about its axis to orient the two beams in a vertical plane (Figure 32b) to measure V_ϕ and w'. In all the measurements the forward scattering mode was adopted to improve the signal to noise ratio.

Refraction corrections were applied at the stenosis geometry in the case of V_Z-measurements and all locations in

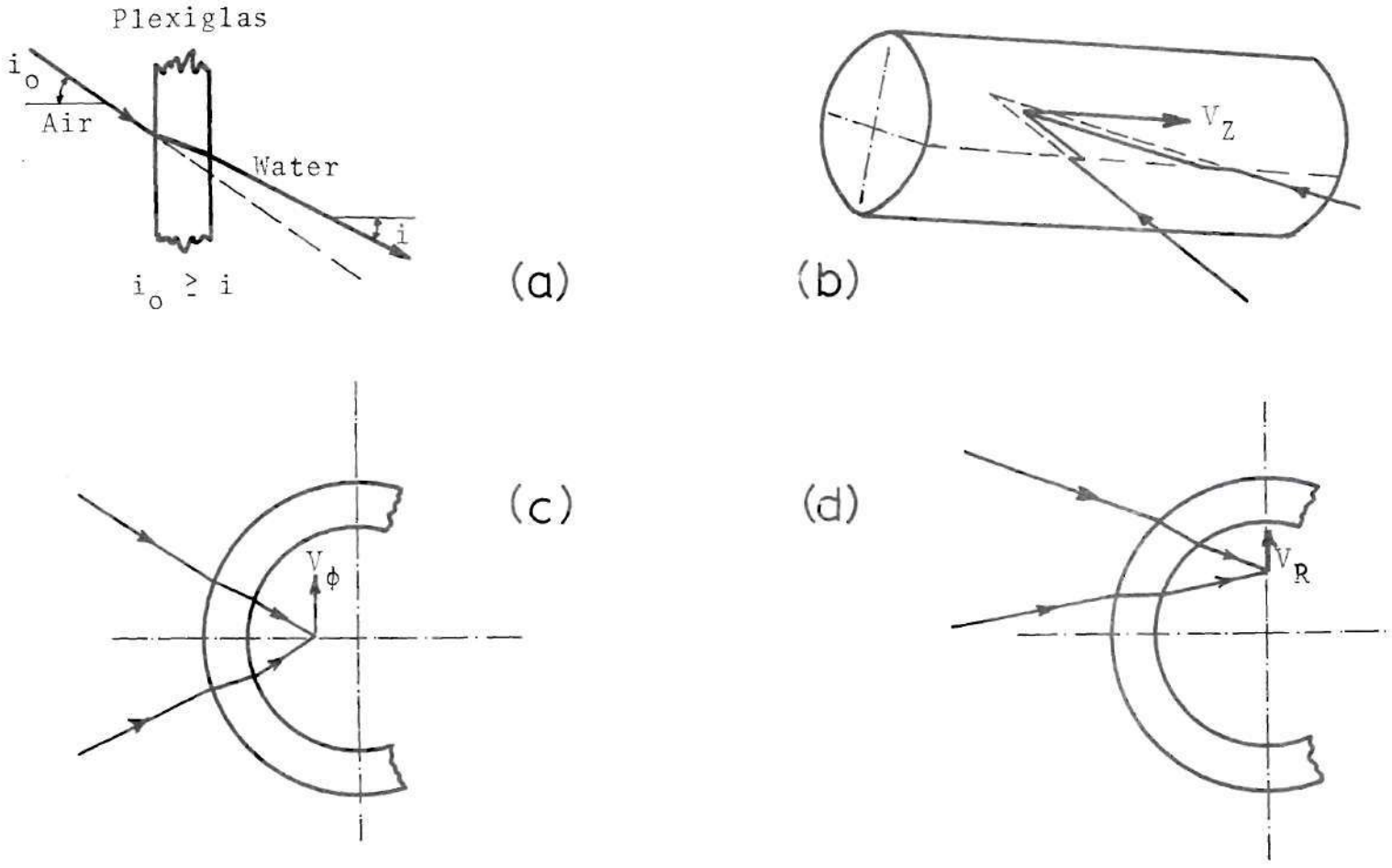

Figure 32. Optical Arrangements

case of V_ϕ-measurements. Due to the refraction at the tube wall, corrections must be made to account for the following.

(i) Change in the beam intersection angle 2i.

(ii) Displacement of the measuring volume in the radial direction in case of V_ϕ-measurements, and in both axial and radial directions in case of V_Z-measurements.

(iii) Change in the direction of the bisector of the beam intersection angle 2i, in case of V_Z-measurements.

Correction for the last item is small and was not applied due to the difficulty involved. Corrections for the first two changes were simplified for the ease of application; the details are discussed in Appendix A4.

Flow rate was kept constant while measuring the velocity profiles at a given station. The maximum change in temperature during such a measurement was ±0.5°C, which corresponded to a variation in the Reynolds number in the range 15,000 ± 350. This variation was due to the change in the kinematic viscosity of water. When measurements were undertaken at a new cross-section, the flow rate was adjusted to account for the change in the temperature.

The mass flow rate was checked by integrating the velocity profile. There was a disagreement of 8.7% just distal to the stenosis, which reduced to more acceptable values as one moved downstream. At Z = -1, which is inside

the stenosis geometry, there was a large discrepancy of 14.5%. These errors can be compensated to certain extent when presenting the velocity data in the nondimensional form by using $\bar{u}$, the average velocity in the unoccluded portion of the tube, corresponding to the flow rate obtained by integrating the velocity profiles. The centerline velocity distributions for all the three Reynolds numbers 5000, 10,000 and 15,000 were obtained by adjusting the flow rates after the measuring volume was fixed on the axis. This allowed an accurate determination of the influence of the Reynolds number without moving the measurement point. The average velocity $\bar{u}$ as obtained from the flowmeter reading was used in nondimensionalizing in this case. Integration time to secure mean velocity varied from 30 to 300 seconds. In the case of the turbulence intensity measurements, as mentioned earlier, the net sampling time was either 50 or 100 seconds. The distal velocity fluctuations close to the stenosis were large and needed a longer sampling time; there were short periods of complete reversal of velocity even on the axis. In this situation a simple hot film probe is clearly inadequate.

Long integration times were required to determine the "reattachment point." In a turbulent flow it is difficult to assign importance to this single point where the mean velocity changes direction. The mean shear stress does not necessarily vanish at this point. It is proper to think

of a region of reattachment. In the following discussion the reattachment point is referred to as the position where mean velocity changes sign. This was located by measuring the velocity close to the wall at several points 0.1 inch apart in the axial direction. By plotting the velocity at each point the position where the mean velocity changes sign could be found. Integration time for each velocity measurement varied from 45 to 500 seconds, with longer duration being necessary close to the reattachment point. This was required due to high values of fluctuating velocity and integral time scale, and to mean velocity which was nearly zero. The reattachment point was determined for several Reynolds numbers. The net integration time combined for all cases was nearly 8 hours. These experiments should highlight the difficulties involved in determining the reattachment point in a turbulent flow using dye injection techniques.

The static pressure holes were drilled after completing the velocity measurements. They were 14 in number, (1/32) inch in diameter, countersunk to (1/16) inch diameter size, and were drilled perpendicularly to the inside surface of the test section. Short stainless steel tubes of (1/16) inch outer diameter were glued in these holes and Tygon plastic tubes connected them to an inclined tube manometer. Sufficient time was allowed for the water columns to reach equilibrium. Pressure distribution was measured for several Reynolds numbers up to about 16,000, the maximum attainable in the flow system.

CHAPTER V

TURBULENT FLOW RESULTS

The theoretical predictions for the case of turbulent entrance flow, the flow through stenosis models, and also the experimental data obtained for the latter case are presented in this chapter.

5.1. Turbulent Entrance Flow

The turbulent entrance flow problem, as mentioned earlier, served the purpose of a test case for the computational procedure. The Reynolds number selected for the study was 388,000 which enables a comparison of the predictions with the experimental data of Barbin [72] and Barbin and Jones [73], where detailed flow measurements are available. The laminar entrance flow problem was first solved for a Reynolds number of 400 with the assumption of zero vorticity at the entrance plane. The results obtained were in good agreement with the numerical computations obtained by McDonald et al. [81].

Richman and Azad studied [74] the turbulent entrance flow problem experimentally and analytically. The analysis used an effective viscosity model. The comparison between the velocity profiles measured and predicted was good. An effective viscosity variation based on the Van Driest

correction [82] was employed. The velocity profiles predicted were insensitive to the value of the effective viscosity assumed near the centerline. This model, however, did not permit them to calculate turbulence intensity. In the present study these values are computed and compared with the experimental data.

5.1.1. Flow Velocities

The axial velocity profiles are plotted in Figure 33 for several locations. The inlet conditions assumed for computation were a constant $V_Z = 0.5$ and zero vorticity (instead of $V_R = 0$). It is believed that this closely represents the well rounded contraction (see, e.g. reference [83] for discussion) used by Barbin [72].

The development of the boundary layer can be seen from the axial velocity profiles. The retardation of the flow in the boundary layer accelerates the core, which is gradually decreasing in diameter. For locations close to the inlet, the peak velocity does not occur on the axis. However, this peak is only slightly greater than the centerline velocity and cannot be distinguished in the graphical representation of Figure 33. As may be expected, the flow reaches its final fully developed state at a faster rate near the wall than it does near the axis. The predicted axial velocity is slightly lower than the experimental values near the wall whereas it is in close agreement near the axis.

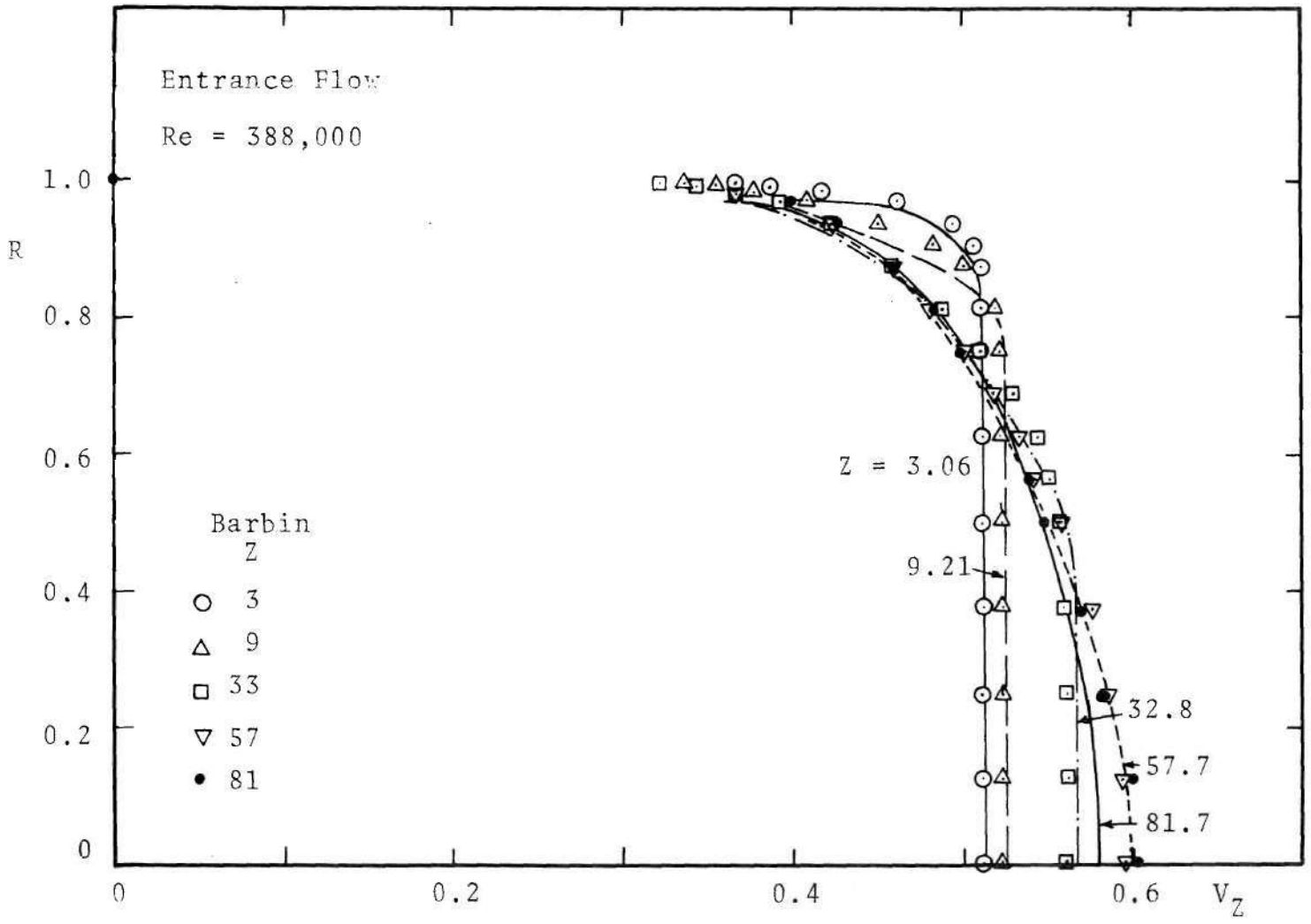

Figure 33. Axial Velocity Profiles for Turbulence Entrance Flow

An interesting picture arises as one moves far downstream. The computations show a relative maximum in the velocity at the centerline as can be seen from Figure 34. There seems to be a major discrepancy for Z > 69 where the experimental data show a peak which is not very distinct. It is ascertained, however, that the peak in the experimental data is not due to reading the graphical results. The tabular results [72] indicate a peak at Z = 69 and then the centerline velocity decreases at the subsequent stations. The Reynolds stress profiles [72,73] substantiate this behavior. The predicted peak is very prominent and occurs slightly ahead of the peak found experimentally. One should, however, be careful in interpreting the results in this area as the pipe used by Barbin was only 87 radii long and the last data point plotted corresponds to the exit plane itself. The fully developed state was not attained in this length. Experimental data by Milliat and also by Dean reported in [84] for two dimensional entrance flow show a pronounced peak in centerline velocity. Richman and Azad [74], on the other hand, report that they did not notice such an overshoot in the centerline velocity for the three experimental Reynolds numbers of 1×10^5, 2×10^5 and 3×10^5. That their analytical method also did not predict this is due to their particular choice of the effective viscosity which varied little in the axial direction. This was verified in the present study for the Reynolds number of

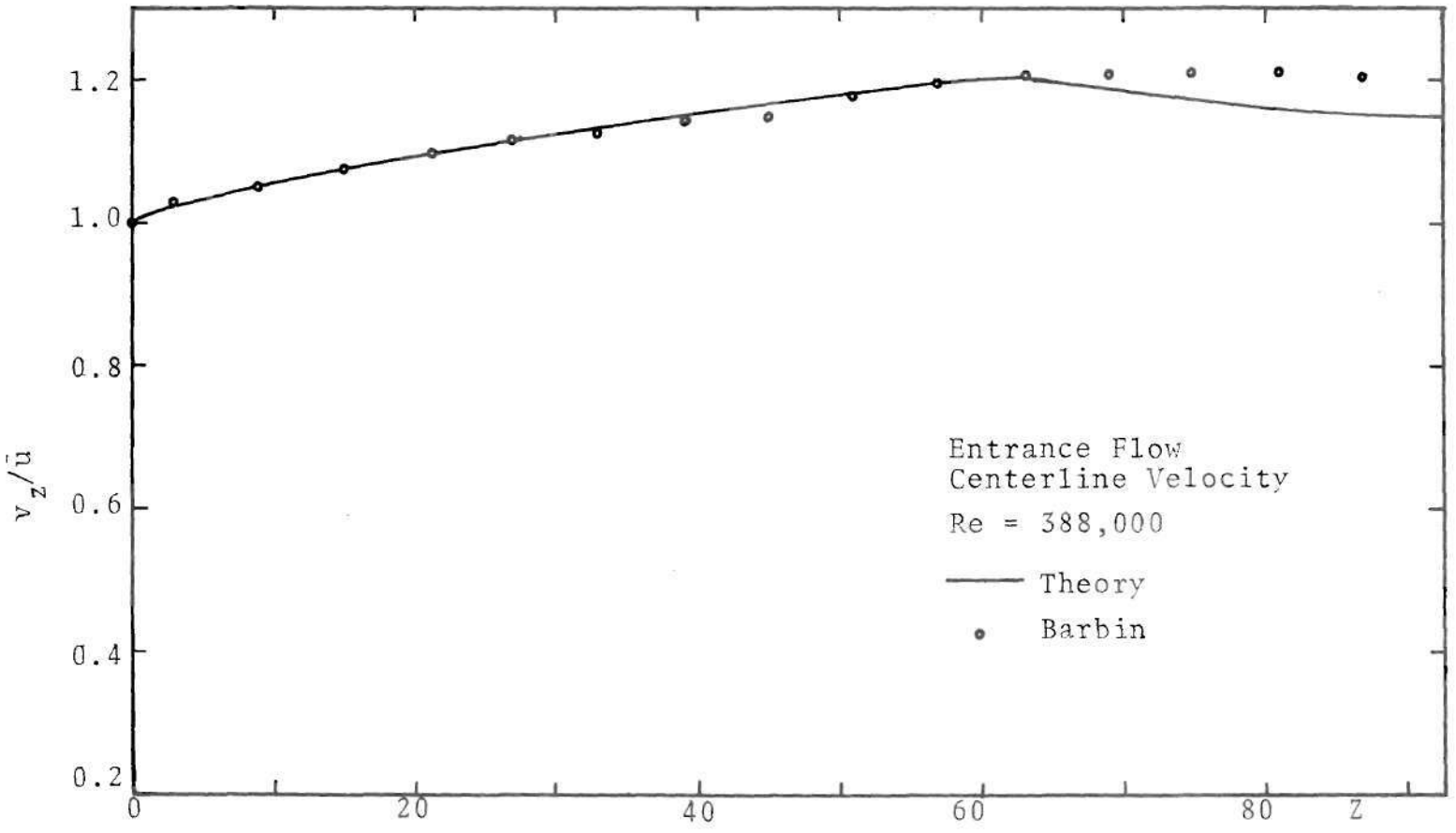

Figure 34. Axial Variation of Centerline Velocity for Turbulence Entrance Flow

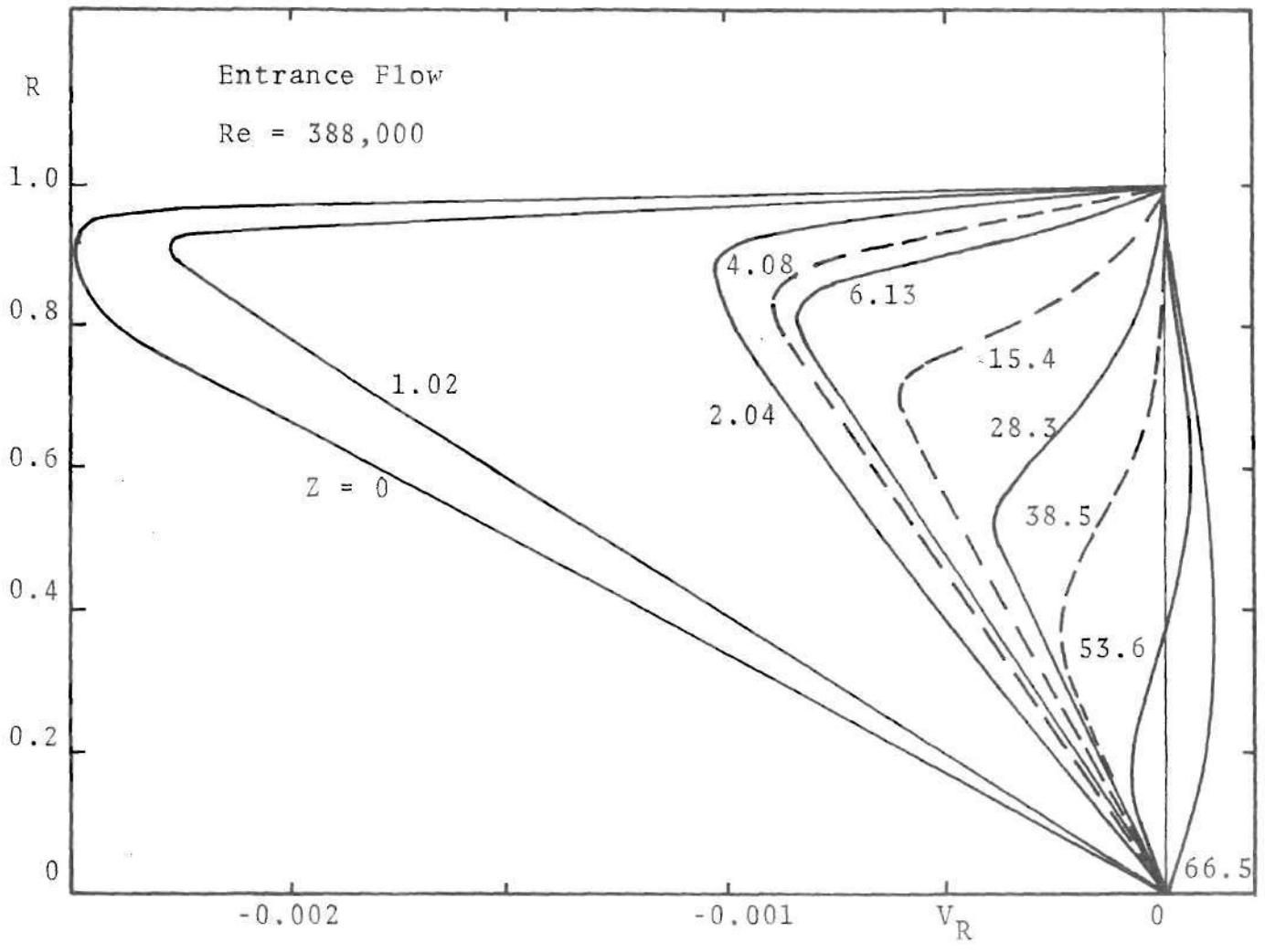

Figure 35. Radial Velocity Profiles for Turbulence Entrance Flow

3.88×10^5 by assuming the effective viscosity to be equal to the value for the fully developed flow case, i.e. it varied in the radial direction only. The centerline velocity then increased monotonically to the fully developed value. It may be mentioned here that for the laminar entrance flow problem also this variation is monotonic. The ability of the present model to predict this peak should be considered as a distinct superiority over simpler models, despite the lack of close agreement between theory and experiment beyond this peak.

The radial velocity profiles in Figure 35 also indicate a gradual thickening of the boundary layer and an overshoot in the centerline velocity represented by *positive* V_R. The occurrence of the maximum of radial velocity at Z = 0 is a direct consequence of the irrotational inlet conditions assumed there.

5.1.2. Pressure and Shear Stress Distribution

Pressure and shear stress measurements are available [72] and are compared with present computational results. The nondimensionalized pressure gradient is plotted along the axis up to 20 diameters in Figure 36. The pressure gradient in the initial entrance region of the pipe is higher than the fully developed value. This is required to accelerate the fluid in the core and to overcome the high initial wall shear stress. Pressure is plotted by taking the pressure at Z = 40 as zero, and comparison with the

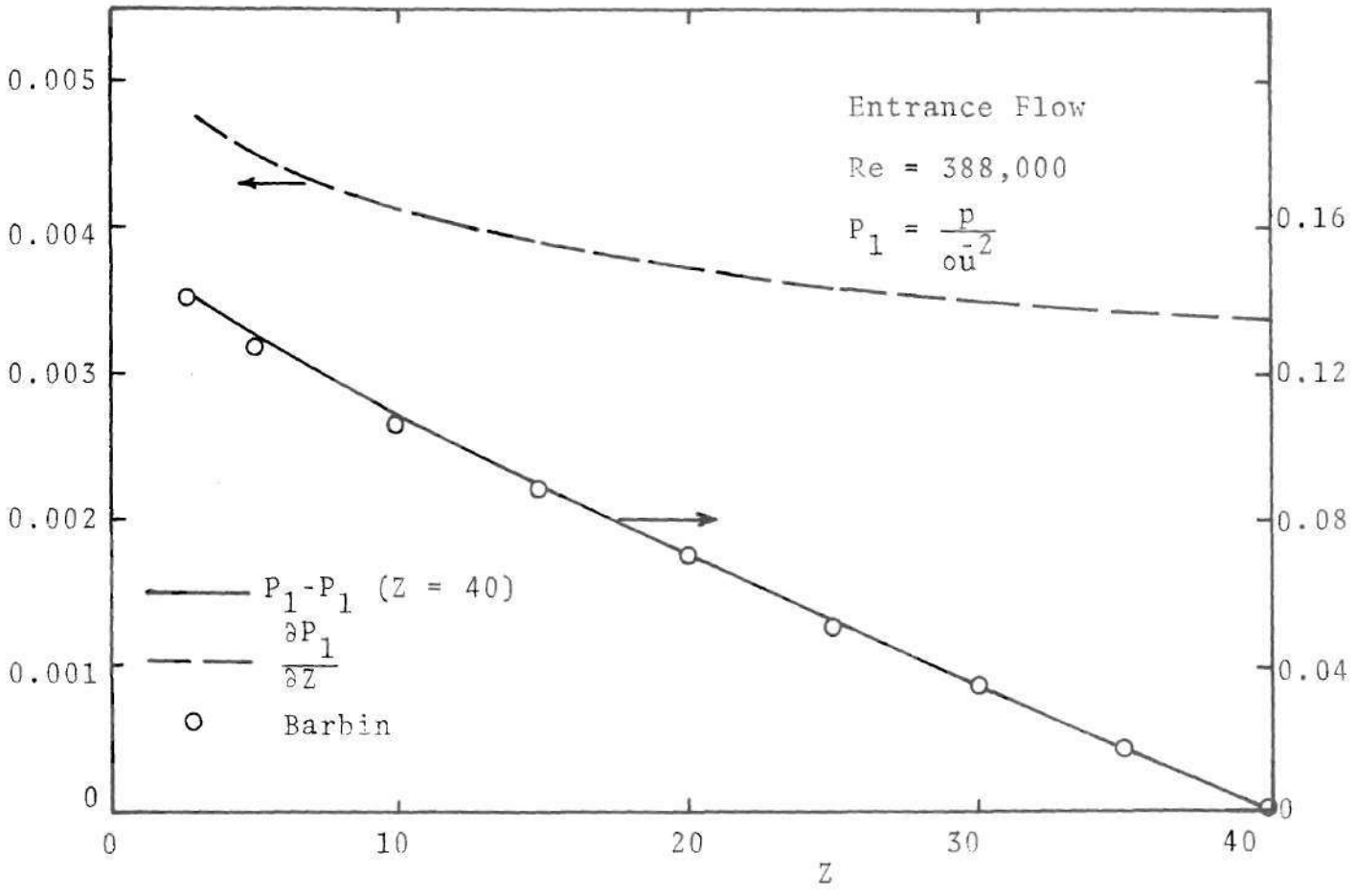

Figure 36. Axial Variation of Pressure and Pressure Gradient for Turbulence Entrance Flow

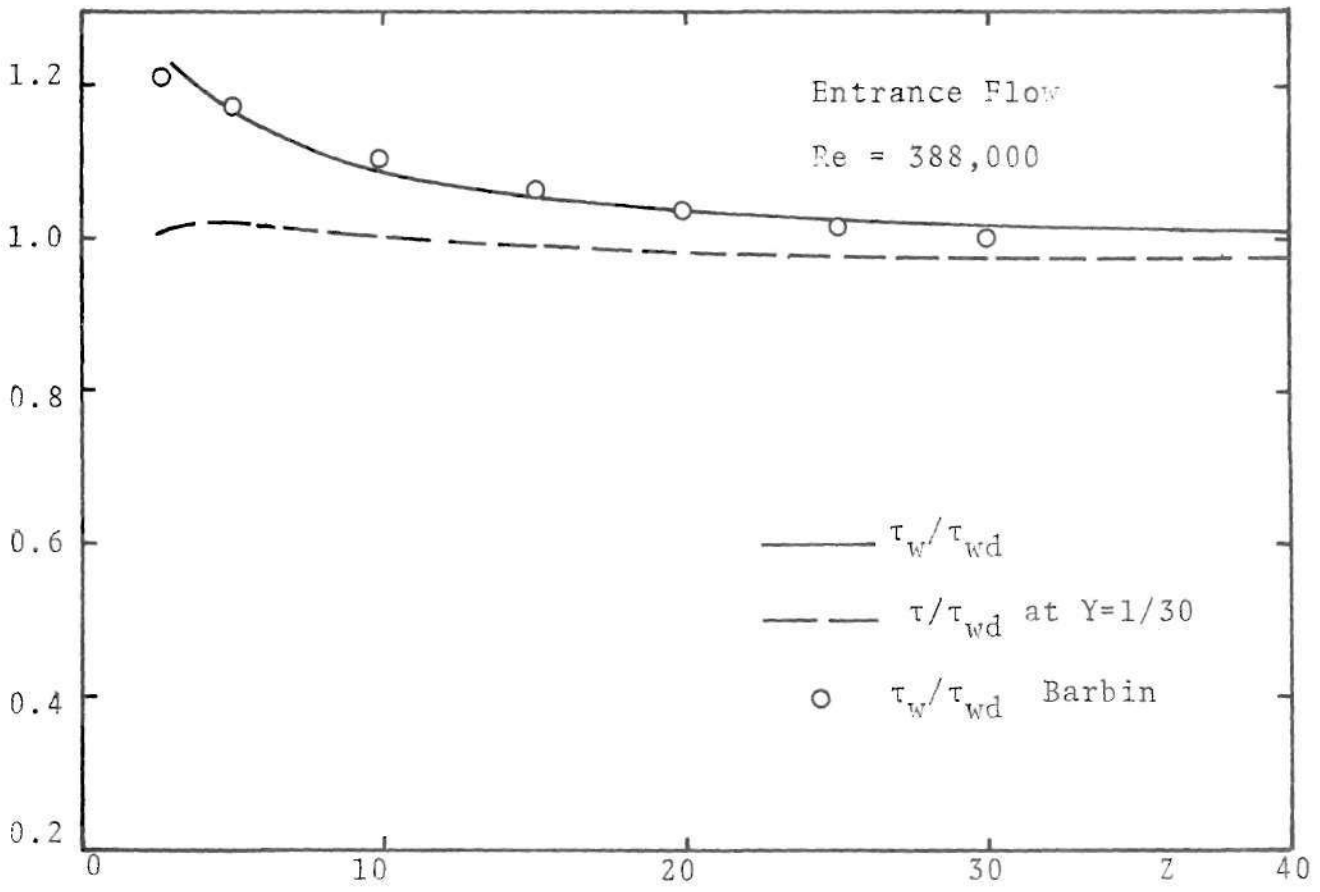

Figure 37. Axial Variation of Shear Stresses for Turbulence Entrance Flow

experimental data is seen to be good.

Wall shear stress is normalized using its fully developed value and is compared with the experimental data in Figure 37. Barbin [72] obtained these wall shear stress values by graphically integrating the velocity profiles from the axis to the wall. Agreement is seen to be very satisfactory. The experimental data indicates a slightly faster attainment of the fully developed value. The dotted line is the shear stress at the first grid point away from the wall where the boundary conditions are applied. The procedure for obtaining it from the wall shear stress was described in the third chapter. The wall shear stress reaches the highest value at the inlet plane Z = 0 whereas the shear stress at the first grid point goes to zero at the inlet. It is quite clear from these plots that reasonable values of the wall boundary conditions for ω, k and ε cannot be obtained from equations (20-22) close to the inlet. The success of the present procedure is indicated by the correct behavior of τ, k etc. as we move away from inlet and good comparison of the results with the experimental data.

5.1.3. Turbulence Fluctuations

Although turbulence kinetic energy is an important characteristic feature of any turbulent flow, it is difficult to obtain analytically. It also requires additional efforts to measure it experimentally since all three velocity components are required. Barbin [72] measured u' and w' components

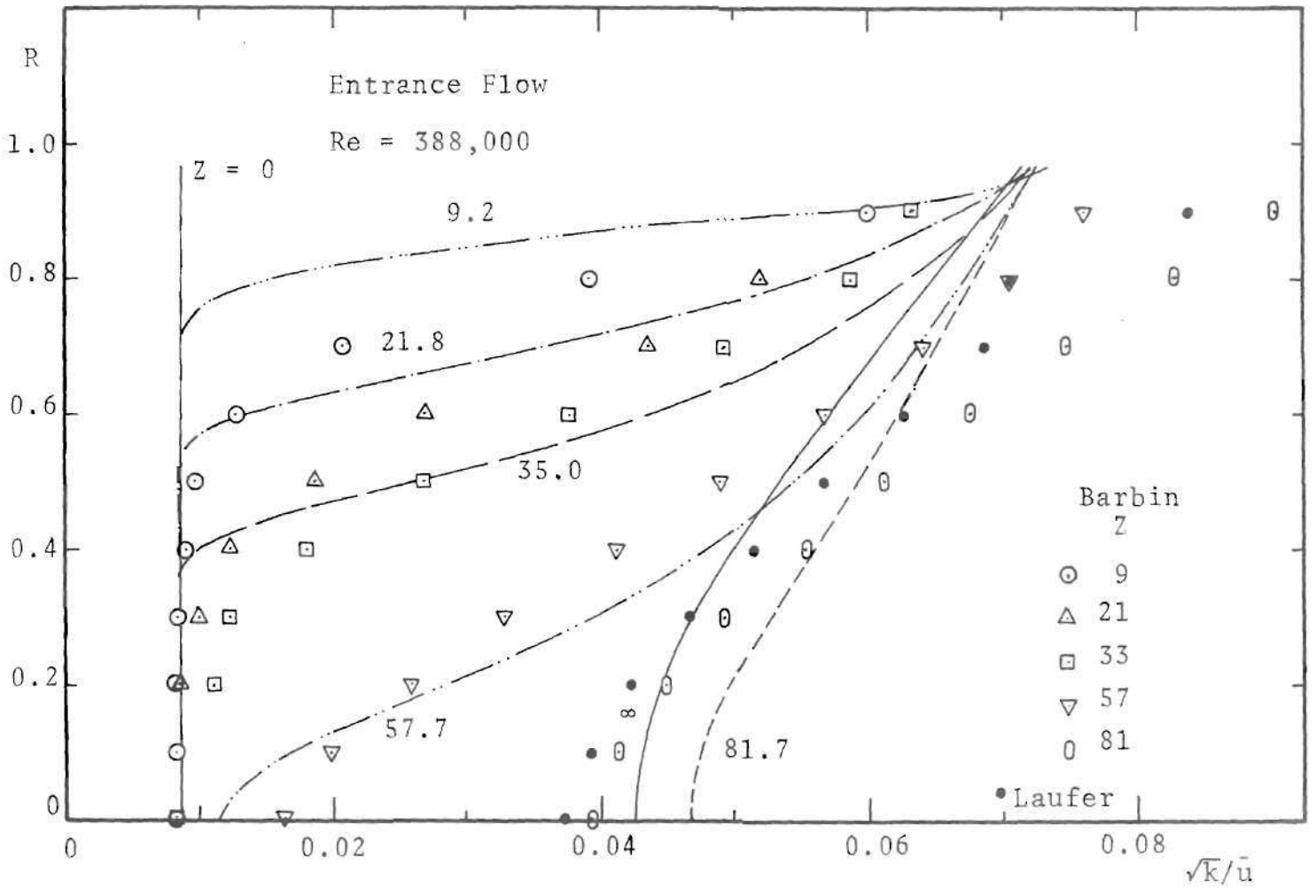

Figure 38. Turbulence Kinetic Energy Profiles for Turbulence Entrance Flow

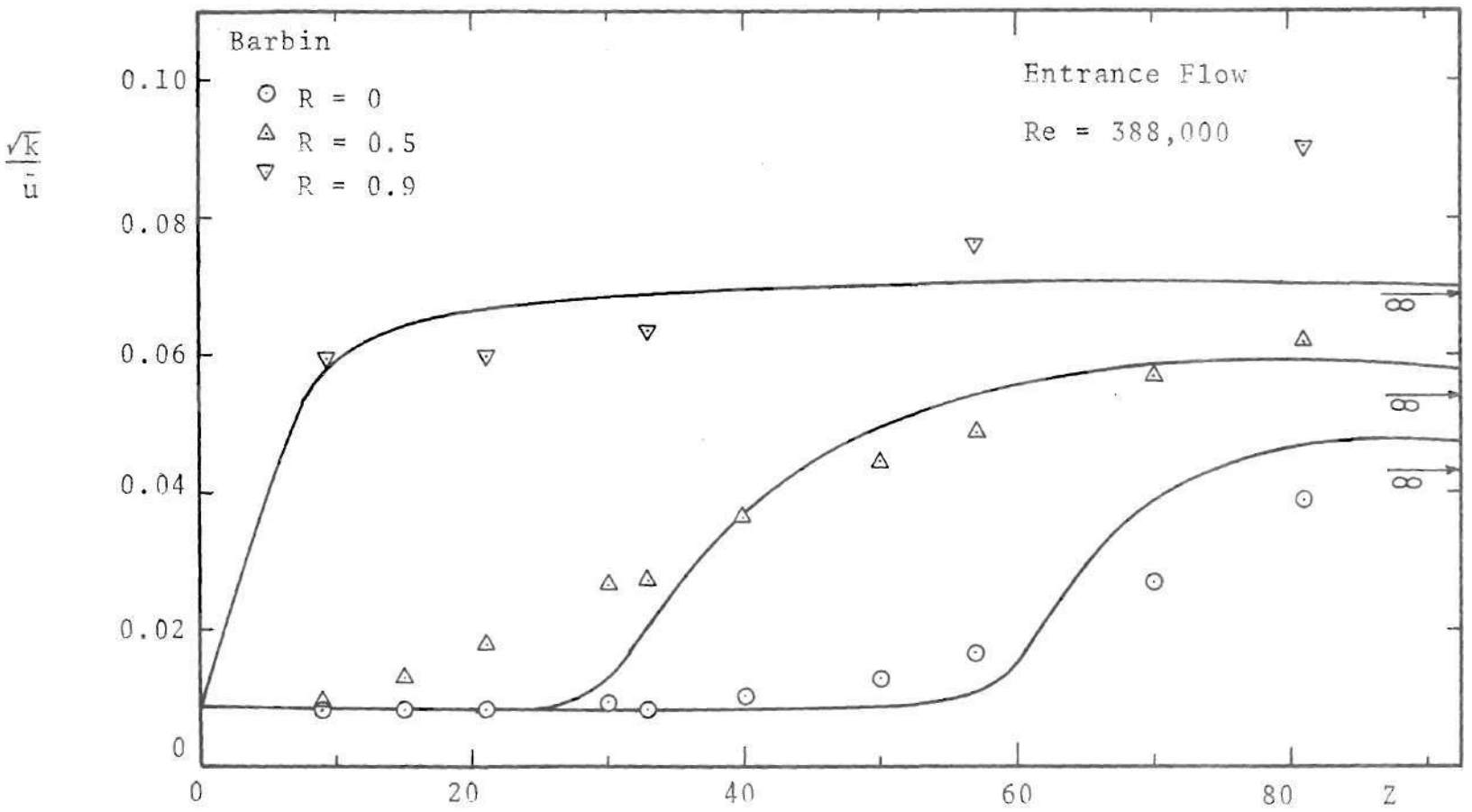

Figure 39. Axial Variation of Turbulence Kinetic Energy for Turbulence Entrance Flow

of the turbulence velocity. The values of k are approximated from these data by assuming v' and w' to be equal. In the case of fully developed pipe flow [85] this gives exact results on the axis and overpredicts $\sqrt{k}$ by about 6.5% at R = 0.9 and Re ≃ 420,000.

Profiles of k are plotted in Figure 38 for various locations and then are crossplotted in Figure 39 for three radial positions R = 0, 0.5 and 0.9 as functions of Z. The initial profile of constant k quickly changes near the wall toward its final values. The turbulence kinetic energy k diffuses toward the axis as the velocity boundary layer thickens. As seen from Figure 39, for large values of Z the wall boundary condition for k is an underestimate in comparison with the experimental data. In the entrance region, the turbulence kinetic energy produced near the wall is converted downstream and diffused radially, apart from being dissipated locally. As the flow gradually develops, the production of k increases in the core region and so does ε and turbulence shear stress. However, these develop much more slowly as compared to the velocity profiles. In Figure 39 the predictions of the locations of maximum rate of rise of k for a given R are in good agreement with the data. However, the model predicts a delayed and more abrupt increase in k as can be seen from both the figures. Turbulent quantities like k and ε become higher than their fully developed values somewhere between Z = 60 and 90, and then

gradually relax to their fully developed values.

The disagreement between the computed and experimentally obtained values of k forewarns of the difficulties that are likely to arise in the case of the more complex stenotic flow. The gross behavior of the flow is predicted correctly. Hoffman [87] modified the k-ε equation model with the diffusion constants changed to $\sigma_k = 2.0$ and $\sigma_\varepsilon = 3.0$, and computed the fully developed channel flow. This modification improved the value of k close to the axis. However, the disagreement between theory and experiments was still noticeable close to the wall even for this simple flow. A large disagreement between theory and experiments will be seen in the next section for the values of k in the stenotic flow.

5.1.4. Discussion of Entrance Flow Results

Turbulence entrance flow is an interesting problem in fluid mechanics. The flow starts from a uniform condition and reaches an equilibrium state and different parts of the flow reach this state of higher turbulence level at different rates. This change is also not monotonic. The flow has boundary layer features but is elliptic in nature in the entrance region. There is also an experimentally observed region of intermittency which gradually moves from wall toward the axis. Turbulence levels in the core increase slightly before this front reaches a particular point. Intermittency on the centerline begins at Z = 50.

The overshoot phenomenon is interesting and seems to be real, as evidenced by the experimental results of several investigators. The experimental data of Richman and Azad [74], however, do not show this. Measurements by Barbin [72] indicate that flow does not reach a fully developed state in his pipe of 43.5 diameter length. The shear stress distribution measured at the end of the tube using a hotwire probe is found to be still different from the fully developed linear profile. The wall shear stress from the same reference [72] plotted in Figure 37 was obtained by integrating the velocity distribution from axis to the wall.

Turbulence entrance flow differs from the laminar entrance flow problem in the overshoot phenomenon. In the core, the increase in the turbulence level is delayed as compared to the changes in the mean velocity because of the distance required for the lip-generated disturbances to meet at the axis. Further adjustments are made in the mean velocity after the changes are brought about in the turbulence quantities. Absence of such characteristics results in a monotonic change in flow properties on the axis in case of laminar entrance flow problem. The fact that it takes a large fraction of the total distance for the development just for the turbulence to fill the entire cross section is of importance. By artificially creating turbulence in the entire cross section at the entrance plane itself, one can considerably decrease the length required for flow development.

This idea was applied in the design of the flow system described in the fourth chapter, in the form of a screen and a sharp edged ring to trip the boundary layer at the tube inlet.

The k-ε model was adequate to describe the gross features of the flow. But it failed to predict with precision the finer details such as the distribution of k. That these difficulties exist even for the simpler case of fully developed two-dimensional channel can be seen from reference [87]. We can anticipate, therefore, such difficulties in the case of stenotic flow.

5.2. Turbulent Flow Through Modeled Stenoses

As discussed previously, the objective of this portion of the study was to determine whether or not the k-ε model equations could be employed to accurately predict the flow environment in the neighborhood of subtotal vascular stenosis models at Reynolds numbers sufficiently high to yield a turbulent flow throughout. This entails a direct comparison of computational and experimental results. The turbulence modeling inherent in the k-ε equations was based on intuition and measurements for high Reynolds numbers, whereas arterial flows typically occur at low to moderate Reynolds numbers. To effect a compromise, it was decided to make comparisons of theory and experiment at a Reynolds number of 15,000. This is at, or perhaps beyond, the extreme

upper limit found in the human circulatory system but is hopefully large enough to expect high Reynolds number assumptions inherent in the equations to be reasonably accurate.

In a theoretical study, flow field determination for several different degrees of stenosis over a wide range of Reynolds number is straight forward and is only a matter of investing in additional computer time. Such is not the situation with the laboratory measurements. These require a great expenditure in time and effort for each separate case. Hence, detailed experiments were conducted solely for Model M4 and only at a Reynolds number of 15,000. Data obtained include mean and turbulence velocity profiles and turbulence energy spectra. Additional mean velocity profiles were measured at Reynolds numbers of 5,000 and 10,000, and the pressure distribution and reattachment point locations were obtained for several Reynolds numbers between 1,500 and 16,000.

Theoretical solutions were computed for the four models M1, M2, M3 and M4 (see Table 1). Although the Reynolds number of primary interest was 15,000, computations were also performed at 10,000, 30,000, and 388,000. This allows some insight into flow field variation with changing stenosis geometry and Reynolds number.

5.2.1. Separation and Reattachment Points

The reattachment point, as discussed in the fourth

chapter, was obtained by measuring the velocity at several points close to the wall. This was repeated for several Reynolds numbers and results are plotted in Figure 40. The separation and reattachment points found in the theoretical analysis for Reynolds numbers 10,000 and 15,000 are also indicated. The theory predicts too short a length for the recirculation region. This point will be discussed at a later stage. The experimental data by Roschke and Back [51] for the length of the recirculation in an abrupt expansion in a pipe are also plotted for comparison. Although the geometries used are not exactly the same in the two cases, the results are in reasonable agreement for the Reynolds number range of overlap.

The data of Roschke and Back [51] covers laminar, transitional and turbulent flow regimes. For small Reynolds numbers, flow is laminar and the length of the recirculation region varies approximately linearly in Re. This trend was found to be true for the four stenosis models studied when the flow remained completely laminar. When the Reynolds number is increased, the experiments of Roschke and Back [51] indicate a maximum length of the recirculation region of 24 step heights which corresponds to Z = 12 in this plot. For Reynolds numbers still higher than this, the length of the recirculation region decreases and reaches a minimum around Re = 2,000 as shown in Figure 40.

The present experimental data reveal that the length

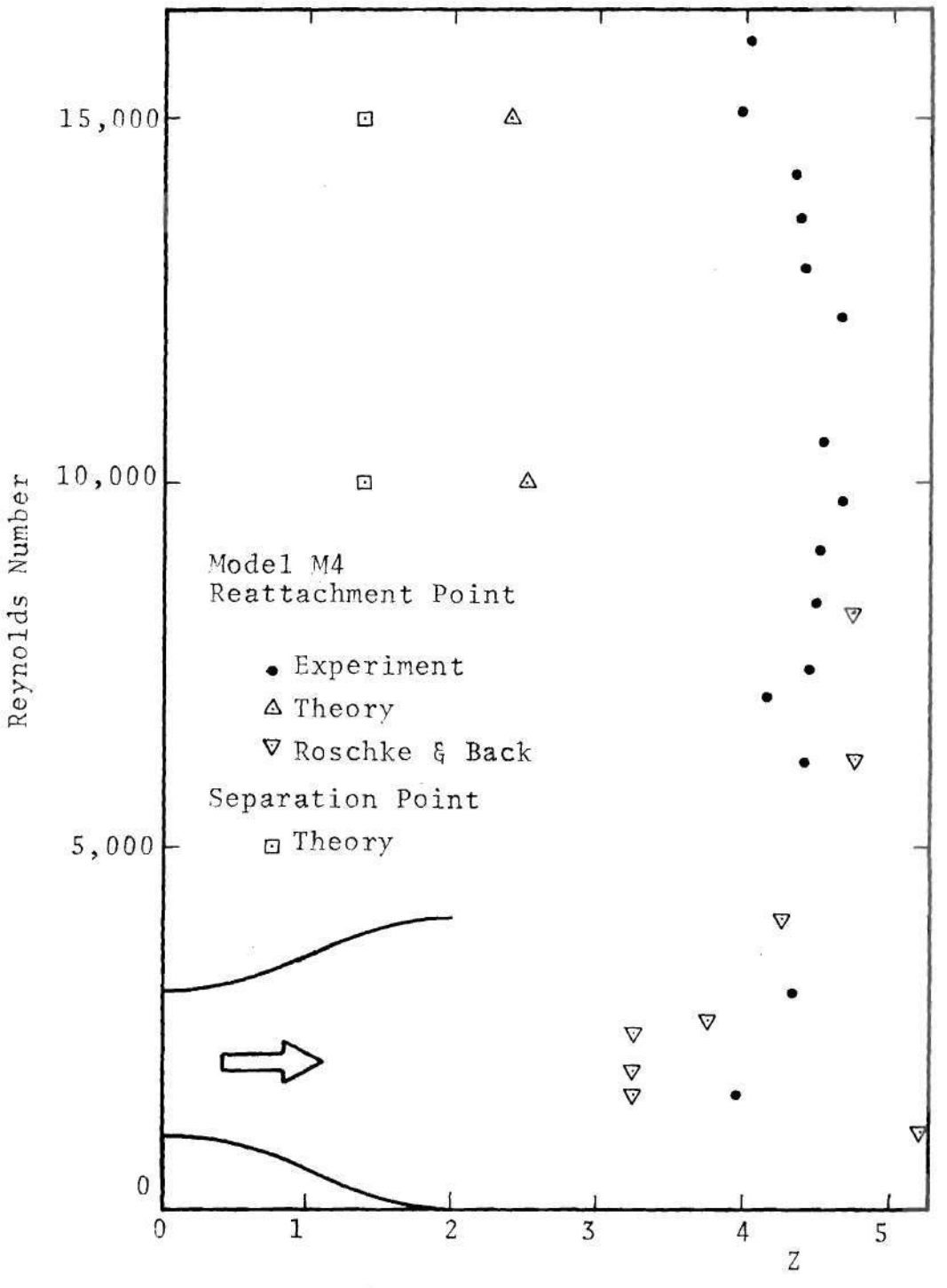

Figure 40. Separation and Reattachment Points

of the recirculation region is not very sensitive over the Reynolds number variation examined, although there is a slight, but noticeable, decrease in length for Reynolds numbers less than 6,000 and greater than 13,000. Analytical results also agree with this trend. In fact, the computations show that no recirculation exists at the Reynolds number 388,000 for Model M4. At all the Reynolds numbers employed for computations, recirculation is found to be absent for Model M1 and it was present for Models M2 and M3.

The inability of the analytical method to predict the correct length of the recirculation region has far-reaching consequences. A shorter and thinner recirculation is predicted with the flow closely following the diverging geometry, whereas the experiments exhibit a jet-like flow with a large recirculation region. The analytical results thereby indicate reduced values of rate of strain in the shear layer distal to the separation point, leading to reduced production of turbulence kinetic energy. These points will be considered again along with the discussion of other results.

5.2.2. Flow Velocities

Several velocity profiles are documented next. Velocity profiles for four locations for a Reynolds number of 5,000, Model M4, are presented in Figure 41, and at several locations for the Reynolds number 10,000 in Figures 42 and 43. Similar plots for a Reynolds number of 15,000 are compared with the theoretical predictions in Figures 44

and 45.

The experimental data indicate the presence of a recirculation region for all cases studied with separation beginning just distal to the throat of the stenosis. The profiles at the throat, for all three Reynolds numbers, show a maximum velocity occurring away from the centerline. These off-axis peaks were readily detected with the laser anemometer system. The velocity gradients very near to the wall were found to be extremely large. The profiles downstream of the throat exhibited a jet-like character, being rather blunt at the axis, for several radii downstream. Again, gradients in the zone separating forward and reverse flows were quite large. The recirculation region becomes slightly thinner as the Reynolds number is increased from 10,000 to 15,000 and the magnitude of the reverse velocity (nondimensionalized by $\bar{u}$) decreases somewhat.

The comparison of the computational results with experimental data exhibit several interesting features which can be inferred from Figure 44. In the contracting section of the stenosis the peak velocity is predicted very well (also, see Figure 46); and there is, in fact, good agreement with the entire velocity profile except at positions quite near the wall. There, the experimental data show a steeper wall gradient than do the computations, which would presumably lead to an underestimation of wall shear stress by the analysis.

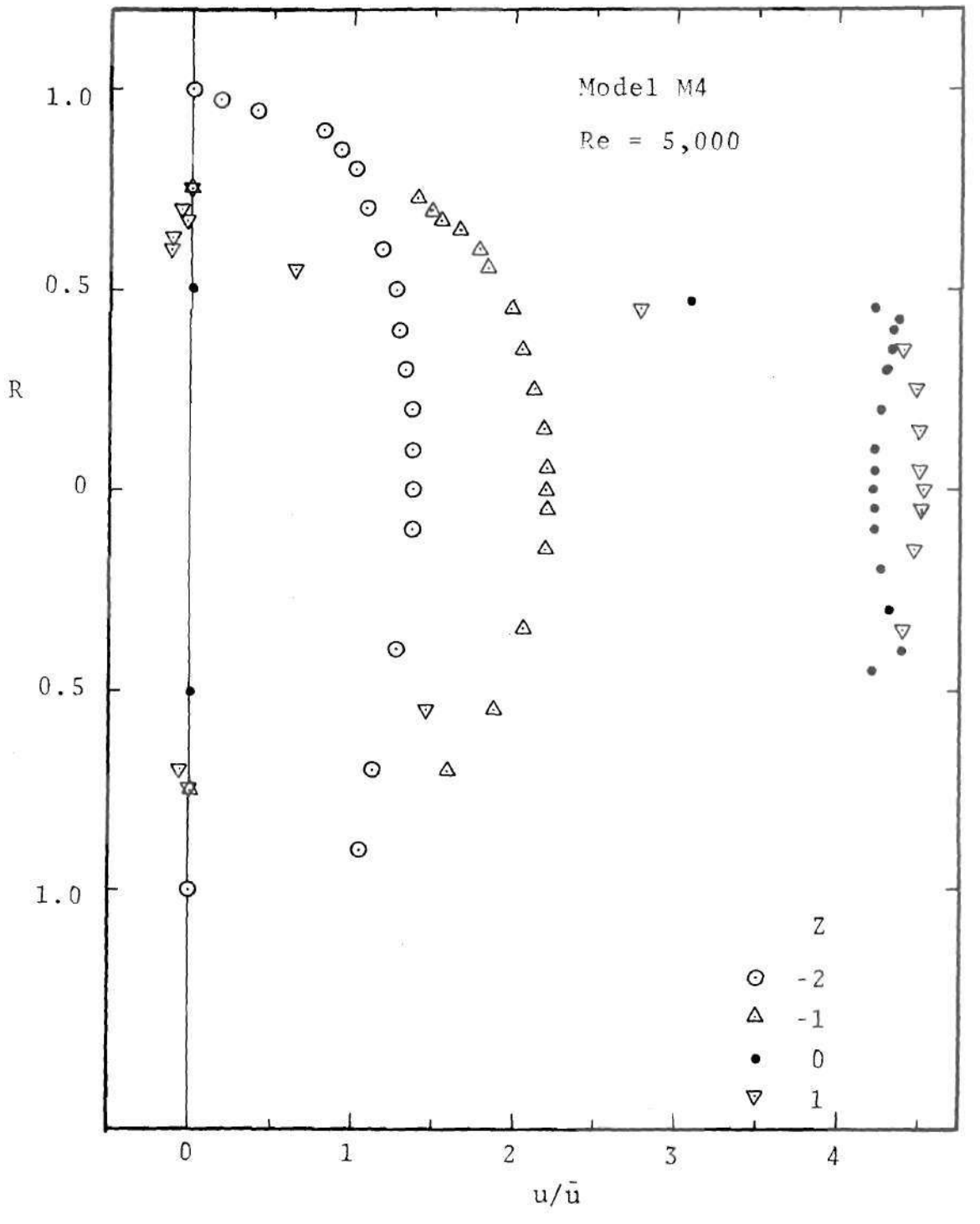

Figure 41. Axial Velocity Profiles, Model M4, Re = 5,000 (Experiments)

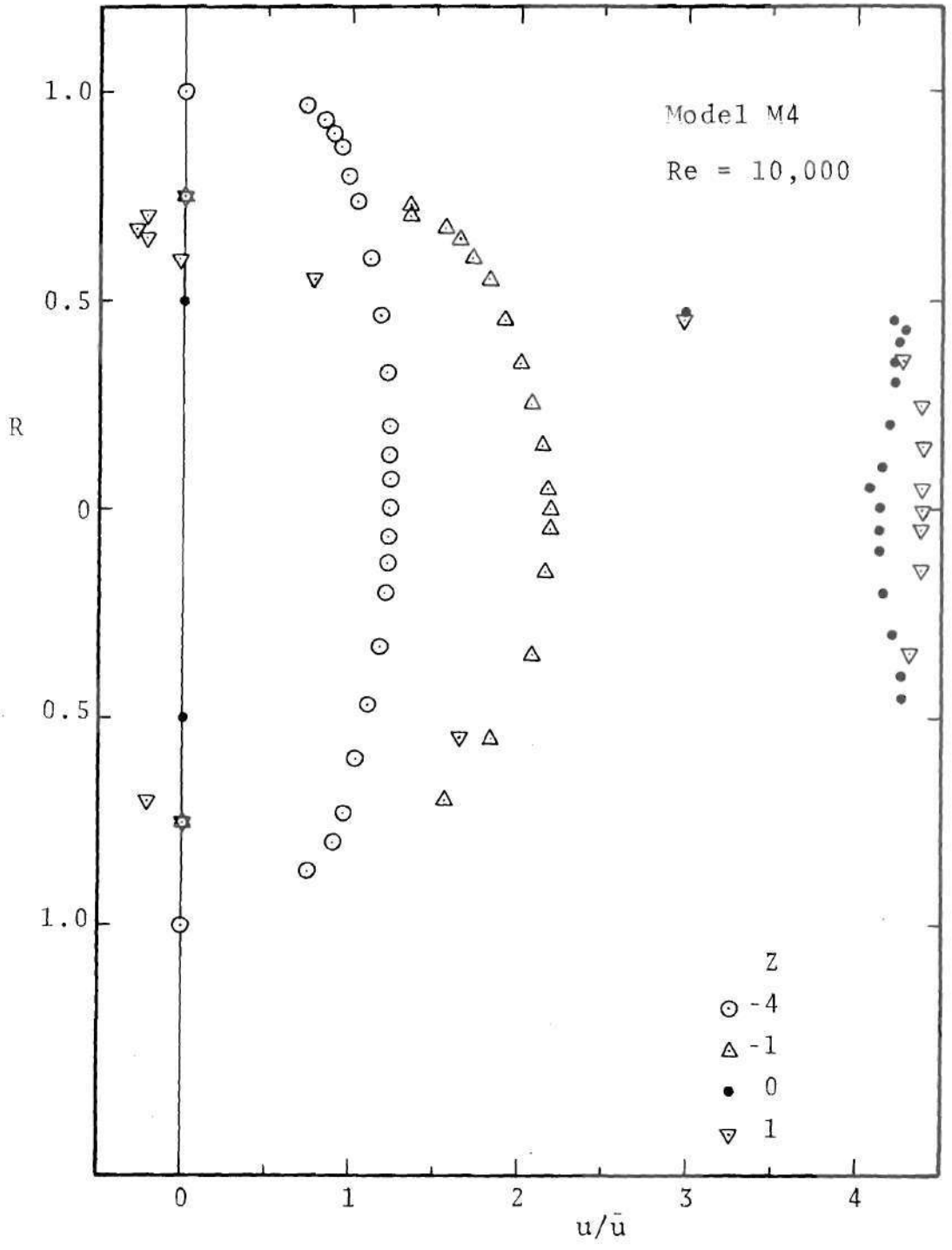

Figure 42. Axial Velocity Profiles Model M4, Re = 10,000 (Experiments) (A)

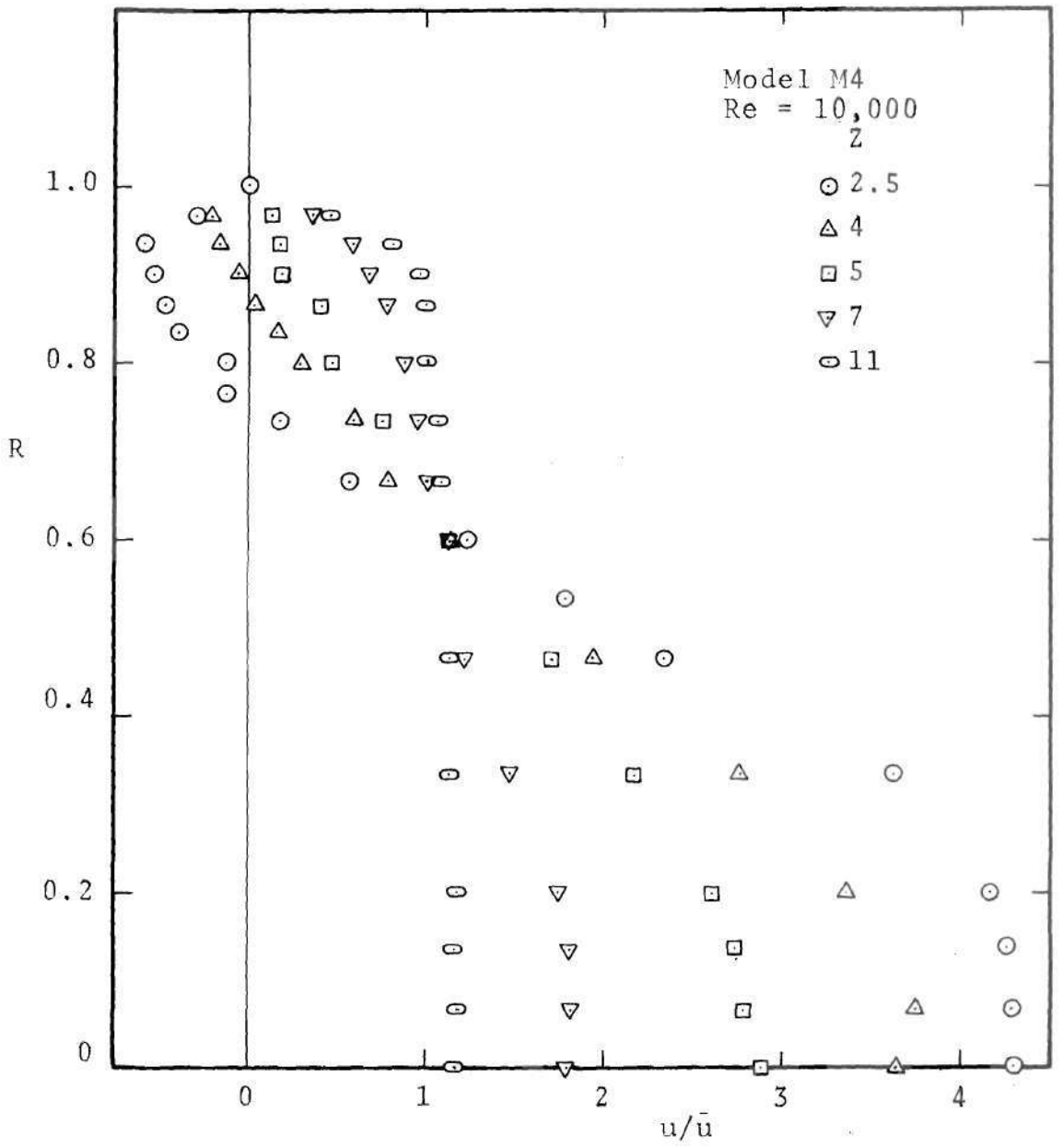

Figure 43. Axial Velocity Profiles, Model M4, Re = 10,000 (Experiments) (B)

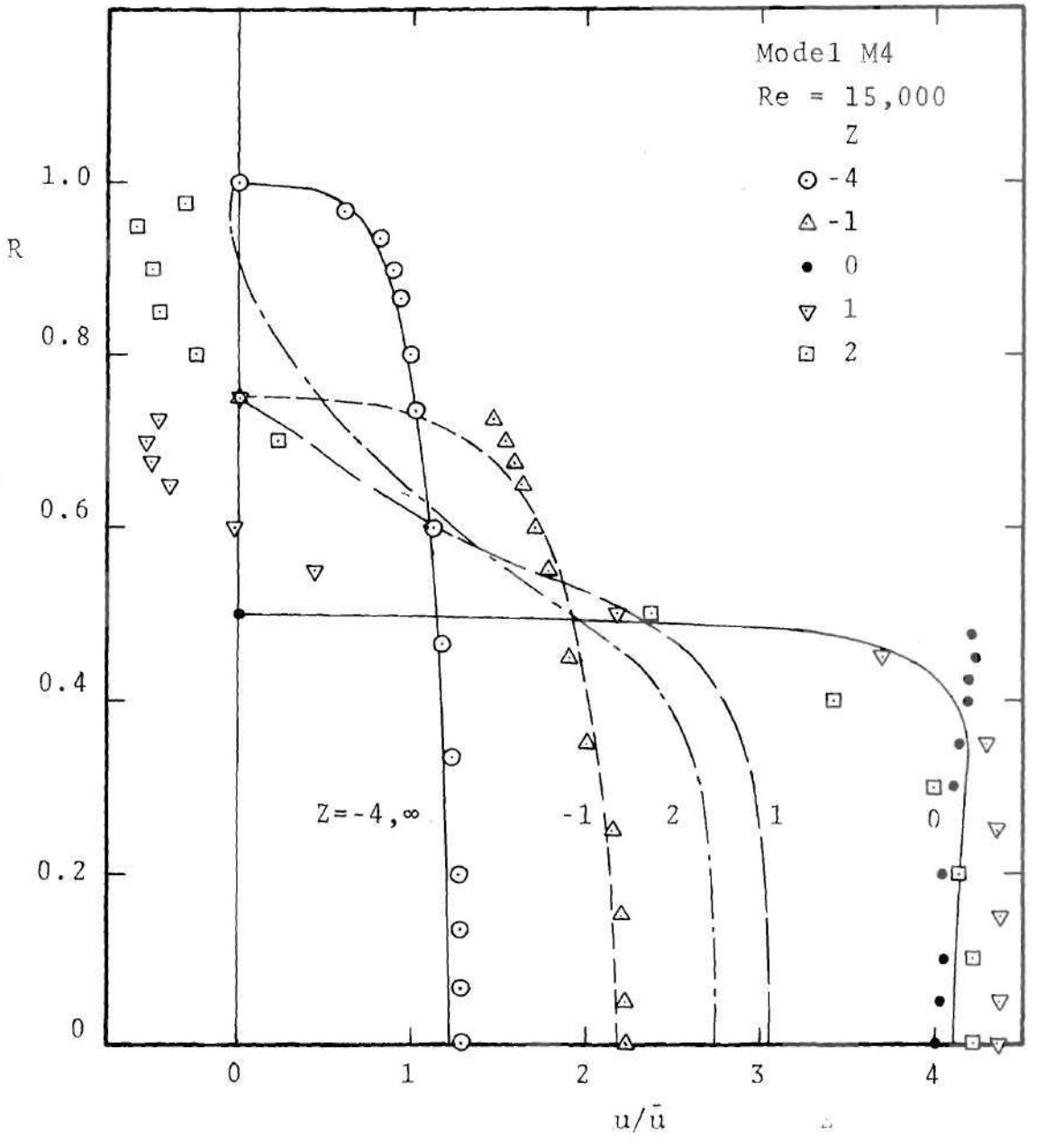

Figure 44. Comparison of Axial Velocity Profiles, Model M4, Re = 15,000 (A)

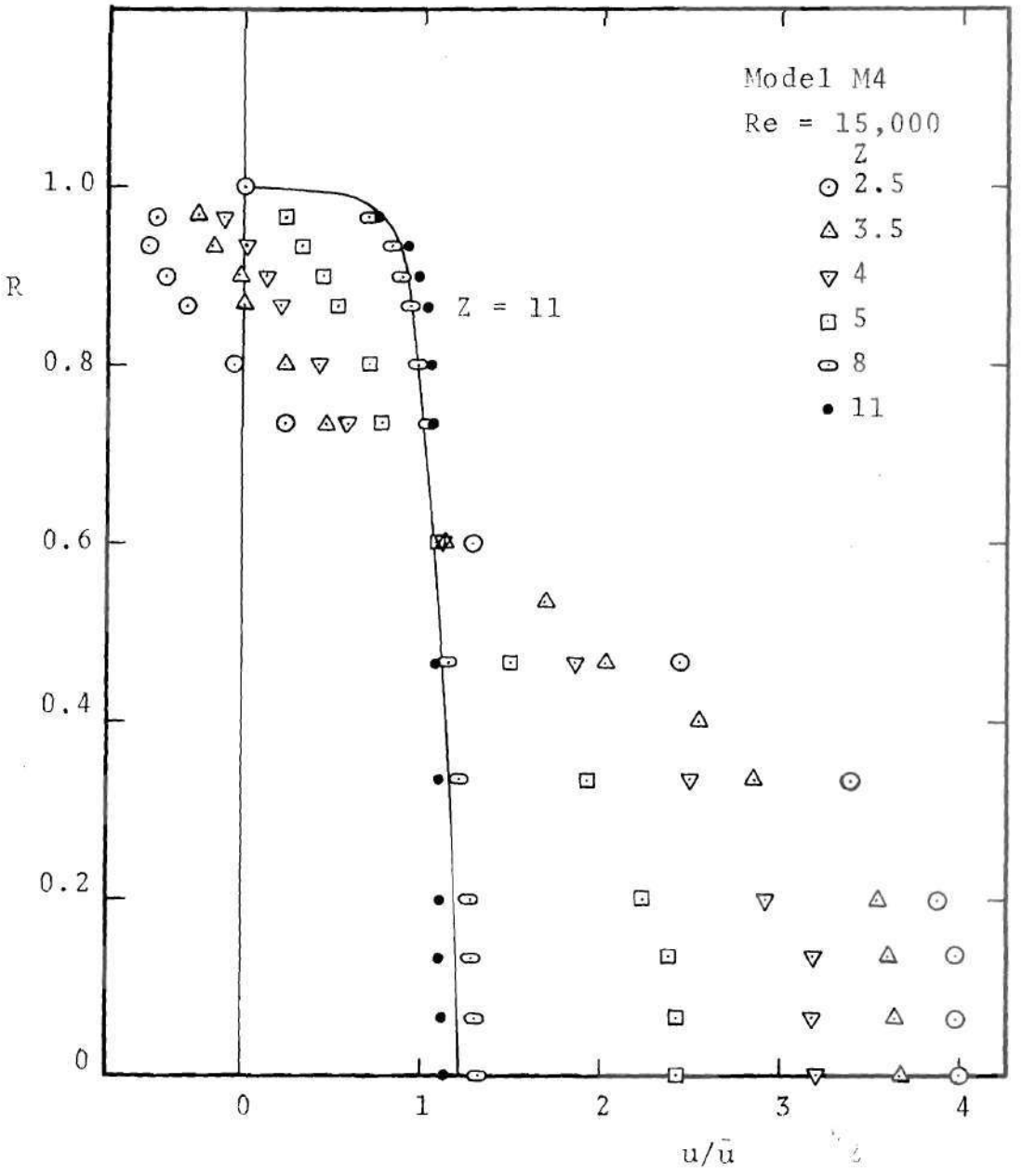

Figure 45. Comaprison of Axial Velocity Profiles, Model M4, Re = 15,000 (B)

Considerably downstream from the divergent section the theoretical and experimental results are likewise in reasonably good agreement. This can be seen from Figure 45 for Z = 11 and from Figure 46. However, in the divergent section itself and in its immediately downstream neighborhood, there is a noticeable discrepancy between theory and experiment. The recirculation region actually begins much sooner than is predicted, as can be seen by a comparison of profiles at Z = 1 in Figure 44. At this section the calculations show the flow to be attached while the experiments indicate a substantial region of reverse flow. The theory also predicts a much thinner recirculation region than was measured and, as discussed previously, predicts reattachment at a much earlier station than that actually found. From the standpoint of the continuity equation, then, it would be expected that the velocity profiles will show considerable differences between theory and experiment. This can be seen in the curves for Z = 1 and 2 in Figure 44. Note that the velocity profiles from the experiment are much flatter and have higher maximum velocities than do those of the computations. This is consistent with conservation of mass when it is recalled that the experiments show substantial regions of flow reversal near the wall which must be compensated for by increased forward flow near the axis. This is highlighted in Figure 46 which shows a plot of centerline velocity versus axial position. This figure also gives

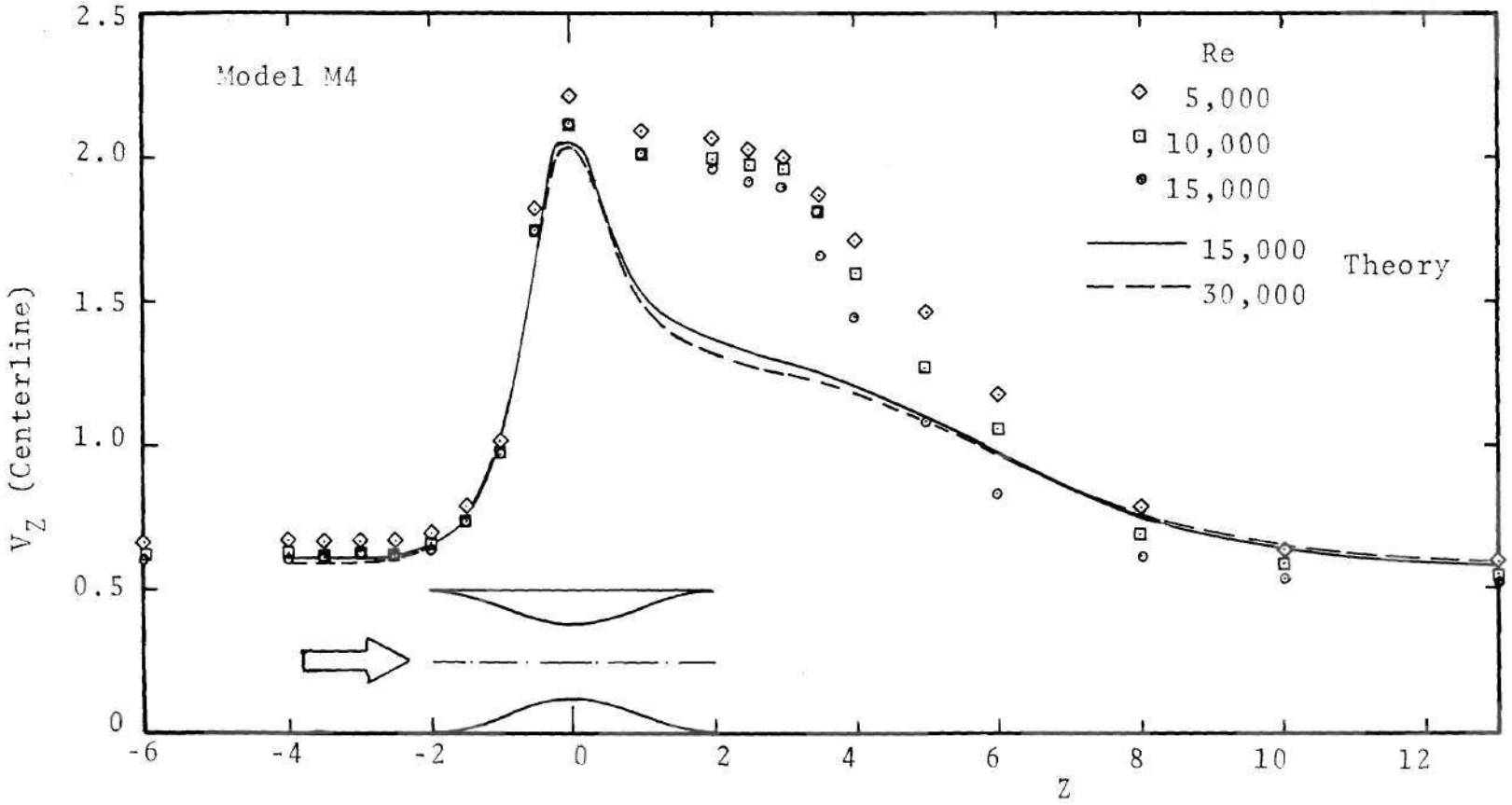

Figure 46. Axial Variation of Centerline Velocity, Model M4

experimental results for Re = 5,000 and 10,000 to show trends as Re increases. The nondimensionalized peak velocity tends to decrease as Re increases and there is a tendency for the jet-like character to persist further downstream. This trend is correctly predicted by the theory, as demonstrated by curves for Re = 15,000 and 30,000 in Figure 46; but clearly the accuracy is not good.

As will be seen subsequently, the kinetic energy of turbulence in the experiments is found to be much greater in the high shear layer than the theory predicts. Thus, several discrepancies between theory and measurement arise. These will be discussed along with the validity of the k-ε model after all the data has been presented.

Figures 47-49 show additional calculations. Since the theoretical model has been qualitatively correct, although not quantitatively accurate in certain regions, it might be hypothesized that trends shown in the computations at other Reynolds numbers and for other degrees of stenosis might be indicative of trends to be expected experimentally. This, of course, can only be validated by eventual comparison with measurements.

Figure 47 gives velocity profiles for Model M4 at the very high Reynolds number of 388,000. Again the maximum velocity in the throat section occurs off-axis. Also, for this case there is no recirculation region predicted. Figures 48 and 49 show profiles for Models M1 and M2 at Re = 15,000.

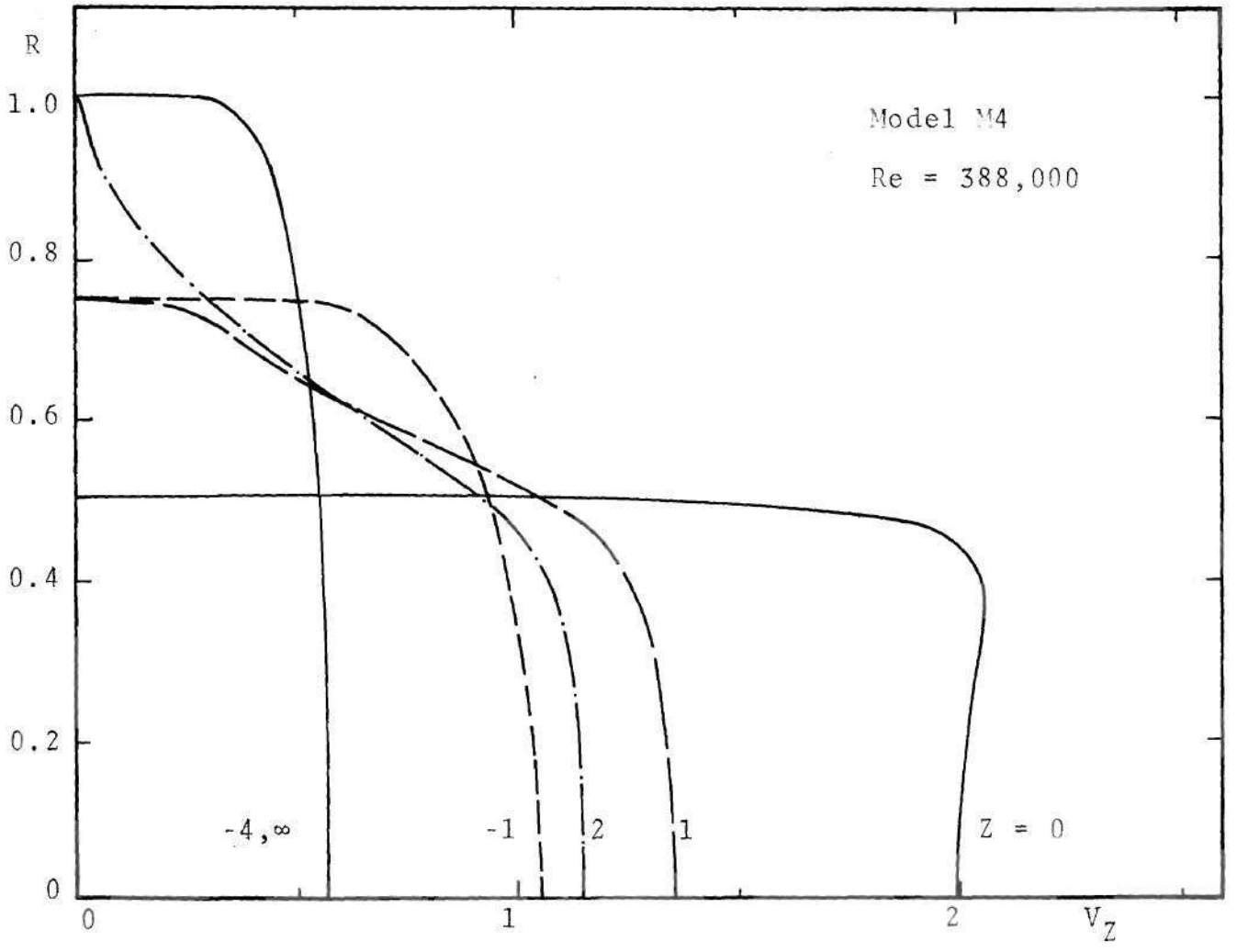

Figure 47. Axial Velocity Profiles, Model M4, Re = 388,000 (Theory)

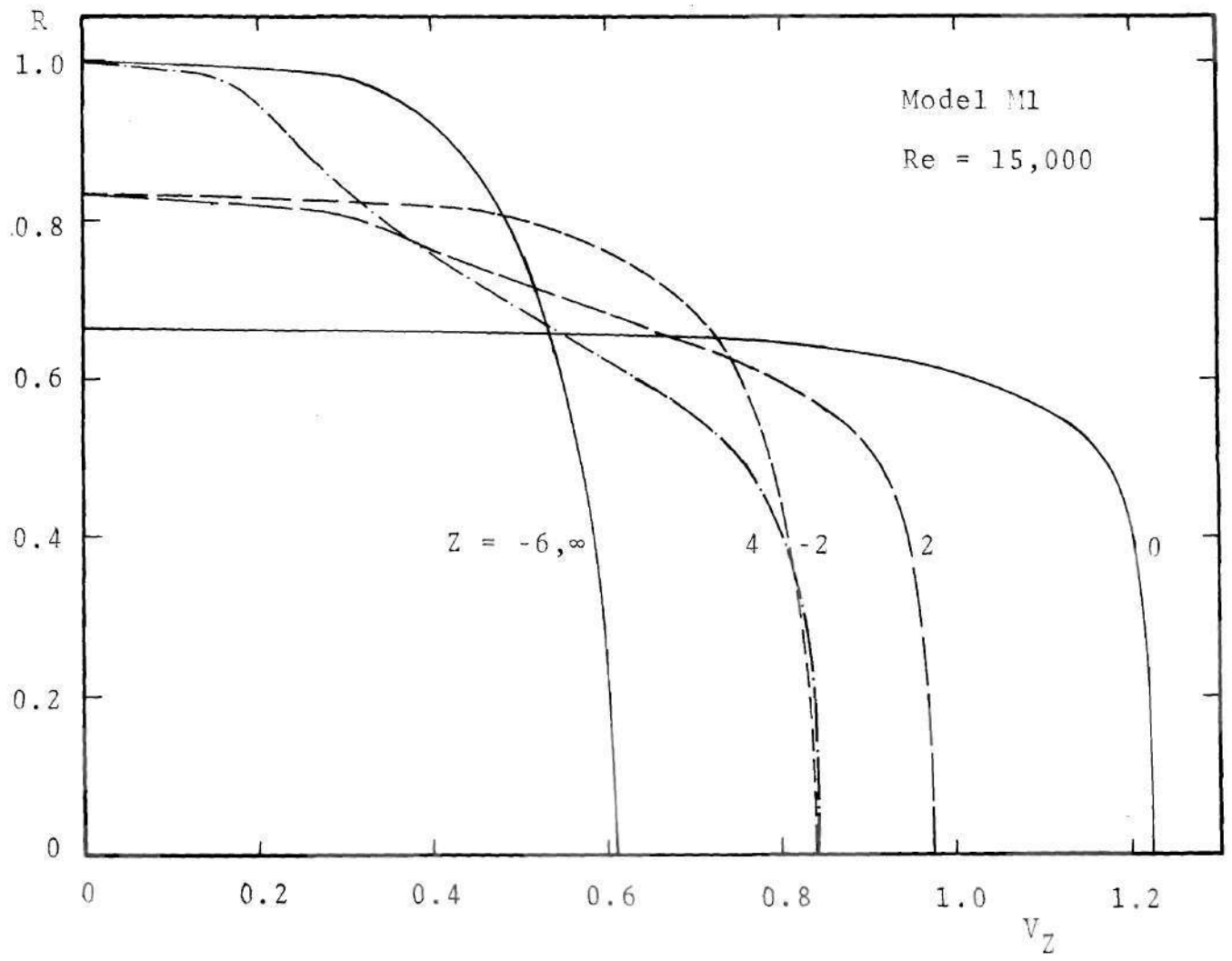

Figure 48. Axial Velocity Profiles, Model M1, Re = 15,000 (Theory)

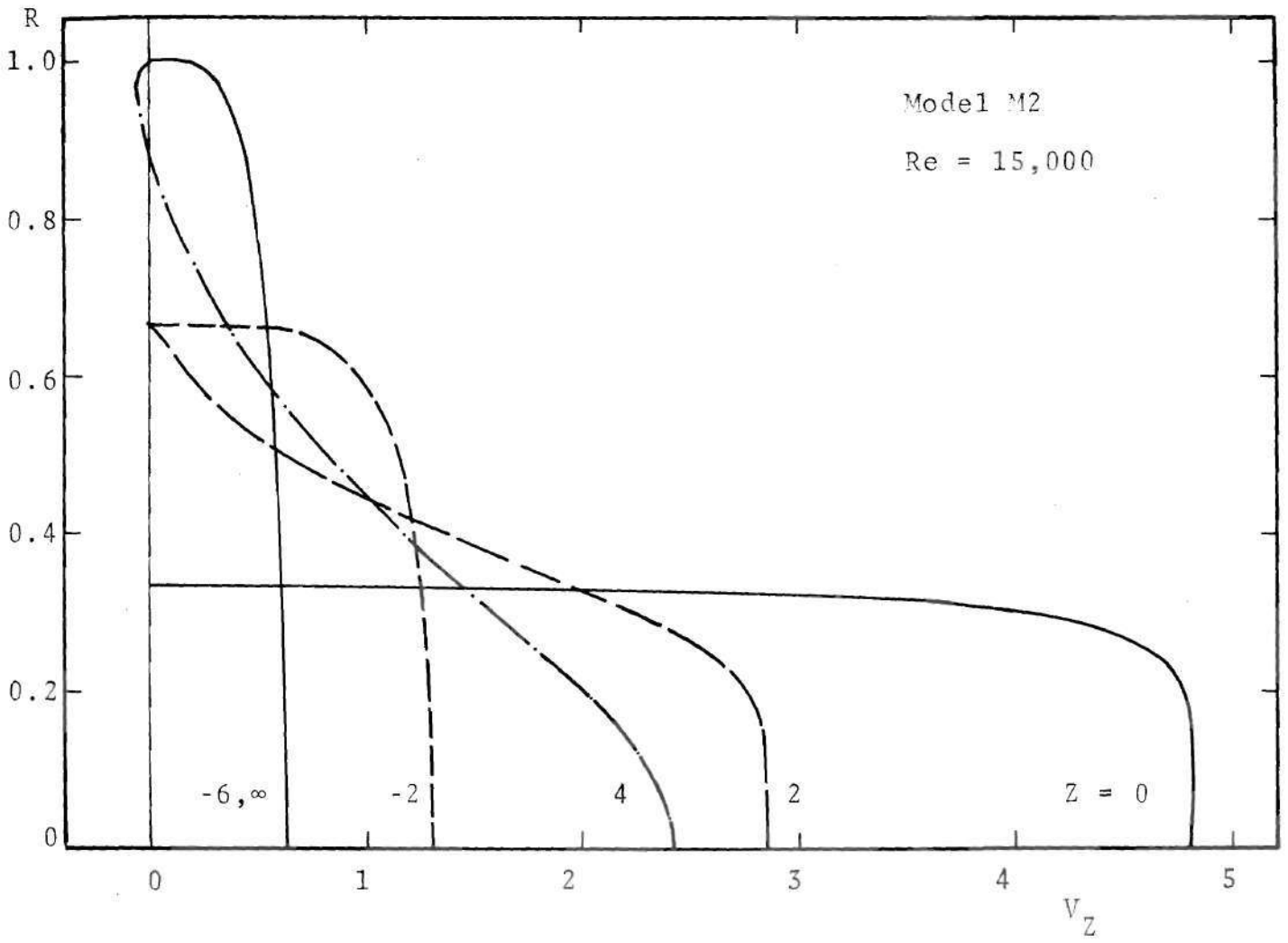

Figure 49. Axial Velocity Profiles, Model M2, Re = 15,000 (Theory)

Recall that M1 is a milder, and M2 is a more severe, stenosis than the basic model studied, M4. The theory predicts no recirculation region for M1 and there is no off-axis peak in the throat profile. Model M2, which represents a severe constriction, does exhibit a recirculation region and a small, but perceptible, peak off-axis in the velocity profile. Thus, the theory predicts a decreasing size for the recirculation zone with decreasing degree of stenosis (at a fixed Re) and with an increasing Reynolds number (at a fixed degree of stenosis). This should occur experimentally, also.

Figures 50 and 51 give the calculated centerline velocities for Models M1 and M2 at two Reynolds numbers, 15,000 and 388,000. It is seen that there is little variation in these curves with Reynolds number, even over such a wide range of values. In this nondimensional form of presenting the data the values of centerline velocity are more elevated, and these persist farther downstream, for lower Reynolds numbers. Again, this is also the trend in the experimental data. Note that the peak velocity in the case of the severe stenosis Model M2 is about four times higher at the same Reynolds number than that for the moderate stenosis M1, but at Z = 12 it has returned much closer to the final downstream value. This is caused by a more effective momentum transport arising from increased turbulence intensity for the more severe stenosis.

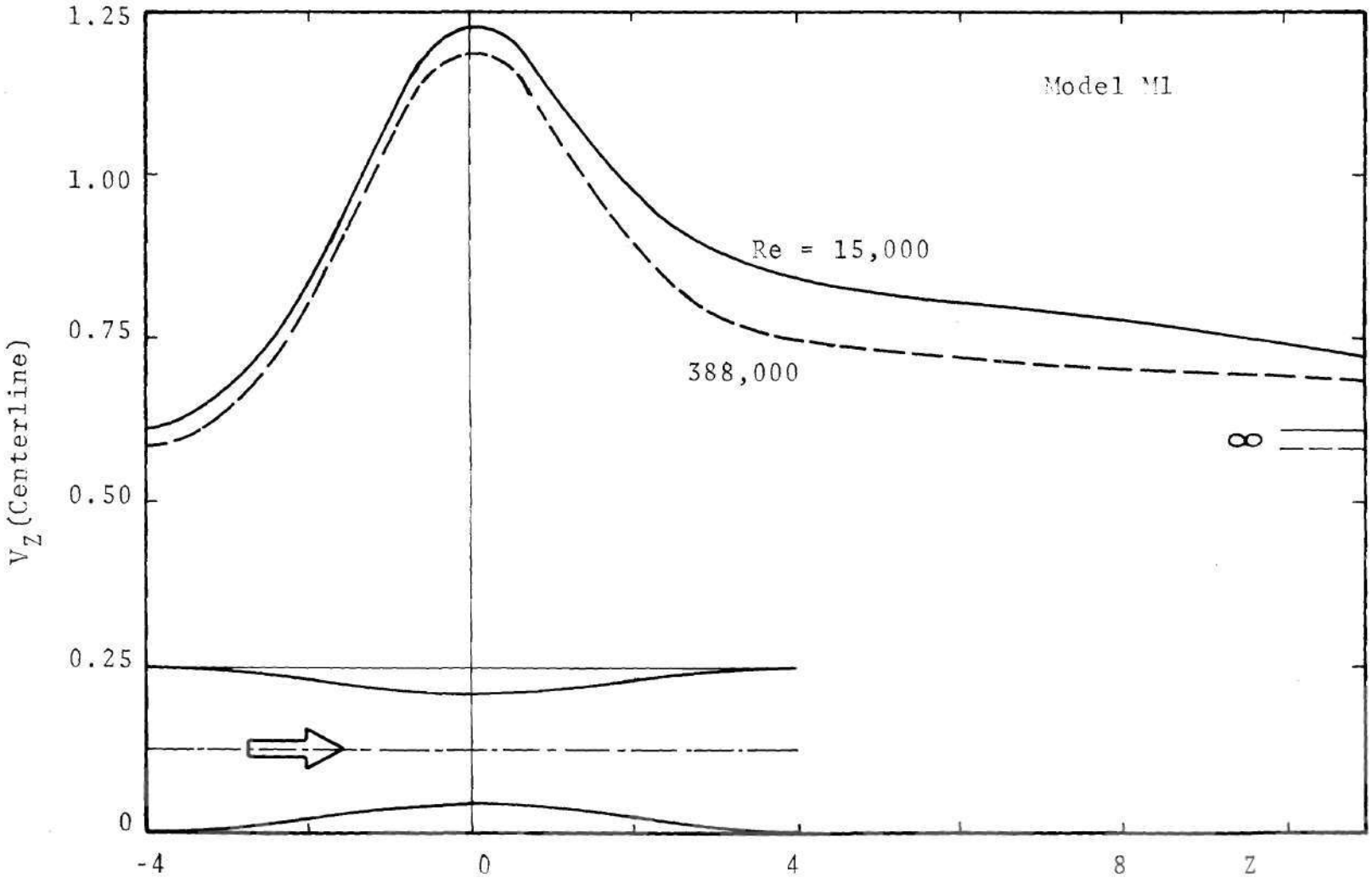

Figure 50. Axial Variation of Centerline Velocity, Model M1, Re = 15,000 and 388,000 (Theory)

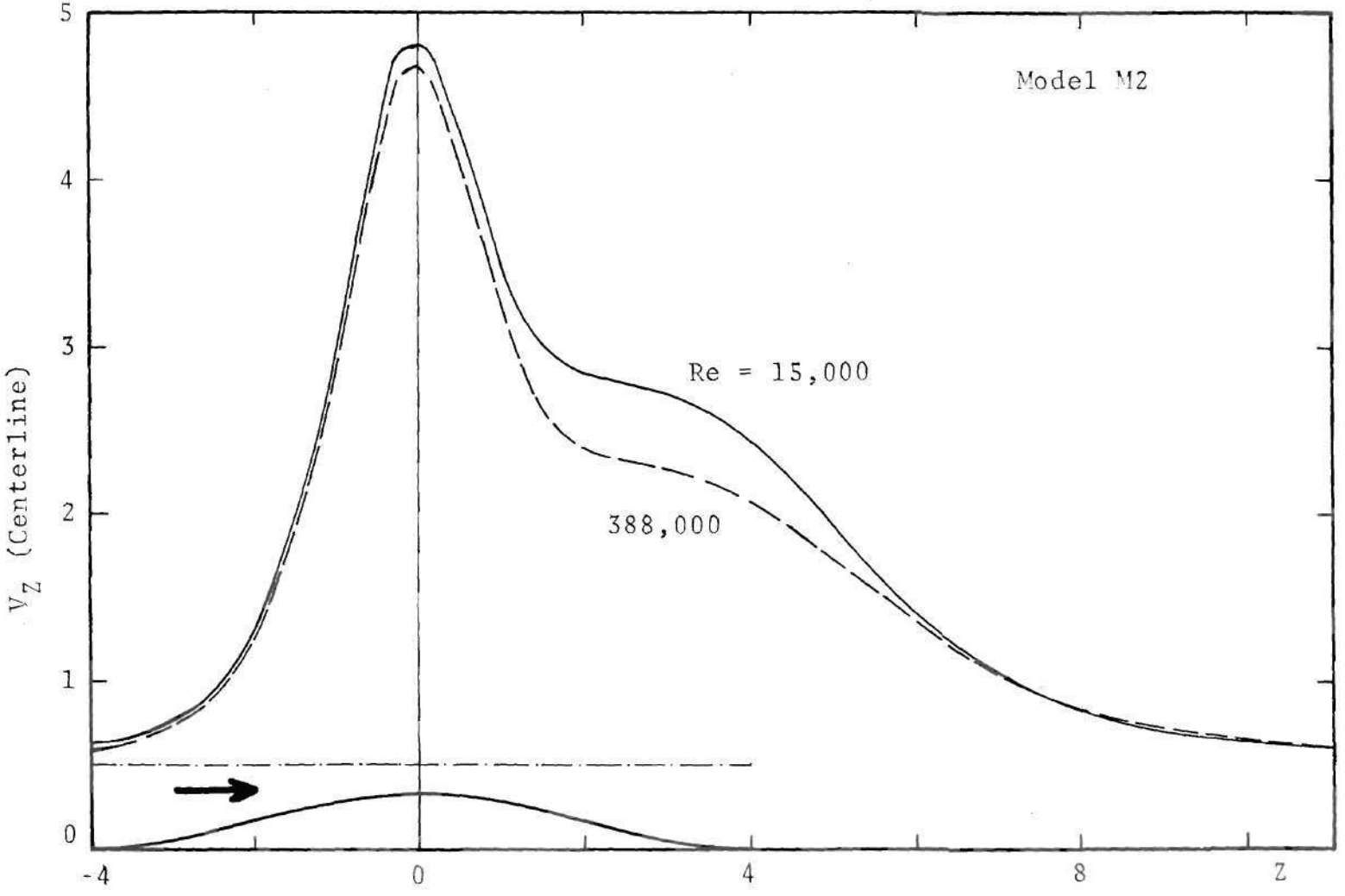

Figure 51. Axial Variation of Centerline Velocity, Model M2, Re = 15,000 and 388,000 (Theory)

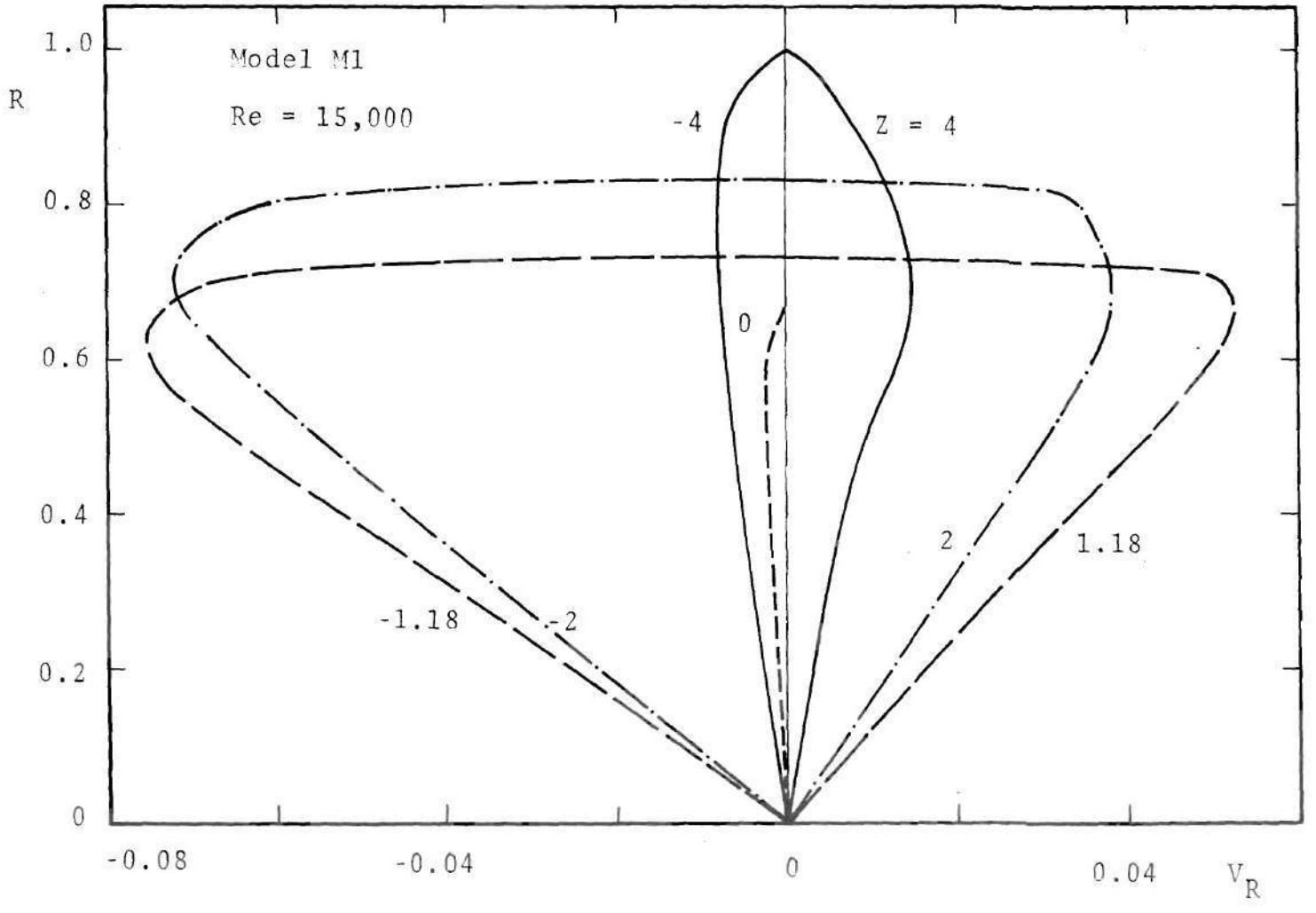

Figure 52. Radial Velocity Profiles, Model M1, Re = 15,000 (Theory)

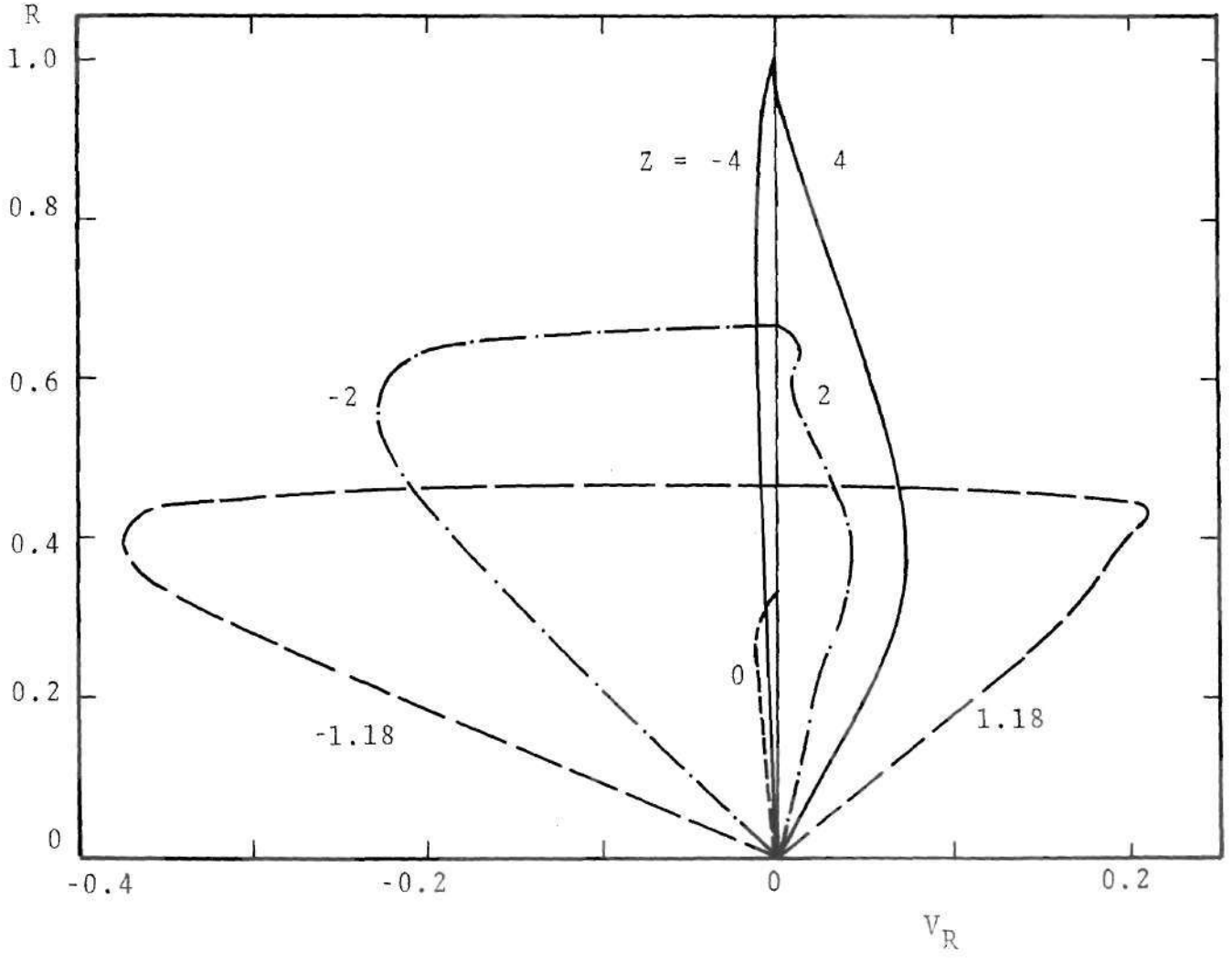

Figure 53. Radial Velocity Profiles, Model M2, Re = 15,000 (Theory)

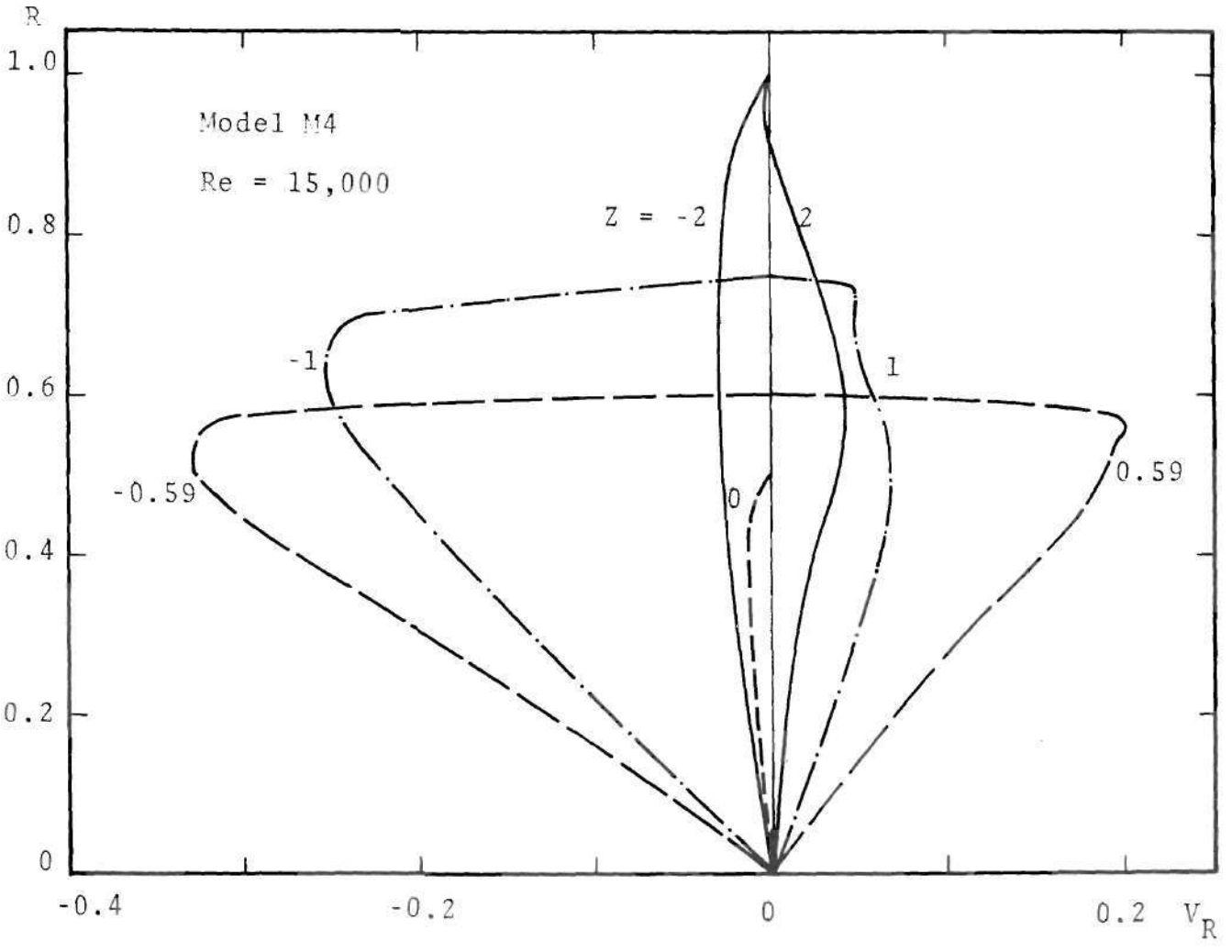

Figure 54. Radial Velocity Profiles, Model M4, Re = 15,000 (Theory)

The radial velocity profiles are displayed for Models M1, M2 and M4 for the Reynolds number of 15,000 in Figures 52-54. The trend and the order of magnitude of the relative velocities are comparable to similar profiles in the laminar flow. In the light of the earlier results, the magnitudes of the radial velocity in the diverging portion of the stenoses are likely to be overestimated.

5.2.3. Pressure Variation

The pressure drop across the stenosis increases considerably when the flow changes from laminar into turbulent. The wall pressure distribution was measured for several Reynolds numbers for flow through Model M4. It is plotted in Figure 55 for five of these values. It can be seen that there is a steep drop in the pressure in the converging portion of the stenosis and a part of this is recovered in the decelerating flow. A substantial portion of the pressure recovery occurs beyond the exit plane of the stenosis itself. There is also a considerable increase in the pressure in the initial section of the diverging portion, and only a small amount of the recovery is in the later part of the diverging section. The reason for this can immediately be attributed to the recirculating flow and the centerline velocity variation in Figure 46 supports this idea. Because of the presence of turbulence the flow does not separate until somewhat downstream of the throat so that there is a noticeable pressure recovery from throat to

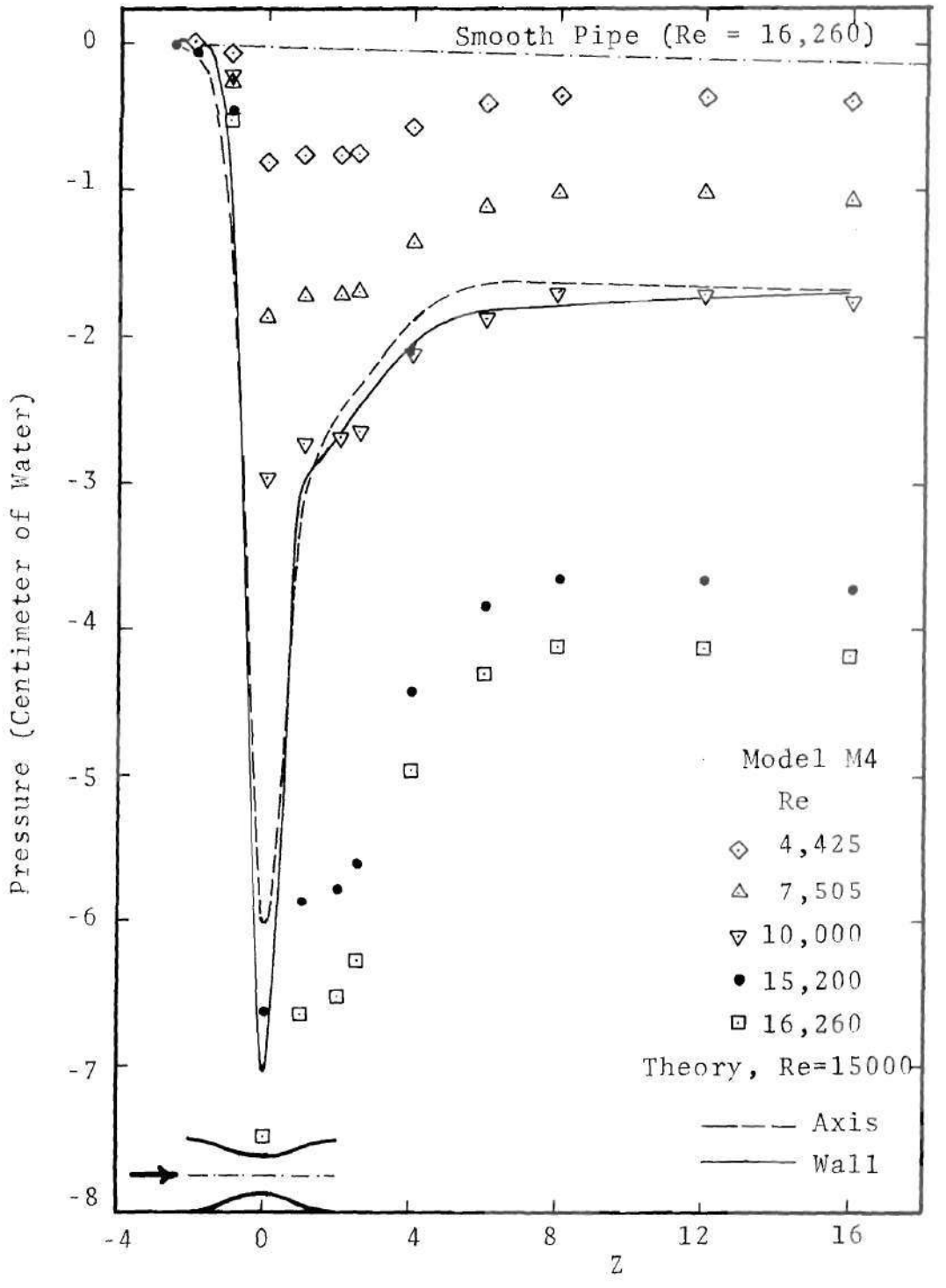

Figure 55. Pressure Distribution Along Tube in Turbulent Flow, Model M4

separation point. The near parallel flow adjacent to the recirculating region has very little pressure recovery and can be viewed as the cause of a substantial net pressure loss. The pressure distribution described is similar to that in a laminar flow. A larger part of the gross pressure drop in the converging section, however, is recovered in case of the turbulent flow. There is a relative maximum in the pressure, occurring around Z = 8. In case of laminar flow, this point is more sensitive to the Reynolds number and also occurs far downstream for higher Reynolds number laminar flows.

The predicted pressure at the axis and the wall is also plotted in Figure 55. The agreement with the experimental data is good in the converging section. A large discrepancy is evident in the decelerating flow. The reason for this was already seen, in that the circulating flow is predicted to be thinner and shorter than experiment indicates. A correct flow prediction in the diverging part of the tube should considerably improve the estimated pressure drop across the stenosis. Computed pressures at both axis and the wall are indicated. Radial pressure gradients are generally smaller than the axial values but are seen to be of importance close to the throat and in the distal region in comparison with the laminar flow. The pressure gradient approaches the fully developed value distal to the stenosis after reaching a minimum. This non-monotonic behavior is in

accordance with the variation of velocity and wall shear stress in this region. The pressure distribution in a smooth pipe, given by the Blasius formula [56] is also plotted. The predicted nondimensional pressure distribution for Models M1 and M2 is illustrated in Figures 56 and 57. The predicted pressure drop across the stenosis may be expected to be an underestimate. There is very little change in the nondimensional pressure in the converging section when the Reynolds number is increased from 15,000 to 388,000. Changes in nondimensional pressure gradients with Reynolds number are substantial only close to the throat and the diverging portion of the stenosis.

The net loss in the nondimensional pressure $\Delta p/(\rho \bar{u}^2)$ between the points Z = -2.5 and Z = 16 is exhibited in Figure 58. The pressure drop in a smooth pipe due to laminar (Poiseuille flow) and turbulent flow (Blasius formula [56]) in a smooth pipe of 18.5 radii length are also given for comparison. The pressure loss increases with the severity of the stenosis. The reason for the discrepancy in the predicted and the experimental results for Model M4 was discussed previously. The experimental data for Model M4 is represented by

$$\frac{\Delta p}{\rho \bar{u}^2} = \frac{24.5}{Re^{0.174}} \qquad (30)$$

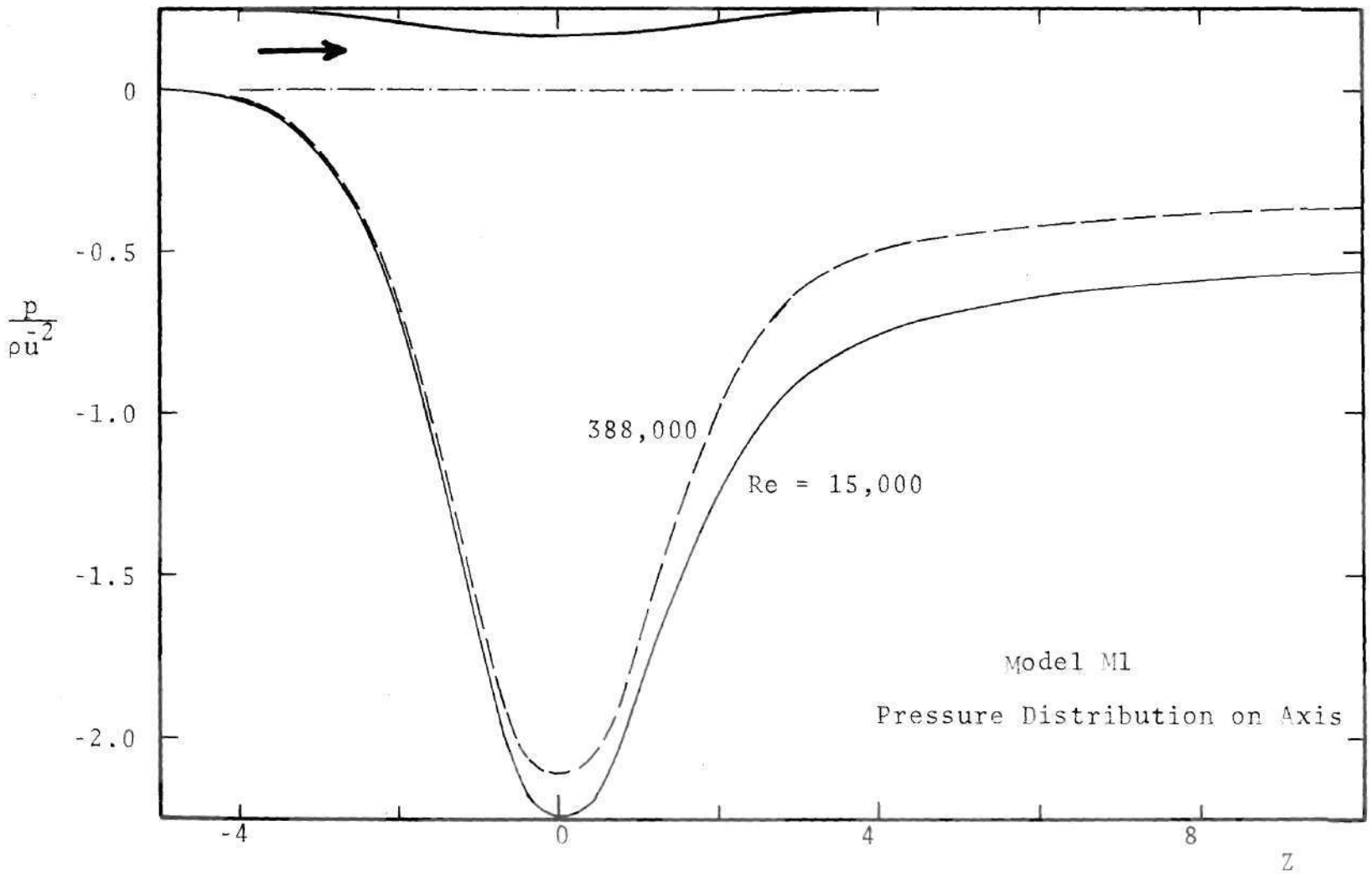

Figure 56. Pressure Distribution Along Tube in Turbulent Flow, Model M1, Re = 15,000 and 388,000 (Theory)

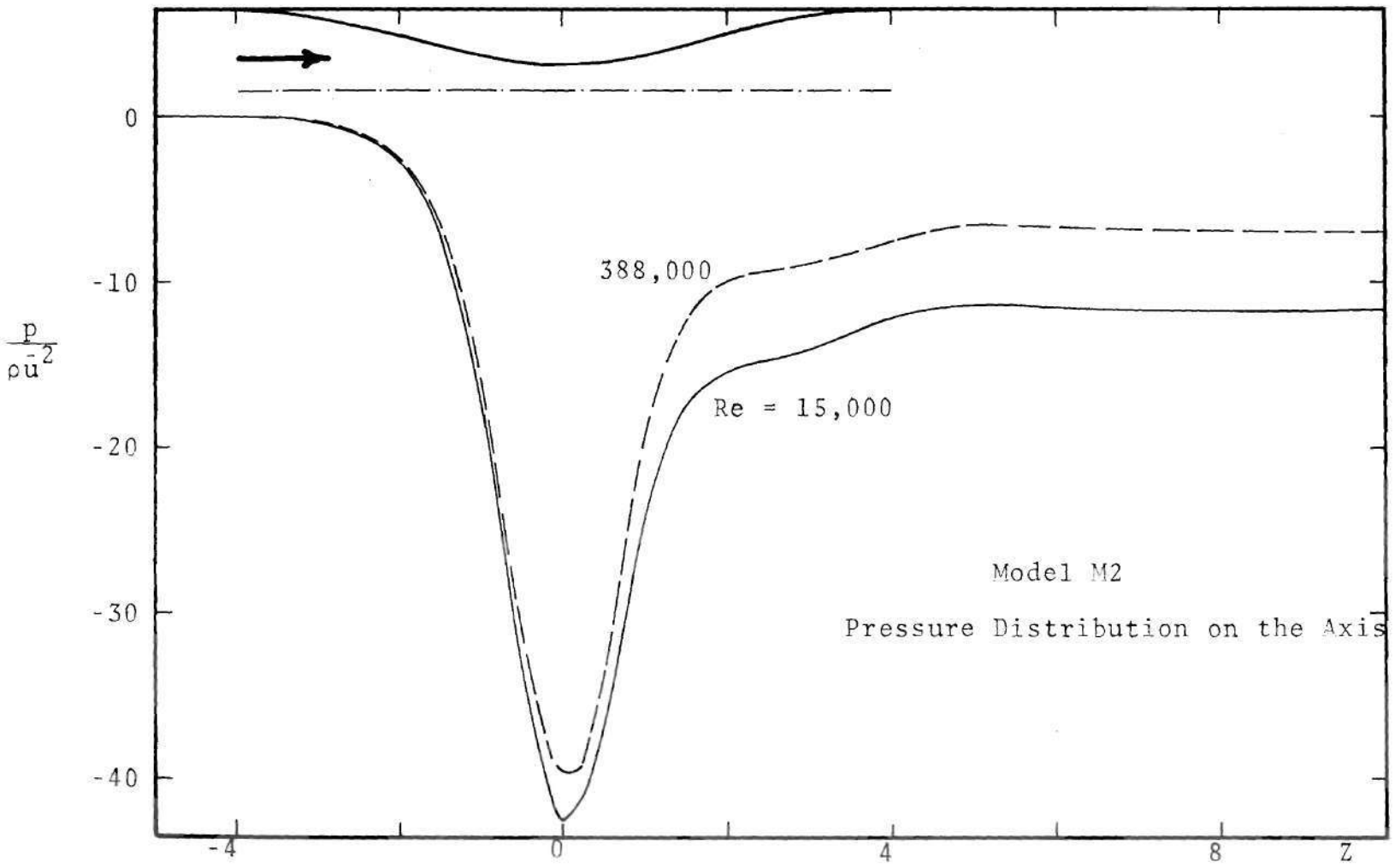

Figure 57. Pressure Distribution Along Tube in Turbulent Flow, Model M2, Re = 15,000 and 388,000 (Theory)

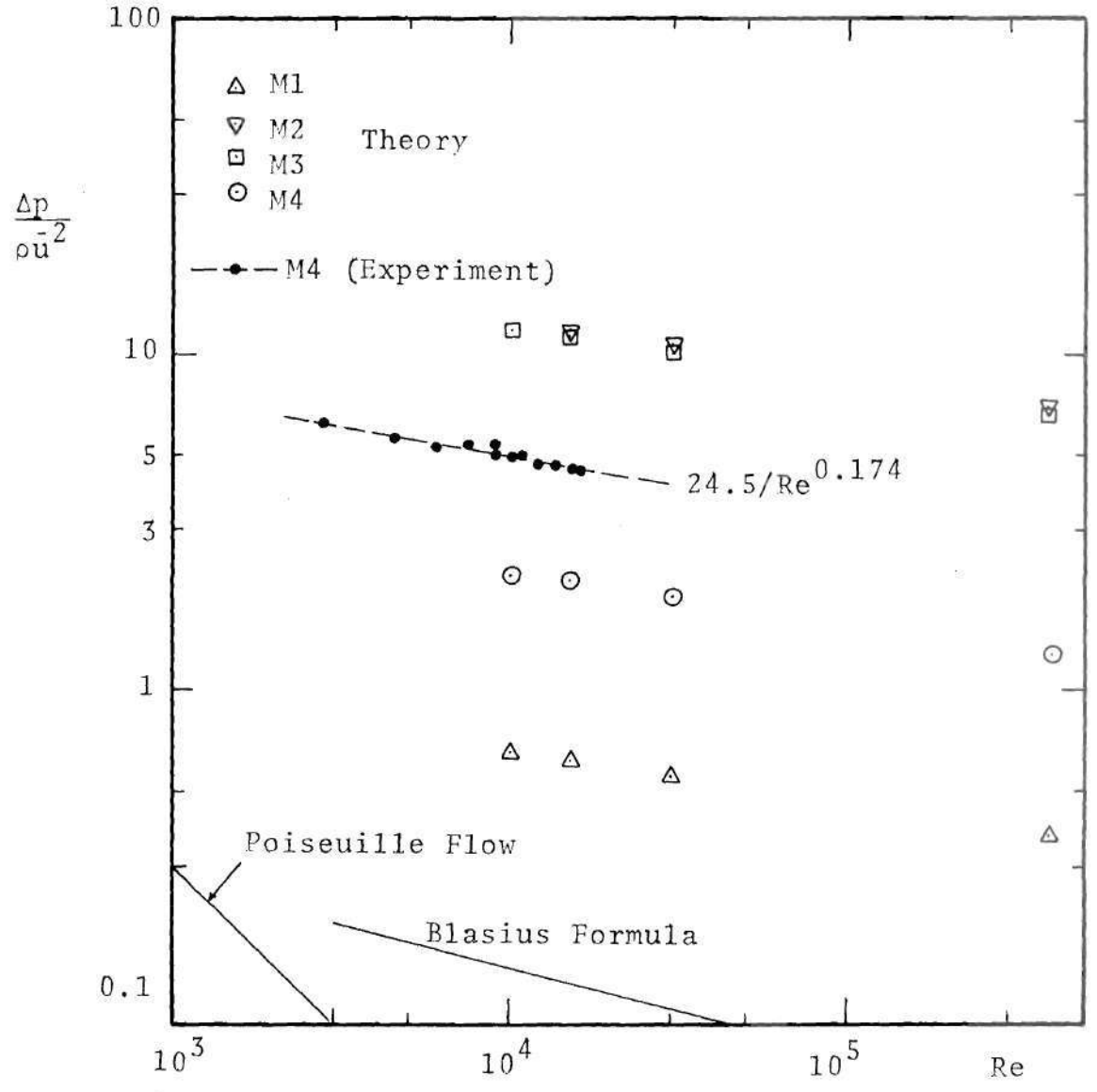

Figure 58. Pressure Drop Across Stenoses in Turbulent Flow

5.2.4. Wall Shear Stress

Wall shear stress is of considerable physiological importance. It is difficult to measure this quantity experimentally and hence the theoretical results are valuable. It should be recalled, however, that the law of the wall is employed to assess this quantity and hence the absolute magnitude predicted near the recirculation region is less reliable. The square root of this quantity nondimensionalized by the average velocity in the unoccluded tube is plotted for the three Models M4, M1 and M3 in Figures 59, 60 and 61, respectively. The negative square root is used whenever the shear stress τ is negative. Again, a comparative examination for Reynolds numbers 15,000 and 388,000 is chosen.

The behavior of this quantity is somewhat similar to that in the laminar flow. However, it is characterized by a shorter recirculation region and an overshoot in the shear stress distal to the reattachment point before it returns to the fully developed value. The reason for this overshoot in the shear stress is due to the flatter velocity profiles in this region. Behavior of the recirculation region when the Reynolds number is changed was already discussed. From the comparison between the theoretical and the measured velocity profiles close to the wall as seen in Figure 44, it may be concluded that the shear stress predicted in the converging portion is an underestimate of the actual value.

The maximum value of the shear stress which is

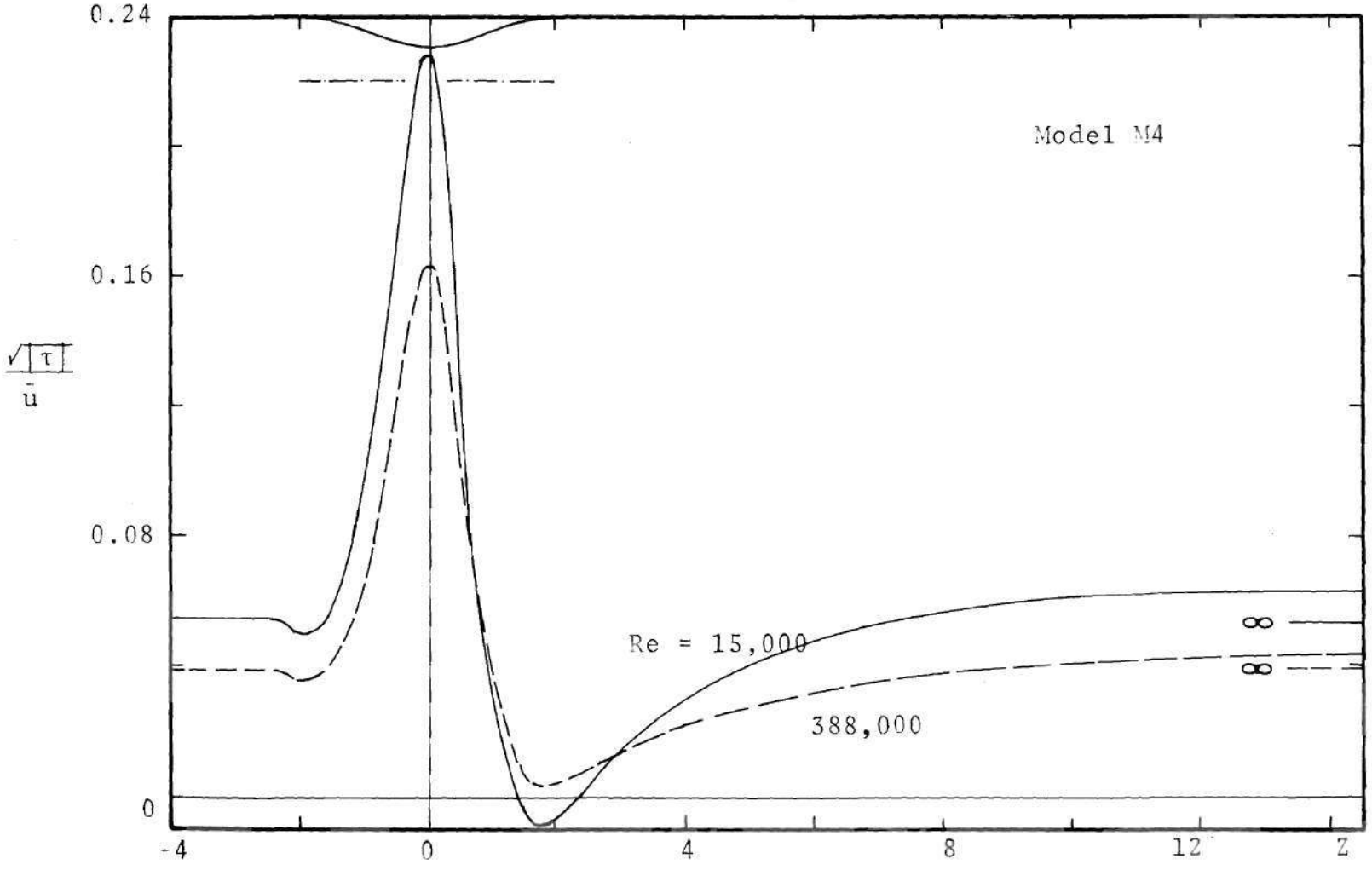

Figure 59. Wall Shear Stress Distribution, Model M4, Re = 15,000 and 388,000 (Theory)

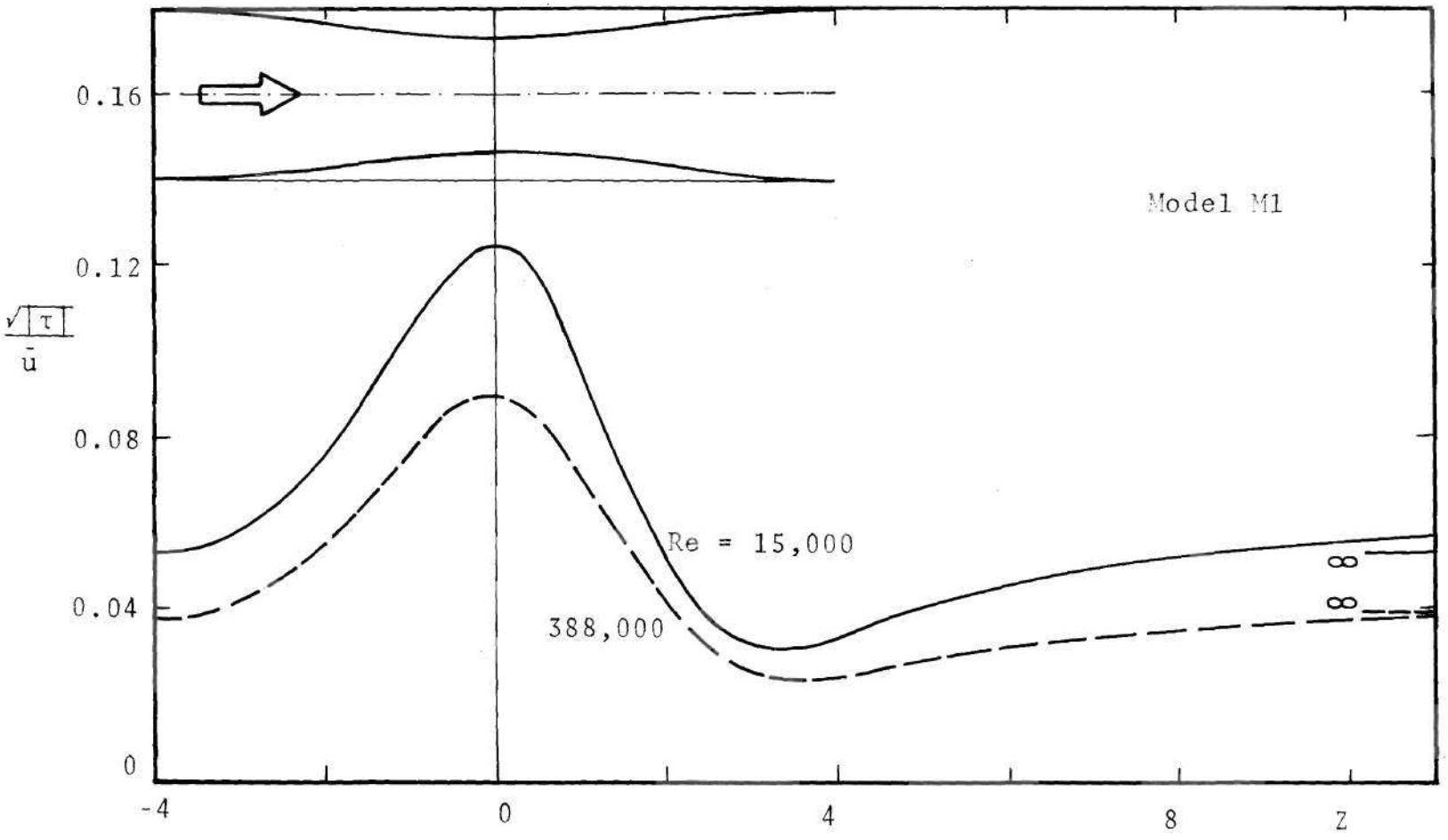

Figure 60. Wall Shear Stress Distribution, Model M1, Re = 15,000 and 388,000 (Theory)

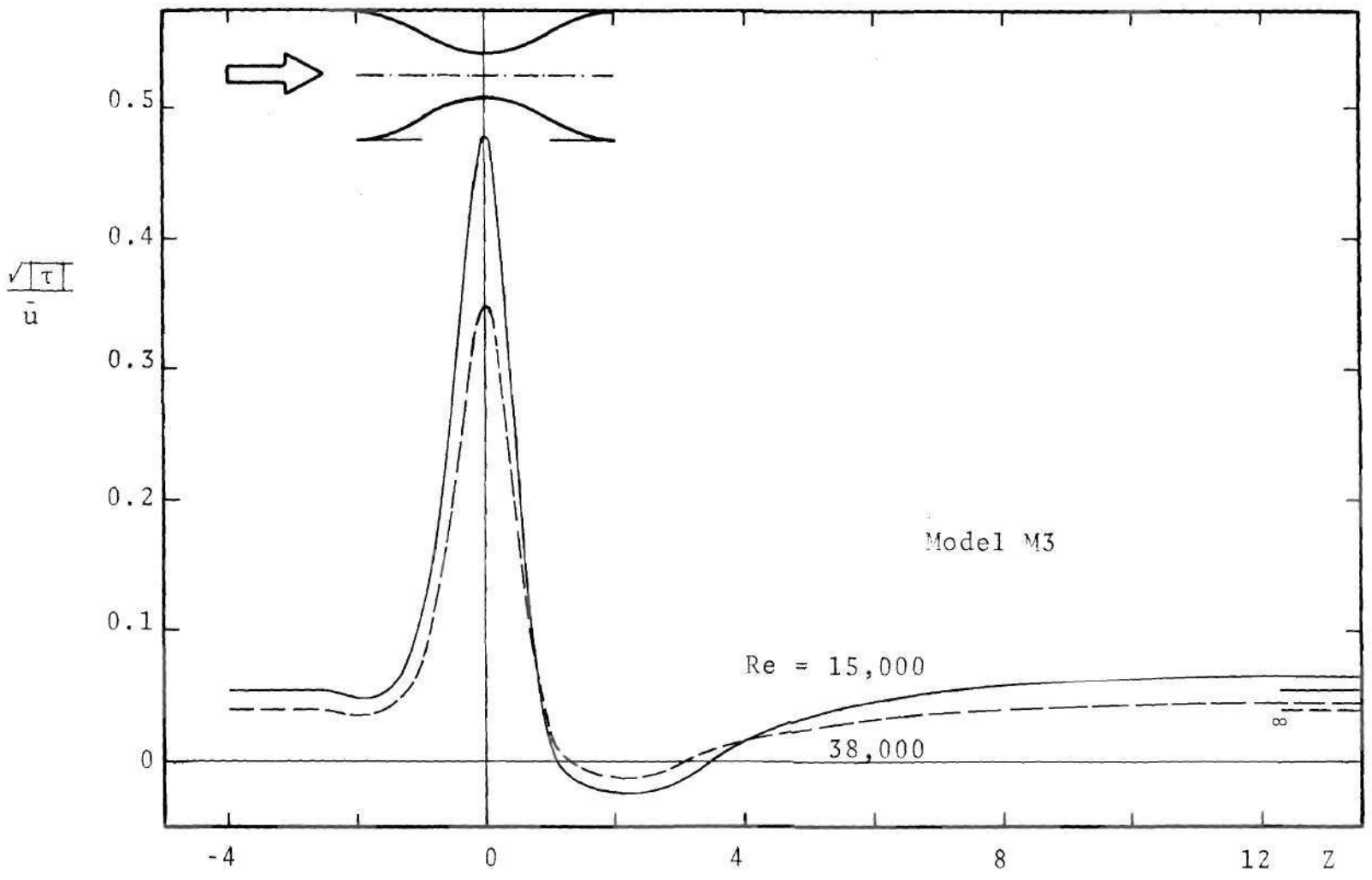

Figure 61. Wall Shear Stress Distribution, Model M3, Re = 15,000 and 388,000 (Theory)

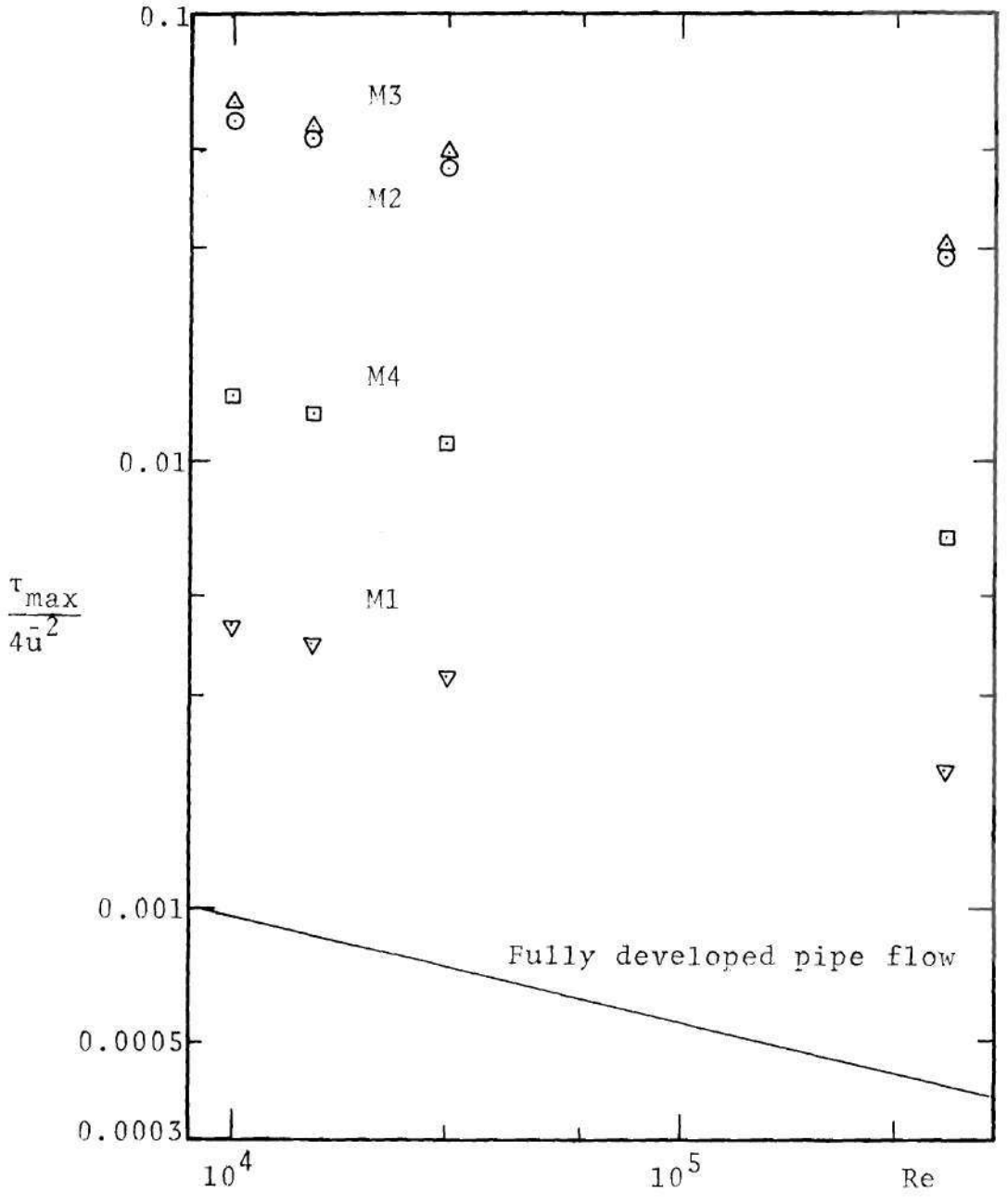

Figure 62. Maximum Wall Shear Stress for Stenoses (Theory)

predicted to occur at the throat is compared in Figure 62 for all the four models and the four Reynolds numbers for which computations were performed. The same quantity in a fully developed pipe flow obtained using the Blasius formula [56] is represented by a straight line. The increase in the shear stress with an increase in the severity of the stenosis is evident. Models M2 and M3 have an area reduction of 89%. The shorter Model M3 attains a higher maximum shear stress whereas the pressure drop was higher in Model M2 (Figure 58). The same behavior was found in laminar flow.

5.2.5. Turbulence Velocity Fluctuations

The turbulence kinetic energy k is predicted theoretically and the turbulence fluctuation velocities u' and w' are measured experimentally for Model M4 at the Reynolds number 15,000. The measured components u' and w' are combined subject to the assumption that w' = v' to obtain k, and this quantity is referred to as the experimental value. The implications of such an assumption have been discussed earlier in this chapter. The comparison of the turbulence intensity with the experimental data is a severe test of the model. The turbulence kinetic energy is plotted in the nondimensional form $\sqrt{k}/\bar{u}$.

Figure 63 presents measurements for the turbulence velocities and calculations for the kinetic energy at the station Z = -4. Also presented are curves which have been obtained from the experimental data of Laufer [85] for fully

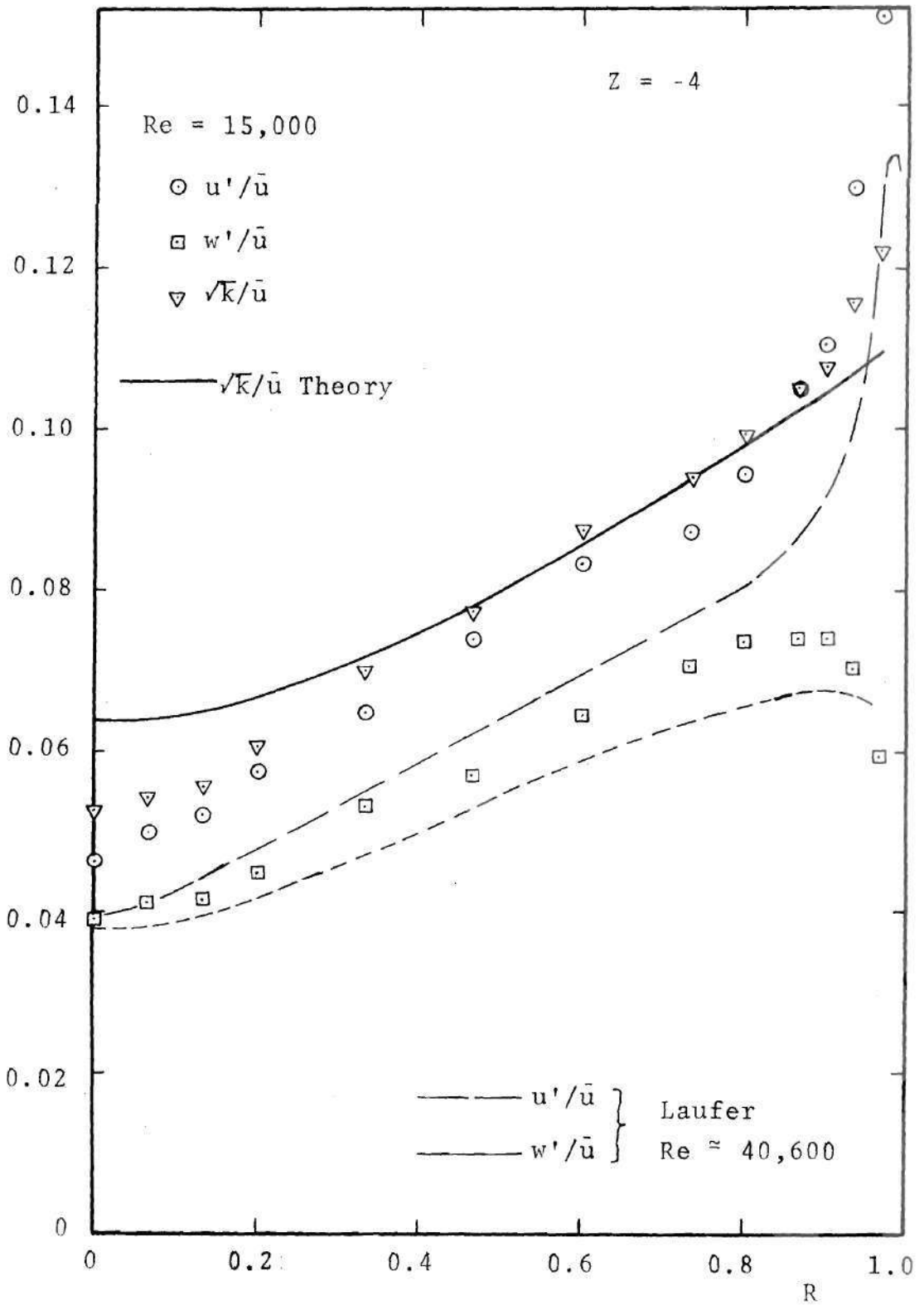

Figure 63. Comparison of Turbulence Fluctuations

developed pipe flow. A two-fold comparison is intended in this figure. First, consider a comparison of the present experimental data with the data of Laufer. Although Laufer did not give results of Re = 15,000, it is possible to extrapolate his measurements to this value of Re in the following approximate manner. When the turbulence velocities u', v' and w' reported in Ref. [85] are nondimensionalized by the friction velocity u_* and compared for two Reynolds numbers (40,600 and 418,500), they are seen to be independent of Re in the core region, $R \lesssim 0.8$. If the Blasius formula [56] relating the pressure gradient and Reynolds number in a fully developed turbulent pipe flow and the fact that pressure gradient varies as u_*^2 are combined, the experimental values may be extrapolated to Re = 15,000 with the expectation of achieving reasonably accurate results. The outcome of this exercise is that the turbulence velocity fluctuations as nondimensionalized by $\bar{u}$, at Re = 15,000 should be approximately 13% higher than the corresponding values at Re = 40,600. These extrapolated results agree very well with the present measurements at Z = -4. This comparison, although somewhat indirect, indicates that the inlet length of the pipe proximal to the stenosis, coupled with the turbulence generating devices at the inlet described earlier, are sufficient to allow the achievement of a fully developed flow. The comparison also enhances the confidence in the measurement of u' and w' using the LDA system.

The second phase of the comparison is between the theoretical and experimental values of k. The predicted value is seen to be a gross representation of the true (experimental) value. The constants in the k-ε model equation were changed systematically to explore the possibility of improving the prediction of the fully developed values. The attempts were not successful, and it was elected to employ the constants recommended in the literature.

Figures 64-75 record the turbulence intensities measured experimentally for Z locations between -2 and 11, for model M4 and Re = 15,000. The theoretically predicted k-profiles are also plotted for comparison.

Figure 64 presents the experimental results and a comparison with the computation at Z = -2, the station just at the inlet of the contraction. The agreement is qualitatively good, although the predicted values of k are somewhat higher than experiment in the "core" region but lower than the measurements near the wall. It will be recalled that this was also the case for the fully developed pipe flow comparison in section 5.1. Figure 65 gives the experimentally obtained results for w' at Z = -1.5 and +1.5. Due to the difficulty involved in applying refraction corrections at these stations, the u'-component was not measured. The results indicate the strongly turbulent nature of the flow distal to the stenosis. In most regions of the field the w'component is increased by an order of magnitude as a result

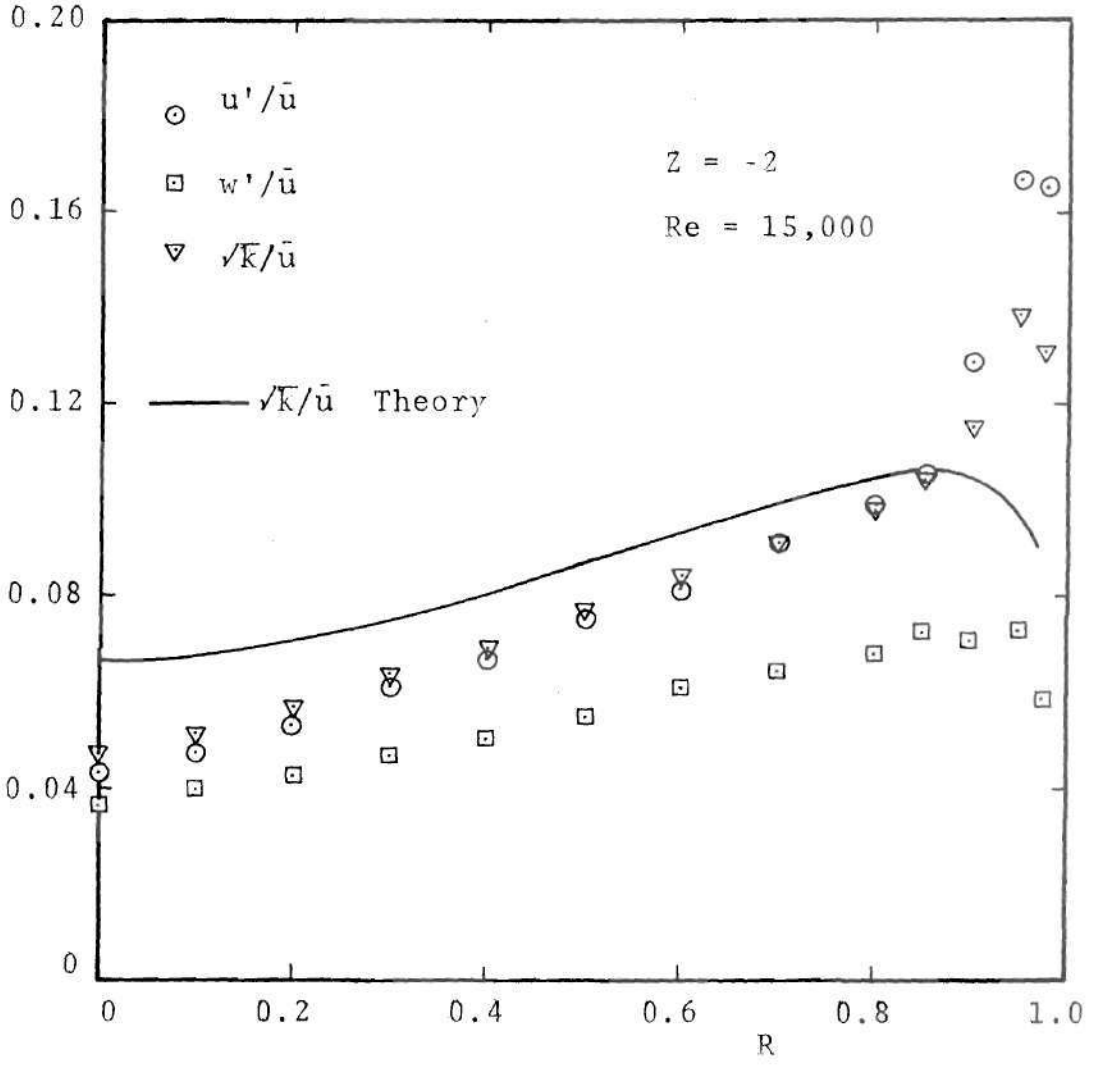

Figure 64. Turbulence Fluctuations, Model M4, Re = 15,000, Z = -2

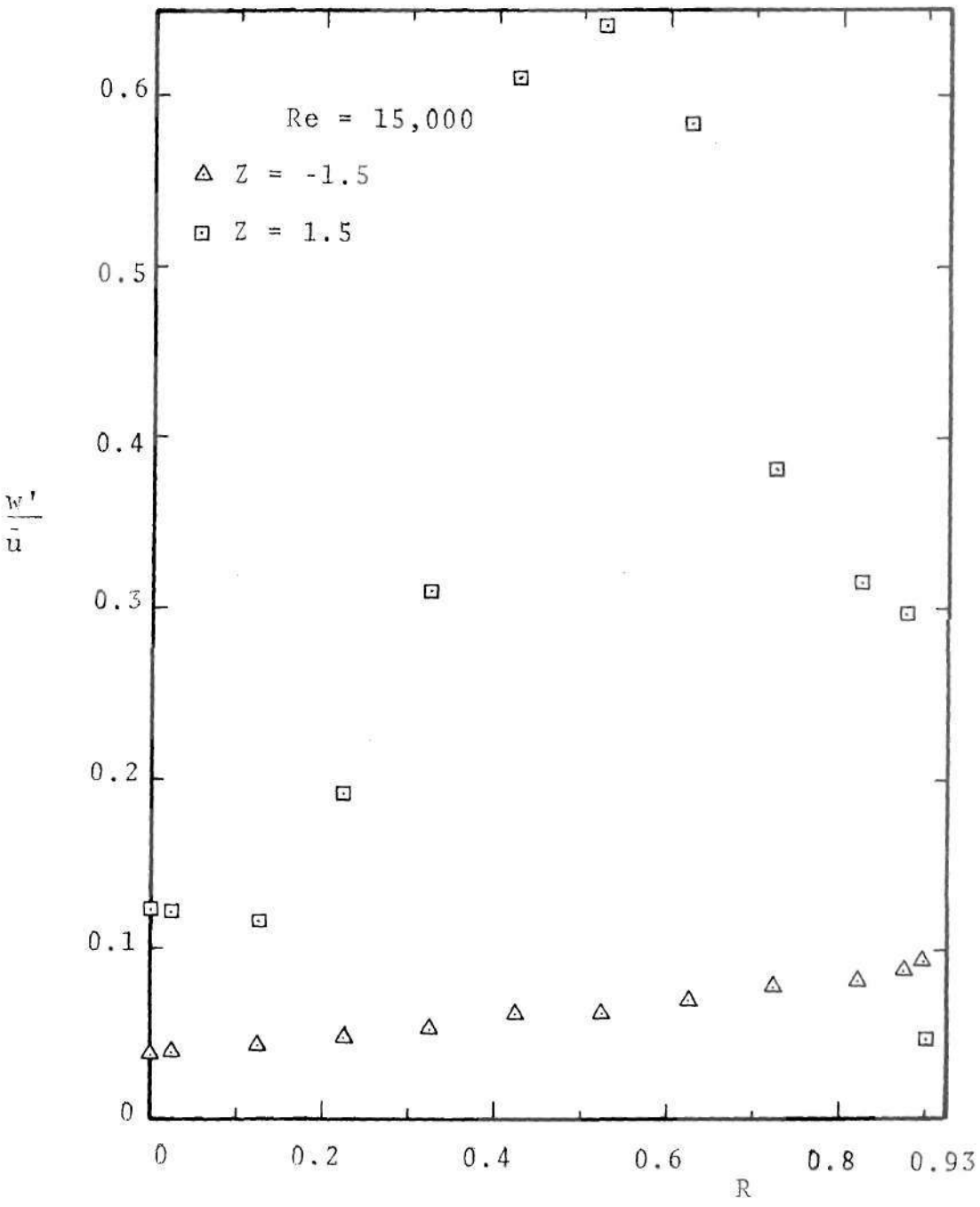

Figure 65. Turbulence Fluctuation w', Model M4, Re = 15,000, Z = -1.5 and +1.5

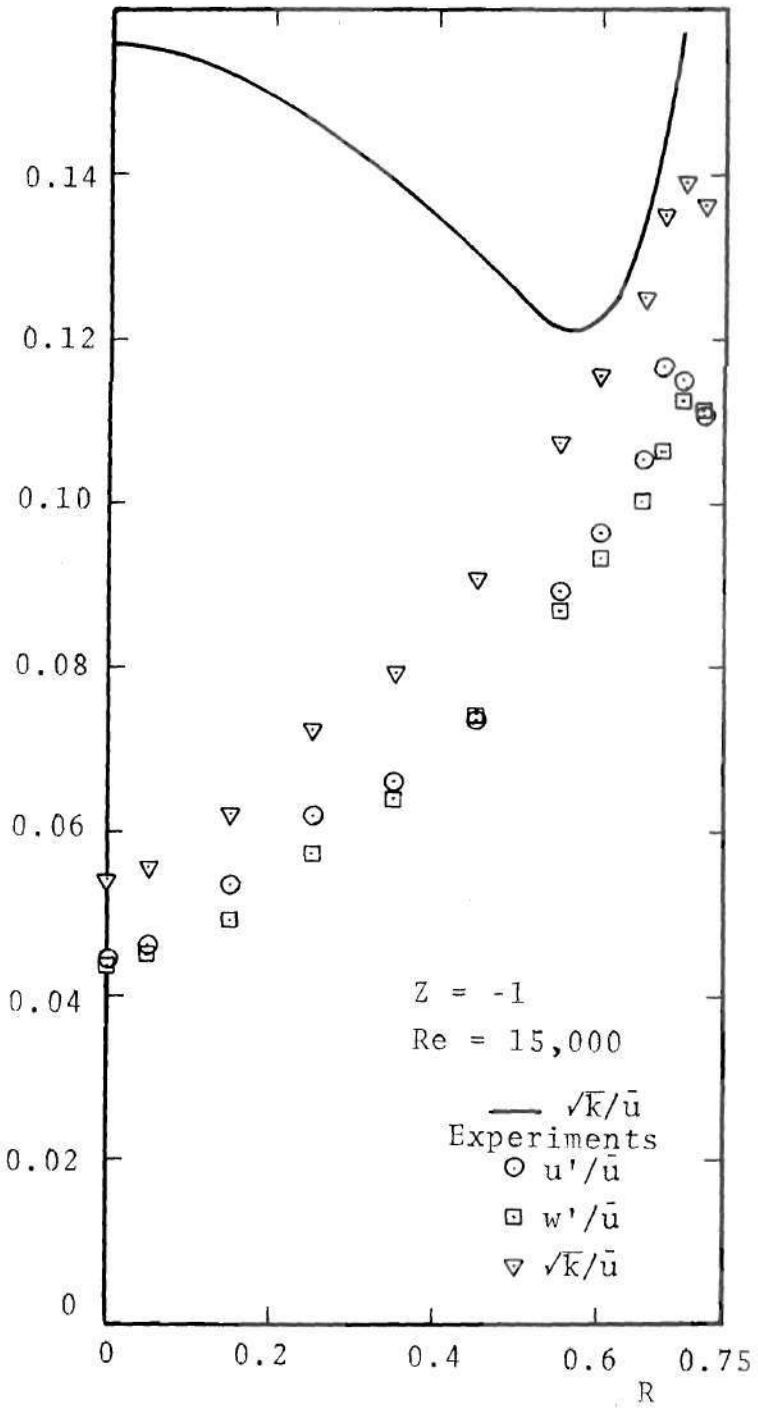

Figure 66. Turbulence Fluctuations, Model M4, Re = 15,000, Z = -1

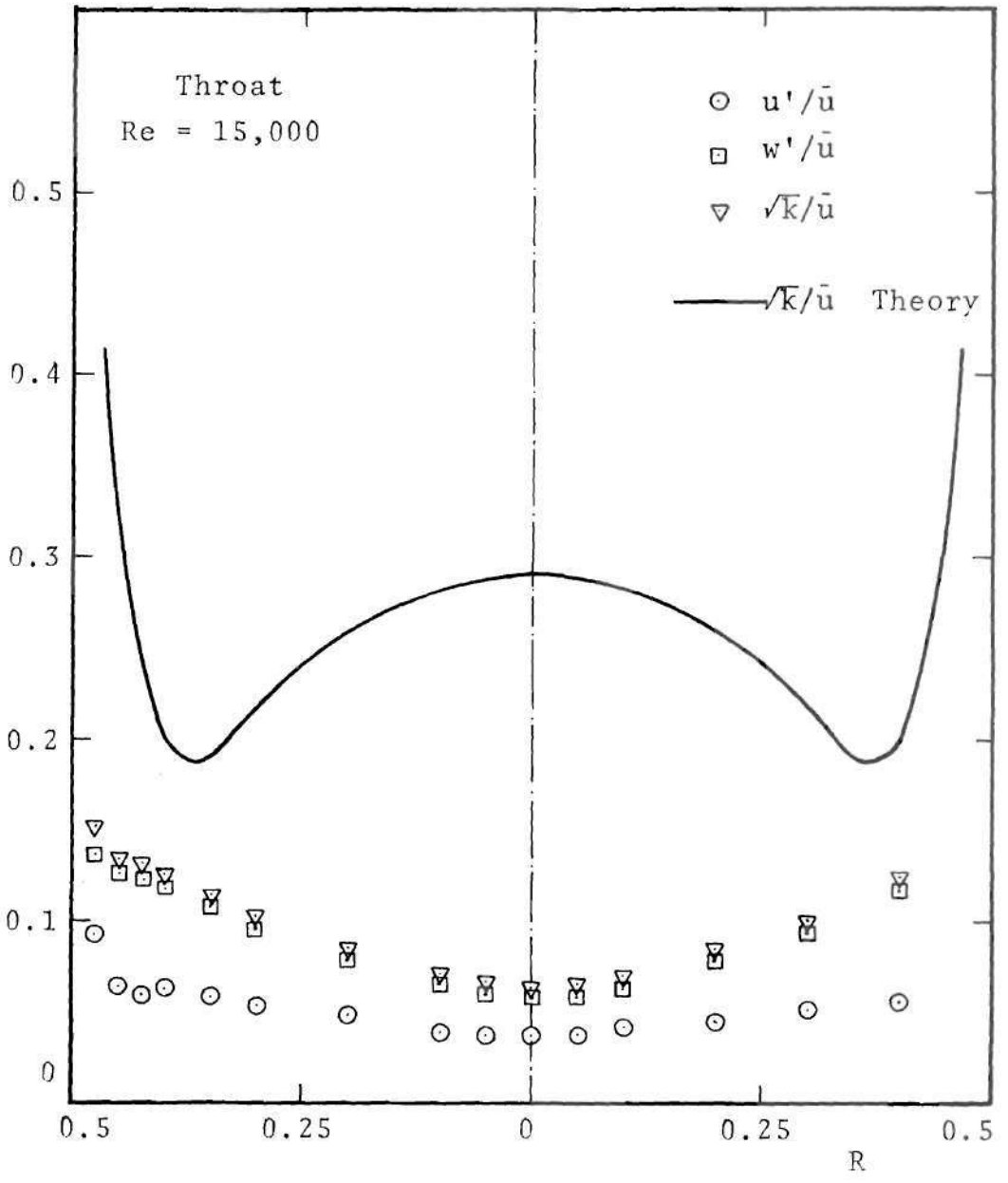

Figure 67. Turbulence Fluctuations at Throat, Model M4, Re = 15,000

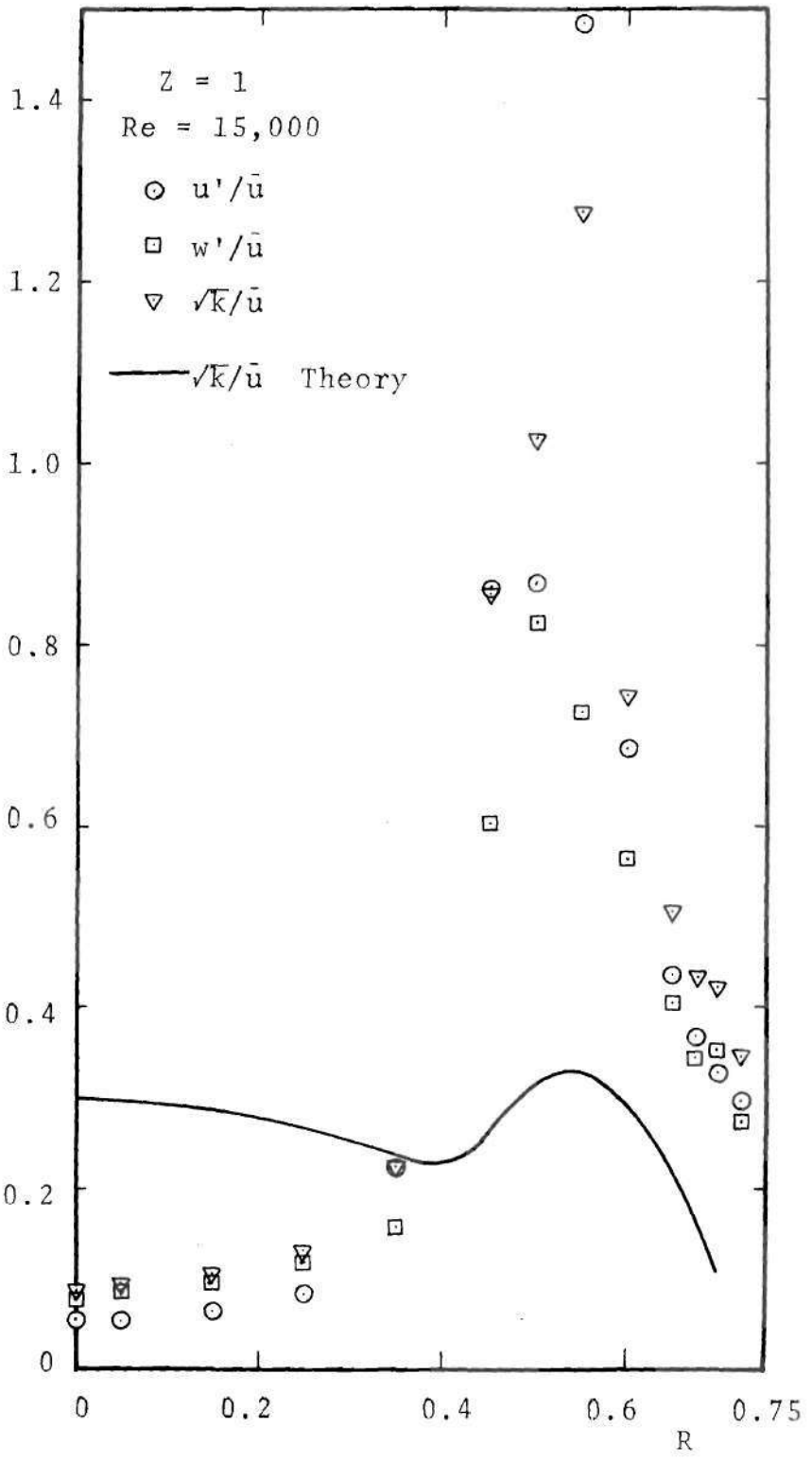

Figure 68. Turbulence Fluctuations, Model M4, Re = 15,000, Z = 1

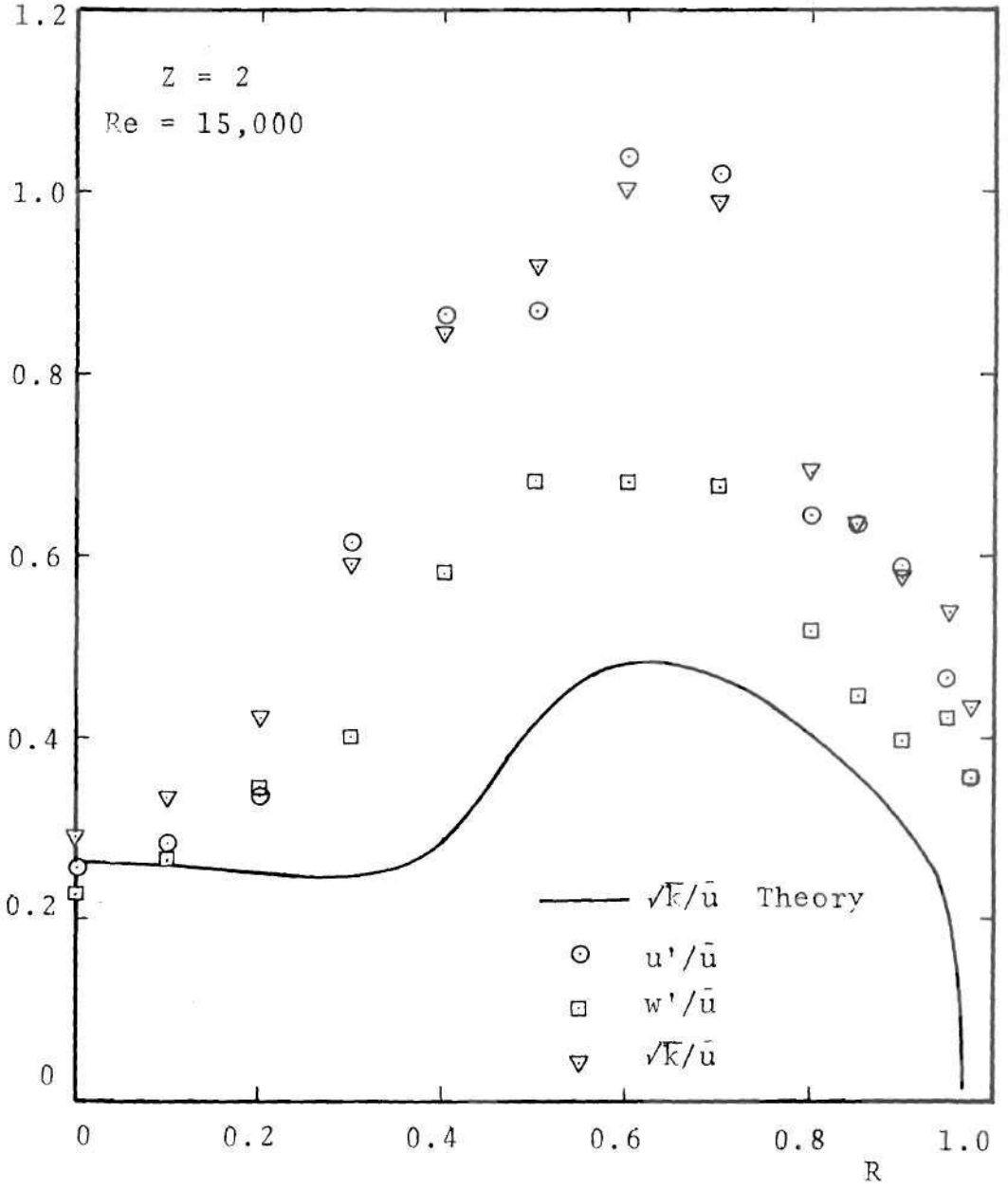

Figure 69. Turbulence Fluctuations, Model M4, Re = 15,000, Z = 2

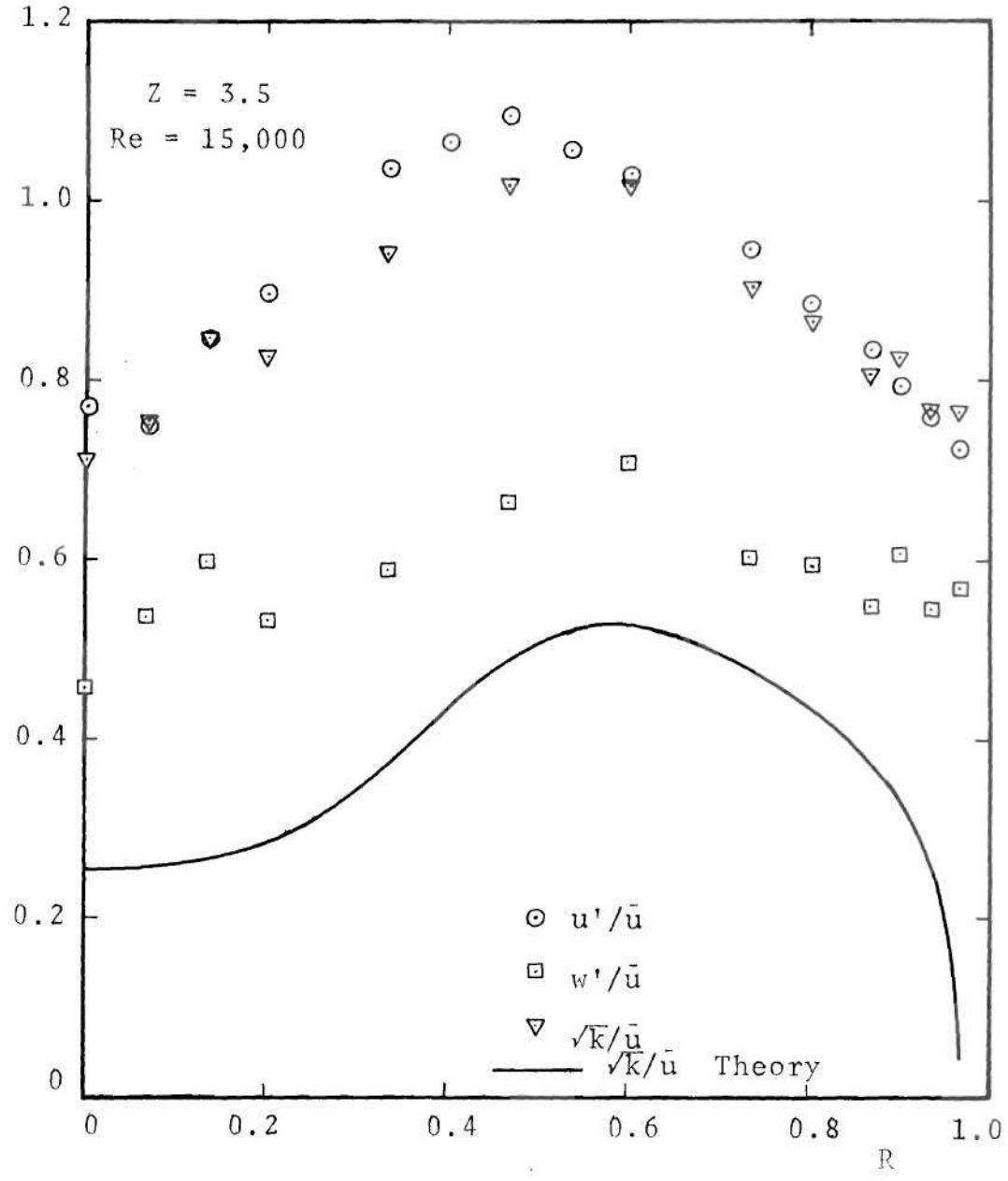

Figure 70. Turbulence Fluctuations, Model M4, Re = 15,000, Z = 3.5

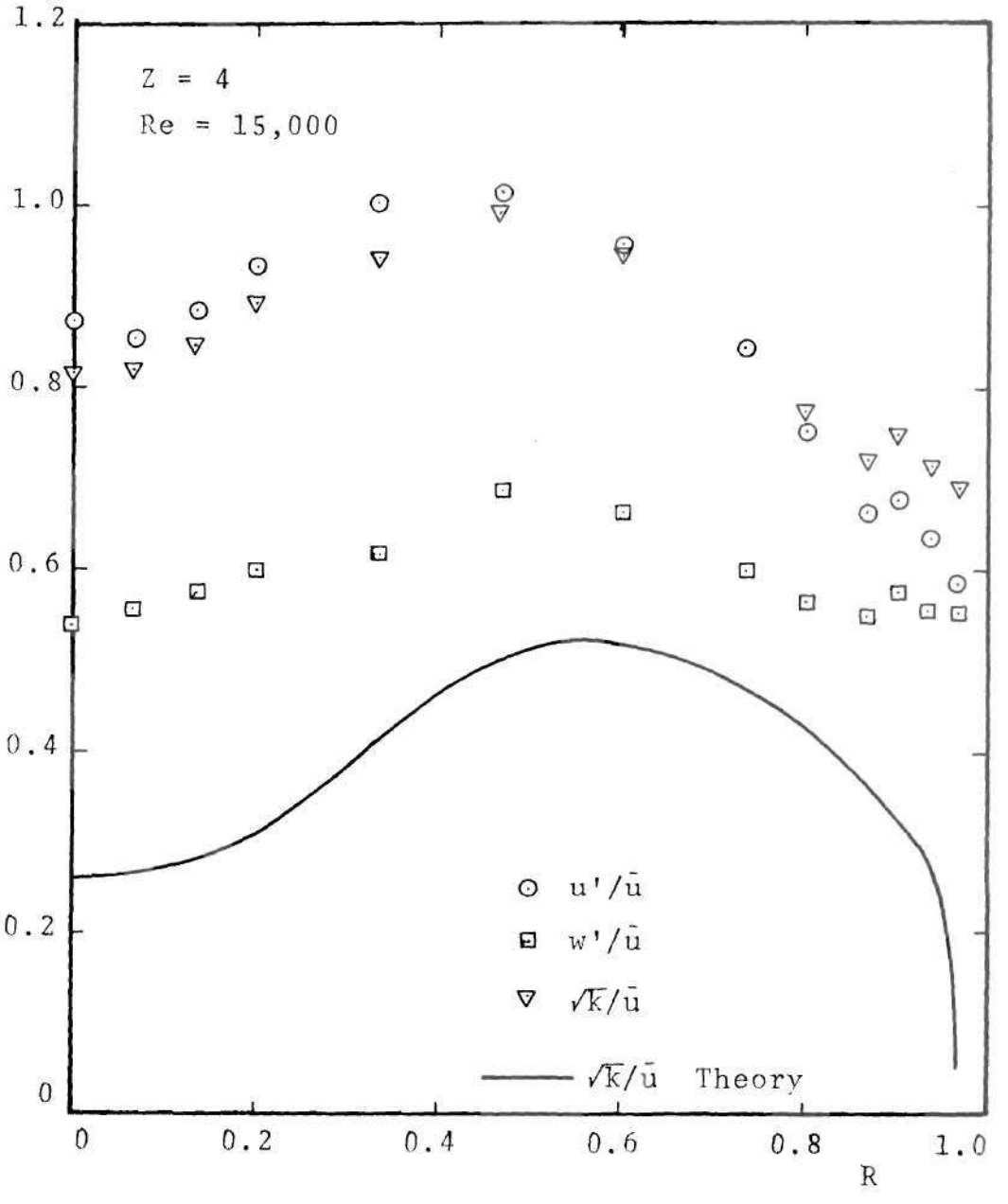

Figure 71. Turbulence Fluctuations, Model M4, Re = 15,000, Z = 4

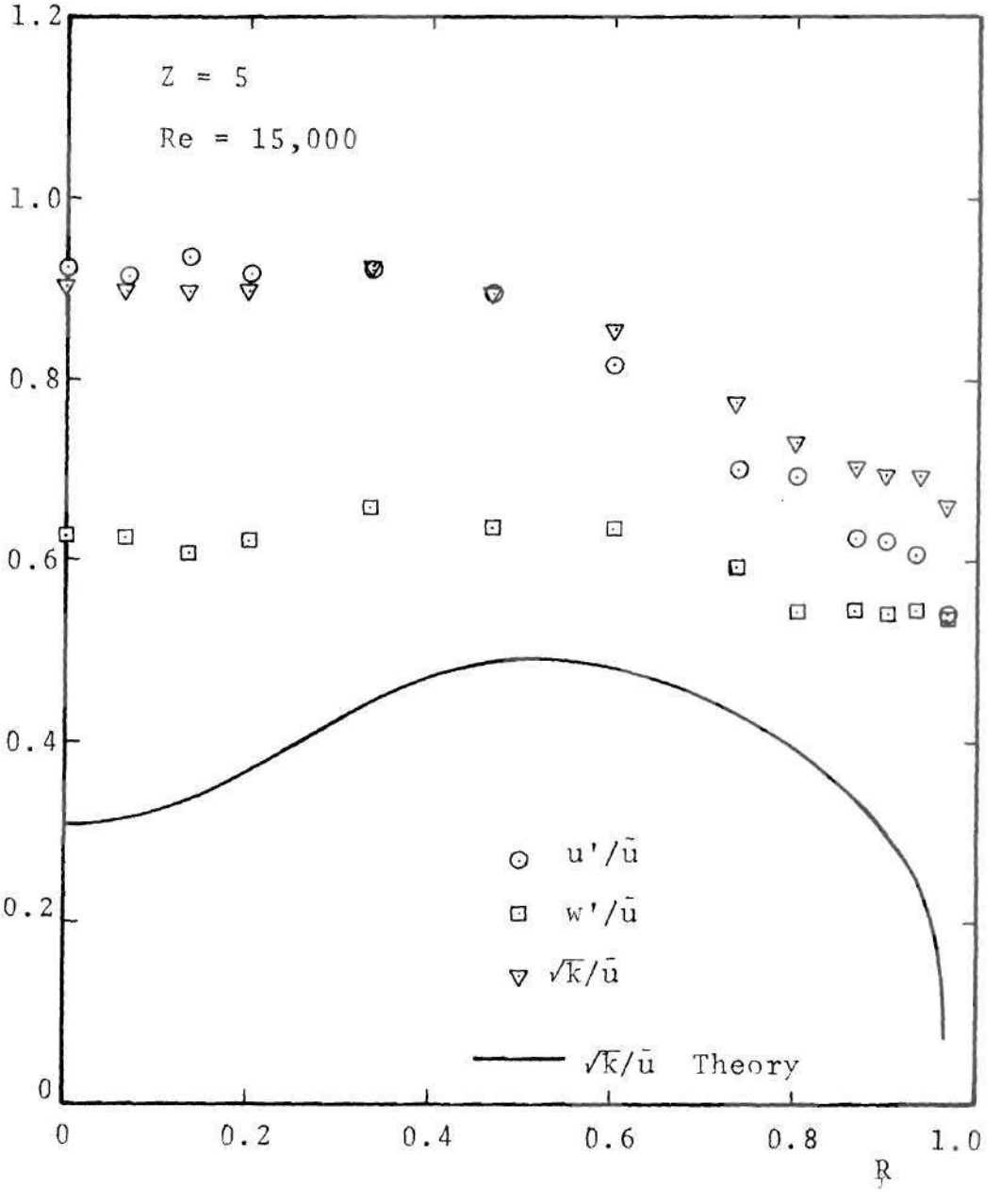

Figure 72. Turbulence Fluctuations, Model M4, Re = 15,000, Z = 5

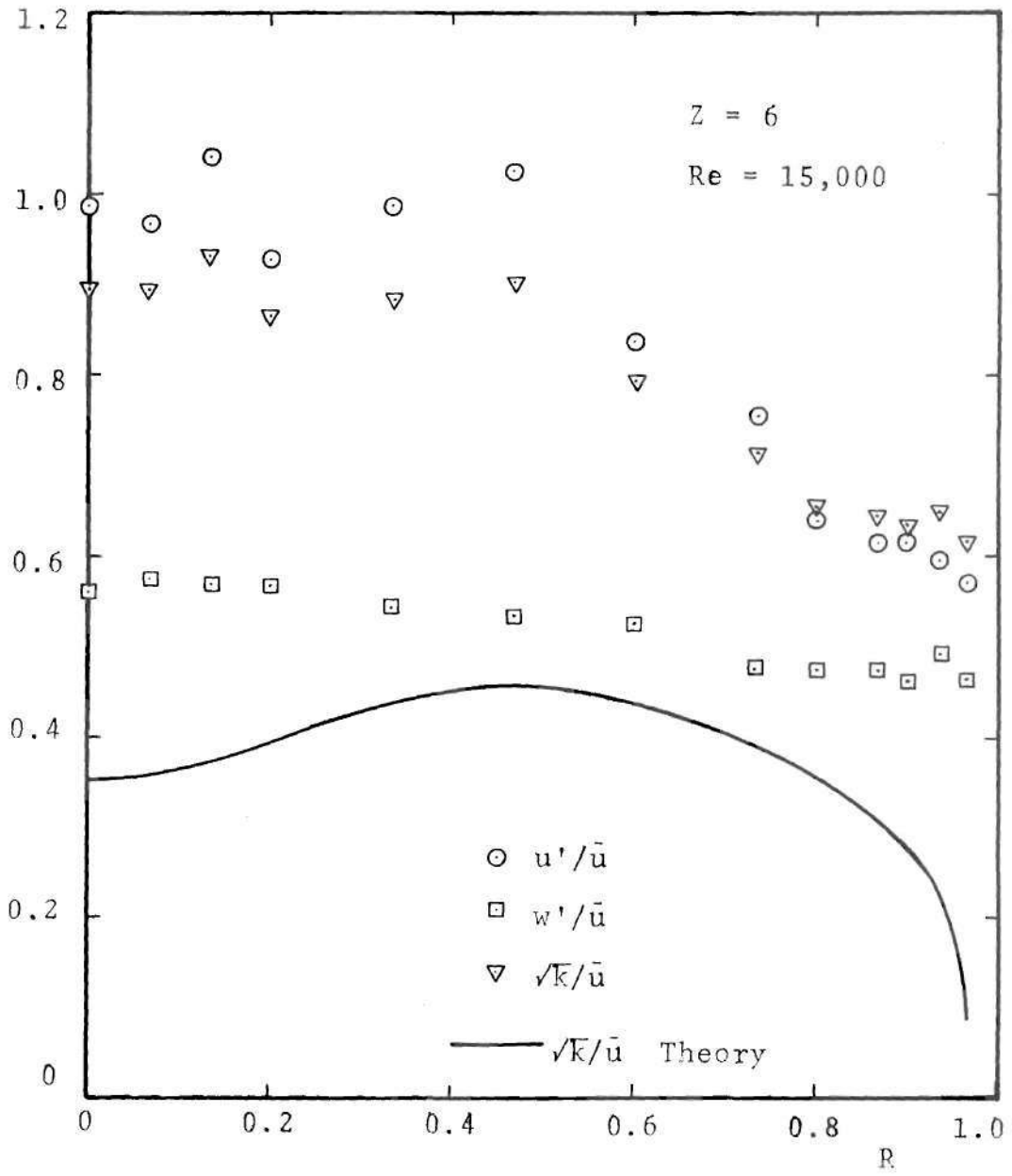

Figure 73. Turbulence Fluctuations, Model M4, Re = 15,000, Z = 6

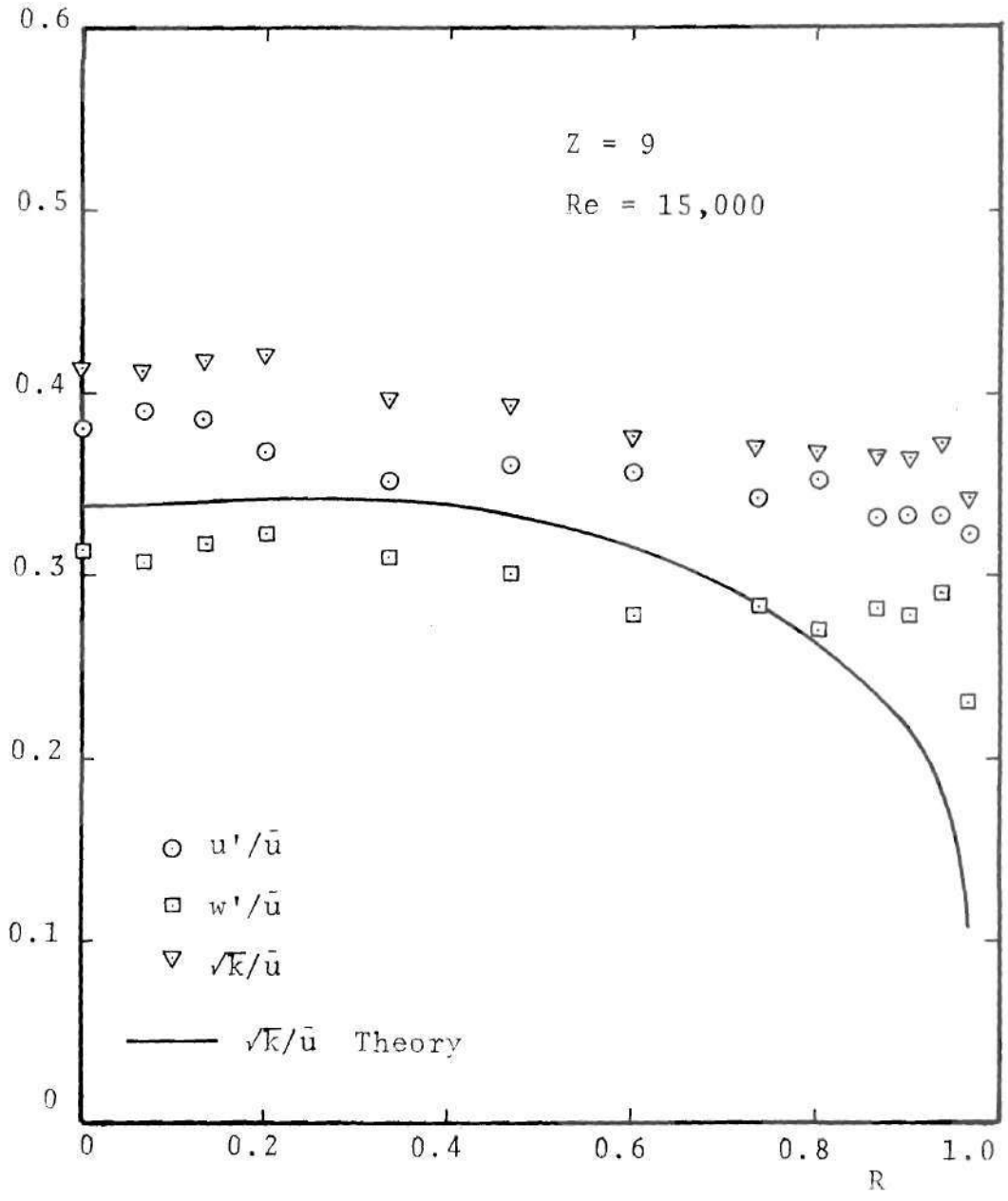

Figure 74. Turbulence Fluctuations, Model M4, Re = 15,000, Z = 9

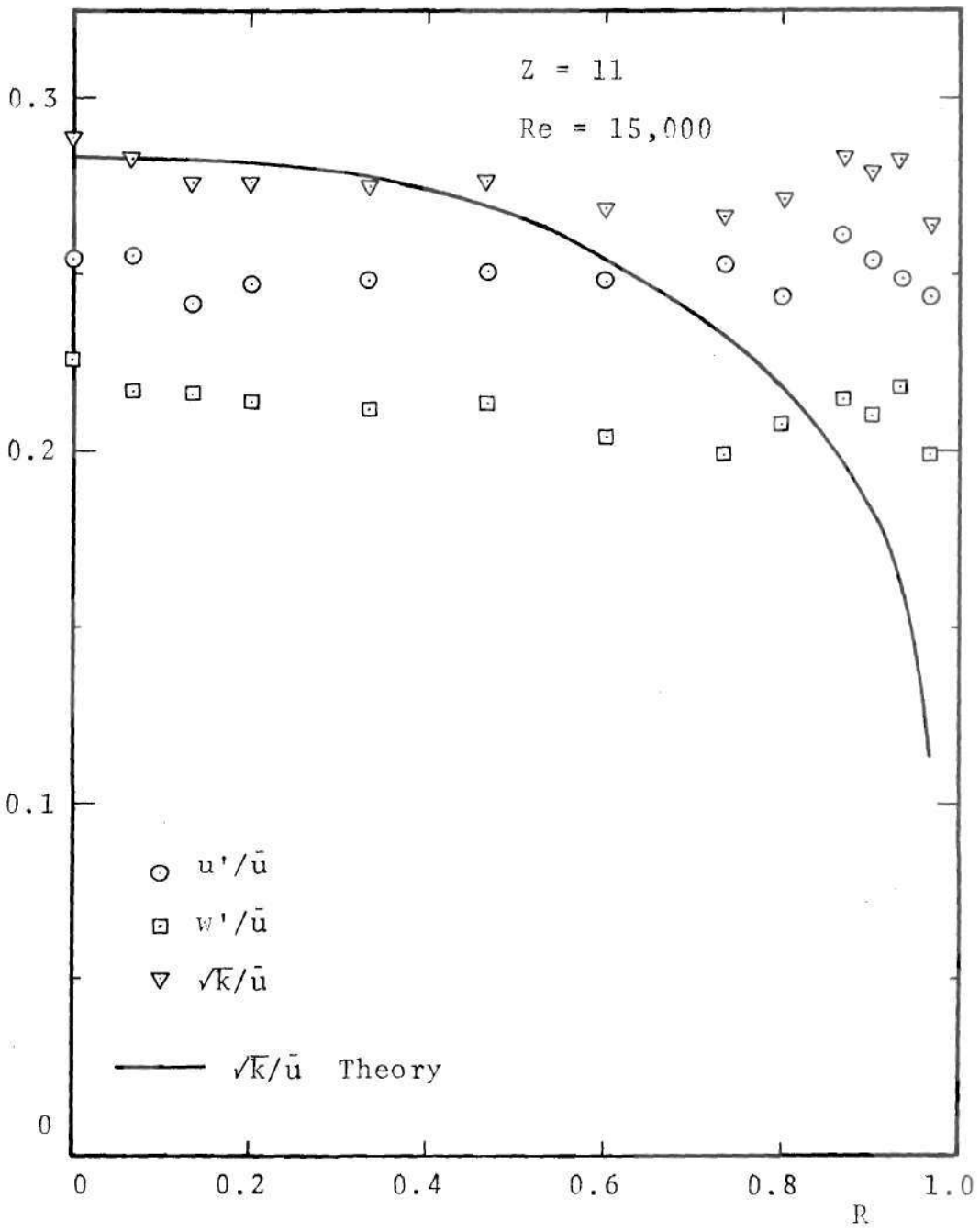

Figure 75. Turbulence Fluctuations, Model M4, Re = 15,000, Z = 11

of passing through the contraction. The u', w' and k' profiles at Z = -1 and 0 are shown in Figures 66 and 67 and the theoretical k values are also indicated for comparison. The theory is seen to overpredict especially in the core region. It also indicates a minimum in the k profile away from the axis, whereas experiments show the minimum to be at the axis.

The longitudinal fluctuation component u' is seen to attenuate slightly in the accelerating flow in the convergent nozzle whereas the azimuthal component w' is amplified. The rapid distortion theory by Batchelor and Proudman, and by Ribner and Tucker (see reference [86]) assumes homogeneous turbulence and suggests a 54% decrease in u' and 74% increase in w' due to the present contraction with 75% area reduction. When the results provided by the linear theory are applied to the present experimental data, the estimations give better results close to the wall and overpredict both the attenuation of u' and the amplification of w' on the axis. Due to the contracted flow, the w' component is seen to be higher than u' at the throat.

Other interesting events take place in the flow distal to the convergent section. There is a sharp increase in the u' and w' components in the divergent section due to the increased production in the shear layer. At Z = 1 (Figure 68), w' is still higher than u' near the axis, whereas u' is about 80% higher than w' in the shear layer where most

of the kinetic energy is concentrated. The reason that the theoretical model underpredicts turbulence kinetic energy was already discussed. The picture is modified at Z = 2 (Figure 69) where u' is higher than w' almost everywhere. The peaks are seen to have moved slightly away from the axis due to the flow expansion and the energy is distributed over a wider area in the cross section. The peak values decrease. The kinetic energy siphoned into the random turbulence motion from the mean flow does so mainly into the longitudinal component and then it is redistributed into the other two components of velocity fluctuations. This results in the u' peak being higher than that of w'.

As one moves to Z = 3.5 (Figure 70) there is a slight increase in the peak values of u' and w'. The values at the axis and near the wall are also increased. The predicted k profile has the general shape of the experimental data but is still far below. At the next station Z = 4, Figure 71, the fluctuations at the axis are seen to be higher than the ones near the axis. The peaks are seen to be reduced. This process continues at the next two stations Z = 5 and 6 (Figures 72 and 73); and at Z = 9 and 11 (Figures 74 and 75) the profiles of the fluctuations are seen to be almost constant in the entire cross-section. Only at these last two stations are the predictions close to the experimental data. The peaks in the fluctuations are seen to migrate toward the axis in the region distal to the stenosis. The

turbulence kinetic energy is converted downstream and diffused radially. This increases the level at the centerline and leads to an almost uniform profile at Z = 11. This, however, cannot be sustained due to low levels of production of k close to the axis and hence the distribution must return to the fully developed state, with higher levels of fluctuations toward the wall.

The theoretical predictions clearly fall short of describing this complex phenomenon, though they have the general features described above. First of all, the wall boundary conditions need improvement. They have been based on the law of the wall. An explicit relation between k and the local shear stress is assumed in the form of equation (21) or (23) which underestimates the value of k in the recirculating region. The theory predicts an amplification of k in the converging section and this is seen to be true experimentally and is also given by the linear theory [86] referred to earlier. However, the predicted values are much higher than those realized experimentally, especially close to the axis. This is due to underestimating the destruction terms in the transport equation for k. The predicted values of k show a minimum away from the axis, which is not the case with the experimental data.

In the decelerating flow, the position of the peak is predicted accurately at Z = 1.0, 2.0 and 3.5 in Figures 68-70, though its shift toward the axis is not sufficiently

rapid in the latter sections (Figures 71-74). The value at the peak is seen to be an underprediction. The reason for this, as mentioned earlier, is due to a thinner and shorter predicted recirculation region. This results in reduced velocity gradients in the shear layer and hence the reduced generation of turbulence kinetic energy. Far downstream, the predicted values are closer to the experimental data (Figures 74 and 75) though the expected profiles are not so flat. The major culprit, one may suspect, is the transport equation for ε; part of the blame may be attributed to the wall boundary conditions, also.

The predicted profiles of k for Model M4 for a Reynolds number of 388,000 are exhibited in Figure 76. They indicate the same features as those for a lower Reynolds number (Figures 63-75). The relative magnitude of turbulence intensity $\sqrt{k}/\bar{u}$, as one may expect is seen to be reduced. The next three figures (77-79) are similar plots for Models M1, M2 and M3 at Re = 15,000. The predictions may be expected to be underestimates in the light of the experience gained. Increase of the severity of the constriction increases the turbulence fluctuations. The profile for k at Z = -2 for a relatively mild stenosis Model M1 (Figure 77) does not show a minimum away from the axis as is the case with Model M2 (Figure 78) or with the profiles at the corresponding points Z = -1 for Models M4 and M3 (Figures 66, 76 and 79). Such a minimum is not suggested by the

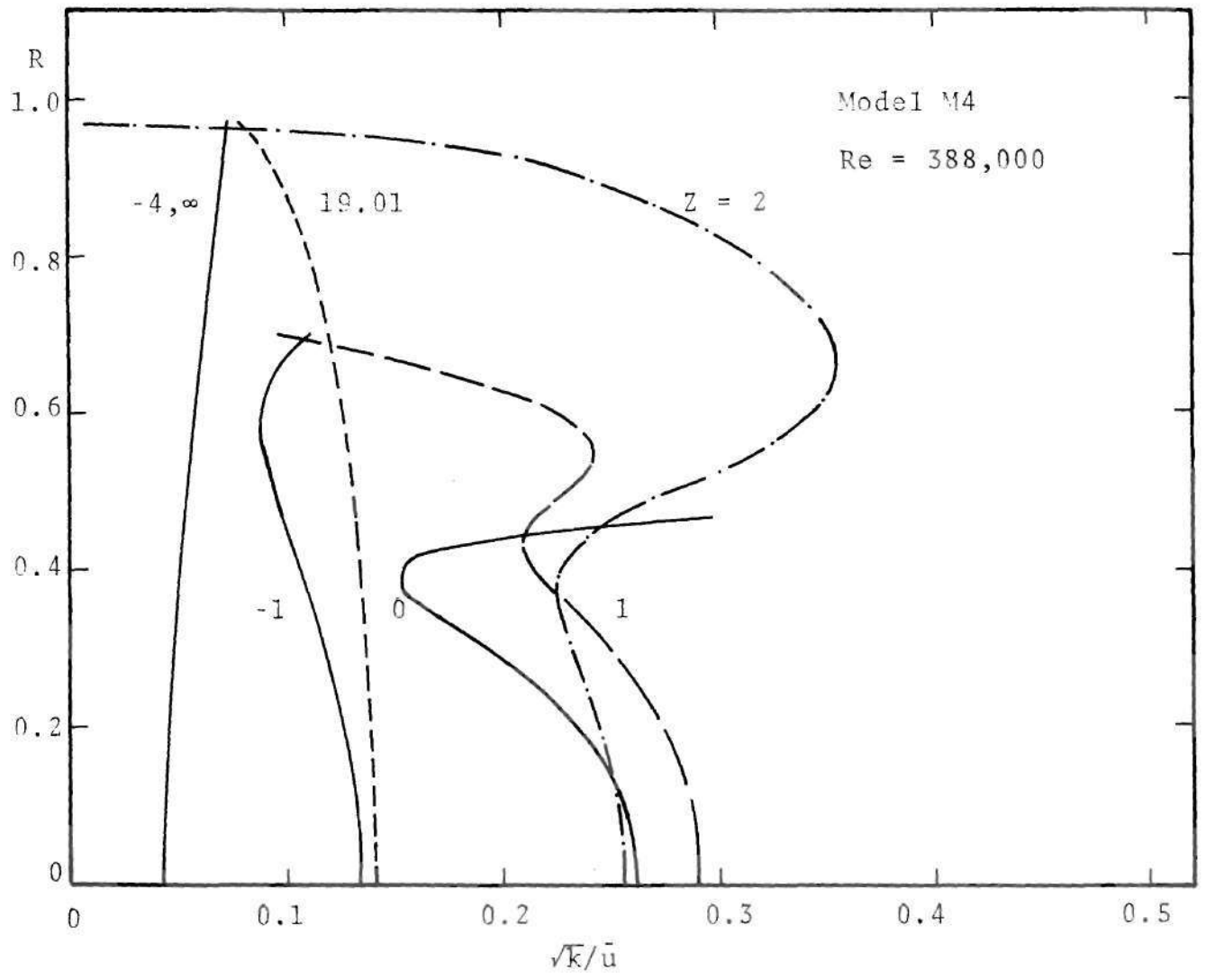

Figure 76. Turbulence Kinetic Energy Profiles, Model M4, Re = 388,000 (Theory)

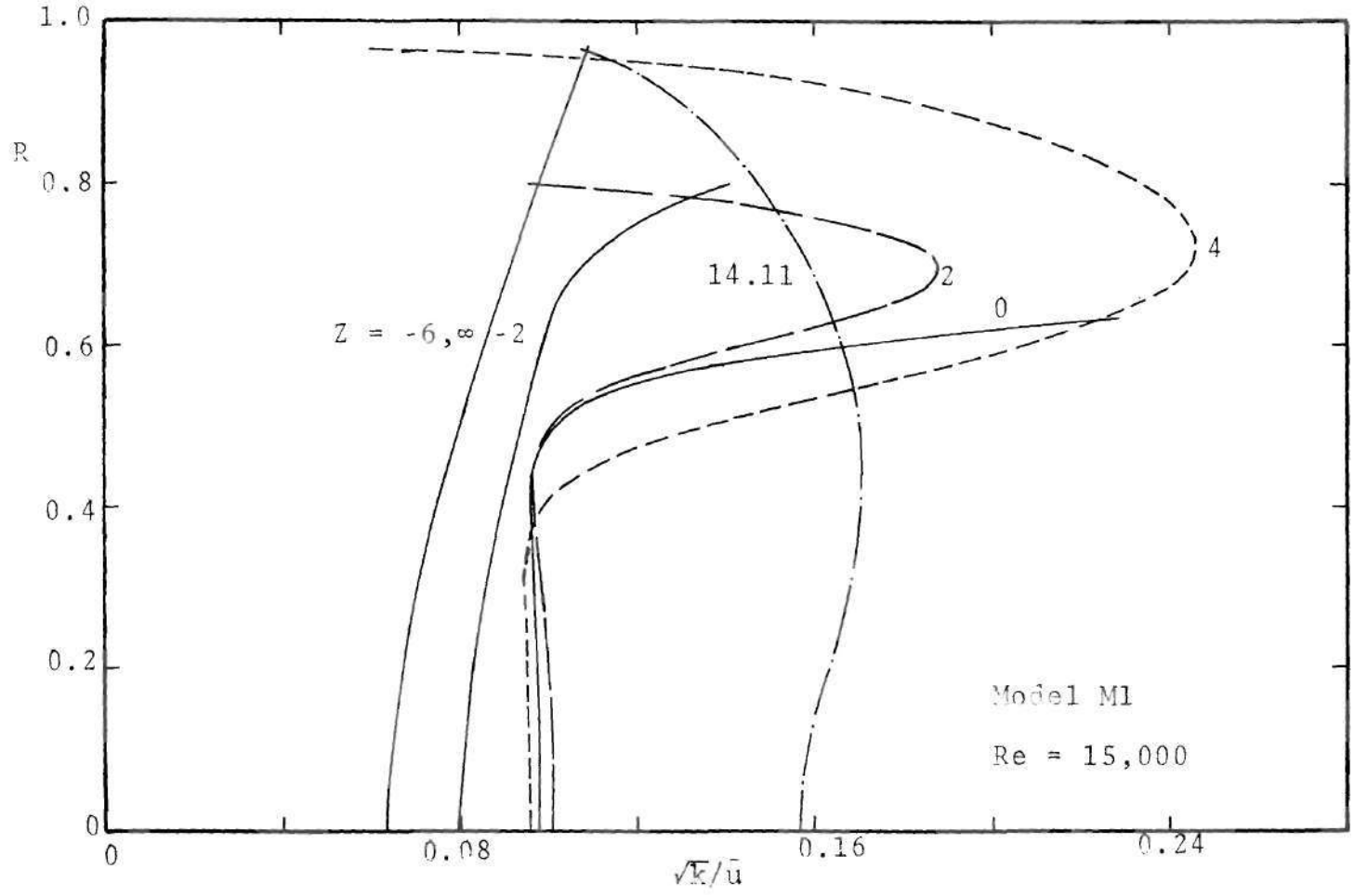

Figure 77. Turbulence Kinetic Energy Profiles, Model M1, Re = 15,000 (Theory)

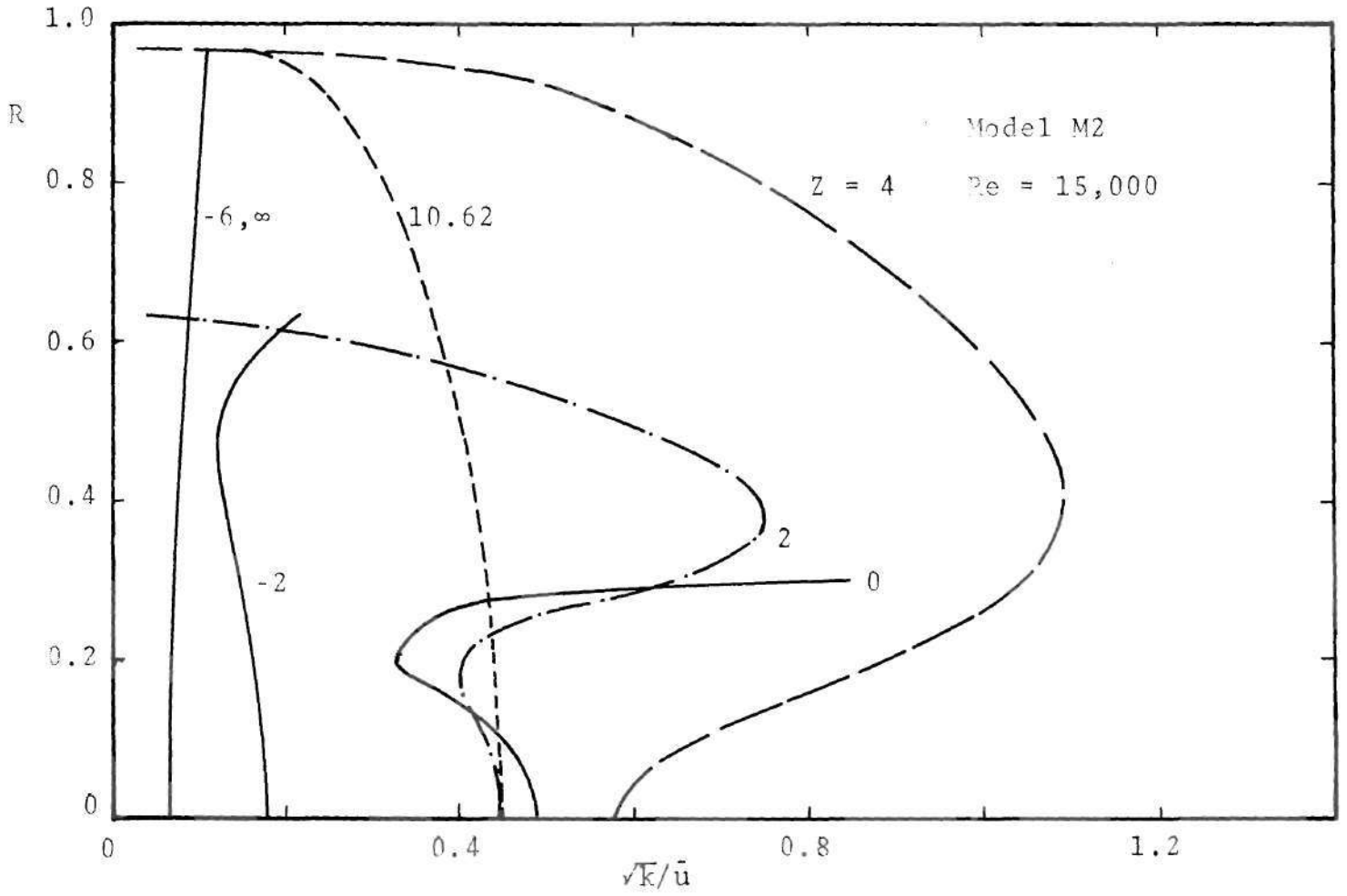

Figure 78. Turbulence Kinetic Energy Profiles, Model M2, Re = 15,000 (Theory)

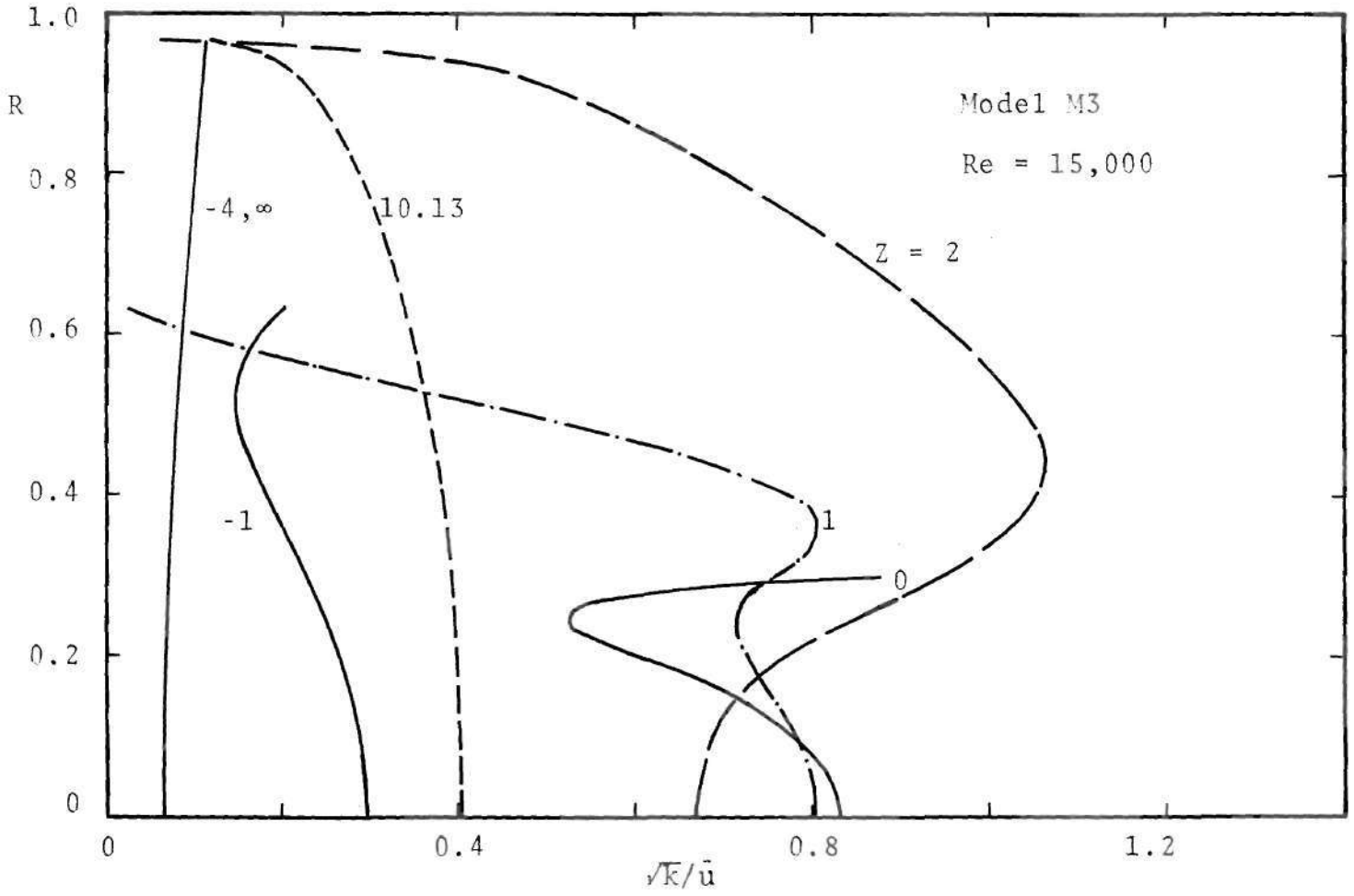

Figure 79. Turbulence Kinetic Energy Profiles, Model M3, Re = 15,000 (Theory)

experimental data for Model M4. Again, in the case of Model M1 the predicted minimum suggested at the throat is very shallow. One might expect better agreement for milder stenoses. As the severity of the stenosis increases, the flow becomes more complex and is more difficult to predict accurately. A comparison between Figures 78 and 79 indicates that the turbulence level inside the stenosis is generally higher in case of the shorter Model M3, whereas the turbulence level distal to the stenosis is slightly higher for the longer Model M2. It may be repeated at this stage that the shorter Model M3 exhibited a higher peak wall shear stress and lower pressure drop as compared to Model M2. All these observations are consistent.

The variation of the turbulence kinetic energy on the centerline is presented in Figures 80-83 for Models M4, M1, M2 and M3, respectively. The experimental data for u', w' and $\sqrt{k}$ are also shown for Model M4 in Figure 80. The comparison between the theory and the experiment has been presented previously. The shortcomings of the theory apparent in this figure serve as cautions in interpreting the subsequent figures (81-83). Predicted values for a higher Reynolds number (30,000 or 388,000) are also plotted in each figure. A longer distance is required for the value of k on the centerline to reach a maximum when the constriction becomes less severe. Increasing the Reynolds number has the same influence, especially when the stenosis is mild.

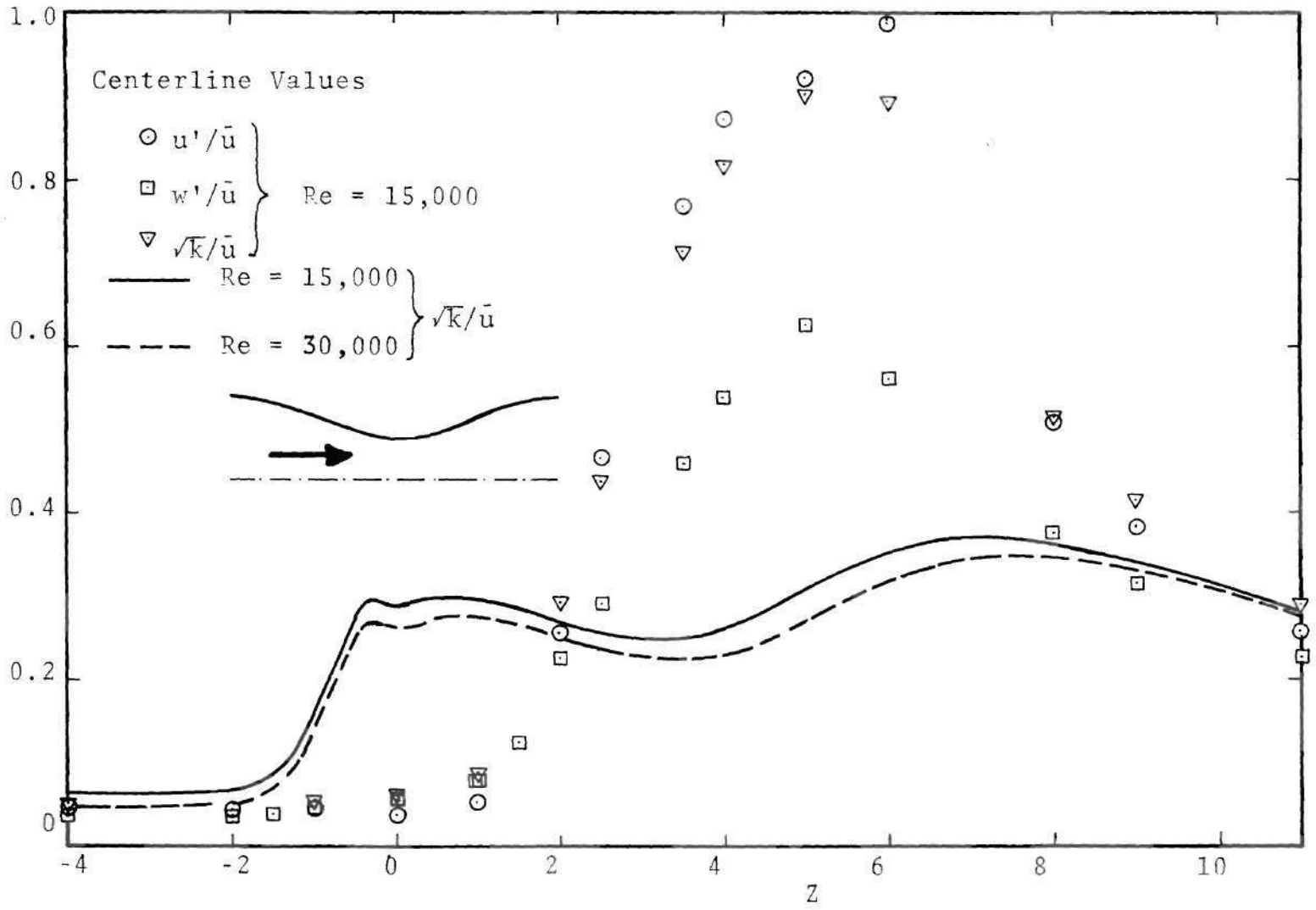

Figure 80. Axial Variation of Centerline Turbulence Fluctuations, Model M4, Re = 15,000 and 30,000

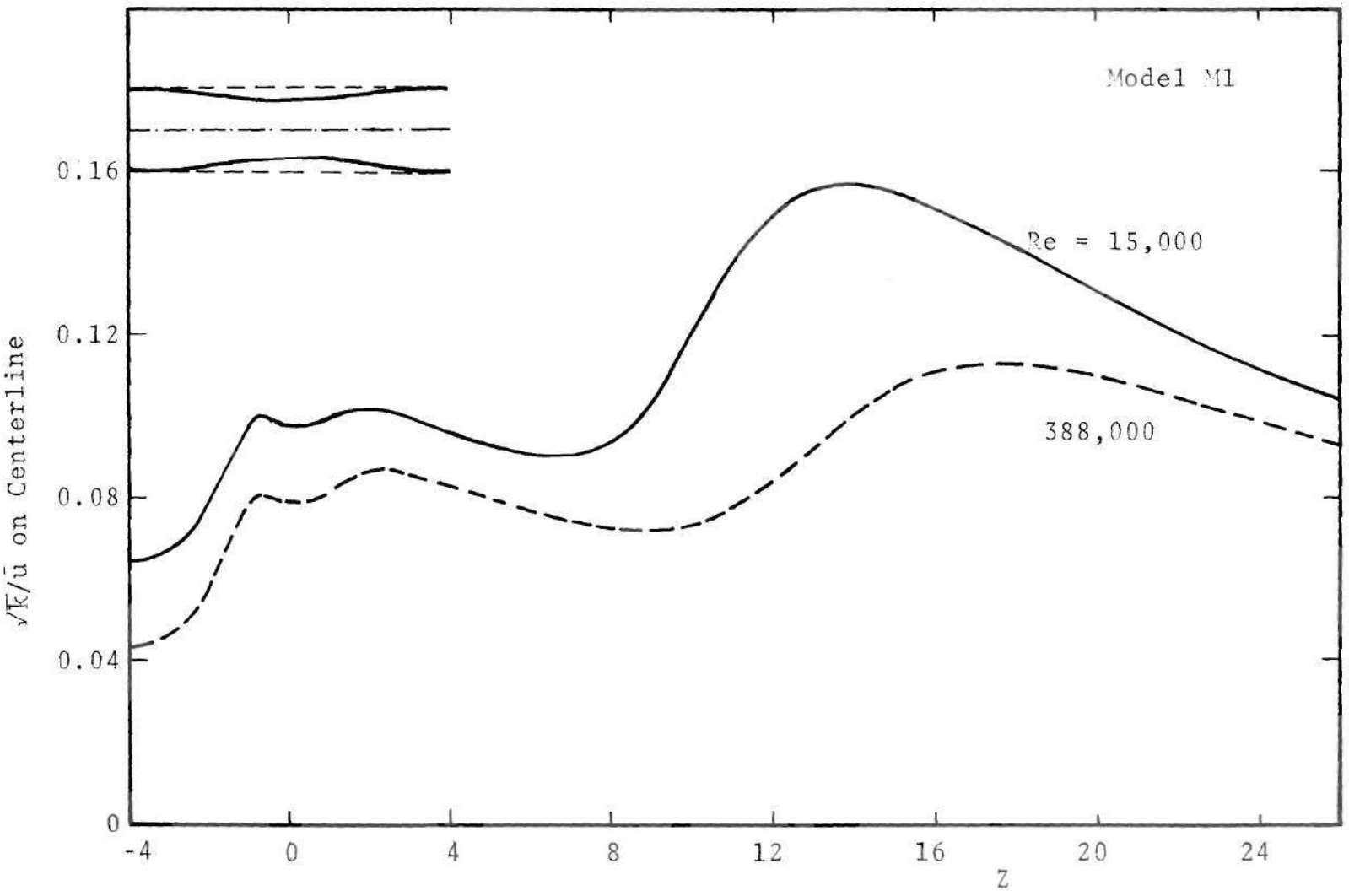

Figure 81. Axial Variation of Centerline Turbulence Kinetic Energy, Model M1, Re = 15,000 and 388,000 (Theory)

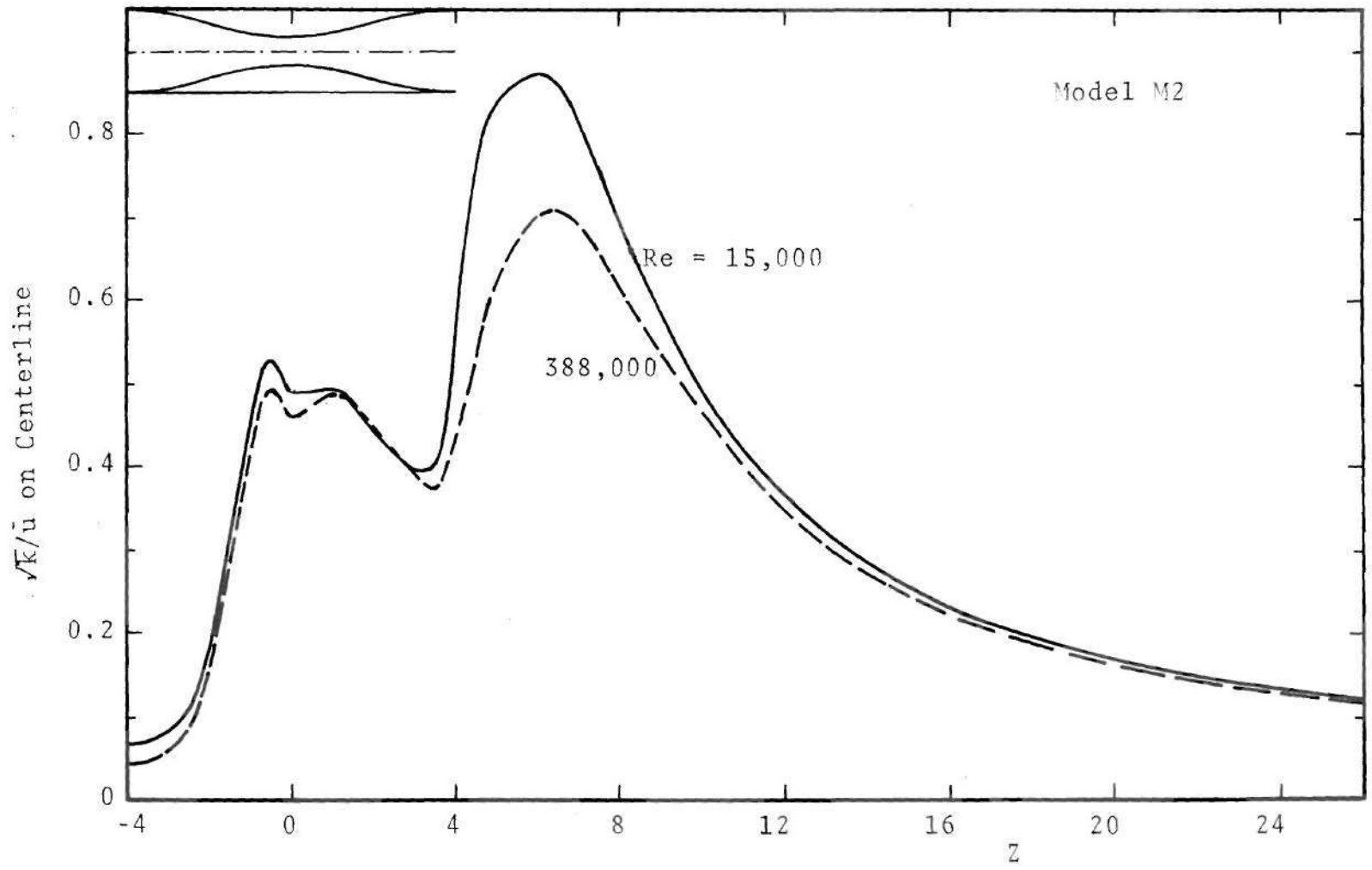

Figure 82. Axial Variation of Centerline Turbulence Kinetic Energy, Model M2, Re = 15,000 and 388,000 (Theory)

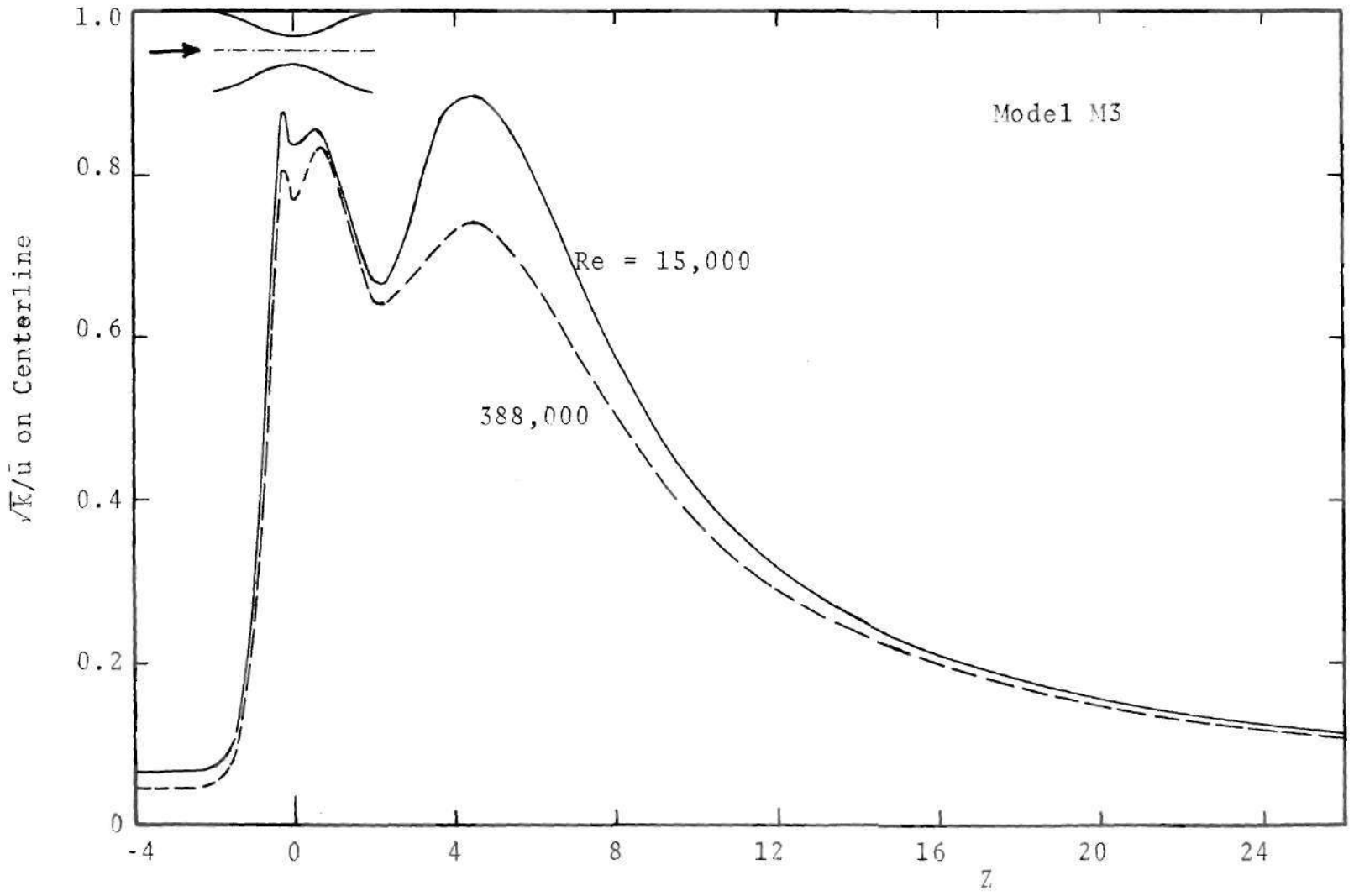

Figure 83. Axial Variation of Centerline Turbulence Kinetic Energy, Model M3, Re = 15,000 and 388,000 (Theory)

5.2.6. Energy Spectra

The energy spectra for u'^2 and w'^2 were measured for Model M4 and a Reynolds number of 15,000. They represent the energy content of the velocity fluctuations as a function of the frequency and hence give a description of the fine structure of the flow. They were obtained by performing a Fourier analysis of the analogue output from the LDA. The details of this procedure [77] were described briefly in section 4.2.2. The maximum frequency retained in the signal after passing it through a low pass filter was 512 Hz, and the frequency resolution selected was one Hertz. Either 50 or 100 data samples of one second duration were ensemble averaged to obtain statistically reliable data.

The energy spectra for u'^2 are displayed in Figures 84-88 for the axial locations Z = -4, 0, 1, 2 and 6. Several radial locations are included in each figure. The energy spectra for w'^2 are presented in Figures 89-94 for locations Z = -4, 0, 1, 1.5, 2 and 6. The integrals of these spectra give the turbulence intensities u'^2 and w'^2. The distribution of these quantities has been described already.

The spectra for u'^2 and w'^2 at Z = -4 (Figures 84 and 89) are the familiar spectra in a fully developed pipe flow. The w'^2 spectra close to the axis have the peak off-axis. There is no significant change in the spectral shapes as one moves radially outwards; the total energy content is seen to increase. The Doppler ambiguity and the noise in the system

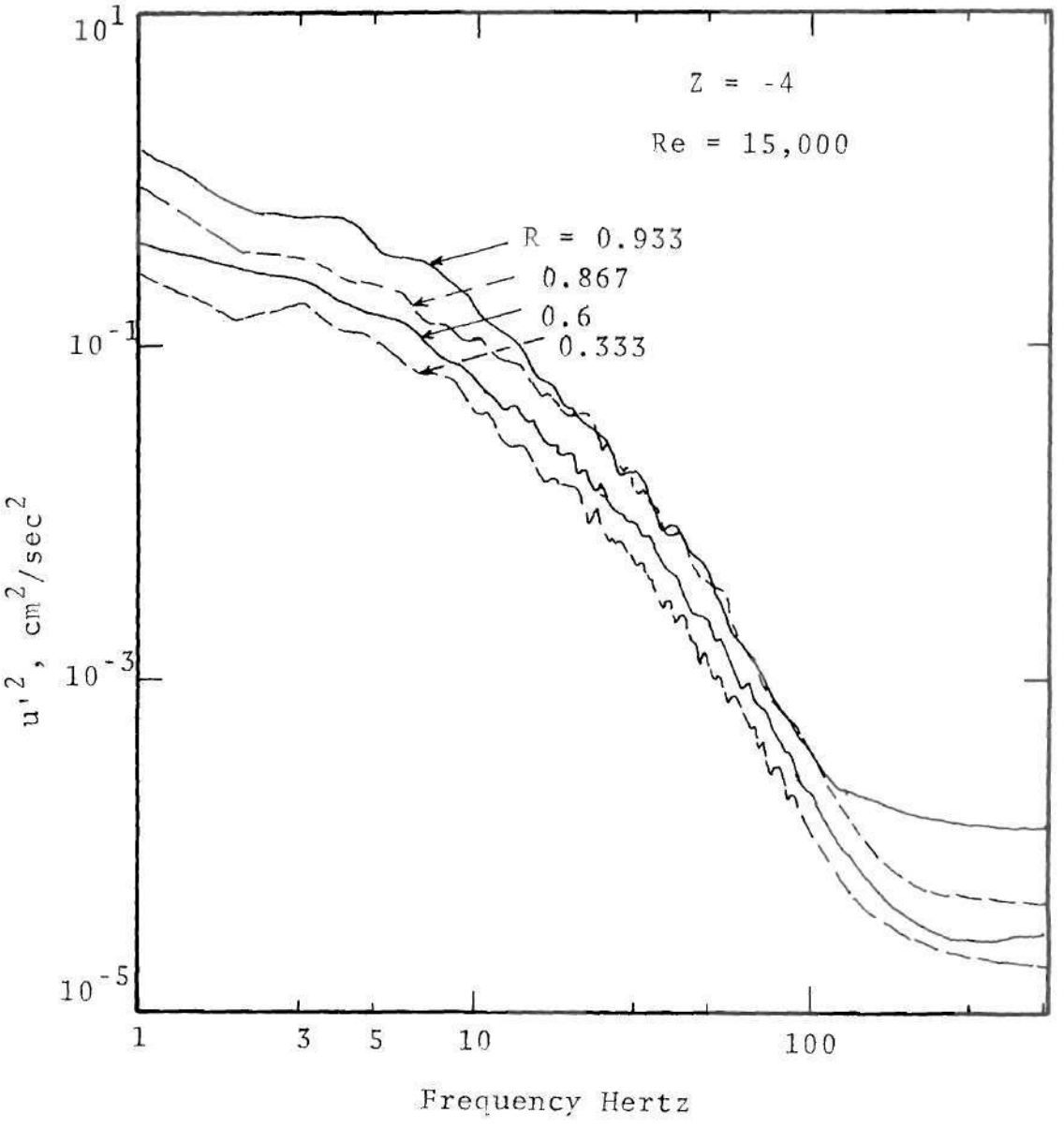

Figure 84. Energy Spectra for u'^2, Model M4, Re = 15,000, Z = -4

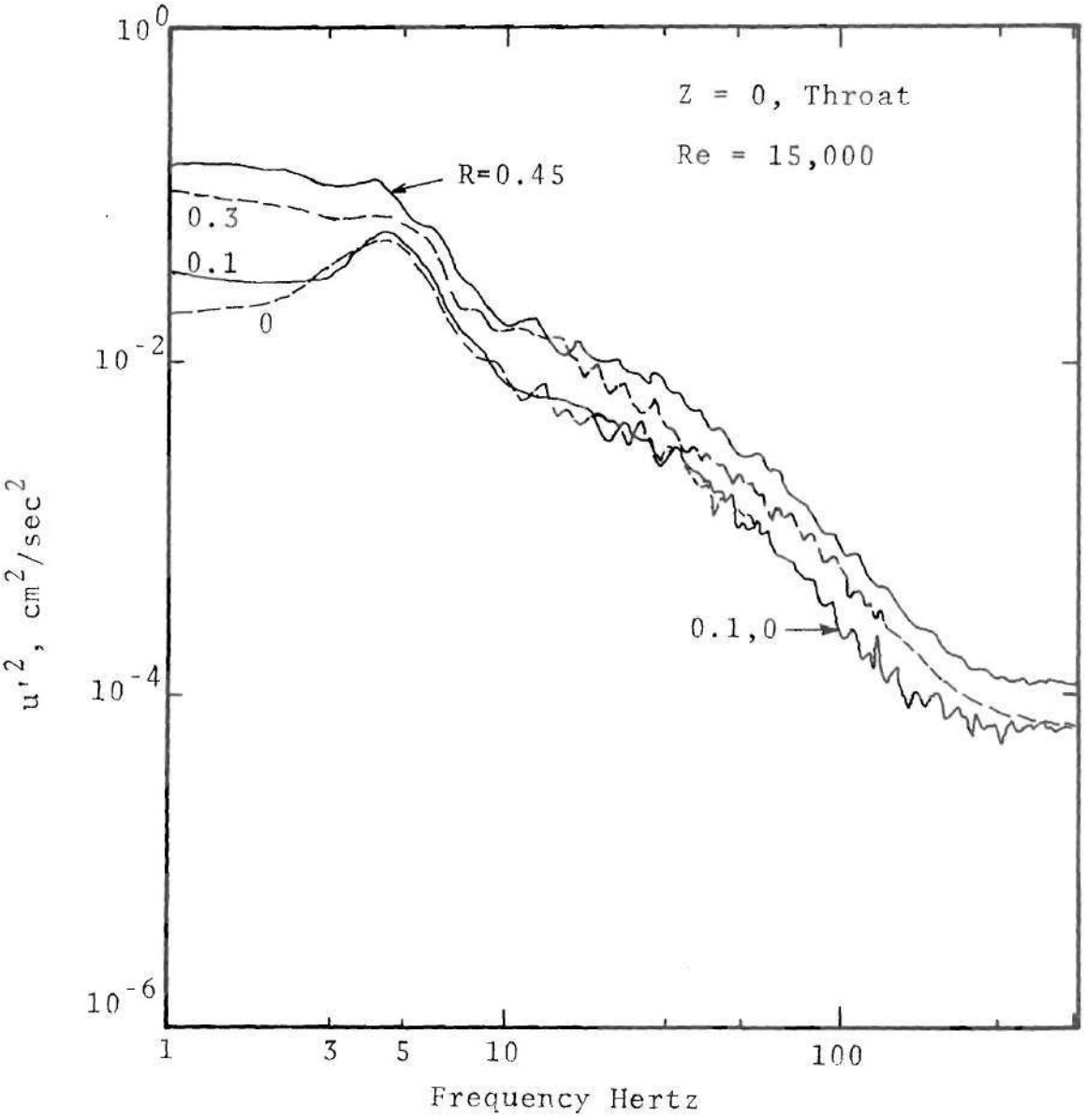

Figure 85. Energy Spectra for u'^2, Model M4, Re = 15,000, Z = 0

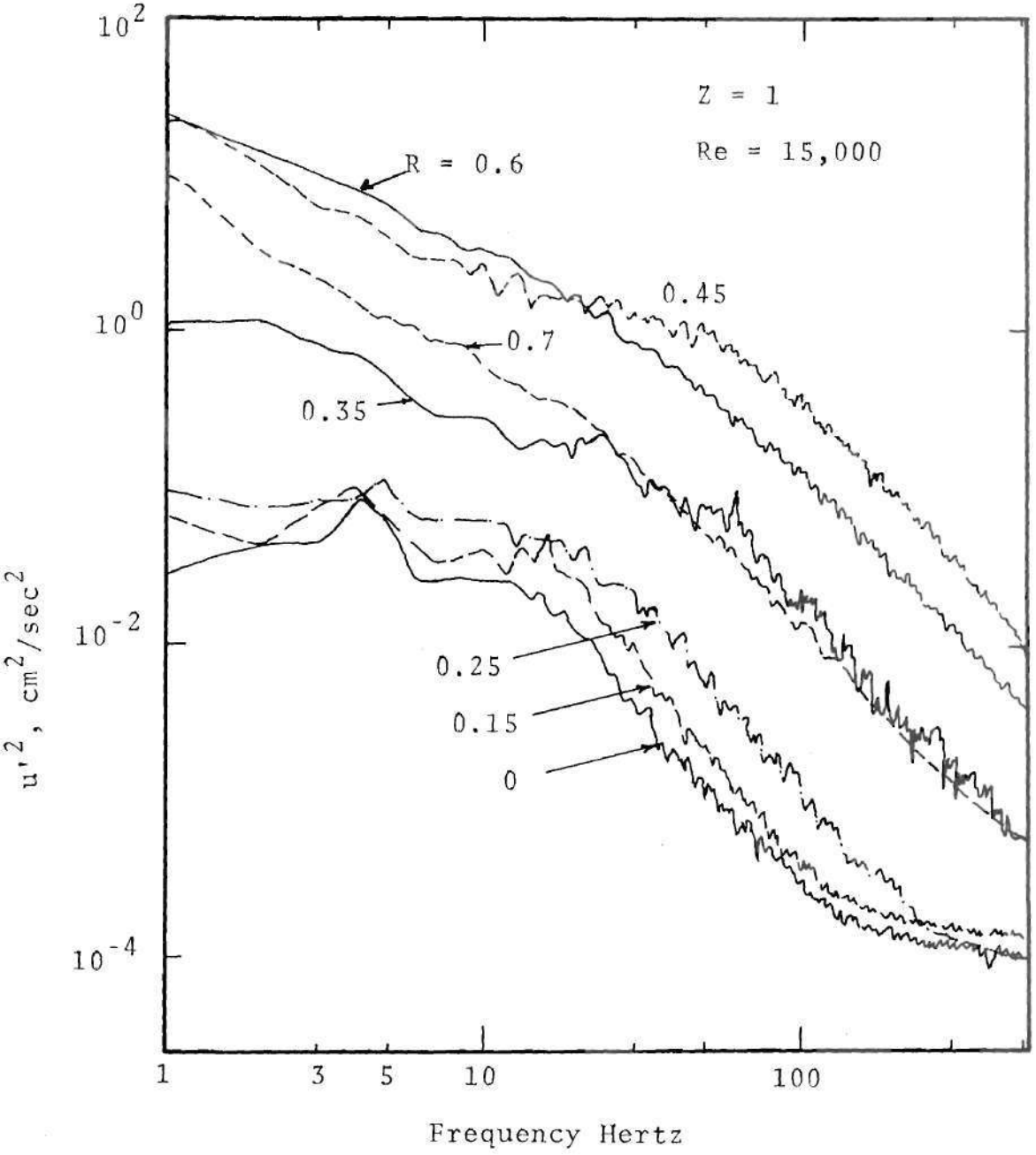

Figure 86. Energy Spectra for u'^2, Model M4, Re = 15,000, Z = 1

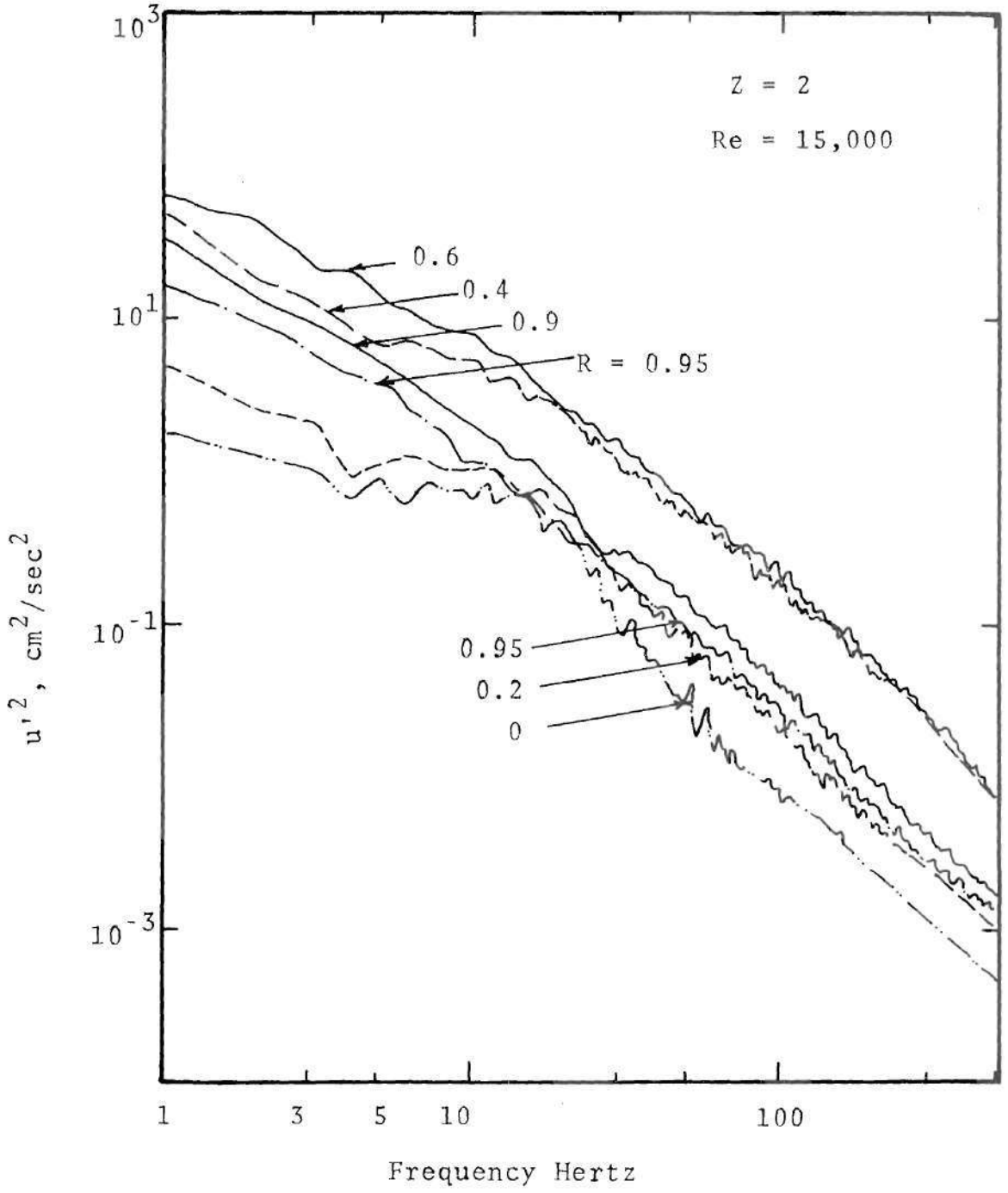

Figure 87. Energy Spectra for u'^2, Model M4, Re = 15,000, Z = 2

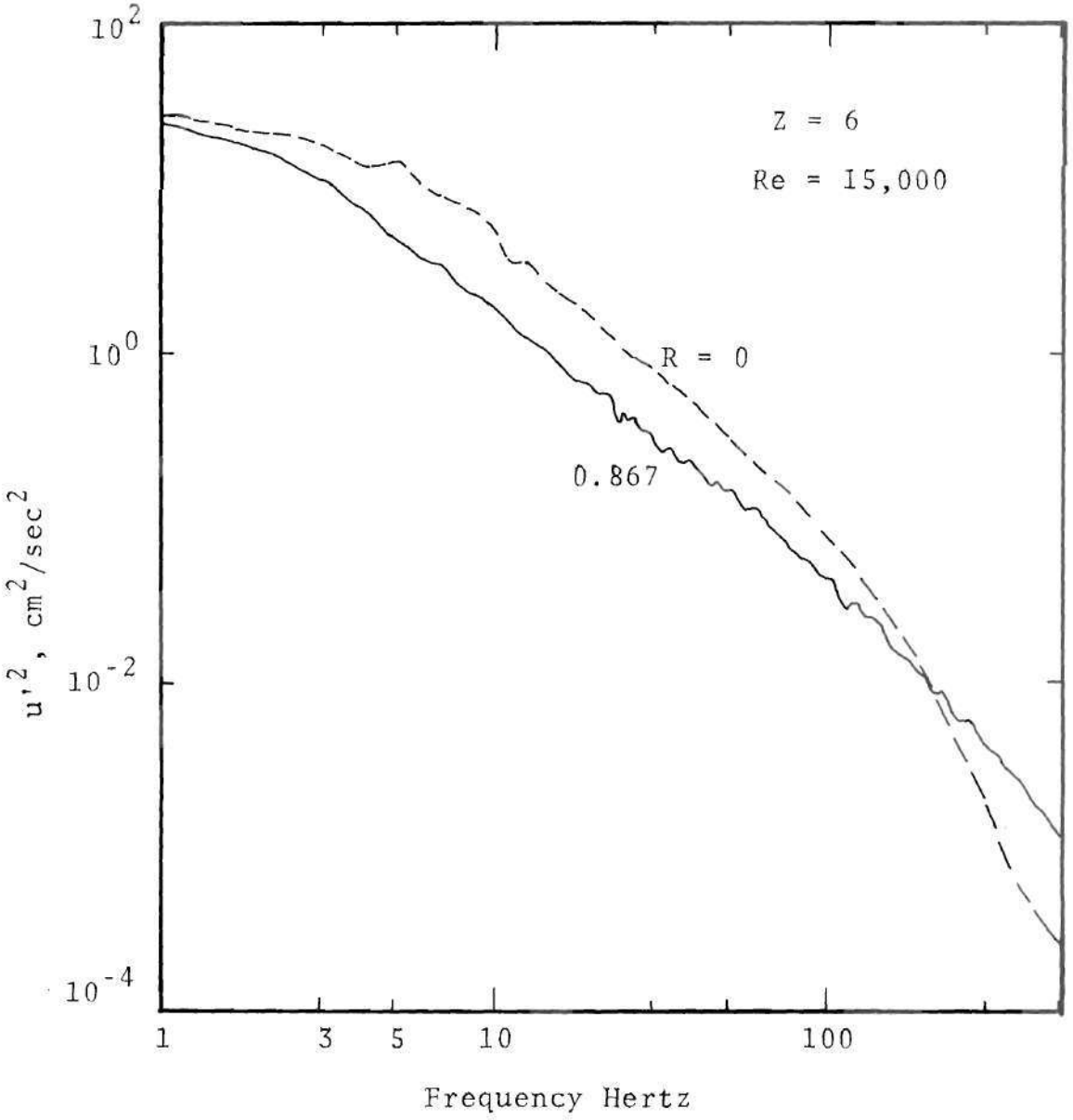

Figure 88. Energy Spectra for u'^2, Model M4, Re = 15,000, Z = 6

become significant in relation to the signal strength for a frequency of about 200 Hz. This is not a serious problem, as mentioned earlier, in the evaluation of the turbulence fluctuations.

The u'^2 spectra at the throat (Figure 85) indicate a decrease in the turbulence level due to the acceleration in the convergent portion of the stenosis. The decrease is primarily in the low frequency, or large wave number, components. There is a peak in each of the spectra around a frequency of four Hertz for the radial locations R = 0 and 0.1. The cause of these peaks was not examined in this study. The damping effect of the wall at R = 0.3 and 0.45 (R = 0.5 corresponds to the wall at this location) is clearly seen by the shape of the spectra around this frequency of four Hertz. The u'^2 spectra at the upstream station Z = -1 did not show this influence and are not included here. The w'^2 spectra at the throat (Figure 90) do not indicate such a distinct peak. A probable reason for this could be the w' value being large (w' is larger than u' at this location). All the frequencies in the w' fluctuations are amplified in the accelerating flow.

Several u'^2 spectra are illustrated in Figure 86 for the location Z = 1.0. Recirculation is present at this station (see Figure 44), and R = 0.75 corresponds to the wall. The spectra closer to the wall and in the shear layer have undergone a structural change with considerable increase

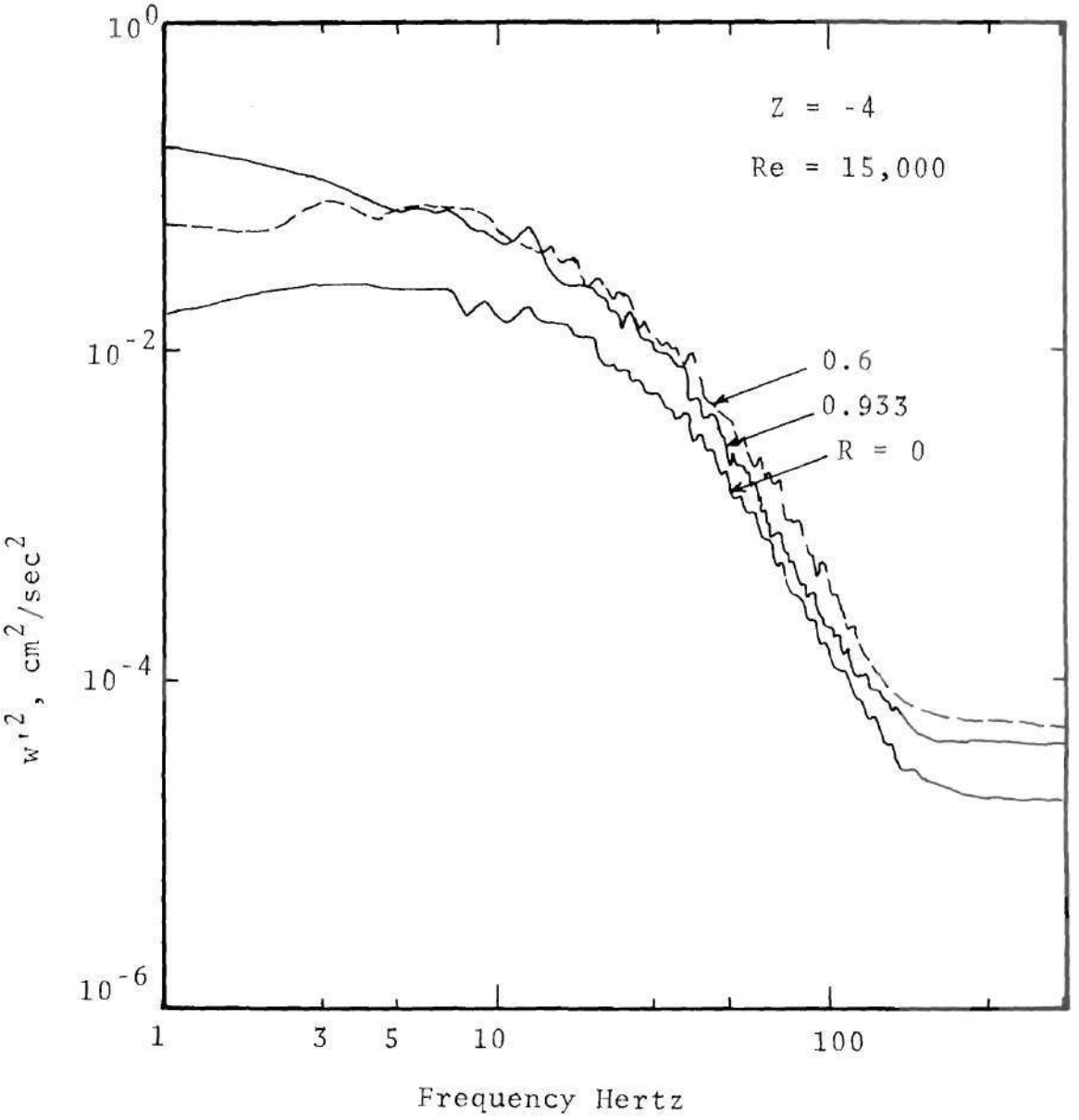

Figure 89. Energy Spectra for w'^2, Model M4, Re = 15,000, Z = -4

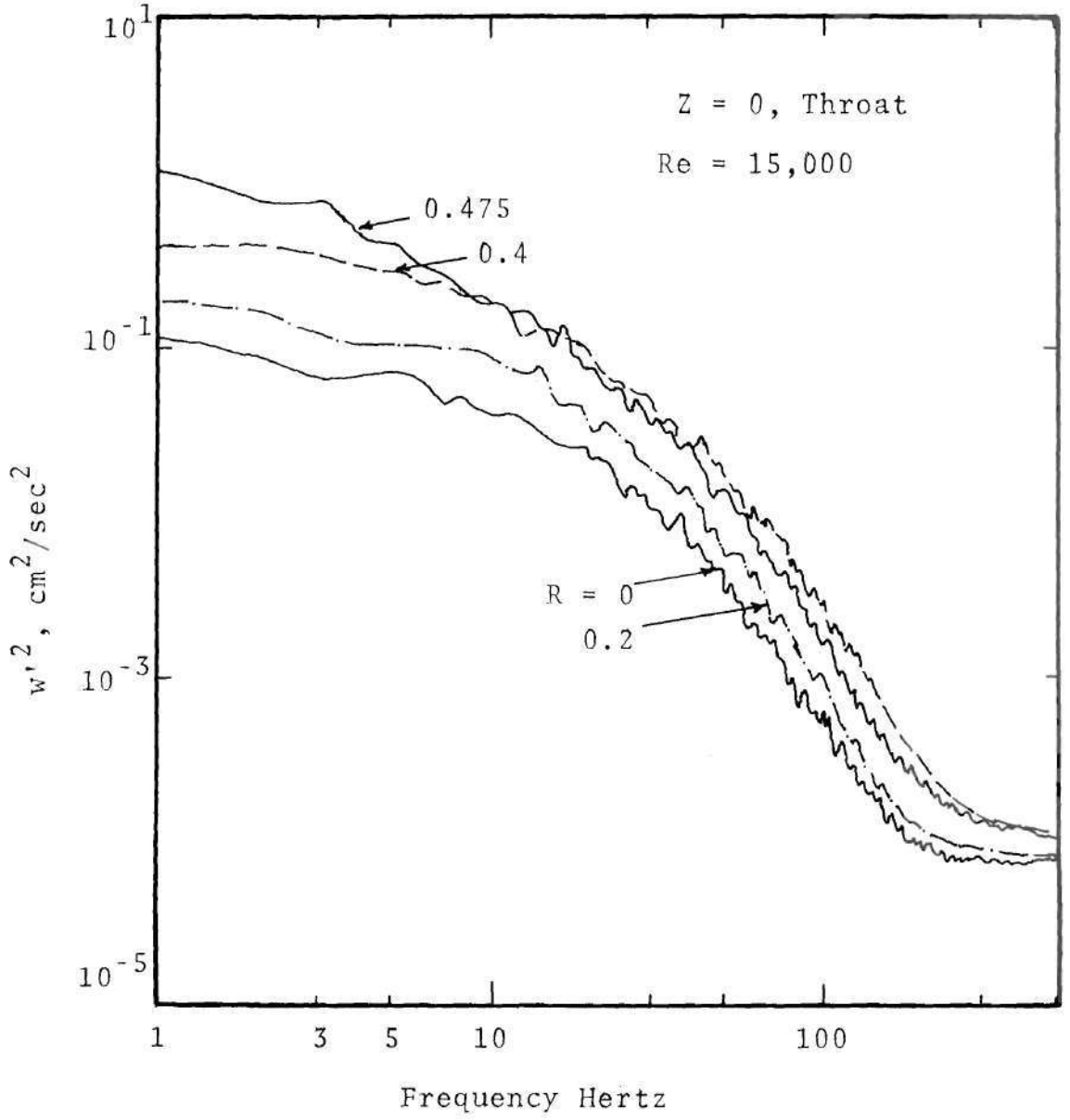

Figure 90. Energy Spectra for w'^2, Model M4, Re = 15,000, Z = 0

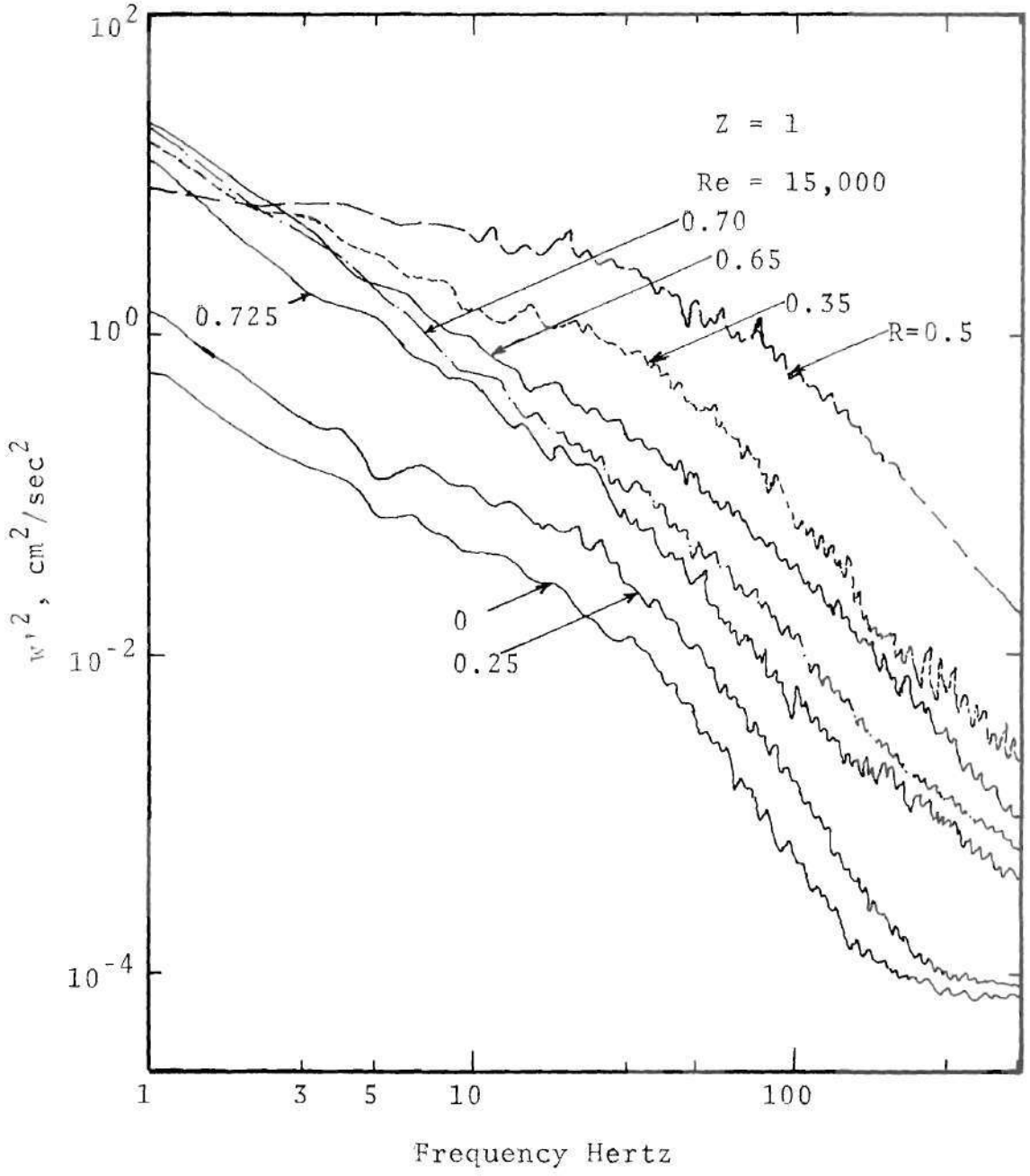

Figure 91. Energy Spectra for w'^2, Model M4, Re = 15,000, Z = 1

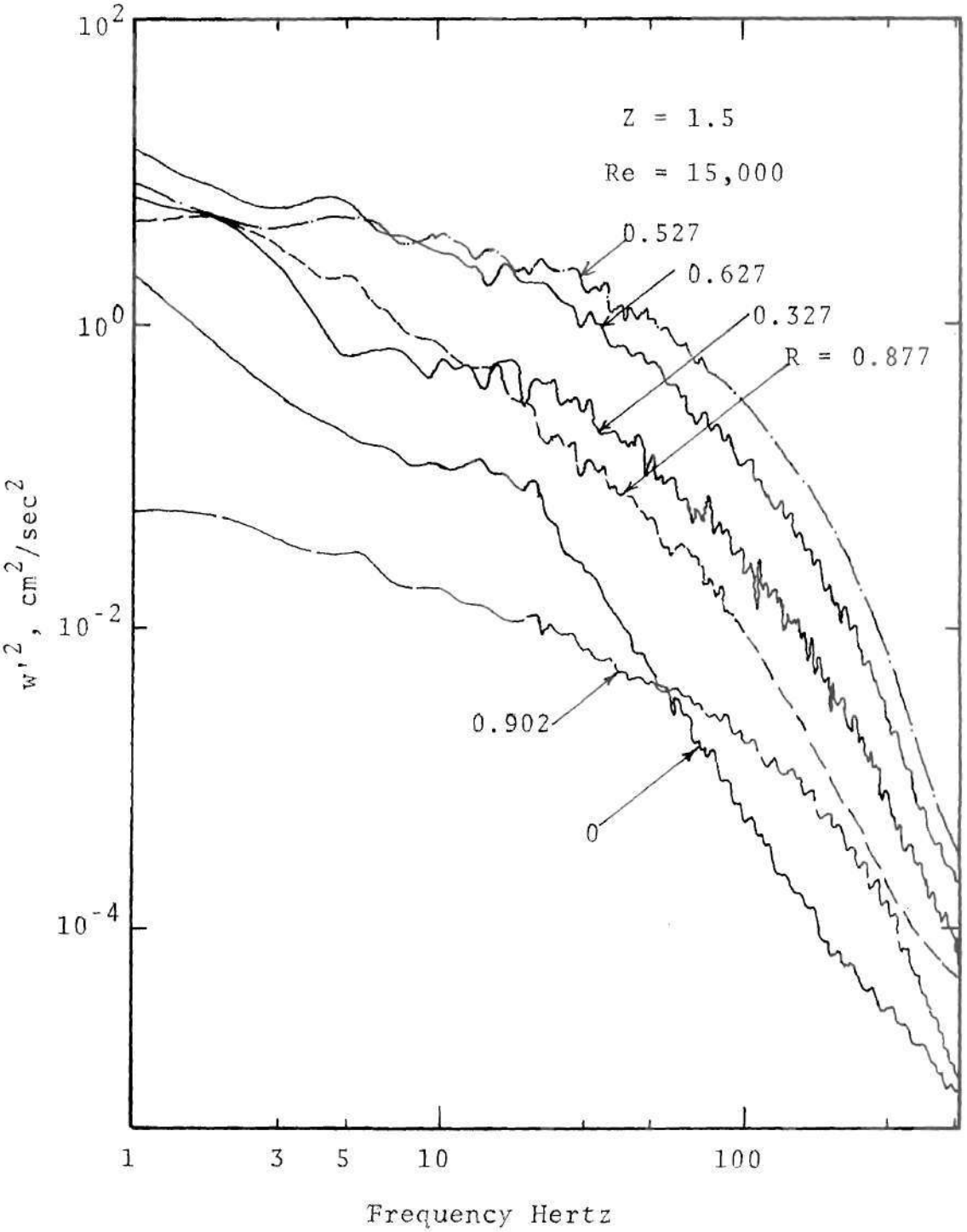

Figure 92. Energy Spectra for w'^2, Model M4, Re = 15,000, Z = 1.5

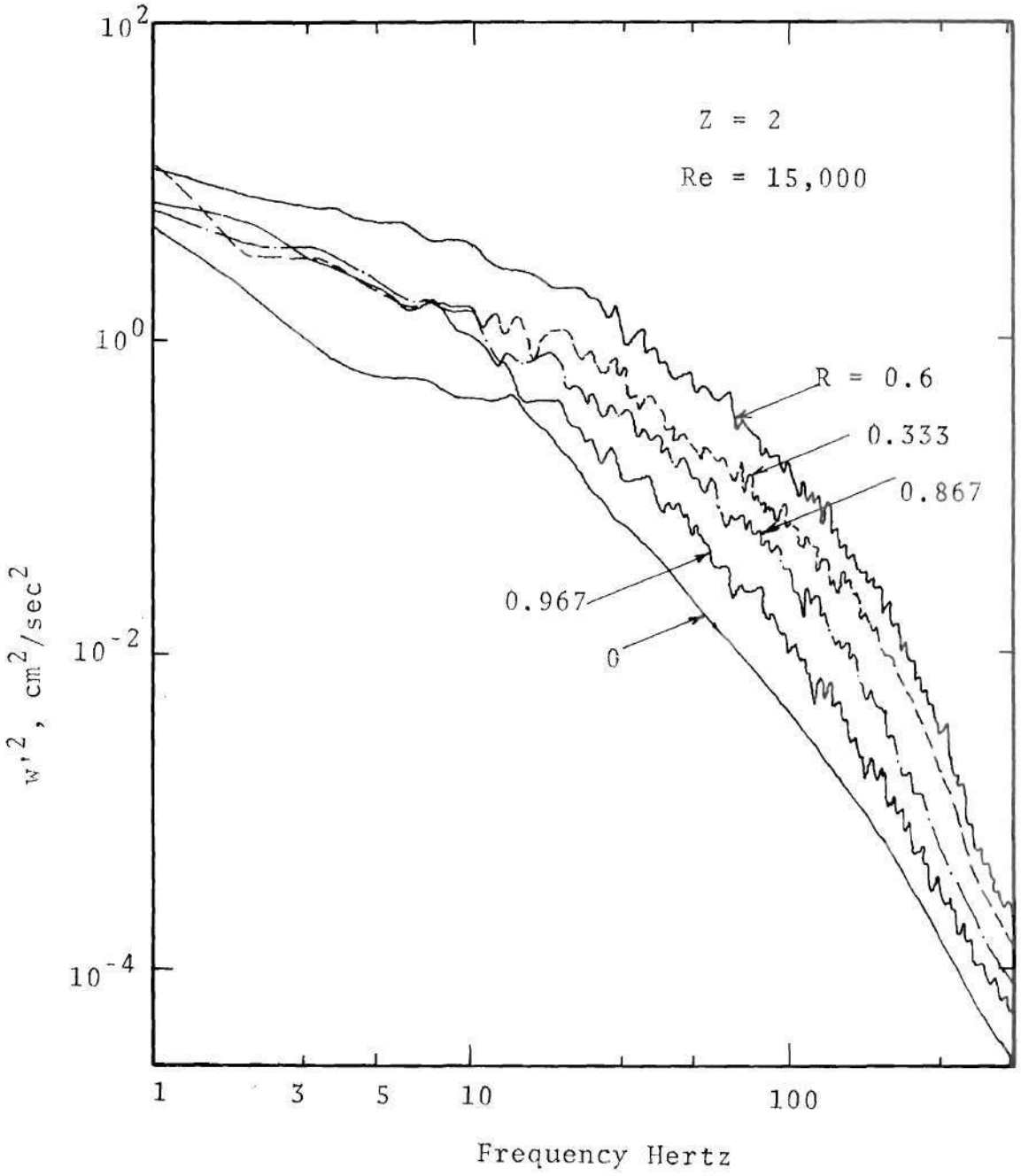

Figure 93. Energy Spectra for w'^2, Model M4, Re = 15,000, Z = 2

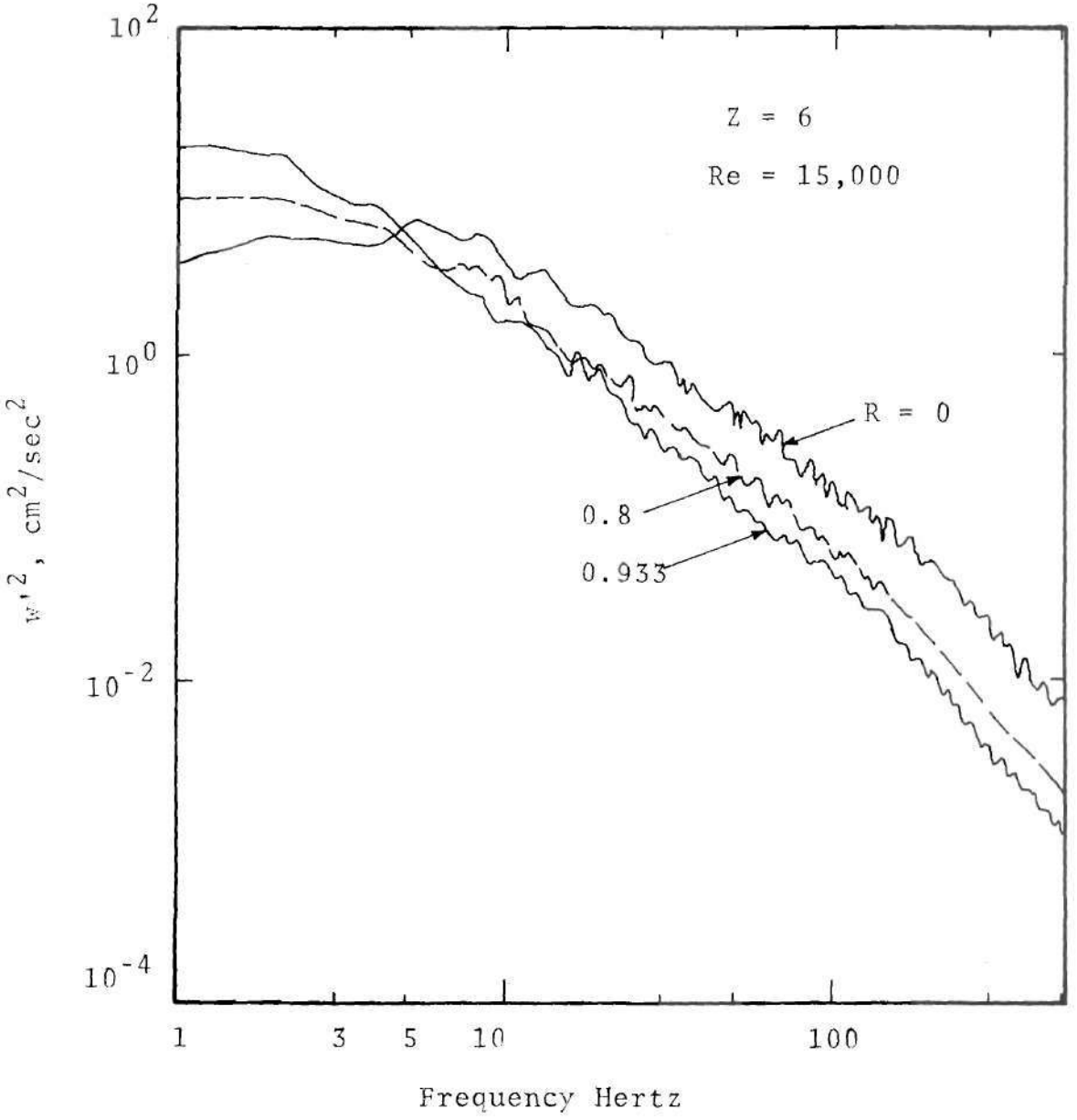

Figure 94. Energy Spectra for w'^2, Model M4, Re = 15,000, Z = 6

in the energy level at all the frequencies, whereas the spectra close to the axis have gained only a small amount of energy. The peak in the spectra in the vicinity of the axis around the frequency of four Hertz is still present. The spectra in the recirculation region are characterized by a larger fraction of their energy in the lower frequency range. All the observations made above, except the presence of a peak, are applicable to the w'^2 spectra at this location Z = 1.0 (Figure 91). In Figures 86 and 91 the flattening of the spectra, due to the Doppler ambiguity and the noise in the system is seen to be absent for the spectra with higher energy level since the signal to noise ratio has now greatly increased.

The w'^2 spectra at Z = 1.5 (Figure 92) are further modified from those at the previous station Z = 1.0. The wall at this station is given by R = 0.927. The spectrum at the axis has acquired more energy especially at lower frequencies. The spectra in the shear layer have lost part of the energy, especially at higher frequencies. The spectra taper off faster at this station, indicating increased dissipation. The large differences among the individual spectra at a given cross section are indicative of the large gradients in the flow properties in the radial direction. The diffusive action due to turbulence is seen to reduce these gradients and bring the spectra closer together as one moves downstream, and the characteristics of the spectra become very similar.

The u'^2 and w'^2 spectra in the exit plane of the stenosis Z = 2, are presented in Figures 87 and 93, respectively. The peak in the u'^2 spectra is already smoothed out at this location. It is imperative that the spectra should change toward their fully developed values. Those at Z = 6 for u'^2 and w'^2 (Figures 88 and 94) exhibit the further evolution. They still have high energy at all the frequencies as compared to their fully developed values represented in Figures 84 and 89 for Z = -4. Both Figures 88 and 94 indicate more energy on the axis than close to the wall and this is more so at higher frequencies for w'^2 spectra. This situation is to be interchanged by a faster decay of energy on the center-line so that the turbulence energy near the wall will be higher than that near the axis. This state is not yet reached at Z = 11, the last station where the measurements were made (spectra not included here). It is also interesting to follow the peak in the w'^2 spectra on the centerline. It is seen to be already formed at Z = 1.5 around a frequency of 13 Hz.and gradually moves towards the lower frequency in the downstream direction. At Z = 11 it is present at a frequency of two Hertz.

CHAPTER VI

CONCLUSIONS

Steady laminar and turbulent flows through axisymmetric constrictions were studied theoretically and, in addition, the turbulent flow was studied experimentally. Apart from furnishing the comparison tests for the theoretical results, the experiments also provide valuable data such as turbulence spectra which cannot be obtained theoretically. The laminar flow results were compared with experimental data already available in the literature. The objective of these varied efforts was to obtain a comprehensive description of steady flow through vascular stenosis models, which is needed to understand the role of fluid-dynamics in the pathology of atherosclerosis. Important observations originating from the study are listed below.

6.1. Laminar Flow

1. Flow distrubances, including flow separation, can occur even for a relatively mild stenosis. The critical Reynolds number at which separation occurs decreases with the increase in the severity of the constriction. The length of the recirculation region increases approximately linearly with the Reynolds number, as long as flow remains laminar. Flow disturbances travel farther downstream for higher

Reynolds number.

2. As expected the pressure drop across the stenosis and the maximum wall shear stress reached are higher for larger reductions of area of the stenosis. Most of the pressure drop occurs in the convergent section and a part of this is recovered in the flow distal to the throat. The wall shear stress reaches a maximum slightly upstream of the throat.

3. The maximum in the velocity on the centerline moves slightly downstream from the throat with an increase in the Reynolds number. Further, the maximum in the velocity profile at the throat may not occur at the centerline, especially for a short and severe stenosis. For larger Reynolds numbers the centerline velocity, having attained a maximum just distal to the throat, decays very gradually as the flow proceeds along the Z-axis. Thus, there is a region of relatively constant centerline velocity immediately downstream of the stenosis.

4. The radial velocities are generally larger in magnitude in the convergent section in comparison with the corresponding values in the divergent section, especially for a large Reynolds number.

6.2. Turbulent Flow

1. Flow is likely to separate for the more severe stenosis geometries. The length of the recirculation region

is shorter than for high Reynolds number laminar flows, and is less sensitive to changes in the Reynolds number. At high Reynolds numbers it reduces in length with an increase in the Reynolds number. This is the opposite trend from that for laminar flow.

2. The distances over which stenosis-induced flow alterations are propagated downstream are also less sensitive to the Reynolds number as compared to the laminar flow case. This is because the influence of increased axial momentum at higher Reynolds numbers is counterbalanced by increased turbulence diffusion in the radial direction.

3. The fraction of the pressure recovery in the divergent section is larger than in the laminar case. The net pressure drop, as anticipated, increases with an increase in the area reduction and the length of the stenosis.

4. The maximum wall shear stress occurs at the throat and increases with the area reduction and decreases slightly with an increase in the length of the stenosis.

5. The velocity on the centerline decreases toward the fully developed value faster than in the laminar flow case. Its return to the fully developed value need not be monotonic.

6. The longitudinal component of turbulence fluctuation u' is attenuated in the convergent section while as the azimuthal component w' is amplified, as expected.

7. High levels of turbulence intensity are generated in the shear layer in the decelerating flow. This radial

distribution generally becomes smoother as one moves downstream. The turbulence intensity close to the wall reaches a maximum inside the recirculating region and close to the "reattachment point." The maximum in the turbulence intensity on the centerline is attained at a section beyond the reattachment point. At this section the turbulence intensity on the axis is higher than that close to the wall, for a part of the length beyond this section it is relatively uniform in the cross section.

8. Consistent with other studies, the turbulence fluctuations reach their final fully developed values more slowly than the mean velocity does.

9. By comparison with measurements in the main stream, the turbulence spectra in the recirculating region contain a large fraction of their energy at relatively low frequencies.

10. The comparisons of experimental data with computations employing the k-ε model for turbulence agree reasonably well in regions proximal to the stenosis and for regions downstream of approximately four tube radii distal to the stenosis. However, for the zone between the throat and a portion somewhat downstream of the reattachment point the agreement between theory and experiment is not very good (although qualitative trends are predicted correctly). The calculations show a much shorter recirculation region and much lower k-values than those obtained experimentally.

6.3. Implications to the Physiological Situation

The physiological environment, as emphasized earlier, is much more complex than that studied in the present model. It is presumptuous to apply the present results directly to the vascular system where several factors are interplaying. Painstaking efforts are needed in implementing these results to connect fluid mechanics to atherosclerosis. However, certain important phenomena relevant to the actual case are illuminated by the research reported here.

The transport of nutrients and lipids in the neighborhood of an atherosclerotic plaque is of importance. The separated flow region, high wall shear stress and increased turbulence have been associated with atherosclerosis [9]. It is generally believed that the separated flow regions have reduced mass flux. Platelet and fibrin coalescence, and chemical reactions are also attributed to this region on the assumption that it is quiescent. Apart from the over-simplification involved, the basic assumption implied in such theories is not likely to be valid in a pulsatile flow or with disturbed flow patterns. The present study has shown that, even for a steady condition, this region is anything but quiescent at large Reynolds numbers. The recirculation region in a turbulent flow exhibited much greater fluctuation activity than expected and this activity undoubtedly acts to purge the recirculating zone much more readily than would a laminar recirculation.

Certainly, it must be re-emphasized that these studies were for a Reynolds number which is higher than one would expect to find in the arterial circulation. However, stenotic flows are rather unstable, even for considerably lower Reynolds number [22,48] and previous experiments have indicated an active recirculation region even when proximal flow is laminar [48]. All of this evidence taken together may imply that estimations of mass transport from the arterial wall which use boundary layer type conditions are quite likely to be seriously in error when applied to recirculating physiological flows. However, this unstable recirculation region is characterized by substantial flow disorder and this may lead to a disorientation of endothelial cells which adversely affects the protective barrier at the arterial wall [3].

There has been considerable interest in the role of elevated shear stresses as a factor in atherogenesis. Of importance in this regard are Fry's results [2] which demonstrated that shear stresses on the order of 400 dynes/cm^2 caused acute endothelial cell damage to the walls of arteries. He has later shown [3] that much lower stresses can cause reorientation of these cells over a prolonged period of time. Another phenomenon which is of great significance is that of the "sudden" cerebrovascular accident or myocardial infarction. Plaques may, if sufficiently high shear stresses are imposed, disgorge emboli which may move distally to

precipitate these accidents.

It is therefore instructive to estimate the maximum wall shear stress, which occurs essentially at the throat of the constriction, for example cases in laminar and turbulent flow, based upon the results of the present study.

(a) Laminar Flow (89% stenosis)

Reynolds number:	500
Vessel diameter:	1 cm
Kinematic viscosity:	0.03 cm^2/sec
$\bar{u}$:	15 cm/sec
Maximum wall shear stress $\simeq$	300 $dynes/cm^2$

(b) Turbulent Flow (89% stenosis)

Reynolds number;	5,000
Vessel diameter:	2 cm
Kinematic viscosity:	0.03 cm^2/sec
$\bar{u}$:	75 cm/sec
Maximum wall shear stress $\simeq$	1,700 $dynes/cm^2$

Although these estimates are not directly related to atherogenesis since they presuppose the presence of a stenosis, they do demonstrate the very hazardous conditions which exist in the advanced disease state. Sudden exercise which quickly elevates peak velocities through the constriction can create a rapid increase in shear stress acting on the plaque. This can promote further damage chronically or, in the case of emboli dislodgement, acutely.

Previous studies have suggested that turbulence is a

causative factor in poststenotic dilatation [10]. The present experiments indicate extremely high turbulence intensities near the wall in the region of recirculation and reattachment. Further, the frequency content, although weighted more heavily toward the lower frequencies, indicates relatively large energy in a wide frequency band. Thus, the poststenotic flow is rather violent. The information presented here may be of interest to investigators concerned with the dilatation problem.

From the diagnostic viewpoint, the present study contributes very important information. Although the degrees of stenosis studied here varied from moderate (56 percent) to severe (89 percent), the results do indicate a substantial disruption of streamline patterns for all stenoses. Furthermore, the data indicates that the field immediately distal to the throat contains a region of fairly high (and almost constant) centerline velocity. This gives hope of effective "searching" for velocity "hot spots" with noninvasive ultrasound instrumentation. In addition, the results help to explain previous in vivo findings that the centerline velocity immediately distal to stenoses in the dog aorta remained constant for one or two vessel diameters before rapidly decaying [22]. Also, the activity and extent of the recirculation zone indicates that this region may be identified at a relatively early stage of disease progression, provided instrumentation can be developed to accomplish

turbulence measurements noninvasively.

The interpretation of pressure drop across stenosis must be considered cautiously. The resistance for the flow in an artery in the normal circulatory system is a small fraction of the total resistance. Hence, the flow rate is reduced very little until the reduction in area is quite advanced. Due to this reason along with compensatory mechanisms like vasodilation and collateral circulation a patient is not seriously inconvenienced until the disease reaches an advanced stage unless a sudden accident due to emboli occurs. Thus, diagnostic procedures based upon pressure drop estimates are but a crude indicator of the presence of localized stenoses. On the other hand, flow disturbances are caused by even a mild stenosis and have the potential of being indicators of the atherosclerotic plaque by a noninvasive method such as an ultrasonic Doppler velocimeter. The basic flow description of the present study is an essential ingradient in such an effort.

It is interesting to make a comparison with the in vivo hot film data of Giddens et al. [22]. The comparison can only be qualitative because the in vivo flow conditions correspond to a pulsatile flow and for moderate Reynolds numbers (peak Re $\simeq$ 2,000 and mean Re $\simeq$ 1,100). These data were taken at the centerline of the canine aorta and two centimeters distal to the constricting band. They show an increase in turbulence intensity distal to the stenosis with

an increase in the severity of the constriction. These are consistent with the present findings. For a 74% occlusion the turbulence velocity fluctuation was about 30% of the mean velocity and is comparable to the present data. Those results for a 50 percent stenosis also indicated a rapid decay of turbulence velocity beyond a region where it was fairly constant. These are in qualitative agreement. The maximum values of u', w' and k at each cross section are plotted for the present study in Figure 95; (see Figure 80 for the variation of these quantities on the centerline). These experimental data for Model M4 indicate a length of about two diameters where the maximum velocity fluctuations remain constant and then decay very rapidly. This fairly large region of intense turbulence activity is of clinical significance as one can hope to develop diagnostic procedures using noninvasive turbulence detection. The present study suggests the feasibility of such an effort and also indicates where to search.

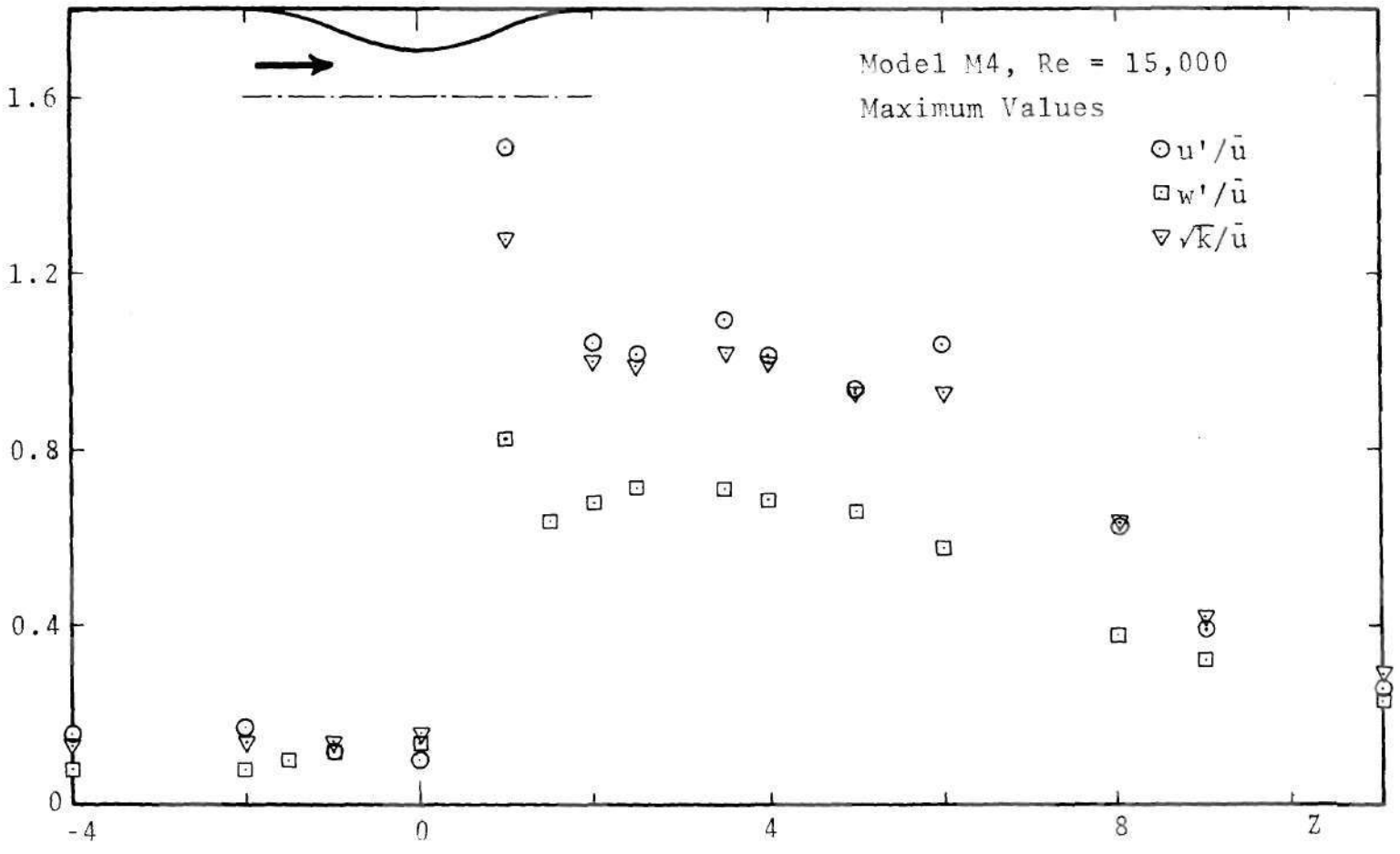

Figure 95. Axial Variation of Maximum Values of Velocity Fluctuations, Model M4, Re = 15,000 (Experiments)

APPENDICES

APPENDIX A1

DERIVATION OF BOUNDARY CONDITION FOR ω ON THE CURVED WALL

The boundary condition for ω is to be derived using no slip boundary conditions on the wall (equations 12) and the governing equation (6). For a flat boundary, the derivation can be obtained from Lester's paper [58]. The major difficulty in extending it to a curved wall is that governing equations are specified in Z-R coordinates, and we can write no slip boundary conditions for higher order derivatives of ψ in tangential direction-s and normal direction-n to the wall (Figure 96). These boundary conditions at any point P on the wall are

$$0 = \left(\frac{\partial\psi}{\partial s}\right)_P = \left(\frac{\partial\psi}{\partial n}\right)_P = \left(\frac{\partial^2\psi}{\partial s^2}\right)_P = \left(\frac{\partial^2\psi}{\partial s\partial n}\right)_P = \left(\frac{\partial^3\psi}{\partial s^3}\right)_P$$

$$= \left(\frac{\partial^3\psi}{\partial s^2\partial n}\right)_P. \qquad \text{(A-1)}$$

If we define Y_1 and Z_1 as the local coordinates along P-1 and P-2 (Figure 96) where 1 and 2 are the closest grid points in R and Z directions,

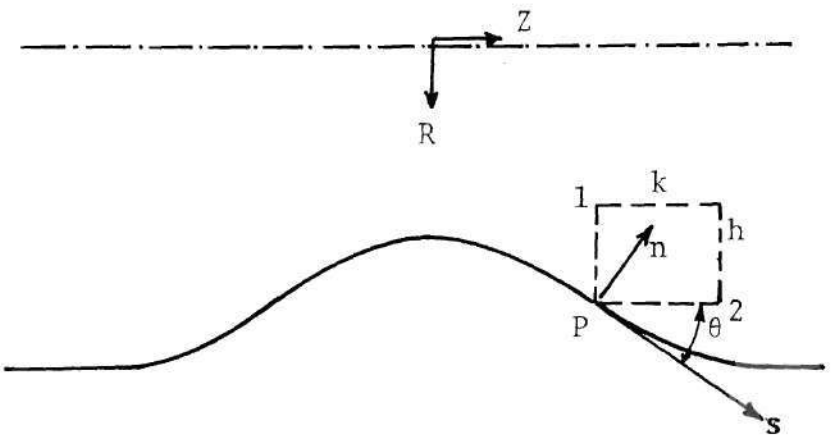

Figure 96. Geometry for Derivation of Boundary Condition for ω on Curved Wall

$$Z_1 = sC + nS; \quad Y_1 = -sS + nC, \tag{A-2}$$

where S = sin θ, C = cos θ and θ is the inclination of the wall to the axis.

The functions ψ and ω are expanded in Taylor series about their boundary values in R_1 and Z_1 directions;

$$\psi_1 - \psi_P = -h\dot{\psi}_P + h^2\ddot{\psi}_P/2 - h^3\dddot{\psi}_P/6 + 0(h^4), \tag{A-3}$$

where $(\dot{})$ and $(\,)'$ indicate differentiation in R and Z directions. The suffix P for ψ and ω is omitted in what follows. After using

$$\dot{\psi} = \psi' = 0 \tag{A-4}$$

$$6\,\Delta\psi_1/h^2 = 3\ddot{\psi} - h\,\dddot{\psi} + 0\,(h^2), \tag{A-5}$$

and similarly

$$6\,\Delta\psi_2/k^2 = 3\psi'' + k\psi''' + 0(k^2) \tag{A-6}$$

$$\omega_1 - \omega = -h\dot{\omega} + 0(h^2) \tag{A-7}$$

$$\omega_2 - \omega = k\omega' + 0(k^2), \tag{A-8}$$

where $\Delta\psi_1 = \psi_1 - \psi_P = \psi_1 - \psi$ and $\Delta\psi_2 = \psi_2 - \psi$.

The governing equation (6),

$$\ddot{\psi} + \psi'' = -R\omega + \dot{\psi}/R, \tag{A-9}$$

is differentiated and after using relations (A-4) we get

$$\ddot{\psi} + \psi'' = -R\omega \tag{A-10}$$

$$\dddot{\psi} + \dot{\psi}'' = -R\dot{\omega} - \omega + \ddot{\psi}/R \tag{A-11}$$

$$\ddot{\psi}' + \psi''' = -R\omega' + \dot{\psi}'/R. \tag{A-12}$$

Equations (A-5, A-6, A-10) are combined to get

$$6(\Delta\psi_1/h^2 + \Delta\psi_2/k^2) = -3R\omega - h\dddot{\psi} + k\psi'''. \tag{A-13}$$

To eliminate $\dddot{\psi}$ and ψ''' from (A-13) derivatives along Z and R directions are related to derivatives along s and n coordinates using transformation (A-2). Suffixes s and n in these relations below indicate differentiation;

$$\psi_s = 0 = \psi' C + \dot{\psi} S \tag{A-14}$$

$$\psi_n = 0 = \psi' S - \dot{\psi} C \tag{A-15}$$

$$\psi_{ss} = 0 = \psi''C^2 + 2\dot{\psi}'CS + \ddot{\psi}S^2 \qquad \text{(A-16)}$$

$$\psi_{sss} = 0 = \psi'''C^3 + 3\dot{\psi}''C^2S + 3\ddot{\psi}''CS^2 + \dddot{\psi}\,S^3 \qquad \text{(A-17)}$$

$$\psi_{sn} = 0 = \psi''CS + \dot{\psi}'(S^2-C^2) - \ddot{\psi}SC \qquad \text{(A-18)}$$

$$\psi_{sss} = 0 = \psi'''C^2S + \dot{\psi}''(2CS^2-C^3) + \ddot{\psi}'(S^3-2C^2S) - \dddot{\psi}\,S^2C. \qquad \text{(A-19)}$$

The set of 7 equations (A-10 to A-12 and A-16 to A-19) in 7 derivatives of ψ can be solved to get

$$\psi''' = -2S^3C(R\dot{\omega}+\omega) - R\omega'S^2(2C^2+1) + S^3C\omega \qquad \text{(A-20)}$$

$$\dddot{\psi} = -C^2(2S^2+1)(R\dot{\omega}+\omega) - 2C^3S(R\omega') + C^4\omega. \qquad \text{(A-21)}$$

ψ''' and $\dddot{\psi}$ are substituted in (A-13) after evaluating $\dot{\omega}$ and ω' using equations (A-7 and A-8) to get

$$\omega_P = [-\frac{6}{R_P}(\frac{\Delta\psi_1}{h^2} + \frac{\Delta\psi_2}{k^2}) - \omega_1A-\omega_2B]/(E-D) + 0(k^2,h^2), \qquad \text{(A-22)}$$

where

$$A = C^2(2S^2+1) - (2S^3C)k/h$$

$$B = - (2C^3S)h/k + S^2(2C^2+1)$$

$$D = C^2(S^2+2)h/R_p - (S^3C)k/R_p$$

$$E = 2 - 4S^2C^2 + 2SC\,(h^2C^2+k^2S^2)/(hk).$$

For the particular case of wall being parallel to Z-axis (e.g. straight portion of the tube), equation (A-22) reduces to the correct limit [40]

$$\omega_p = [- \frac{6}{R_p} (\frac{\Delta\psi_1}{h^2}) - \omega_1]/[2-2h/R_p] + O(h^2), \qquad (A-23)$$

and for wall being perpendicular to Z-axis (not present in this study),

$$\omega_p = [- \frac{6}{R_p} (\frac{\Delta\psi_2}{k^2}) - \omega_2]/2 \qquad (A-24)$$

While using the relation (A-22) one should keep in mind the sign convention used in its derivation. Useful points applicable for this study are summarized below to help in the application of equation (A-22) to any general case.

(1) A minus sign was already associated with h in

the Taylor series expansions (A-5 and A-7) and hence h should be taken as positive.

(2) On the other hand, k is positive on the downstream side ($Z > 0$) and negative on the upstream side ($Z < 0$).

(3) The angle θ is positive for $Z > 0$ and negative for $Z < 0$.

(4) If the negative sign is interchanged in the relations between velocity and stream function (equations 5), the first term in the numerator of equation (A-22) turns out to be positive.

APPENDIX A2

DETAILS OF DIFFERENCE EQUATIONS

Equation (14) is integrated over the control volume shown by dotted lines in Figure 2 and hence the definite integral of each term is expressed as the difference of two terms evaluated at opposite boundaries.

The two convection terms in equation (14) yield four integrals, the first one being

$$I_{c1} = \bar{a}_P \int_s^n \phi_e \left(\frac{\partial \psi}{\partial R}\right)_e dR = \bar{a}_P \bar{\phi}_e (\psi_{ne} - \psi_{se}),$$

where the overbar indicated an average over the control volume. Upwind differencing is introduced at this stage by taking $\bar{\phi}_e$ as ϕ_P or ϕ_E depending on whether V_Z (which has the same sign as $\psi_{ne} - \psi_{se}$) is positive or negative. Hence,

$$I_{c1} = \bar{a}_P \left[\phi_E \left\{\frac{(\psi_{ne} - \psi_{se}) - |\psi_{ne} - \psi_{se}|}{2}\right\} + \phi_P \left\{\frac{(\psi_{ne} - \psi_{se}) + |\psi_{ne} - \psi_{se}|}{2}\right\}\right]$$

and ψ_{ne} and ψ_{se} are taken as the average of four values at surrounding points.

After adding all the four terms, the total convective term is

$$I(CONV) = \sum_j A_j(\phi_P - \phi_j); \quad j = E,W,N,S,$$

where

$$A_E = a_P[(\psi_{SE}+\psi_S-\psi_{NE}-\psi_N) + |\psi_{SE}+\psi_S-\psi_{NE}-\psi_N|]/8$$

$$A_W = a_P[(\psi_{NW}+\psi_N-\psi_{SW}-\psi_S) + |\psi_{NW}+\psi_N-\psi_{SW}-\psi_S|]/8$$

$$A_N = a_P[(\psi_{NE}+\psi_E-\psi_{NW}-\psi_W) + |\psi_{NE}+\psi_E-\psi_{NW}-\psi_W|]/8$$

$$A_S = a_P[(\psi_{SW}+\psi_W-\psi_{SE}-\psi_E) + |\psi_{SW}+\psi_W-\psi_{SE}-\psi_E|]/8$$

All four coefficients A_E, A_W, A_N and A_S are non-negative which can be shown to stabilize the difference equations.

The procedure for diffusion terms is similar to the above and the first of the four integrals is

$$I_{d1} = \int_s^n (b_1 R)_e \{\frac{\partial}{\partial \eta}(c\phi)\}_e dR = B_E[(c\phi)_E - (c\phi)_P]$$

and the total diffusion term is

$$I(DIFF) = \sum_j B_j[(c\phi)_j - (c\phi)_P]; \quad j = E,W,N,S,$$

where

$$B_E = (b_{1E}+b_{1P})(R_E+R_P)(R_N-R_S)/[8(\eta_E-\eta_P)]$$

$$B_W = (b_{1W}+b_{1P})(R_W+R_P)(R_N-R_S)/[8(\eta_P-\eta_W)]$$

$$B_N = (b_{2N}+b_{2P})(R_N+R_P)(\eta_E-\eta_W)/[8(R_N-R_P)]$$

$$B_S = (b_{2S}+b_{2P})(R_S+R_P)(\eta_E-\eta_W)/[8(R_P-R_S)].$$

The source term (Rd) integrates to

$$I(SOURCE) = R_P d_P(\eta_E-\eta_W)(R_N-R_S)/4.$$

Addition of all the integrals leads to the complete equation

$$\phi_P = \frac{\sum_j [\{A_j' + c_j(b_{ij}+b_{iP})B_j'\}\phi_j] - d_P}{\sum_j \{A_j' + c_P(b_{ij}+b_{iP})B_j'\}},$$

with

$$A_j' = A_j/V_P, \quad B_j' = B_j/[V_P(b_{ij}+b_{iP})],$$

$$V_P = R_P(\eta_E-\eta_W)(R_N-R_S)/4, \quad \text{and}$$

$i = 1$ for $j = E,W$, and $i = 2$ for $j = N, S$.

Convective terms adjacent to the curved boundary are to be treated specially. Figure 3 corresponds to the upstream side of the stenosis. The point ne, which would be inside the wall if the curvature is convex, is relocated to the wall surface where ψ is known from the boundary condition. This deviation from the procedure for the rest of the flow alters the expressions for A_E and A_N on the upstream side, and for A_W and A_N on the downstream side. Only one of these new coefficients is listed below.

$$A_E(\text{WALL}) = a_P[(\psi_S+\psi_{SE}-3\psi_E+\psi_P)+|\psi_S+\psi_{SE}-3\psi_E+\psi_P|]/8.$$

APPENDIX A3

DIRECT SOLUTION OF TWO LINEAR SYSTEMS OF EQUATIONS FORMING COUPLED TRIDIAGONAL-TYPE MATRICES

A method is presented for solving two sets of linear algebraic equations forming tridiagonal-type matrices and coupled in such a way that each set contains a variable from the other set in its right hand side (RHS). These equations arose in the third chapter from the finite difference approximations of equations for k and ε. Equations (26,27) written for the j node are repeated here.

$$A_j\, k_{j-1} + B_j\, k_j + C_j\, k_{j+1} = D_j \varepsilon_j + E_j \qquad \text{(A3-1a)}$$

$$a_j\, E_{j-1} + b_j \varepsilon_j + c_j\, \varepsilon_{j+1} = d_j\, k_j + e_j \qquad \text{(A3-1b)}$$

$$j = 2, 3, 4, \ldots, M.$$

The coefficients A_j, B_j, ..., e_j have known values, and k and ε at j = 1 and M+1 are the applied boundary conditions.

These equations can be solved by evaluating the values of ε_j and k_j on the RHS from the previous iteration. The resulting form of this linearization is equation (25) and a simple procedure is available to solve this tridiagonal

system [74]. It is reported in the third chapter that the convergence of the general iterative scheme to solve the flow equations was not satisfactory after this linearization. If equations (A3-1a and A3-1b) are to be solved independently of the flow problem under consideration, i.e. if it is not possible to linearlize the RHS using good estimates of k and ε, one can resort to an iterative method. (This, however, should not be confused with the general iterative procedure of the third chapter to solve the flow equations.) In this method one guesses the values of ε_j in the RHS of equation (A3-1a) and solves this tridiagonal system of equations. The resulting values of k_j are substituted in (A3-1b) which can now be solved to gain a better estimate of ε_j in (A3-1a). Iteration is continued and hopefully it converges. The results obtained should be superior to those by the earlier linearization method because no approximations are involved in the RHS when the final solutions are attained. Apart from the stability considerations, the objection for using this method in the general iterative procedure of flow solution is the additional computer time it needs. A direct method of solution of equations (A3-1) is presented here. It is an extension of the procedure for the tridiagonal system [74].

Equations (A3-1) are written in the matrix form

$$A\,\bar{\psi} = f \qquad \text{(A3-2)}$$

Now A is an (nxn) quindiagonal matrix (see Figure 97) with semibandwidth p = M = 1 + n/2. Evans [87] proposes a direct method to solve a general quindiagonal matrix with arbitrary semibandwidth p. The present method is restricted to p = 1 + n/2 and the type of the matrix indicated but is much simpler to implement and takes considerably less computer time.

- Recursion relations are assumed as

$$k_j = -\phi_j\, k_{j+1} + \gamma_j\, \varepsilon_{j+1} + \xi_j$$

$$\varepsilon_j = -\bar{\phi}_j\, \varepsilon_{j+1} + \bar{\gamma}_j\, k_{j+1} + \bar{\xi}_j \qquad \text{(A3-3)}$$

$$j = 2, 3, \ldots, M-1$$

These relations can be used to evaluate k_j and ε_j if the six unknowns ϕ_j, γ_j, ..., $\bar{\xi}_j$ and also k_M and ε_M are determined. To do this equations (A3-3) are written for the (j-1) node and combined linearly with equations for the j node. The results are

$$\alpha_1\, k_{j-1} + (\alpha_1\, \phi_{j-1} + \alpha_2)\, k_j + \alpha_2\, \phi_j\, k_{j+1} = \qquad \text{(A3-4a)}$$

$$\alpha_1\, \gamma_{j-1}\, \varepsilon_j + \alpha_2\, \gamma_j\, \varepsilon_{j+1} + \alpha_1\, \xi_{j-1} + \alpha_2\, \xi_j,$$

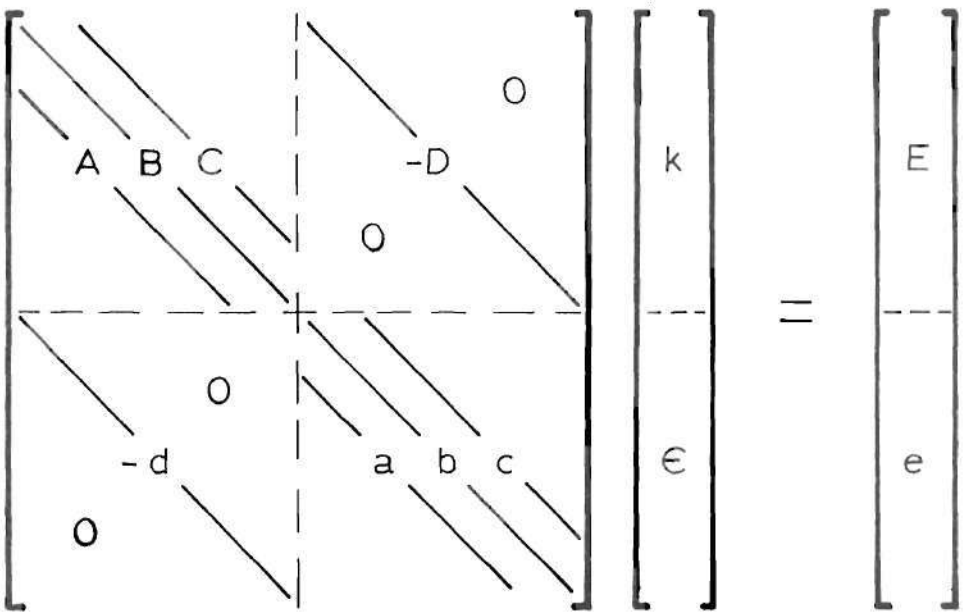

Figure 97. Coupled Tridiagonal-Type Matrix

$$\beta_1 \varepsilon_{j-1} + (\beta_1 \bar{\phi}_{j-1} + \beta_2) \varepsilon_j + \beta_2 \bar{\phi}_j \varepsilon_{j+1} = \qquad \text{(A3-4b)}$$

$$\beta_1 \bar{\gamma}_{j-1} k_j + \beta_2 \bar{\gamma}_j k_{j+1} + \beta_1 \bar{\xi}_{j-1} + \beta_2 \bar{\xi}_j$$

where the constants α_1, α_2, β_1 and β_2 are to be determined. Now, equations (A3-4) are made to represent the difference equations (1). This is accomplished as follows. Equations (A3-1a) and (A3-1b) are added and equations (A3-4a) and (A3-4b) are added. The two resulting equations are compared term-by-term for the coefficients of k_{j-1}, k_j, ..., ε_{j+1} and the constant terms. This gives seven equations, such as $\alpha_1 = A_j$, $\beta_1 = a_j$, etc. Then α_1, α_2, β_1, and β_2 can be eliminated from these seven equations to give three equations in twelve unknowns, ϕ_j, ϕ_{j-1}, ..., $\bar{\xi}_j$, $\bar{\xi}_{j-1}$. This procedure is repeated by subtracting equation (A3-1b) from (A3-1a) and equation (A3-4b) from (A3-4a). Again, a term-by-term comparison gives a similar set of seven equations, which, after elimination of α_1, α_2, β_1, β_2 results in three more equations in the same twelve unknowns. The set of six equations can now be manipulated to obtain the recursion relations

$$\phi_j = \frac{1}{Q_j} b_{\bar{\phi}} C_j, \qquad \gamma_j = -\frac{1}{Q_j} D_\gamma c_j,$$

$$\bar{\phi}_j = \frac{1}{Q_j} B_\phi c_j, \qquad \bar{\gamma}_j = -\frac{1}{Q_j} d_{\bar{\gamma}} C_j, \qquad \text{(A3-5)}$$

$$\xi_j = \frac{1}{Q_j}\left[b_{\bar{\phi}}\,(E_j - A_j\,\xi_{j-1}) + D_{\gamma}\,(e_j - a_j\,\bar{\xi}_{j-1})\right],$$

$$\bar{\xi}_j = \frac{1}{Q_j}\left[d_{\bar{\gamma}}\,(E_j - A_j\,\xi_{j-1}) + B_{\phi}\,(e_j - a_j\,\bar{\xi}_{j-1})\right]$$

where

$$B_{\phi} = B_j - A_j\,\phi_{j-1}, \qquad b_{\bar{\phi}} = b_j - a_j\,\bar{\phi}_{j-1},$$

$$D_{\gamma} = D_j - A_j\,\gamma_{j-1}, \qquad d_{\bar{\gamma}} = d_j - a_j\,\bar{\gamma}_{j-1}, \qquad \text{(A3-6)}$$

$$Q_j = B_{\phi}\,b_{\bar{\phi}} - D_{\gamma}\,d_{\bar{\gamma}}$$

In equations (A3-5) and (A3-6) terms with suffix j-1 are to be dropped when j = 2. Also, we have $k_M = \xi_M$ and $\varepsilon_M = \bar{\xi}_M$; and equations (A3-3) can now be used to obtain k and ε for j = M-1, ..., 3, 2.

The equations for stream function and vorticity arising in both laminar and turbulent flow problems (e.g. refer second and third chapters) can also be cast in the present form and solved simultaneously. A FORTRAN program for solving the coupled linear system of equations given by the form in equations (A3-1) is included.

```
      SUBROUTINE TRISIM(JFLT,W1,W2)
C       THIS SUBROUTINE SOLVES TWO COUPLED TRIDIAGONAL TYPE EQUATIONS
C       A1*W1(J-1)+B1*W1(J)+C1*W1(J+1) = D1*W2(J)+E1          AND
C       A2*W2(J-1)+B2*W2(J)+C2*W2(J+1) = D2*W1(J)+E2          WHERE
C       A1 IS WRITTEN FOR A1(J),.....,E2 FOR E2(J).     W1, W2 ARE SOLN.
C       VECTORS.   ALL THE DIMENSIONED VARIABLES HAVE DIMENSION JFLT.
C       BOUNDARY CONDITIONS FOR DIFFERENCE EQUATIONS ARE APPLIED AT J=1
C       AND J=JFLT.   HENCE COEFFICIENTS A1 THRU E2 ARE ZERO FOR J=1 AND
C       J=JFLT.   M=JFLT-1.    WE SOLVE FOR W1 AND W2 FOR J=2,3,....,M.
C       ALSO  0=A1(2)=C1(M)=A2(2)=C2(M).          WE GET AN (N X N)
C       QUIN-DIAGONAL MATRIX OF SEMIBANDWIDTH P,   N=2*(JFLT-2),  P=M.
C       COMMON BLOCKS BLKK & BLKE SUPPLY COEFFICIENTS A1 THRU E2.
C
      COMMON/BLKK/A1(31),B1(31),C1(31),D1(31),E1(31)
      COMMON/BLKE/A2(31),B2(31),C2(31),D2(31),E2(31)
      DIMENSION PHI1(31),PHI2(31),GAM1(31),GAM2(31),XI1(31),XI2(31)
      DIMENSION W1(31),W2(31)
C
      M=JFLT-1
      L1=JFLT-2
      J=2
      BP1=B1(J)
      DG1=D1(J)
      BP2=B2(J)
      DG2=D2(J)
      Q = 1.0/(BP1*BP2-DG1*DG2)
      PHI1(J)=Q*BP2*C1(J)
      PHI2(J)=Q*BP1*C2(J)
      GAM1(J)=-Q*DG1*C2(J)
      GAM2(J)=-Q*DG2*C1(J)
      EE1=E1(J)
      EE2=E2(J)
      XI1(J)=Q*(BP2*EE1+DG1*EE2)
      XI2(J)=Q*(DG2*EE1+BP1*EE2)
      DO 1000 J=3,L1
      BP1=B1(J)-A1(J)*PHI1(J-1)
      DG1=D1(J)-A1(J)*GAM1(J-1)
      BP2=B2(J)-A2(J)*PHI2(J-1)
      DG2=D2(J)-A2(J)*GAM2(J-1)
      Q = 1.0/(BP1*BP2-DG1*DG2)
      EE1=E1(J)-A1(J)*XI1(J-1)
      EE2=E2(J)-A2(J)*XI2(J-1)
      PHI1(J)=Q*BP2*C1(J)
      PHI2(J)=Q*BP1*C2(J)
      GAM1(J)=-Q*DG1*C2(J)
      GAM2(J)=-Q*DG2*C1(J)
      XI1(J)=Q*(BP2*EE1+DG1*EE2)
 1000 XI2(J)=Q*(DG2*EE1+BP1*EE2)
      J=M
      BP1=B1(J)-A1(J)*PHI1(J-1)
      DG1=D1(J)-A1(J)*GAM1(J-1)
      BP2=B2(J)-A2(J)*PHI2(J-1)
      DG2=D2(J)-A2(J)*GAM2(J-1)
      Q = 1.0/(BP1*BP2-DG1*DG2)
      EE1=E1(J)-A1(J)*XI1(J-1)
      EE2=E2(J)-A2(J)*XI2(J-1)
      XI1(J)=Q*(BP2*EE1+DG1*EE2)
      XI2(J)=Q*(DG2*EE1+BP1*EE2)
      W1(M)=XI1(M)
      W2(M)=XI2(M)
      DO 2000 J2=2,L1
      J=M+1-J2
      W1(J)=-PHI1(J)*W1(J+1)+GAM1(J)*W2(J+1)+XI1(J)
 2000 W2(J)=-PHI2(J)*W2(J+1)+GAM2(J)*W1(J+1)+XI2(J)
      RETURN
      END
```

APPENDIX A4

CORRECTIONS FOR THE REFRACTION AT THE TUBE WALL

Corrections are needed to account for the refraction at the tube wall. As is mentioned in the fourth chapter, the corrections are applied only to account for the displacement of the measuring volume and the change in the beam intersection angle 2i. Several simplifications are possible as half the beam-intersection angle i (7.1 degrees in water) is small. The relations obtained here are satisfactory for the particular study, but they should not be considered as general laws in optics. However, the principles involved are general and can be adopted elsewhere. The wavelengths of light changes from λ to λ/μ_w, where μ_w is the refractive index of water. This change along with the change in the beam-intersection angle evaluated in this appendix is to be accounted for while applying equation (29).

A4.1. Corrections in V_Z-Measurements

The general optical arrangement can be seen from Figure 98, where a single laser beam is shown. The relation between semiangles i_o in air and i in water is

$$\frac{\sin i_o}{\sin i} = \mu_w = 1.33 \qquad \text{(A4-1)}$$

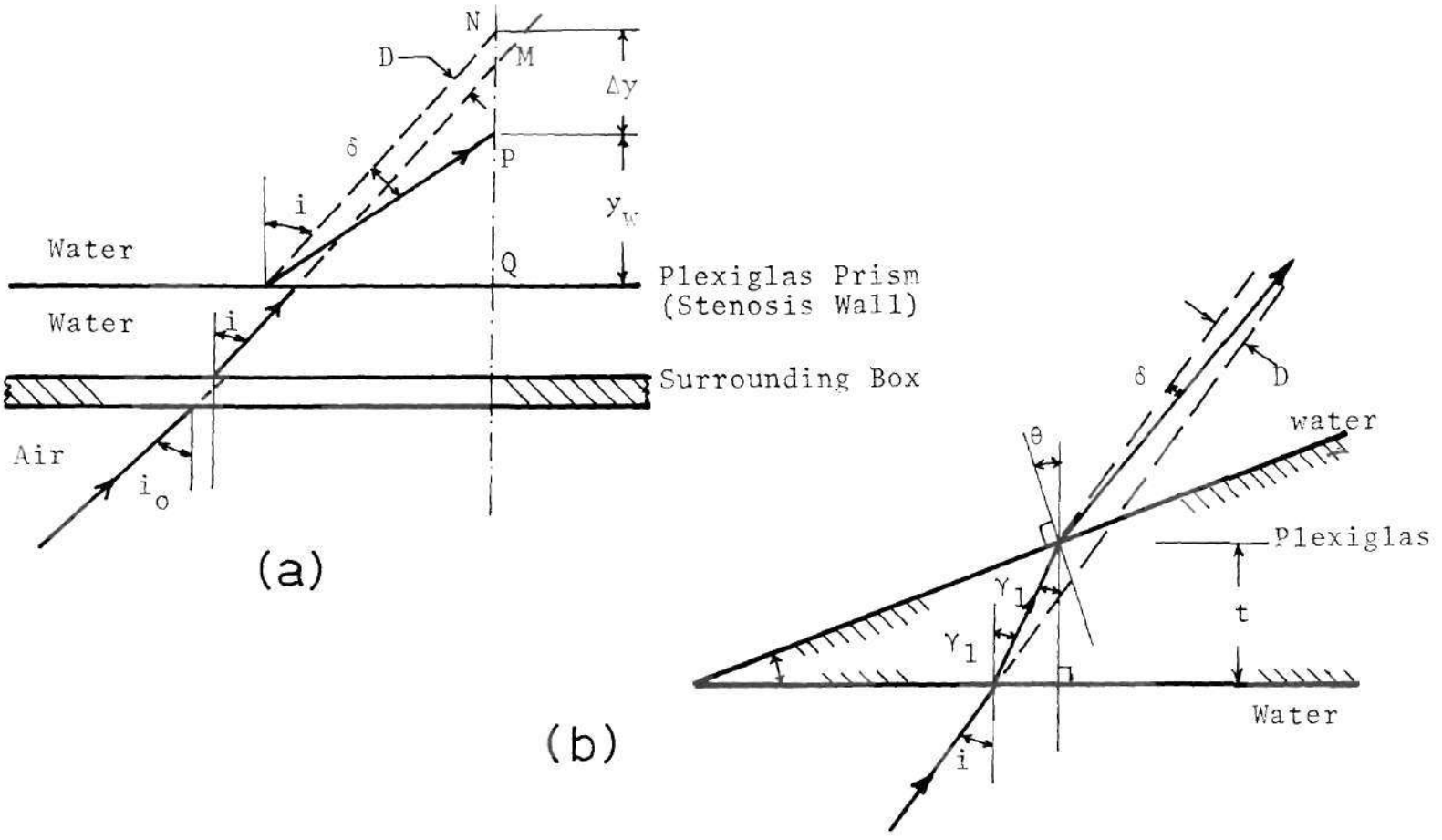

Figure 98. Refraction at Stenosis Wall; Measurements of Axial Velocity

For $i_o = 9.46°$, the value of i is 7.1°. The displacement of the beams at the plexiglas wall of the surrounding tank is of no consequence. The beam suffers a displacement D and refraction δ at the wall of the test section, and as a result the point M is relocated at P (Figure 98a). To move this point from Q on the wall by a distance y_w, the laser is to be traversed by y(air) in the same direction. When the test section wall is of constant thickness (e.g. straight portion of the tube), the relations between y_w and y(air) can be written immediately as

$$\frac{y_w}{y(air)} = \frac{\tan (i_o)}{\tan (i)} = \mu'. \qquad (A4\text{-}2)$$

Here, μ' is very close to μ_w and for the present case $\mu' = 1.34$.

When the test section wall acts like a prism, equation (A4-2) can be extended to

$$(y_w + \Delta y - \frac{D}{\sin(i)})_P - (y_w + \Delta y - \frac{D}{\sin(i)})_o = \mu' y(air), \qquad (A4\text{-}3)$$

where suffix "o" corresponds to any reference point. It is convenient to measure the distance from point Q on the wall. Then equation (A4-3) reduces to

$$y_w + \Delta y - \frac{D-D_o}{\sin(i)} = \mu' y(air). \qquad (A4\text{-}4)$$

The details of the refraction at the tube wall are considered in Figure 98b to evaluate the terms in this equation. Here

θ = local slope of the stenosis wall; $\theta = \theta(Z)$. It changes when the laser is traversed radially also.

μ_p = refractive index of plexiglas (1.49)

μ = refractive index of plexiglas w.r.t. water

$= \mu_p/\mu_w = 1.120.$

Now, referring to Figure 98b

$$\mu = \frac{\sin(i)}{\sin(\gamma_1)} = \frac{\sin(i+\theta+\delta)}{\sin(\gamma_1+\theta)} \qquad \text{(A4-5)}$$

For small i, this simplifies to

$$\sin\delta \simeq (\mu \frac{\cos\gamma_1}{\cos i} - 1)\tan\theta \simeq 0.12176 \tan\theta. \qquad \text{(A4-6)}$$

$$D = \frac{t \sin(i-\gamma_1)}{\cos(\gamma_1)} \simeq t \sin(i-\gamma_1) \qquad \text{(A4-7)}$$

It can be shown that in the present study, $(D-D_o)/\sin(i)$ is negligible compared to Δy and hence equation (A4-4) simplifies to

$$y_w + \Delta y = \mu' y(\text{air}) \qquad \text{(A4-8)}$$

Now equations (A4-6 and A4-8) are to be solved iteratively subject to a known (sinusoidal) variation of θ. This variation is simplified further at the five stations where measurements are undertaken.

(i) Throat (Z = 0)

The angle θ is assumed to vary linearly with Z or y(air), not y_w. Then this variation is 0° to 4.727° when the measuring volume is translated from the inner wall (one closer to the laser) to the outer wall. The corresponding variation in δ is 0 to δ_o (δ_o = 0.575°). Both the beams bend symmetrically and the measuring volume remains in the plane Z = 0. The semi-angle of beam intersection changes from i (7.1°) to $i+\delta_o$. It is necessary to traverse the laser by 0.807" to cover the throat diameter of 1". In the absence of the prismatic effect it would have been 0.752", the only contributing factor being the first refraction at the wall of the surrounding tank.

(ii) Midplanes (Z = ±1)

At this station θ is assumed to be constant and equal to 22.5° resulting in a constant δ of 2.89°. When the laser is traversed towards the outer wall, both the rays bend towards the throat by the same angle δ and the intersection angle 2i remains unaffected. Now the laser is to be moved axially, away from the throat by an amount

$$\Delta z \simeq \frac{y_w \sin(\delta)}{\cos^2(i)} \qquad \text{(A4-9)}$$

to retain the measuring volume in the same plane. Further, Δy in equation (A4-8) is

$$\Delta y \simeq \frac{y_w \sin^2(\delta)}{\cos^2(i)} \qquad \text{(A4-10)}$$

(iii) Entrance and exit planes of the stenosis ($Z = \pm 2$)

Only the beam closer to the throat bends by an angle δ towards the throat and correction factors Δy and Δz are given by

$$\Delta y \simeq - \frac{(y_w - \Delta y)\sin(\delta)}{\sin(2i-\delta)} \qquad \text{(A4-11)}$$

$$\Delta z \simeq \Delta y \tan(i) \qquad \text{(A4-12)}$$

and

$$\theta \simeq 35.343\, y_w \tan(i-\delta) \qquad \text{(A4-13)}$$

$$\delta \simeq 4.3034\, y_w \tan(i-\delta). \qquad \text{(A4-14)}$$

A4-2. Corrections in V_ϕ-measurements

Details of the optical arrangement and the refraction of the laser beam in different positions are displayed in

Figure 99a. Symmetry is maintained and hence only one beam is considered. When the beam passes through the center of the tube as in position C, it does not bend anywhere; while in the positions B and E on either side of C, it bends in the opposite directions as shown. The positions A and F are the extreme positions of B and E. Equations derived in the first part are used here. Referring to Figures (99a and b)

ϕ--the angular measure of the point where the beam emerges inside the tube.

$\Delta\phi$--the prismatic angle leading to deflection of the beam by angle δ.

i, γ_1--angles of incidence and refraction. They are not constant any more.

q, q_1--inclination of the beam to the horizontal, outside the tube and in the plexiglas wall respectively.

t--$R_2 - R_1$ = thickness of the wall

β--$(i - \gamma_1) = (q - q_1)$

D--displacement of the beam due to thickness t.

D_o--D at $\phi = 0$

The angle q_1 changes with ϕ but can be assumed to be constant and equal to q. One can write

$$\Delta\phi = \frac{t}{R_2} (q - \phi) \qquad \text{(A4-15)}$$

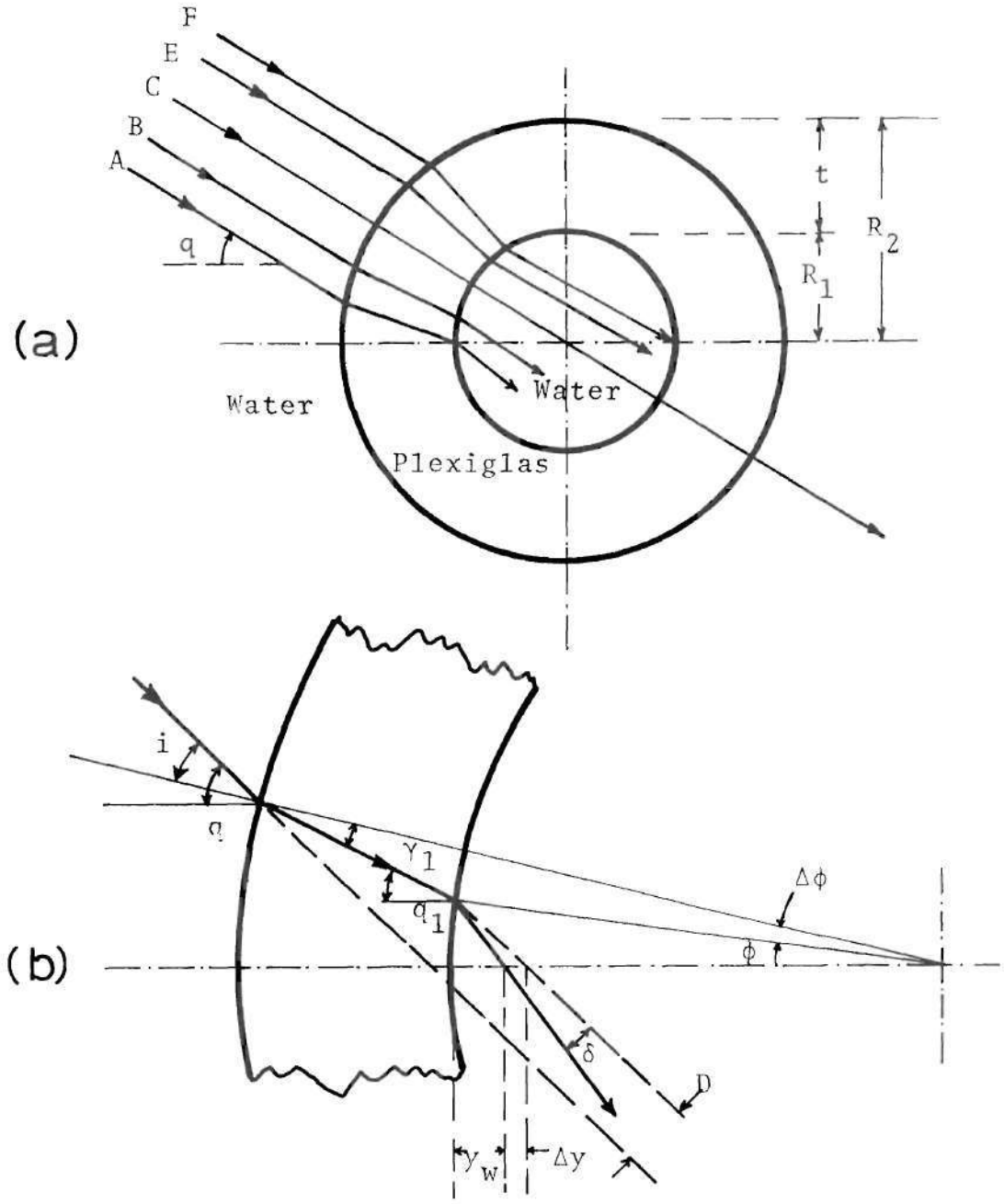

Figure 99. Refraction at Pipe Wall; Measurements of Azimuthal Velocity

Equation (A4-6) is simplified now to

$$\delta = 0.12\ \Delta\phi = 0.12\ \frac{t}{R_2}\ (q-\phi) \qquad \text{(A4-16)}$$

Some of the terms are approximated as shown below

$$i = q-\phi-\Delta\phi = (q-\phi)\ \frac{R_1}{R_2}$$

$$\beta = i-\gamma_1 = (\frac{\mu-1}{\mu})\ i = (\frac{\mu-1}{\mu})(q-\phi)\ \frac{R_1}{R_2}$$

$$\Delta y = y_w\ \frac{\delta}{q} \qquad \text{(A4-17)}$$

$$(y_w+\Delta y)/R_1 = \phi/q \qquad \text{(A4-18)}$$

The displacement term cannot be neglected now as was done earlier. It is evaluated as

$$D = t\beta = t\ (\frac{R_1}{R_2})(\frac{\mu-1}{\mu})(q-\phi),$$

$$(D-D_o) = -t\ (\frac{R_1}{R_2})(\frac{\mu-1}{\mu})\phi = -0.107\ t(\frac{R_1}{R_2})\phi, \qquad \text{(A4-19)}$$

and is substituted in an equation similar to (A4-4)

$$y_w + \Delta y - \frac{D-D_o}{\sin(q)} = \mu' y(\text{air}). \qquad \text{(A4-20)}$$

Again, $\mu' = 1.34$. Now equations (A4-16,17,18) are to be solved to obtain δ, Δy, and ϕ for a given y_w and then equations (A4-19 and 20) can be solved to estimate the corresponding y(air). It is necessary to traverse the laser by y(air) = 0.744" (instead of 0.752") to cover the throat diameter of 1". The maximum change in the beam intersection angle was 7.2%.

A4.3. Evaluation of the Accuracy of the Corrections

The corrections applied have been obtained from the simple laws of optics and by a straightforward procedure. However, their validity is to be evaluated due to the several approximations assumed and the large number of equations involved. To do this, the measuring volume was traversed from one wall to the other and then the calculated and actual distances of laser traverse were compared. This test gave satisfactory results. A second test is to plot the velocities measured with and without the corrections and examine the trend. Figure 100 is such a display of axial velocity at Z = 0 and -2. Velocity fluctuations u' and w' at the throat are plotted in Figure 101. In these figures the corrections indicated are only for the refraction at the wall of the circular test section. The first refraction at the wall of the surrounding tank is already accounted for even in the uncorrected velocity plots. The general trend towards symmetry heightens the confidence in the corrections. The

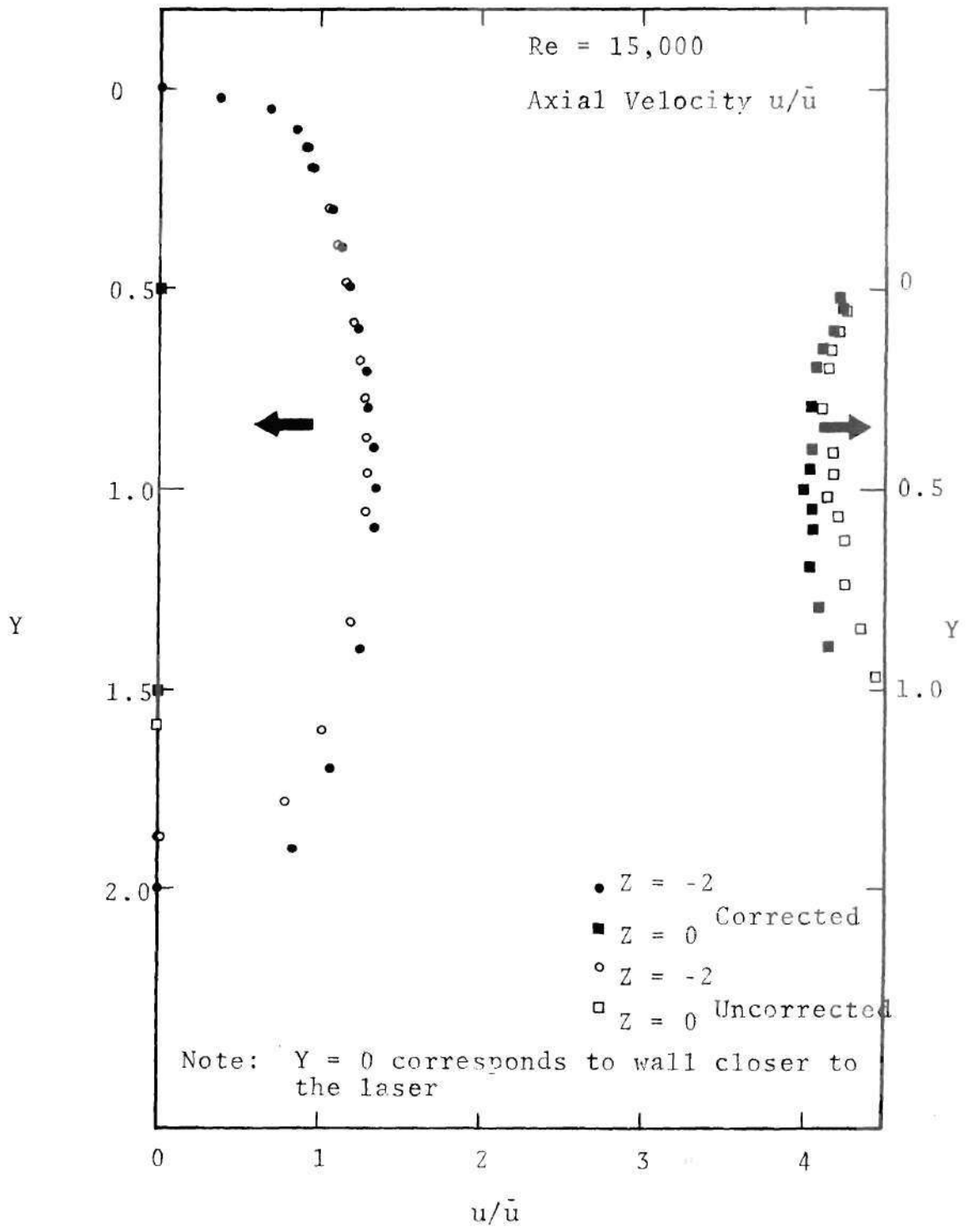

Figure 100. Comparison of Corrected and Uncorrected Velocities

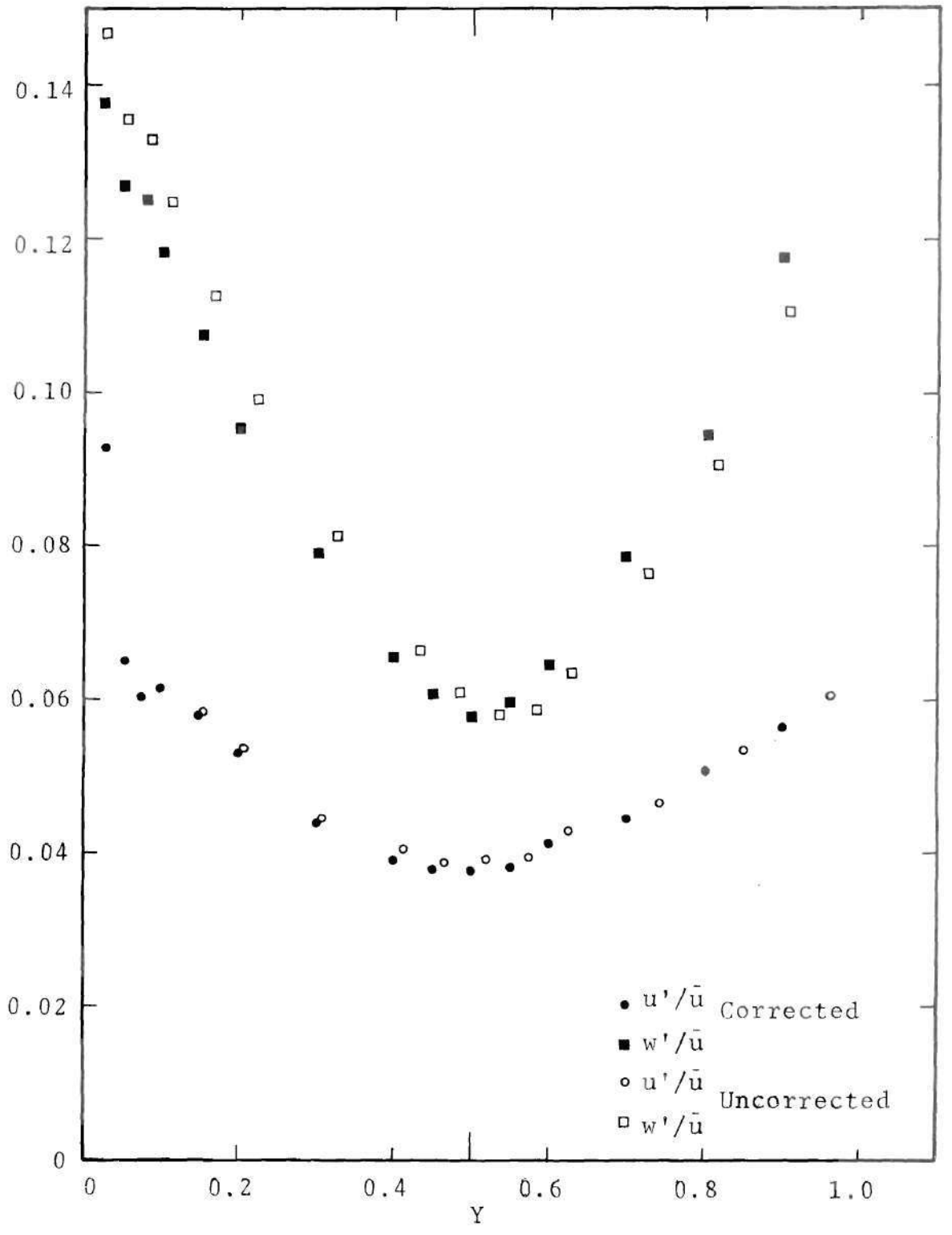

Figure 101. Comparison of Corrected and Uncorrected Velocity Fluctuations

large magnitude of the corrections involved also clearly indicates their necessity. The corrections required in the measurement of the axial component of velocity are small close to the wall toward the laser. This information can be useful in several measurements.

BIBLIOGRAPHY

1. Haust, M. D. and More, R. H. (1971) Development of modern theories on the pathogenesis of atherosclerosis. In the Pathogenesis of atherosclerosis, ed. by Wissler, R. W. and Geer, J. C. American Association of Pathologists and Bacteriologists, Montreal, Canada.

2. Fry, D. L. (1968) Acute vascular endothelial changes associated with increased blood velocity gradients. Circulation Res. 22, pp. 165-197.

3. Fry, D. L. (1973) Responses of the arterial wall to certain physical factors. Atherogenesis: Initiating factors. A Ciba Foundation Symposium 12, pp. 93-125. (New Series.) Elsevier, Excerpta Medica, North Holland, Amsterdam.

4. Caro, C. G., Fitz-Gerald and Schroter, R. C. (1971) Atheroma and arterial wall shear observation, correlation and proposal of a shear dependent mass transfer mechanism for atherogenesis. Proc. Roy. Soc. London. B. 177, pp. 109-159.

5. Caro, C. G. (1973) Transport of materials between blood and wall in arteries. Atherogenesis: Initiating factors. A Ciba Foundation Symposium 12, pp. 127-164. (New Series.) Elsevier, Excerpta Medica, North Holland, Amsterdam.

6. Nerem, R. M., Polsley, J. S., Robinson, D. L. and Carey, W. E. (1973) Shear dependent transport of albumin between blood and arterial wall. 26th Annual Conference on Engineering in Medicine and Biology, p. 413.

7. Adams, C. W. M. (1973) Tissue changes and lipid entry in developing atheroma. Atherogenesis: Initiating factors. A Ciba Foundation Symposium 12, pp. 5-37. (New Series.) Elsevier, Excerpta Medica, North Holland, Amsterdam.

8. Sako, Y. (1962) Effects of turbulent blood flow and hypertension on experimental atherosclerosis. JAMA 179, pp. 36-40.

9. Gessner, F. B. (1973) Hemodynamic theories of atherogenesis. Circulation Res. 33, pp. 259-266.

10. Roach, M. R. (1972) Poststenotic dilatation in arteries. In Cardiovascular fluid dynamics, ed. by Bergel, D. H., Academic Press, London.

11. Smith, R. L., Blick, E. F., Coalson, J. and Stein, P. D. (1972) Thrombus production by turbulence. J. appl. Physiol. 32, pp. 261-264.

12. Stein, P. D. and Sabbah, H. N. (1974) Measured turbulence and its effect upon thrombus formation. Circulation Res. 35, pp. 608-614.

13. Mustard, J. F., Murphy, E. A., Rowsell, H. C. and Downie, H. G. (1962) Factors influencing thrombus formation in vivo. Am. J. Med. 33, pp. 621-647.

14. Leverett, L. B., Hellums, J. D., Alfrey, C. P. and Lynch, E. C. (1972) Red blood cell damage by shear stress. Biophys. J. 12, pp. 257-273.

15. Ritter, R. C., Zinner, N. R. and Sterling, A. M. (1974) Analysis of drop intervals in jets modeling obstruction of the urinary tract. Physics Med. Biol. 19, pp. 161-170.

16. Aiello, G., Lafrance, P., Ritter, R. C. and Trefil, J. S. (1974) The urinary drop spectrometer. Physics to-day 27, September, pp. 23-30.

17. Lighthill, J. (1973) Mathematical biofluiddynamics. Society for Industrial and Applied Mathematics, Philadelphia, Penn.

18. Young, D. F. and Tsai, F. Y. (1973) Flow characteristics in models of arterial stenosis-I. Steady flow. J. Biomechanics 6, pp. 395-410.

19. Young, D. F. and Tsai, F. Y. (1973) Flow characteristics in models of arterial stenoses--II. Unsteady flow. J. Biomechanics 6, pp. 547-559.

20. Seed, W. A. and Wood, N. B. (1971) Velocity patterns in the aorta. Cardiovasc. Res. 5, pp. 319-330.

21. Nerem, R. M. and Seed, W. A. (1972) An in vivo study of aorta flow disturbances. Cardiovasc. Res. 6, pp. 1-14.

22. Giddens, D. P., Mabon, R. F. and Cassanova, R. A. (1976) Measurements of disordered flows distal to subtotal vascular stenoses in the thoracic aortas of dogs. Circulation Res. 39, pp. 112-119.

23. Stein, P. D. and Sabbah, H. N. (1976) Turbulent blood flow in the ascending aorta of humans with normal and diseased aortic valves. Circulation Res. 39, pp. 58-65.

24. Stein, P. D., Sabbah, H. N. and Blick, E. F. (1975) Contribution of erythrocytes to turbulent blood flow. Biorheology 12, pp. 293-299.

25. Golia, C. and Evans, N. A. (1973) Flow separation through annular constrictions in tubes. Exp. Mech. 13, pp. 157-162.

26. Lee, J. S. and Fung, Y. C. (1970) Flow in locally constricted tubes at low Reynolds numbers. J. appl. Mech. 37, pp. 9-16.

27. Morgan, B. E. and Young, D. F. (1974) An integral method for the analysis of flow in arterial stenoses. Bull. Math. Biol. 36, pp. 39-53.

28. Cheng, L. C., Clark, M. E. and Robertson, J. M. (1972) Numerical calculations of oscillating flow in the vicinity of square wall obstacles in plane conduits. J. Biomechanics 5, pp. 467-484.

29. Cheng, L. C., Robertson, J. M. and Clark, M. E. (1973) Numerical calculations of plane oscillatory nonuniform flow--II. Parametric study of pressure gradient and frequency with square wall obstacles. J. Biomechanics 6, pp. 521-538.

30. Daly, B. J. (1976) A numerical study of pulsatile flow through stenosed canine femoral arteries. J. Biomechanics 9, pp. 465-475.

31. McDonald, D. A. (1974) Blood flow in arteries. Edward Arnold, London.

32. Schneck, D. J. (1973) Pulsatile blood flow in a diverging circular channel. Ph.D. Thesis, Case Western Reserve University.

33. Davis, L. A. Jr. (1973) Flow characteristics associated with laminar oscillating flow in horizontal tube containing mild axisymmetric constriction. Ph.D. Thesis, Iowa State University.

34. Cheng, R. T. (1972) Numerical solution of the Navier-Stokes equations by finite element method. Physics Fluids 15, pp. 2098-2105.

35. Chow, J. C. F. and Soda, K. (1973) Laminar flow and blood oxygenation in channels with boundary irregularities. J. appl. Mech. 40, pp. 843-850.

36. Soda, K. and Chow, J. C. F. (1976) Blood oxygenation in tubular oxygenators with wavy walls. J. Biomechanics 9, pp. 135-140.

37. Macagno, E. O. and Hung, T. K. (1967) Pressure, Bernouilli sum, and momentum and energy relations in a laminar zone of separation. Physics Fluids 10, pp. 78-82.

38. Macagno, E. O. and Hung, T. K. (1967) Computational and experimental study of a captive annular eddy. J. Fluid Mech. 28, pp. 43-64.

39. Vrentas, J. S. and Duda, J. L. (1973) Flow of a Newtonian fluid through a sudden contraction. Appl. Sci. Res. 28, pp. 241-260.

40. Mills, R. D. (1968) Numerical solutions of viscous flow through a pipe orifice at low Reynolds number. J. mech. Engng. Sci. 10, pp. 133-140.

41. Zampaglione, D. and Greppi, M. (1972) Numerical study of a viscous flow through a pipe orifice. Meccanica 7, pp. 151-164.

42. Goldstein, R. J. (1970) Laminar separation, reattachment and transition of the flow over a downstream facing step. J. bas. Engng. 92, pp. 732-741.

43. Seeley, B. D. and Young, D. F. (1976) Effect of geometry on pressure losses across models of arterial stenoses. J. Biomechanics 9, pp. 439-448.

44. Clark, C. (1976) The fluid mechanics of aortic stenosis-I. Theory and steady flow experiments. J. Biomechanics 9, pp. 521-528.

45. Clark, C. (1976) The fluid mechanics of aortic stenosis-II. Unsteady flow experiments. J. Biomechanics 9, pp. 567-573.

46. Tsai, F. Y. and Young, D. F. (1973) Some turbulence measurements in an arterial stenosis. Proc. of 10th Annual Rocky Mountain Bioengng. Symp., pp. 59-62.

47. Kim, B. M. and Corcoran, W. H. (1974) Experimental measurements of turbulence spectra distal to stenoses. J. Biomechanics 7, pp. 335-342.

48. Cassanova, R. A. (1975) An experimental investigation of steady and pulsatile flow through partial occlusions in a rigid tube. Ph.D. Thesis, Georgia Institute of Technology.

49. Krall, K. M. and Sparrow, E. M. (1966) Turbulent heat transfer in the separated, reattached, and redevelopment regions of a circular tube. J. Heat Transfer 88, pp. 131-136.

50. Back, L. H. and Roschke, E. J. (1972) Shear-layer flow regimes and wave instabilities and reattachment lengths downstream of an abrupt circular channel expansion. J. appl. Mech. 39, pp. 677-681.

51. Roschke, E. J. and Back, L. H. (1976) The influence of upstream conditions on flow reattachment lengths downstream of an abrupt circular channel expansion. J. Biomechanics 9, pp. 481-483.

52. Runchal, A. K. and Spalding, D. B. (1972) Steady turbulent flow and heat transfer downstream of a sudden enlargement in a pipe of circular cross-section. Warme-und Stoffubertragung 5, pp. 31-38.

53. Gosman, A. D., Khalil, E. E. K. H. and Launder, B. E. (1975) Computations of flows in ducts with sudden elargements. Prepared for use in course on "Turbulent recirculating flows," held at the Pennsylvania State University.

54. Chin, E., Rafiinejad, D. and Seban, R. A. (1972) Prediction of the flow and heat transfer in rectangular wall cavity with turbulent flow. J. appl. Mech. 39, pp. 351-359.

55. Chin, E. (1970) Numerical Solution of Navier-Stokes' equations for flow and heat transfer in a rectangular notch. Ph.D. Thesis, University of California, Berkeley.

56. Schlichting, H. (1968) Boundary layer theory. Mcgraw-Hill Book Company, New York.

57. Gosman, A. D., Pun, W. M., Runchal, A. K., Spalding, D. B. and Wolfshtein, M. (1969) Heat and Mass Transfer in Recirculating Flows. Academic Press, New York.

58. Lester, W. G. S. (1961) The flow past a pitot tube at low Reynolds numbers. Rep. Memo. Aeronaut. Res. Council 3240.

59. Deshpande, M. D., Giddens, D. P. and Mabon, R. F. (1976) Steady laminar flow through modelled vascular stenoses. J. Biomechanics 9, pp. 165-174.

60. Mellor, G. L. and Herring, H. J. (1973) A survey of the mean turbulent field closure models. A.I.A.A. Journal 11, pp. 590-599.

61. Launder, B. E. and Spalding, D. B. (1972) Mathematical Models of turbulence. Academic Press, New York.

62. Harlow, F. H. and Nakayama, P. I. (1967) Turbulence transport equations. Physics Fluids 10, pp. 2323-2332.

63. Hanjalic, K. and Launder, B. E. (1972) A Reynolds stress model of turbulence and its application to thin shear flows. J. Fluid Mech. 52, pp. 609-638.

64. Hanjalic, K. (1974) Prediction of turbulent flow in annular ducts with differential transport model of turbulence. Warme-und Stoffubertragung 7, pp. 71-78.

65. Launder, B. E., Reece, G. J. and Rodi, W. (1975) Progress in the development of a Reynolds-stress turbulence model. J. Fluid Mech. 68, pp. 537-566.

66. Pope, S. B. and Whitwlaw, J. H. (1976) The calculation of near-wake flows. J. Fluid Mech. 73, pp. 9-32.

67. Launder, B. E. (1975) Progress in the modelling of turbulent transport. Supplementary notes for course "Turbulent recirculating flows--Prediction and Measurement," held at the Pennsylvania State University.

68. Launder, B. E. and Spalding, D. B. (1972) Turbulence models and their application to the prediction of internal flows. Heat and Fluid flow 2, pp. 43-54.

69. Jones, W. P. and Launder, B. E. (1972) The prediction of laminarization with a two-equation model of turbulence. Int. J. Heat Mass Transfer 15, pp. 301-314.

70. Jones, W. P. and Launder, B. E. (1973) The calculation of low Reynolds-number phenomena with a two-equation model of turbulence. Int. J. Heat Mass Transfer 16, pp. 1119-1130.

71. Launder, B. E. and Spalding, D. B. (1974) The numerical computation of turbulent flows. Computer Methods in Applied Mechanics and Engineering 3, pp. 269-289.

72. Barbin, A. R. (1961) Development of turbulence in the inlet of a smooth pipe. Ph.D. Thesis, Purdue University.

73. Barbin, A. R. and Jones, J. B. (1963) Turbulent flow in the inlet region of a smooth pipe. J. bas. Engng. 85, pp. 29-34.

74. Richman, J. W. and Azad, R. S. (1973) Developing turbulent flow in smooth pipes. Appl. Sci. Res. 28, pp. 419-441.

75. Carnahan, B., Luther, H. A. and Wilkes, J. O. (1969) Applied Numerical Methods. John Wiley and Sons, Inc., New York.

76. DISA Type 55L Laser Doppler Anemometer Mark II, Instruction Manual, DISA Electronics, Franklin Lakes, N.J. 07417

77. Fourier Analyzer System 5451 Manual (1972) Hewlett-Packard Company, Santa Clara, California 95050.

78. George, W. K. and Lumley, J. L. (1973) The laser-Doppler velocimeter and its application to the measurement of turbulence. J. Fluid Mech. 60, pp. 321-362.

79. Resch, F. J. (1970) Hot-film turbulence measurements in water flow. J. Hydraulics Division, Proc. American Society of Civil Engineers. pp. 787-800.

80. Ballantyne, A. and Bray, K. N. C. (1975) Velocity power spectral measurements in jet diffusion flames using laser anemometry. In the accuracy of flow measurements by laser Doppler methods. Proc. of the LDA-Symp., Copenhagen. pp. 674-683.

81. McDonald, J. W., Denny, V. E. and Mills, A. F. (1972) Numerical solutions of the Navier-Stokes equations in the inlet regions. J. appl. Mech. 39, pp. 873-878.

82. Van Driest, E. R. (1956) On turbulent flow near a wall. J. Aero. Sci. 23, pp. 1007-1011 and 1036.

83. Van Dyke, M. (1970) Entry flow in a channel. J. Fluid Mech. 44, pp. 813-823.

84. Bradshaw, P. Dean, R. B. and McEligot, D. M. (1973) Calculation of interacting turbulent shear layers: Duct flow. J. Fluids Engng. 95, pp. 214-220.

85. Laufer, J. (1954) The structure of turbulence in fully developed pipe flow. NACA Rept. 1174.

86. Hussain, A. K. M. F. and Ramjee, V. (1976) Effects of the axisymmetric contraction shape on incompressible turbulent flow. J. Fluids Engng. 98, pp. 58-69.

87. Hoffman, G. H. (1975) Improved form of the low Reynolds number k-ε turbulence model. Physics Fluids 18, pp. 309-312.

88. Evans, D. J. (1974) Iterative sparse matrix Algorithms. In software for numerical mathematics, ed. by Evans, D. J., Academic Press, London, pp. 49-83.

VITA

Mohan Dhondorao Deshpande was born on April 30, 1945 in Shirhatti, Karnataka State, India and was graduated from the F. M. Dabali High School in 1962. He received a Bachelor of Engineering degree in Mechanical Engineering from the Karnatak University, Dharwar in 1968. He studied at the Indian Institute of Science, Bangalore and graduated in 1970 with a Master of Engineering degree in Aeronautical Engineering. In the fall of 1970 he joined the Georgia Institute of Technology as a graduate student.